1-7-2020

Liquid Phase Adsorptive Desulfurization using Modified Zeolites for Transportation and Fuel Cell Applications

Kevin Lee
University of Connecticut - Storrs, kevin.x.lee@uconn.edu

Liquid Phase Adsorptive Desulfurization using Modified Zeolites for Transportation and Fuel Cell Applications

Kevin Xin De Lee, PhD

University of Connecticut, 2020

Sulfur removal from transportation fuels is essential for maintaining a pollutant-free environment and ensuring a healthy life. Adsorptive desulfurization using zeolites is an attractive desulfurization method, because of its low energy and cost requirements compared with conventional hydrodesulfurization. However, diffusion limitations within the micropores of zeolites can reduce their adsorption capacity, especially when refractory sulfur compounds are present. Moreover, the coexistence of aromatics in fuels exacerbates selective adsorption of sulfur. These challenges may be alleviated through careful physical and chemical modification, without compromising important structural properties of the zeolite. The introduction of mesoporosity via the surfactant-assisted method creates well-ordered mesopores that allow refractory sulfur compounds to access the internal adsorption sites, thus overcoming diffusion limitations. The incorporation of Cerium (Ce) and/or Copper (Cu) via ion-exchange enhances the binding strength of the metal-adsorbate interaction through multiple adsorption configurations. Using a fixed-bed adsorption column, the resulting ion-exchanged mesoporous Y zeolites were tested for their sulfur adsorption capabilities.

Breakthrough curves show that mesoporosity increases the sulfur capacity by allowing refractory sulfur compounds to access internal adsorption sites. Metals significantly increase the selectivity towards sulfur compounds. The adsorption mechanisms of sulfur compounds were

further studied, at the molecular level, using in-situ Diffuse Reflectance Infrared Fourier Transform Spectra (DRIFTS). From DRIFTS studies, it was shown that the metals display high affinity for sulfur, via either π-complexation or direct σ-bond interaction. A reduction in capacity was realized when aromatics were added to the model fuel. Further efforts were made to investigate the role of metal composition and configuration on the selective adsorption of sulfur. It was demonstrated that 2%Cu10%CeSAY exhibits the highest adsorption capacity in the presence of aromatics. Similar adsorption capacities were obtained after two regeneration cycles. To fundamentally understand the adsorption mechanism from a theoretical perspective, density functional theory (DFT) calculations were performed using a two-layer ONIOM cluster. Subsequently, natural bond orbital (NBO) analysis was used to demonstrate the energetic importance between molecular orbitals and further identify correlations between electron transfer patterns and adsorption enthalpies. Finally, these DFT and NBO results were used to explain adsorption behavior from experimental results.

Liquid Phase Adsorptive Desulfurization using Modified Zeolites for Transportation and Fuel Cell Applications

Kevin Xin De Lee

B. S., University of Idaho, **2012**

M.S., Columbia University, **2014**

A Dissertation

Submitted in Partial Fulfillment of the

Requirements for the Degree of

Doctor of Philosophy

at the

University of Connecticut

2020

APPROVAL PAGE

Doctor of Philosophy Dissertation

Liquid Phase Adsorptive Desulfurization using Modified Zeolites for Transportation and Fuel Cell Applications

Presented by

Kevin Xin De Lee, B.S., M.S.

Major Advisor: _____
Julia A. Valla

Associate Advisor: _____
S. Pamir Alpay

Associate Advisor: _____
Jeffrey R. McCutcheon

Associate Advisor: _____
Steven L. Suib

Associate Advisor: _____
Brian G. Willis

University of Connecticut
2020

DEDICATION

This thesis is dedicated to the memory of my loving mother Audrey Ling.

"Wide, wide as the ocean, high as the heaven above;

Deep, deep as the deepest sea is my Savior's love.

I, though so unworthy, still am a child of His care;

For His Word teaches me and His love reaches me everywhere"

– Charles A. Miles

ACKNOWLEDGEMENTS

I would like to first thank my advisor, Prof. Julia Valla, for taking me under her wings and taught me everything there is to know about zeolites and how they can be extremely impactful in the world of adsorption and catalysis. Some of the reasons I joined her group were the care she shows for her students and her desire for them to do well, two characteristics that I have seen throughout my graduate career. Her knowledge and enthusiasm for clean energy research made the group exciting and a motivating environment to be in. I would also like to thank Prof. Pamir Alpay, Prof. Richard Parnas, Prof. Jeffrey McCutcheon, Prof. Steven Suib, and Prof. Brian Willis for serving on my committee. I really appreciate their willingness to take on this responsibility despite their busy schedule. I am also grateful for all the supporting staff at both UCONN ChEG department and C2E2 (Leah, Susan, Amy, Terry and Sheila). Finally, I would also like to extend my gratitude to the C2E2 technical staff, Garry and Pete, for ensuring a safe and productive environment in lab.

Many thanks go to both former and current group members for their help along the way. I was blessed to work alongside Dr. David Gamliel, whom as the first student in Valla group, made it so much easier for me to adapt and work in the group. He, together with Prof. Valla, have established a strong foundation for current and future students, myself included, by putting the group on the world map of catalysis. I would like to acknowledge the current group members including Lei Yu, Tyler Crowl and Henry Sokol for their help and great memories shared in lab. Other C2E2 graduate students that should not be forgotten are Chunxiang Zhu, William Hale and Ryan Ouimet. Special thanks go out to Dr. George Tsilomelekis and Dr. Stavros Karakalos for their collaborative work that resulted in my second and third papers. Another person that I am very grateful for is Dr. Stavros Caratzoulas, for training me on DFT calculations at the University of

Delaware. Last but not least, this work would not have been possible without the help of undergraduate students.

Finally, I would like to thank my family for all their love and support throughout my graduate school career. My mom, Audrey, was and is my biggest inspiration. Her optimism, encouragement and unconditional love played a significant role in shaping me into the person I am today. It was a challenging time when she passed away in my second year of graduate school, but it motivated me to work hard to make her proud. I will always cherish and value her positive words and support toward me. I am also grateful for my dad, Yat Ping, and sister, Elaine, for their continuous love and prayer that got me through the journey of graduate school. I would also like to acknowledge my best friend, John and his wife, Thuy, for their support and encouragement. Finally, I would like to give my biggest gratitude to my girlfriend, Akie, who plays an important role in my success in graduate school. She has been there for me since day one, after which a day never went by without feeling her constant support and love. She deserves all the chocolates and sweets in the world.

TABLE OF CONTENTS

LIST OF TABLES

LIST OF FIGURES

Chapter 1

INTRODUCTION

1.1 Rising Demand for Fossil-Fuel Energy

The demand for clean energy continues to rise with the increased use of fossil fuels. In 2018, the energy consumption in the United States saw a record high of approximately 101 quadrillion British thermal units. Petroleum, being the largest source of energy since 1950, accounts for about 37% of the energy supplied.[1] Figure 1.1 shows that the consumption of fossil-based fuels, especially petroleum and natural gas, has increased by more than 60% since 1950, attributing to growing demands in transportation and electrical power, respectively. Meanwhile, the consumption of renewable energy such as wind, solar, geothermal and biomass has increased tremendously especially since the early 2000s, during which a collective effort has been instigated to rectify toxic pollutions from fossil fuel combustion. Despite the promising growth in renewable energy and the societal mission to make it the energy of the future, there is still a huge disparity in energy density as well as transportation, storage and implementation feasibilities, when compared with fossil energy. Furthermore, renewables cannot compete with fossil fuels in filling the rising demand in energy. 80% of the world energy consumption still relies on fossil fuels as an energy source and will continue to do so for the next decade, especially with the discovery of new oil wells and further advancement of drilling technologies.[2]

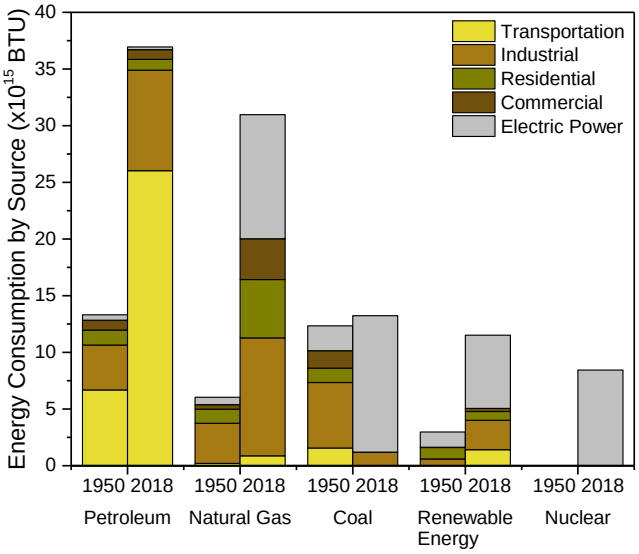

Figure 1.1: Comparison of energy consumption by primary source and sector in 1950 and 2018.[1]

As shown in Figure 1.1, the transportation sector is the largest end-use consuming sector in the United States, with petroleum being the main source of energy (70% of total petroleum consumed in 2018). While renewable energy and electrical power have been introduced in vehicles, fossil fuels are still considered the main source of energy for today and the unforeseeable future. The increasing demand in fossil-based fuels in the transportation sector, however, quickly became a global concern as toxic emissions are being released into the atmosphere. Higher driver population and cheaper car fuels following the outburst of oil discovery, and thus cheaper fuel prices, have driven car sales upward from 2012 to 2016, as indicated in Figure 1.2. Although vehicle industries were experiencing slower sales and higher gas prices 2017, the expansion of other fossil-fuel consuming sectors led to continuous increase in toxic emissions, which consequently threatens the environment and human lives.

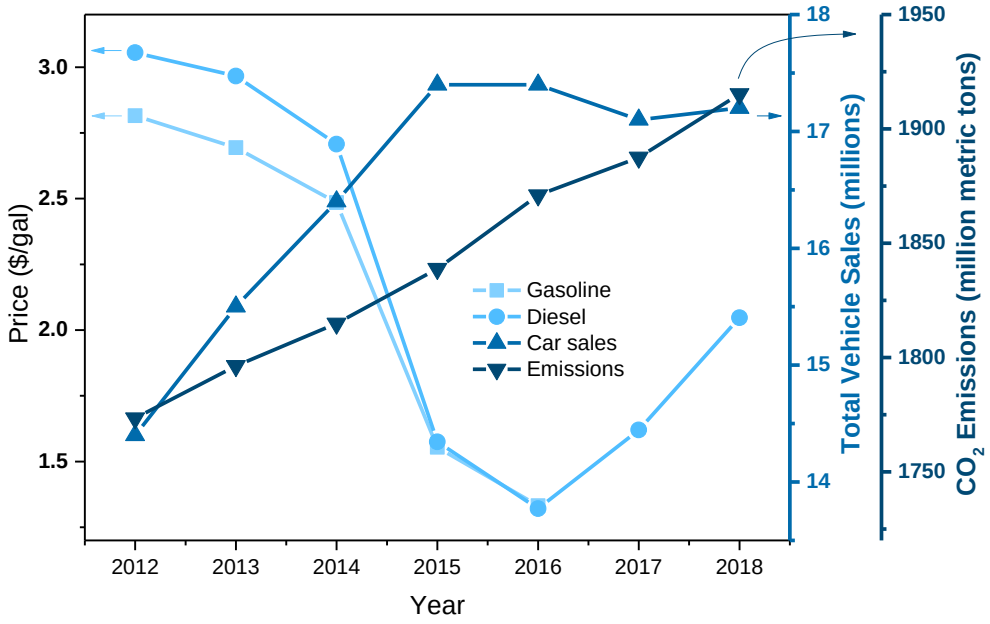

Figure 1.2: The effect of oil prices on total vehicle sales and carbon dioxide emission.

1.2 Origin and Property of Sulfur in Transportation Fuels

The release of toxic gases such as sulfur oxides (SO_x) is inevitable as fossil fuels contain naturally occurring sulfur. Figure 1.3 shows a simple schematic of a petroleum refinery plant showing distillation of crude oil to the production of final oil products. Freshly-drilled crude oil contains up to 4 wt% sulfur before being distilled and processed at the refinery to produce high quality transportation fuel products such as gasoline, jet fuel and diesel, according to the carbon number and boiling range. Once the crude has been separated into appropriate oil fraction, it is directed to hydrotreatment and fluid-catalytic cracking (FCC) steps. Valla et al. has worked on the removal of sulfur in-situ the FCC in the refinery using novel catalysts.[3,4] After hydrotreatment and processing, a typical gasoline fraction contains about 10-1,000 ppm of sulfur, whereas jet fuel and diesel contain up to 3,000 ppm and 10,000 ppm of sulfur, respectively. These levels of sulfur are unacceptably high and must be subjected to deep desulfurization before commercial use.

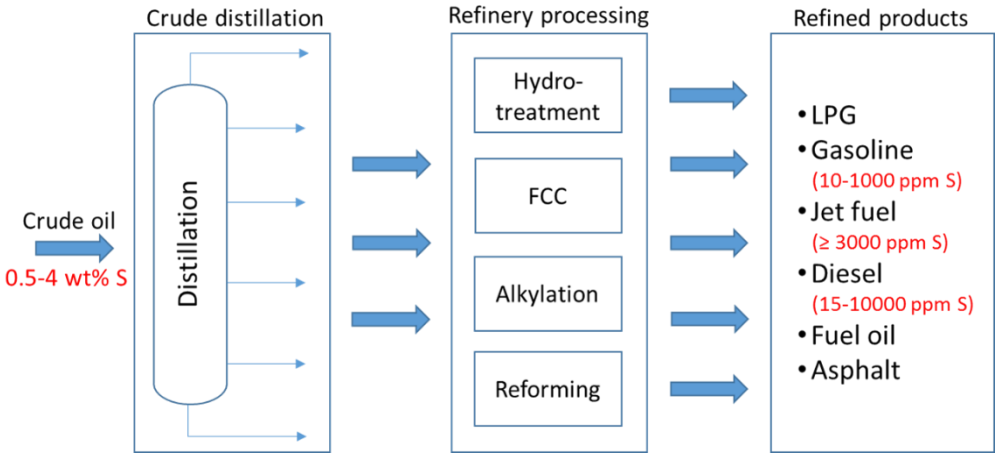

Figure 1.3: Schematic flow chart of a typical petroleum refinery before HDS.

As previously mentioned, residual sulfur molecules, ranging from sulfides to alkylated-dibenzothiophenes, are distributed among various distillate fuel fractions based on their boiling point, as depicted in Figure 1.5. For natural gas range sulfur compounds such as thiols, sulfides and mercaptans, the hydrodesulfurization (HDS) reaction occurs via direct hydrogenolysis due to the absence of aromatic rings, resulting in easy C-S bond scission and rapid production of H_2S. In fact, HDS is the most conventional method of removing sulfur from fuels.[5,6] The next lightest hydrocarbon fuel is gasoline, in which the main sulfur compounds are thiophene (TP) with a kinetic diameter of about 5.3 Å and alkyl-TP which are slightly larger. Due to their relatively small size, gasoline-range sulfur compounds can be effectively removed via HDS. Jet fuels primarily consist of benzothiophenes (BT) with a kinetic diameter of 6 Å and alkyl-BT with a slightly larger diameter. The heaviest hydrocarbon fuel is diesel, which contains not only dibenzothiophenes, but also alkylated-dibenzothiophenes having kinetic diameters of at least 9Å. Contrary to the HDS of sulfur compounds in the natural gas range, the HDS of aromatic sulfur compounds can occur via two pathways, namely hydrogenation (via π-electrons) or hydrogenolysis (via σ-bond).[7] Nonetheless, the reactivity of TP is significantly lower than that of sulfides and mercaptans. In

perspective, the difference in reactivity between the two ranges is in the orders of magnitude, as the reactivity of thiophenes highly depends on the number of rings.[8] This means that sulfur compounds with one or more 6-membered aromatic rings in the heavier fractions of oil would exhibit significantly lower HDS reactivity, as shown in Fig. 1.4(a). As expected, refractory sulfur compounds, such as alkyl-DBT, are the hardest to remove using HDS due to low reactivity and high steric hindrance. Fig. 1.4(b) shows the relative HDS rate of various refractory sulfur compounds as a function of size and boiling point, the data of which were obtained from Ho et al.[9] Despite having a lower boiling point, the pseudo-first-order rate constant for HDS of 4-methyldibenzothiophene (4-MDBT) is orders of magnitude lower compared with dibenzothiophene (DBT). This suggests that the main bottleneck in ultra-deep HDS of heavy oil is the presence of alkyl substituents on dibenzothiophenes, causing a significant decrease in reactivity. As a result, substantially high amounts of catalysts, in addition to intensive operating conditions, are required to meet federal specifications, which lead to high cost. In summary, the level of difficulty in removing these sulfur compounds, at least by conventional hydrotreatment, increases in the following order: gasoline < jet fuel < diesel fuel.

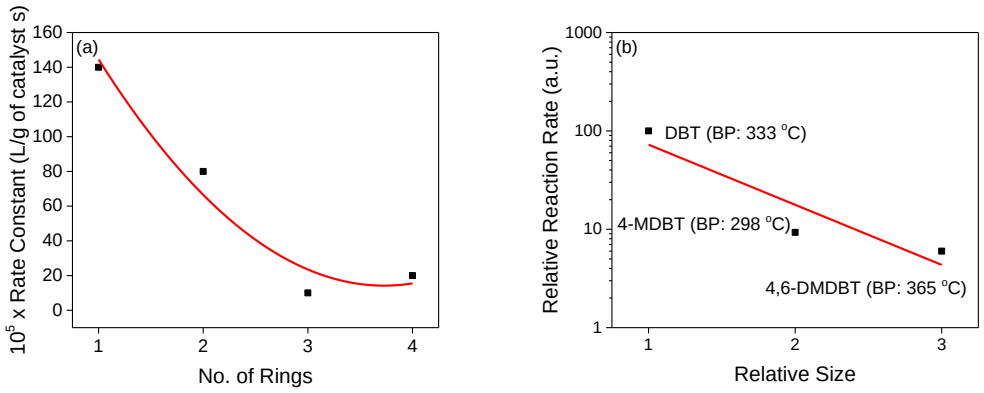

Figure 1.4: (a) The effect of number of rings in thiophenic compounds on the pseudo-first order rate constant of a batch reaction in n-hexadecane solvent at 300 °C and 71 bar over conventional $CoMo/Al_2O_2$.[8] (b) The effect of alkyl group(s) on the reactivity of HDS catalyzed by sulfide $CoMo/Al_2O_2$ at 300 °C and 102 atm.

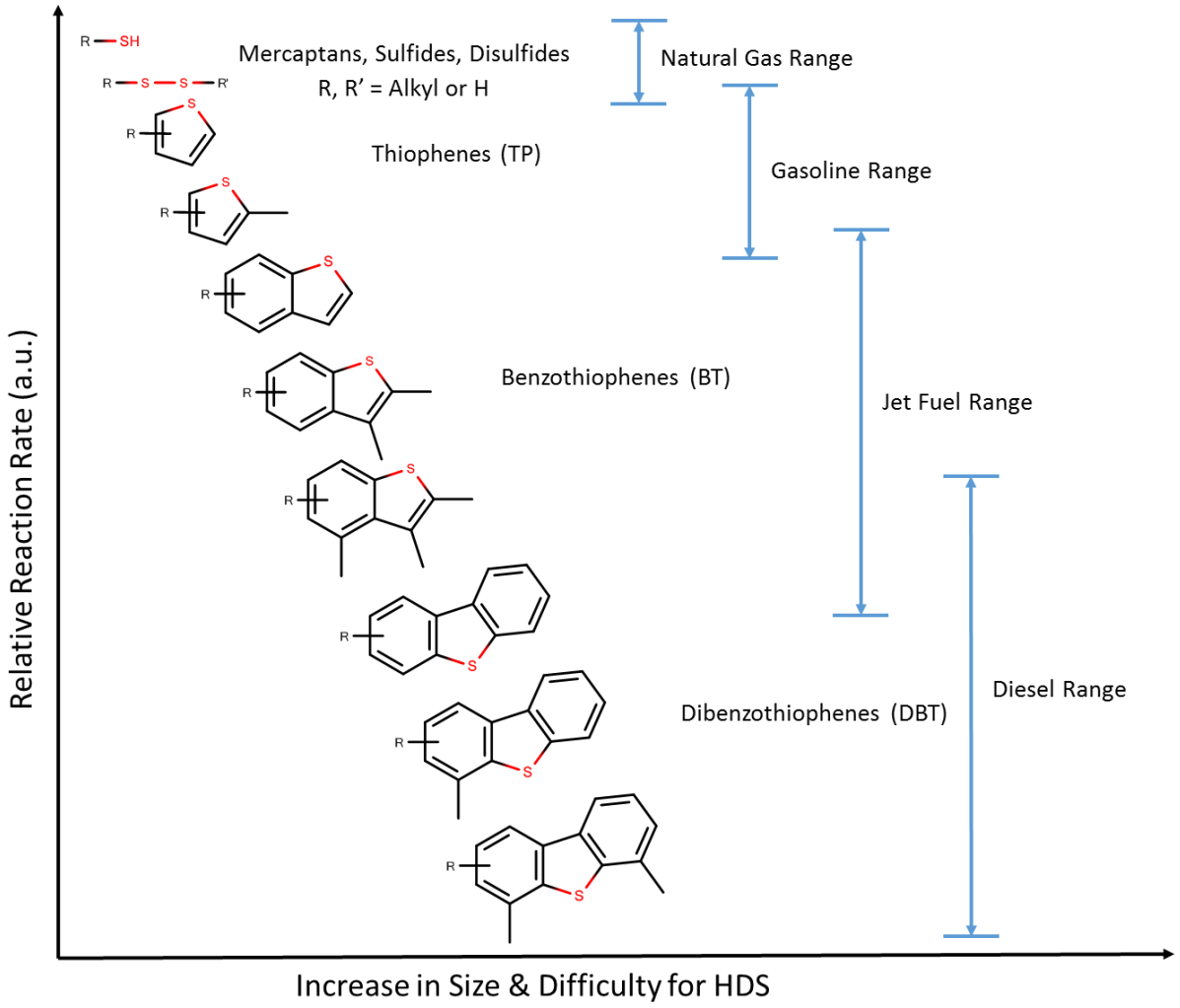

Figure 1.5: Reactivity of sulfur compounds with varying sizes commonly found in fossil-based fuels versus the difficulty in removing them via HDS.

1.3 Detrimental Effect of Sulfur and Its Ramifications

Sulfur emission remains one of the major sources of environmental pollution. During combustion of these transportation fuels, sulfur compounds are converted to SO_x, one of the main precursors of acid rain. Premature deaths, asthma attacks and acid rain are just some consequences that will occur if toxic emissions from fossil fuels are not controlled.[10] As depicted in Figure 1.2, fossil-based fuels will continue to dominate the transportation and other aforementioned sectors at

least for another decade, and hence, the unceasing increase in toxic pollutants in the atmosphere. In addition to human-related and environmental issues, the presence of sulfur in refinery systems can poison or deactivate the catalysts and lead to corrosion in refinery equipment.[11] Moreover, studies have shown that fuels that are directed for fuel cell applications should have ultra-low sulfur concentration. This is because fossil-based fuels such as liquid hydrocarbons and natural gas are currently the most important hydrogen sources for fuel cell stacks. In fact, natural gas accounts for 48% of total hydrogen produced worldwide, hence being the largest contributor of hydrogen production.[12] Despite the high volumetric density of these energy sources, the biggest drawback is the poisoning fuel cell electrodes if the sulfur levels are not administered carefully. Specifically, sulfur levels as low as 1 ppmw could poison the electrode catalysts in a Proton Exchange Membrane Fuel Cell (PEMFC) and solid oxide fuel cell (SOFC), causing failure in the corresponding systems.[13,14] In addition, sulfur impurities can distort the performance of fuel-processor catalysts by strongly adsorbing on the Pt group catalysts, which is common in polymer electrolyte fuel cells (PEMFC).

The combination of its abundance in nature and continuous stringent regulations imposed by the U.S. Environmental Protection Agency (EPA) to limit sulfur concentrations in federal gasoline and diesel fuels, demands the development of effective and versatile deep desulfurization technologies.[10,15] While regulatory legislations require sulfur content to meet strict specifications (e.g. 10 ppmw for gasoline and 15 ppmw for diesel according to the EPA Tier 3 program), these sulfur levels are still considered too high for fuel cell applications, for which liquid fuels must contain no more than 1 ppmw of sulfur.[16,17] In fact, studies have shown that sulfur as low as 0.2 ppmw could poison the electrode catalysts in a Proton Exchange Membrane Fuel Cell (PEMFC), eventually causing degradation of the system.[13] Thus, sulfur compounds in the liquid hydrocarbons

must be reduced close to sulfur-free levels to promise the versatility and efficiency of the fuel cell stack. Furthermore, the EPA has anticipated that by 2030, the Tier 3 program will have prevented 2000 premature deaths, 2200 asthma attacks, 50000 respiratory symptoms in children and 1.4 million restricted activities every year.[10] Conventional hydrodesulfurization, is currently the most common desulfurization process, but has shown to ineffectively remove refractory sulfur compounds such as dibenzothiophenes and alkylated-dibenzothiophenes, unless expensive conditions were applied.[18] Furthermore, excessive hydrogenation of aromatics and olefins in fuels negatively affects other properties of fuel, such as the octane or cetane number. Consequently, development of alternative deep desulfurization processes for transportation fuels becomes one of the major challenges to meet federal specifications.

1.4 Alternative approaches to deep desulfurization

Due to low HDS reactivity refractory organosulfur compounds and the continuous stringent sulfur regulations imposed by the EPA, there has been a high demand for the development of effective and versatile ultra-deep desulfurization alternative technologies. Various desulfurization technologies have been explored either to completely replace or to compliment the current HDS technology. The main alternative techniques include oxidative desulfurization, extractive desulfurization, biodesulfurization and adsorptive desulfurization.[19] Table 1.1 summarizes and compares the features of the aforementioned desulfurization technologies. A more in-depth discussion regarding each process can be found elsewhere.[20]

Among the aforementioned processes, adsorptive desulfurization (ADS) is one of the most studied alternative technologies to replace or supplement conventional HDS. In ADS, sulfur compounds are removed via adsorption using a selective adsorbent. This means that the adsorbent

plays an important role in the selectivity, capacity and sustainability (e.g. regenerability of adsorbents) of the process. A few examples of widely studied adsorbents include metal-organic frameworks (MOF), activated carbons, metal oxides, zeolite-like sorbents and zeolites. A more detailed discussion of each adsorbent will be presented in the next section. Depending on the interaction between the adsorbent and the sulfur compound, sulfur may be removed via two mechanisms; physical or chemical adsorption (e.g. reactive adsorption).[21] In the former, sulfur compounds and adsorbents are mainly bound by Van der Waals forces, which is a relatively weak interaction. This enables the adsorbent to be regenerated relatively easy. On the other hand, chemical adsorption employs chemical bonding between the sulfur compounds and the adsorbents, which may alter the physical and chemical nature or the sulfur compounds. As expected, the adsorbents require higher energy to be regenerated and subsequently, sulfur is removed as H_2S or SO_x.[22] A low energy-intensive regeneration technique is via solvent extraction, in which polar solvents such as DMF can be used to wash the adsorbed sulfur compounds.[23] ADS is a promising technique because it has the potential to be regenerative, cost-effective and environmental-friendly, while operating at ambient conditions. Selectivity and diffusion limitations have been the most important challenges in ADS. Hence, a significant amount of research has been devoted to explore a wide range of potential adsorbents with high sulfur selectivity and capacity.

One of the most studied family of materials is MOFs. MOFs consist of metals or metal clusters that are joined together by an organic material (linker) to establish a framework. They are unique materials with various pore sizes and shapes.[24] Common MOFs for ADS include MIL-101, HKUST-1, NENU-511, and UMCM, among others.[24–28] Their capacity and selectivity depend on the type of metallic cluster, and the organic linker holding it together.[29] One of the key strengths of MOFs is the flexibility in which most of the metals in the periodic table can be linked using the

appropriate linker, contributing to wide physical and chemical properties of the material. While MOFs have shown to exhibit higher capacity than zeolites, their sensitivity to heat prevents them from being used in industry.[25] At high temperature, linkers may collapse and particle aggregation may occur. Furthermore, the porosity of MOFs may be too small for the adsorption of diesel-range refractory sulfur compounds, thus reducing the sulfur capacity compared with other highly porous materials.[30]

Activated carbons (ACs) are a class of microcrystalline materials with large surface area and pore volume. The synthesis of ACs usually involves three main steps: preparation, carbonization and activation.[31] A few examples of raw materials include coal, wood, coconut shells, fruit nuts and other biomass derived sources.[32] While pure ACs have shown high sulfur capacity,[33,34] aromatic hydrocarbons, especially nitrogen-containing compounds, selectivity is one of the major challenges. Thus, metal impregnation (Cu, Co, Ni, P or Mn) on ACs has been studied to improve their sulfur removal rate and selectivity.[35–38] Another challenge of AC in ADS is the low adsorption ability due to the broad distribution of pore sizes, as well as mass transport limitations.[32,39]

Many different types of metal oxides have been used for ADS including Fe, Ni and Co.[40] Ti supported on metal oxides have also shown to be effective in the desulfurization of DBT and TP.[41] Mixed metal oxides utilizing graphene oxide as support have also been studied as sorbents for ADS.[42] The advantage of using mixed oxides is their low cos. Nonetheless, they suffer from low capacity in the adsorption of refractory sulfur compounds. Most studies using metal oxides were aimed at the removal of elemental, non-aromatic sulfur compounds such as thiols[43] or those found in gas phase.[44] Additionally, most of the metal oxides used for desulfurization must be used with expensive supports and are relatively difficult to regenerate.[45,46] It has also been shown that

the regeneration of AC via heat treatment resulted in a loss of about 5-10% carbon, due to oxidation and debilitation over time.[47]

Zeolite-like sorbents such as MCM-41 and SBA-15 are a group of structured mesoporous silicas that can be used as supports for ADS.[48] Unlike metal oxides, zeolite-like sorbents contain mesopores that are in the range of 20-500 Å,[49] which means that accessibility to the internal active sites should not be a limiting factor. The synthesis of materials and the tailoring of the pore structures are relatively easy and cost-effective. Zeolite-like sorbents tend to exhibit high surface area, good thermal stability and they can be functionalized by different metals and metal oxides in order to increase their sulfur removal rate.[50–53] However, zeolite-like sorbents do not exhibit a well-defined crystalline structure.[54] The metals are usually introduced via wet-impregnation, which generally results in lower metal dispersion (or higher amount of agglomerated metal particles), which reduces the selectivity of sulfur molecules.[55,56]

Zeolites are a class of aluminosilicates that occur naturally or are manufactured synthetically at an industrial scale. The research of zeolite materials is broad and includes applications in wastewater treatment,[57,58] catalysis[59,60] and adsorbents,[29] among others. Zeolite properties are determined by their structure and their Si/Al ratio, which can be tuned based on the needs of the different applications. A lower Si/Al ratio leads to more acidic zeolites, making them ideal for ion-exchange.[61] The Y zeolite, in particular, has been very attractive for sulfur adsorption due to the unique three-dimensional pore structure of the faujasite (FAU) framework, as well as the large surface area and widely available acid sites. The acid sites also behave as ion-exchange site to introduce well-dispersed metals. However, the microporous nature of the Y zeolites causes diffusion limitations, especially for refractory sulfur compounds. To overcome this challenge, mesoporous zeolite have been explored.[62,63] Another major challenge is the limited selectivity

towards sulfur molecules in the presence of aromatics in the fuels. Researchers have been trying for years to address this challenge by introducing metals via the ion-exchange.[64,65] It is, therefore, purposeful to study the important roles of pore structure and metals in zeolites for the ADS of transportation fuels.

Table 1.1: Comparison of common desulfurization technologies.

Desulfurization Technologies	Mechanism	Advantages	Disadvantanges
Hydrodesulfurization (HDS)	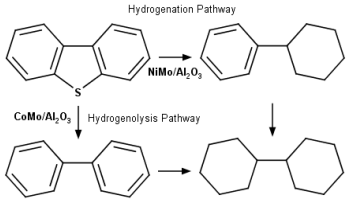	• Well-studied conventional desulfurization process • Effectively removes sulfur from thiols, sulfides and thiophenes • Mild operating conditions • Recyclable solvent	• High cost • High reaction temperature and pressure • Requires expensive metals • Decreased catalyst lifespan • HDS of alkylated-DBT is hindered by steric hindrance • Reduces octane rating
Oxidative Desulfurization (ODS)	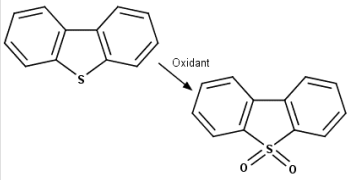	• Requires small reactor • Low cost • Mild operating conditions • Recyclable solvent	• Low solvent selectivity • Slow catalyst recovery • Slow reaction rate • Oxidants may cause low mass transfer, corrosion and high moisture content
Extractive Desulfurization (EDS)	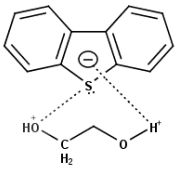	• Low energy consumption • Mild operating conditions • No catalyst use • Does not react with fuels	• Low extractant selectivity • High cost of solvent • Solvent may be lost due to evaporation • Solvent may impose harmful effects on ecosystem
Biodesulfurization (BDS)	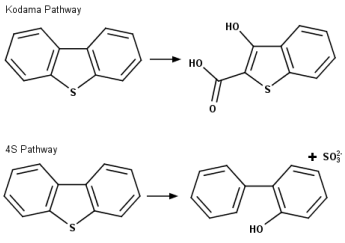	• Low cost • Environmental friendly • Mild operating conditions • Easy recovery of biocatalysts	• Unwanted C-C bond cleavage (Kodama) • Low reaction rate • Short microorganism lifetime • Loss of cells over time • Limited studies on real oil • Limited information on sanitary handling of cells
Adsorptive Desulfurization (ADS)	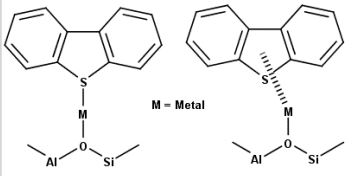	• Low cost • Mild operating conditions • Easy to regenerate • Does not produce H_2S • Environmental-friendly	• Low sulfur selectivity • Diffusion limitations • Efficiency highly depends on sorbent properties

1.5 Objectives

The overarching objective of this thesis is to understand the role of the sorbent on the desulfurization of transportation fuels to meet federal sulfur specifications. According to the EPA, fuel combustion is the main source of SOx production, accounting for over 80% of the total emission.[66] When combusted, sulfur in fossil fuels is almost entirely converted to SO_2 (or SO_3), and studies have shown that as little as 1 ppm of sulfur can lead to negative implications such as catalytic converter failures and fuel cell electrode poisoning.[4,67]

The objective of this PhD thesis is to understand the role of bimetal-exchanged zeolites in adsorptive desulfurization of transportation fuels, gasoline, jet fuels and diesel. While various adsorbents with high sulfur capacity have been discovered as highlighted in Section 1.4, bimetallic mesoporous zeolites have been optimized both physically and chemically to create a lucrative sorbent, that has yet to be studied for adsorptive desulfurization. This sorbent, combining both hierarchical pore structure and metal cations, will revolutionize deep desulfurization technologies to produce high quality low sulfur fuels for both transportation and fuel cell applications.

As demand for fossil-based fuels continues to rise, federal agencies have decided to place stringent regulations on sulfur emissions. As a result, the need for low-cost and effective desulfurization technologies has been the main topic of discussion. Liquid phase adsorptive desulfurization using zeolites has been shown to be a promising alternative to HDS, but continuous adsorption of refractory sulfur compounds may decrease the lifetime of the sorbent. Utilizing liquid phase desulfurization as a complementary technology to HDS can be more practical at the current commercial state.

However there are several challenges that need to be addressed in order to make the liquid adsorptive desulfurization in zeolites a successful technology. These challenges and proposed solutions are described below:

(1) Eliminating diffusion limitations. Introduction of mesoporosity via the surfactant-assisted method would allow larger molecules such as DBT and 4,6-DMDBT to access the internal active sites of the microporous zeolites.[68] This method ensures the introduction of well-ordered pores without compromising the structural integrity of the zeolite framework.

(2) Increasing sulfur capacity. Metal cations can be introduced into the zeolite extra-framework via the ion-exchange method to enhance sulfur uptake. Cu is one of the transition d-block metals that has shown high capacity for sulfur adsorption due to strong π-complexation with the thiophenic ring.[64,69] During this interaction, sulfur forms a σ-bond with the empty 4s-orbital of Cu^{+}, while the d-orbital of Cu^{+} backdonates electron density to the antibonding π-orbitals (π*) of the sulfur ring. This interaction is exceptionally strong, except when other aromatics are present, compromising the selectivity of sulfur adsorption.

(3) Enhancing sulfur selectivity. F-block elements such as Ce prefer to selectively form direct σ-bonds to nearby heteroatom.[46,70] This interaction is highly selective especially in competitive adsorption of sulfur from liquid fuels, but suffers low sulfur capacity due to being located in inaccessible sodalite cages and hexagonal prisms in the zeolite. Steric hindrance can arise since adsorption configuration plays an important role in direct σ-bond interaction.

(4) Designing novel and environmentally friendly sorbents. The prepared metal-exchanged mesoporous Y zeolites will be used as a potential sorbent for adsorptive desulfurization of liquid hydrocarbon fuels. The roles of mesoporosity and metal cations will be the aim of this

section. The synergy between Cu and Ce will be studied to understand how the combination of metals impact the capacity and selectivity of thiophenic compounds.

(5) Understanding the mechanism of sulfur adsorption. The aim of this section is to investigate the adsorption pathway of sulfur compounds adsorbed on Y zeolites. Multiple molecular level techniques will be utilized to shed light on the adsorption configuration and binding energy. Results from these studies will be compared to experimental data to bridge chemical engineering fundamentals and applications.

(6) Defining the crystalline structure of ion-exchanged Y zeolite. The location and coordination of exchanged-metals in the Y zeolite play a significant role in the overall desulfurization performance. XRD techniques will be utilized in this study to obtain accurate diffraction data about the zeolite, which is then subjected to Rietveld refinement. This will give us useful information such as the unit cell size, lattice parameters, occupancy of metals, coordination of atoms, and the location of extra-framework cations. Hopefully, this will allow us to answer fundamentally to the question, “What makes metal-exchanged mesoporous Y zeolite an excellent sorbent for adsorptive desulfurization?”

(7) Predicting the adsorption energy and mechanism of sulfur. Despite the advantage of using bimetals such as Cu and Ce for adsorptive desulfurization, there is still a plethora of metals in the periodic table to be explored, that could be good candidates for sulfur adsorption. Currently, density functional theory has become a popular computational tool to screen for potential adsorbents based on binding energies and adsorption configurations. Using DFT will also help us explain the trends observed in experimental results, and hopefully draw correlations that would beneficial for machine learning.

Based on the challenges described above, a few hypotheses are proposed. Since the Y zeolite already exhibits relatively large pores of about 7.4 Å, TP and BT should have little to no difficulty accessing the internal active sites located in the supercage. However, the adsorption of DBT and larger sulfur compounds, with a kinetic diameter of at least 9 Å, would be severely interfered by steric hindrance and diffusion limitation.[71] A novel method of introducing well-defined pore structures has been proposed to overcome this challenge, without severe consequences on the available active sites. Using transition metal such as Cu or rear-earth metal such as Ce has shown to be advantageous for ADS via different adsorption pathways. We propose that the combination of both elements in our zeolite sorbent would enhance sulfur capacity and selectivity via various adsorption configurations. Metal composition, location, configuration, and oxidation states are all important factors of high sulfur uptake and should be considered. It is also highly likely that other combination of metals might exhibit higher sulfur selectivity and capacity compared with Cu and Ce, but running adsorption experiments for a high number of metals can be time-consuming and expensive. Theoretical studies using DFT have been used to correlate binding energies and material properties, allowing users to make accurate predictions. We propose the use of DFT to calculate adsorption energies and correlating them to adsorption capacities obtain from experiments. The conflation of experimental, spectroscopic and theoretical understanding of sulfur adsorption is essential for the successful implementation of ADS in the real world. The following section highlights the content of each chapter. Without following any particular order, each study aims to address the aforementioned objectives listed above.

1.6 Scope of Dissertation

This dissertation has 7 chapters following the Introduction. Chapter 2 introduces the three main experimental methods used in this work, including N_2 adsorption/desorption, X-ray diffraction (XRD), Fourier transform infrared spectrometer (FTIR) and microscopy. The preparation, modification and analysis of modified Y zeolites are also discussed. Chapter 3 gives a brief overview of the theoretical method used in this study, density functional theory (DFT)

Chapter 4 studies metal-exchanged mesoporous Y zeolite as a potential sulfur adsorbent for transportation fuels. Several modifications such as the introduction of mesoporosity and metal cations, are made to the fresh zeolite to overcome diffusion limitation and selectivity challenges, respectively. The adsorption capacities derived from the breakthrough curves are correlated to the adsorption energies determined using isosteric heat of adsorption calculations.

In Chapter 5, the sulfur adsorption study is extended to include aromatic compounds in the model fuel, to mimic real transportation fuels. It is demonstrated that the presence of aromatics significantly decreases the capacity of previously studied Y zeolites. Bimetallic mesoporous Y zeolite is prepared to show the synergistic effect of Cu and Ce on selective adsorptive desulfurization. The adsorption strength and configuration of the modified zeolites are also discussed using FTIR.

In Chapter 6, the previous work for adsorptive desulfurization on CuCe mesoporous Y zeolite is extended to study the selective removal of 4,6-dimethyldibenzothiophene (4,6-DMDBT), which is extremely difficult to break down using conventional HDS. A model fuel containing 4,6-DMDBT and naphthalene is used in this study. It is realized that the metal composition and configuration can be controlled to enhance the adsorption capacity of 4,6-DMDBT. The most optimum material is chosen to study the effect of regeneration.

In Chapter 7, DFT calculations are performed on HY and CuY to predict the binding energy of various sulfur compounds. Rietveld refinement was first performed to gain information on the coordination of Cu. Then, a two-layer ONIOM model was built to represent the zeolite cluster, for which quantum mechanics is used to treat the adsorption site, and molecular mechanics to deal with everything else in the framework. The adsorption mechanisms are further understood using NBO analysis, which gives detailed information about electronic contributions from participating natural bond orbitals. The results from DFT are then used to explain the breakthrough curves from previous adsorption experiments and to justify that theoretical calculations are essential for predicting adsorbents with high sulfur capacity and selectivity.

Chapter 8 contains summaries from each chapter, which are used to reach a general conclusion regarding ADS. The potential of ADS as a standalone alternative or complementary technology is discussed. Commercialization of ADS is restricted by several challenges that should be addressed in the future. Finally, some suggestions for future work are proposed.

Chapter 2

EXPERIMENTAL METHODS

2.1 Introduction

Adsorption using zeolites sees a wide application in chemical, petroleum and energy industries. The quality of the zeolite determines the performance of any adsorptive separation or purification process. In adsorptive desulfurization of transportation fuels, the main challenge is the selective adsorption of sulfur in the presence of aromatics. Refractory sulfur compounds such as dibenzothiophene and alkylated-dibenzothiophenes are bulky molecules that may cause steric hindrance, especially within the narrow channels and cages of the Y zeolite. The aforementioned challenges in combination with the stringent sulfur regulations for transportation fuels and fuel cells are the motivation behind this dissertation. To help execute the relevant investigations, a range of advanced characterization and analytical techniques were used and are discussed in detail below. In addition to bench-scale experiments, this dissertation also focuses on the fundamental understanding of sulfur adsorption at the molecular level.

2.2 Sorbent Preparation

2.2.1 Surfactant-assisted method

The introduction of mesoporosity in zeolites has been studied since the early 2000s for applications in the petrochemical industry.[72–74] Various strategies of preparing mesoporous zeolites, including both bottom-up and top-down approaches, have been discussed elsewhere.[68] The surfactant-assisted method has been employed in this study to allow for more controlled mesoporosity, the detailed procedures of which have been previously published.[75,76] This approach

is a single-step process that uses mild base solution such as ammonium hydroxide (NH_4OH) and surfactants such as cetyltrimethyl ammonium bromide (CTAB). In some cases where the zeolite contains high aluminum content (low Si/Al ratio), an acid pre-treatment step using mild acid such as citric acid is required. The acid-pretreated zeolite is then added to the NH_4OH and CTAB solution. During the mixing, some of the Si atoms are dissolved by the base solution, resulting in negatively charges sites in the zeolite framework that attract the more positively-charged surfactants. To minimize the interaction of hydrophobic surfactant tails in the solution, the surfactants spontaneously self-assemble to form micelles, creating a templating effect within the zeolite framework. The mixture is typically heated to 80 °C and stirred for approximately 24 hours, after which the resulting solid is filtered, washed and dried. Then, the zeolite is calcined at 550 °C for approximately 5 hours to remove the surfactants, leaving uniform distribution of mesopores. Compared with traditional desilication, the surfactant-assisted approach does not result in significant loss of silica or damage of zeolite framework, leading to a significant improvement in physical properties such as crystallinity, acidity and hydrothermal stability. Furthermore, the size of the mesopores can be easily controlled based on the length of the surfactant hydrophobic tail. Figure 2.1 highlights the important steps during the formation of surfactant-templated mesopores in the Y zeolite.

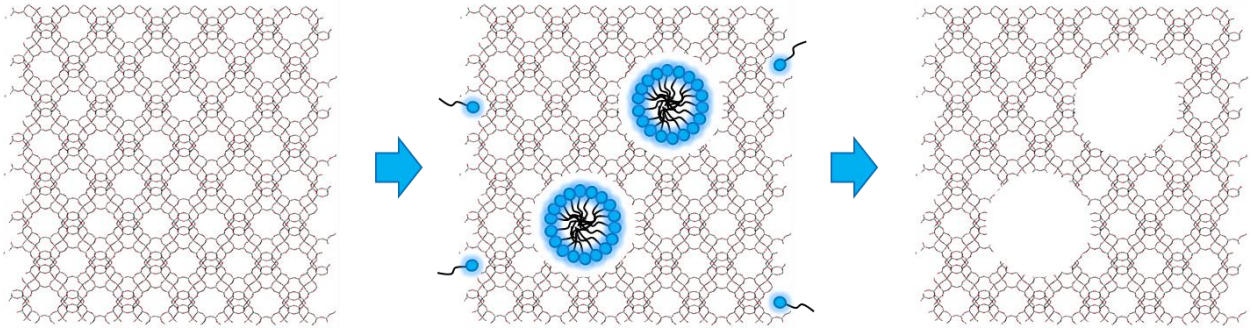

Figure 2.1: The proposed mechanism for the formation of surfactant-templated mesopores. From left to right: Fresh Y zeolite is used as the starting material; Mild desilication in basic media and rearrangement of crystal structure around the assembly of surfactants (micelles); removal of templates leaving behind well-defined mesoporous structures.

2.2.2 Ion-exchange of Y zeolite

The Y zeolite framework is composed of SiO_4 and AlO_4 tetrahedra, which are joined to form a 3-dimensional crystalline structure, consisting of polyhedral building blocks such as sodalite cages and hexagonal prism. The polymerization of these units results in the formation of uniform pore structure and inter-connecting channels and cavities. Since Si is tetravalent and Al trivalent, the net charge of the zeolite framework is negative and this net anionic charge defines the ion-exchange behavior of the Y zeolite. This means that the ion-exchange capacity of a zeolite depends on the SiO_2/Al_2O_3 ratio, where higher Al content leads to higher ion-exchange capacity. To account for electroneutrality, the negative charge is compensated by cations of equal charge. Typically, the compensating cations in the Y zeolite exist in the form of Na^+, Li^+, and NH_4^+ which can be further ion-exchanged with desired transition metals or rare-earth metals. A basic representation of the neutral zeolite framework is shown in Figure 2.2. Notice that two Al atoms cannot share the same oxygen as per Loewenstein's rule.[77] Therefore, for a unit cell containing a total of 192 tetrahedra, maximum allowable number of Al is 96 atoms per unit cell, corresponding to a Si/Al ratio of 1.

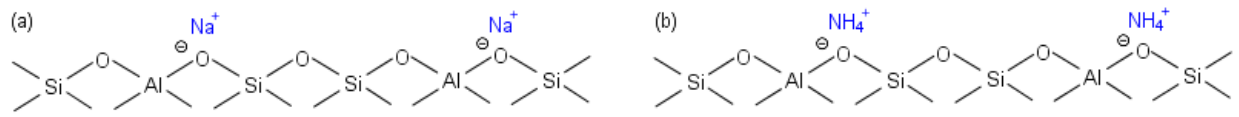

Figure 2.2: Schematic of negatively-charged zeolite framework balanced by (a) Na^+ and (b) NH_4^+ cations.

Ion-exchange of zeolite is generally performed in aqueous systems, in which the appropriate amount of cation precursor is added to the mixture and allowed to stir for approximately 48 hours at ambient conditions. The stirring temperature may be raised to increase the ion-exchange rate. At elevated temperature, water is stripped from the ions, allowing for better penetration through the pores of the zeolite.[72] In addition to temperature, other main factors that influence the rate and degree of ion-exchange in zeolites are the type of the cation being exchanged including its size and charge, the concentration of cations, the location of cations in the zeolite and the Si/Al ratio of the zeolite.[78,79] The mechanism of ion-exchange proceeds by assuming a state of equilibrium between the cation in the zeolite and the corresponding cation in the solution. This relationship may be represented by the following equation:

$$bA_S^{a+} + aB_Z^{b+} \rightleftarrows bA_Z^{a+} + aB_S^{b+} \qquad \text{Equation 2.1}$$

where a and b are the oxidation state of cations A and B, and S and Z are the solution and zeolite phases, respectively. The selectivity of ion-exchanging the existing cation in the zeolite with a new cation depends on the free energy of the above reaction, given as:

$$\Delta G^0 = -\frac{RT}{ab}\ln K \qquad \text{Equation 2.2}$$

where K = the dynamic equilibrium constant of Equation 2.1 Consequently, the reaction with the most negative free energy exhibits the highest selectivity of ion-exchange.

Since the SiO_2/Al_2O_3 ratio of Y zeolite is around 2.5, the unit cell possesses a variety of cation positions that are coordinated with framework oxygen atoms dispersed throughout the supercages, sodalite cages and hexagonal prisms. Figure 2.3 shows the 3-dimensional structure of the Y zeolite unit cell and the corresponding extra-framework cation positions, namely sites I, I', II and II'. Site I and I' are located at the center of the hexagonal prism surrounded by six oxygen atoms and inside the sodalite cage surrounded by three oxygens, respectively. Site I' is known to be highly populated for having octahedral coordination with the surrounding oxygens, but is totally inaccessible for guest molecules. Site I is only accessible to those that are small enough to penetrate the sodalite cage. It should be mentioned that simultaneous occupation of adjacent sites I and II' is forbidden because of Coulombic repulsion.[80] Sites II and II' are located at the faces of the 6-membered ring just inside the supercage and the sodalite cage, respectively. These sites are usually more accessible for the adsorption of guest molecules, and hence the preferred sites for ion-exchanged of cations in the zeolite. Similar to sites I and I', simultaneous occupation of these sites is also forbidden. Upon calcination and activation at elevated temperature, the cations tend to migrate into the highly-coordinated sites to achieve the lowest possible energy. Unfortunately, these sites are located in the hindered positions of the sodalite cage and hexagonal prism, causing minimal interaction with any guest molecules in the supercage cavity.

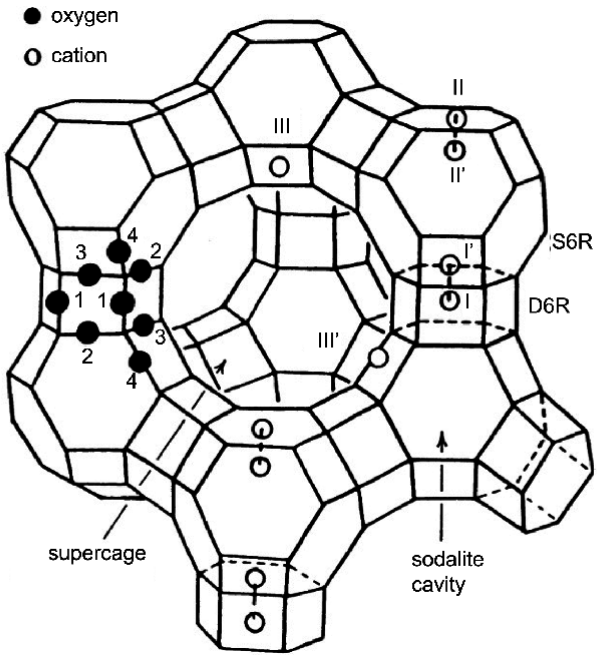

Figure 2.3: Schematic representation of Y zeolite unit cell and extra-framework coordination sites.

2.3 Characterization Techniques

Characterization techniques are necessary to elucidate all kinds of characteristics of a catalyst or adsorbent. With the advancement of science and technology, more sophisticated characterization instruments have been developed and most of them are very accessible in large universities, research institutes and national laboratories. A sample's characteristics can be categorized into physical or chemical properties. Together, these properties are responsible for the performance of a given reaction. Therefore, utilizing the appropriate characterization techniques for a given project is crucial to offer the most comprehensive and supportive data for experimental and theoretical findings. In this section of the thesis, only the main characterization techniques are discussed in detail. They include N_2 adsorption/desorption, x-ray diffraction (XRD), infrared spectroscopy (IR) and microscopy. Information about other supplemental characterization

techniques such as elemental analysis and X-ray photoelectron spectroscopy (XPS) can be found in subsequent chapters.

2.3.1 N_2 adsorption/desorption

The determination of surface area, pore size and pore volume is one of the most fundamental practice of catalysis and adsorption research. These properties are important because they accommodate actives sites and accessibility to those sites. Both the size and pores determine the internal surface area, which play a significant role in the dispersion of active metals. The most common method for determining the internal surface area of zeolites is by gas adsorption. Unlike bound atoms in a solid, surface atoms have the tendency to attract nearby gases to satisfy bond deficiency, and thus lowering the surface energy. Prior to the measurement, the zeolite sample is first degassed in inert gas at approximately 393 K under vacuum for 24 hours to remove water and physisorbed contaminants. Then, the sample is cooled to about 77 K (liquid N_2 temperature) after which is an adsorptive gas is dosed (usually N_2) in gradually increasing pressure. After each dose, the pressure is allowed to equilibrate and the amount of N_2 adsorbed is recorded. Subsequently, the process is reversed by gradually decreasing the pressure, thereby generating a desorption isotherm. Figure 2.4 shows the resulting N_2 adsorption and desorption isotherms of a fresh Y zeolite, compared against that of mesoporous Y zeolite. There are various types of isotherms depending on the pore structure of the zeolite. Figure 2.4(a) shows that the fresh Y zeolite exhibits a Type I isotherm, which is common for microporous solids having relatively small external surfaces. The limiting uptake is controlled by the accessibility of the micropore volume. On the other hand, mesoporous Y (Figure 2.4(b)) shows a Type H4 hysterisis loop and reversible Type IV isotherm, suggesting the presence of ordered-mesoporosity.

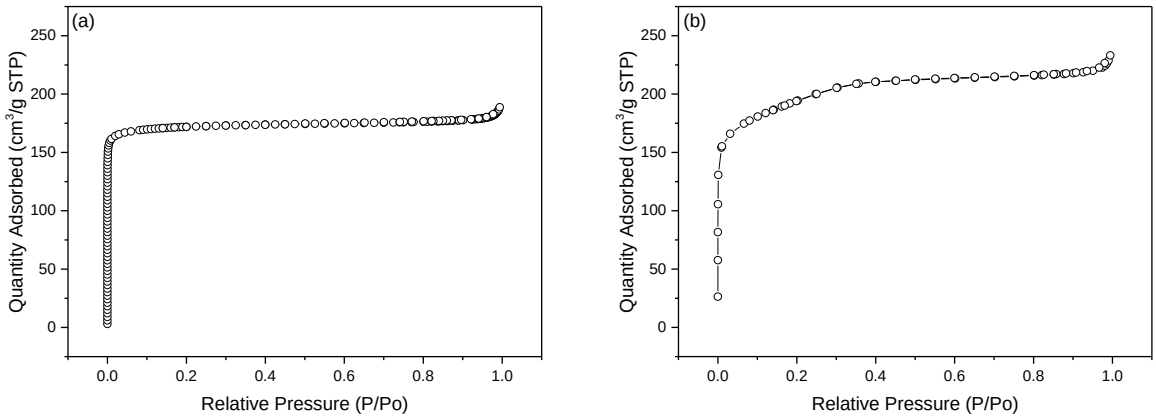

Figure 2.4: N2 adsorption/desorption isotherms of (a) Y zeolite and (b) Mesoporous Y zeolite.

To determine the surface area of zeolites, the collected gas adsorption data must be processed using an adsorption model. The Brunauer-Emmett-Teller (BET) theory is a widely accepted method for analyzing multilayer adsorption of gas molecules on a solid surface to measure the surface area of the solid and the corresponding distribution of pores.[81] The BET is also referred to as an extension of the Langmuir model and makes the following assumptions:

(1) Infinite physisorption of gas molecules on solid surface

(2) Interaction of gas molecules with adjacent layers only

(3) Langmuir theory applied to each layer

(4) First layer exhibits highest enthalpy of adsorption

(5) Subsequent layers have the same adsorption energy

The resulting BET equation is the following:

$$\frac{1}{v[(p_0/p)-1]} = \frac{c-1}{v_m c}\left(\frac{p_0}{p}\right) + \frac{1}{v_m c} \qquad \text{Equation 2.3}$$

where p_0 and p are the equilibrium and saturation pressures of gas adsorbates at the corresponding adsorption temperature, v is the amount of adsorbed gas, v_m is the amount of monolayer adsorbed gas and c is the BET constant, defined by the following equation:

$$c = exp\left(\frac{E_1 - E_L}{RT}\right) \qquad \text{Equation 2.4}$$

where E_1 is the heat of adsorption of the first layer and $E_L$is that for the subsequent layers. To obtain information about the pore structure, the process is extended to allow the gas to condense in the pores. Further increase in the gas pressure will cause the pores to be completely filled and the collected data is used in a pore distribution model such as the method of Barret, Joyner and Halenda (BJH) or density function theory (DFT) to estimate the pore size distribution of the zeolite.

2.3.2 X-ray diffraction

X-ray diffraction (XRD) is an essential tool to determine the crystal structure of zeolites. Specifically, XRD can be used at various stages of synthesis and modification to identify, validate and characterize the corresponding phase changes on the zeolite. XRD provides structural information about the Bragg angles, at which a monochromatic X-ray beam is reflected on crystal planes according to the following Bragg's equation:

$$n\lambda = 2d \sin\theta \qquad \text{Equation 2.5}$$

where n is the integral number of reflection, λ is the wavelength of the beam, d is the distance between the crystal planes and θ is the Bragg angle. For this dissertation, XRD is used in two different ways. The first objective is to obtain a "fingerprint" by which various zeolites structures are compared based on the d-spacings or 2Θ positions of the Bragg reflections. Knowing the factors contributing to the intensity of an *hkl* reflection is essential to obtain information about the atomic structure. The intensity of a given Bragg reflection from the *hkl* plane is given by:

$$I(hkl) = KL_p(\theta)|F(hkl)|^2 \qquad \text{Equation 2.6}$$

where K is the proportionality constant, L_p is the Lorentz-polarization factor as a function of θ, and F is the structure factor. More information about these factors can be found elsewhere.[72] Figure 2.5 shows the XRD spectrum of fresh Y zeolite collected using a Bruker D8 advanced x-ray diffractometer and the corresponding *hkl* reflection indices. Additional information about d-spacings, relative intensities, *hkl* Miller indices and multiplicity of various zeolite samples have been published elsewhere.[82]

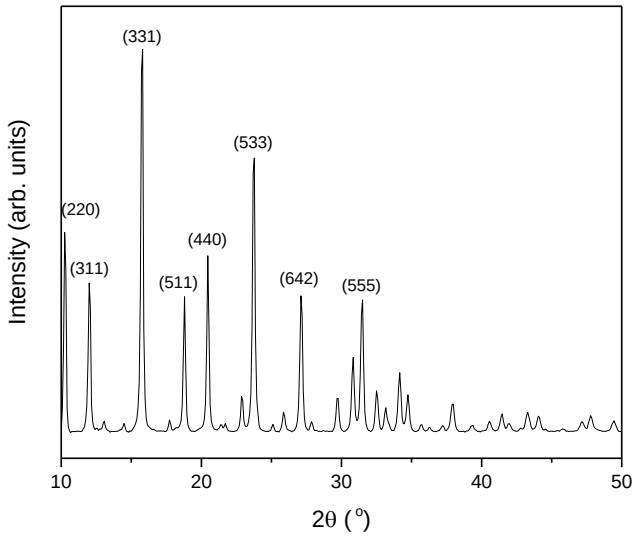

Figure 2.5: XRD spectrum of fresh Y zeolite.

The second objective for obtaining powder XRD patterns is to gather detailed structural information about a crystalline material such as unit cell size, atom positions, bond lengths and occupancy. This can be accomplished by fitting a structural model to the powder diffraction data, and subsequently refining the calculated profile against the observed data until a good match between the two patterns is reached. The idea of profile refinement started in the 1960s when Hugo Rietveld introduced a refinement method that uses the entire powder diffraction pattern instead of

the integrated peak intensities.[83] This allows for the determination of complex asymmetric structures that possess overlapping diffraction peaks, such as zeolites. The Rietveld method uses the least-squares procedure, in which atomic displacement parameters, background and peak profile parameters must be refined, which can be computationally-demanding. Therefore, accurate powder diffraction pattern, reasonable starting model and good refinement experience/skills are essential for the successful outcome of the Rietveld method.

During the refinement process, all parameters responsible for the background and Bragg reflections are varied systematically until the resulting calculated data best match the observed diffraction pattern. This effort can be accomplished by minimizing the following equation:

$$R = \sum_{i=1}^{n} w_i \left(Y_i^{obs} - Y_i^{calc}\right)^2 \qquad \text{Equation 2.7}$$

where n is the number of points measured in the diffraction pattern, Y_i^{obs} is the observed intensity of data point i, Y_i^{calc} is the calculated intensity of data point i and w_i is the weight associated to data point i. For more detailed evaluation of the quality of refinement, the following figures of merit can be used to compare the measured and calculated patterns:

$$Profile\ residual\ factor, R_p = \frac{\sum_{i=1}^{n} \left| y_i^{obs} - y_i^{calc} \right|}{\sum_{i=1}^{n} y_i^{obs}} \qquad \text{Equation 2.8}$$

$$Weighted\ profile\ residual\ factor, R_{wp} = \left[\frac{\sum_{i=1}^{n} \left(y_i^{obs} - y_i^{calc}\right)^2}{\sum_{i=1}^{n} \left(y_i^{obs}\right)^2} \right]^{1/2} \qquad \text{Equation 2.9}$$

$$Expected\ residual\ factor, R_e = \left[\frac{n-p}{\sum_{i=1}^{n} w_i \left(y_i^{obs}\right)^2} \right]^{1/2} \qquad \text{Equation 2.10}$$

$$Goodness\ of\ fit, \chi^2 = \left(\frac{R_{wp}}{R_e} \right)^2 \qquad \text{Equation 2.11}$$

It is important to note that there is no fixed method of performing a Rietveld refinement. Each refinement does not necessarily follow a specific sequence as various groups of parameters are refined differently depending on the starting model. Almost everyone that practices such method possesses their own set of strategies which comes from technical expertise and experience. Nonetheless, everyone shares a common goal to perform Rietveld refinements in the most stable manner possible. Equations 2.8-2.11 are helpful indications regarding the quality of refined data, but those should not be the only criteria. Other parameters such as bond lengths, bond angles, occupancy factors and thermal displacement factors must be physically and chemically reasonable. The following Rietveld refinement procedure is a general guide intended for reference only. It should not be followed blindly for reasons stated above.

In this thesis, Rietveld refinement was performed using the software package Generalized Structure Analysis System (GSAS), developed by Larson and Dreele.[84] In most cases, an accompanying user-friendly graphic interface, EXPGUI, developed by B.H. Toby was also used for convenience.[85] Both softwares are free to download from the web. Before running the samples, alignment of the XRD was checked with a NIST Silicon Standard Reference Material (SRM) 640e, fixing the lattice parameter at 5.4321179 Å. Figure 2.6 compares the powder diffraction pattern of Silicon SRM 640e to that calculated using Rietveld refinement and the corresponding figures of merit in the inset. The difference plot allows users to quickly identify problems related to the background, peak positions or peak shapes, and decide which parameters should be adjusted and refined. The goodness of fit is relatively low and the difference between observed and calculated patterns is small. However, the refinement can be further improved by taking better quality diffraction pattern and further adjusting the background and profile parameters. When the fit is complete, an important instrument parameter called the zero displacement offset is recorded. This

offset represents the sample displacement error relative to the instrument and should be fixed during the refinement of actual samples. In GSAS, the shft (sample displacement) parameter can be refined to minimize the error attributed to the placement of the sample. The next step in performing Rietveld refinement is to do a structureless Le Bail fit to the sample data. It must be emphasized at this point that good crystal structure data such as the space group, unit cell size and atom coordinates and occupancy must be initially defined to ensure a stable refinement outcome. The LeBail fit, another least-squares method, is performed prior to Rietveld refinement, in which the background (manually fitted then released to a Shifted Chebyshev function or other polynomial functions), peak shape function parameters (typically parameterized pseudo-Voigt function or a variation thereof) and unit cell parameters can be refined to give the absolute best possible fit to the observed pattern. These parameters are then fixed, if not refined stepwise during Rietveld refinement until a minimum χ^2 is reached at each stage. The first two parameters to refine are usually the scale factor and the unit cell size. Subsequently, profile shape parameters such as GU, GV, and GW width parameters, as well as LX and LY shape parameters can be released slowly to improve the fit to the data. Sample parameters relevant to Bragg-Brentano instruments such as sample shift (shft) and transparency (trns) can also be adjusted and it is important to note that they are unique to each sample. Before refining the atomic parameters, the addition of constraints and restraints is highly advised to solve the complex crystal structure of zeolites. Constraints impose strict limitation or exact relationships between specific parameters. For example, constraints were applied to the framework Si and Al atoms because they have the same multiplicity, hence the same fractional coordinates and thermal parameter. The occupancy parameter was also constrained so that two tetrahedral atoms cannot simultaneously occupy the same site, and the total fractional occupancy should be 1. On the other hand, restraints, also known as soft constraints, are defined

by user based on known chemical and structural information. For example, the bond lengths of Si-O and Al-O were restrained to 1.59 Å and 1.79 Å, respectively, with a standard error of 0.02 Å. Once these restrictions are applied, the atomic positions, occupancy and thermal parameters can be refined to improve the goodness of fit. The last parameter to refine is usually the background as it can be highly unstable if not done carefully. The final step is then to locate the missing extra-framework cations in the zeolite by performing a Fourier difference analysis. The inclusion of the missing cation in the structure model should improve the fit to the observed pattern and the refinement is repeated a few more times until the lowest χ^2 value is reached.

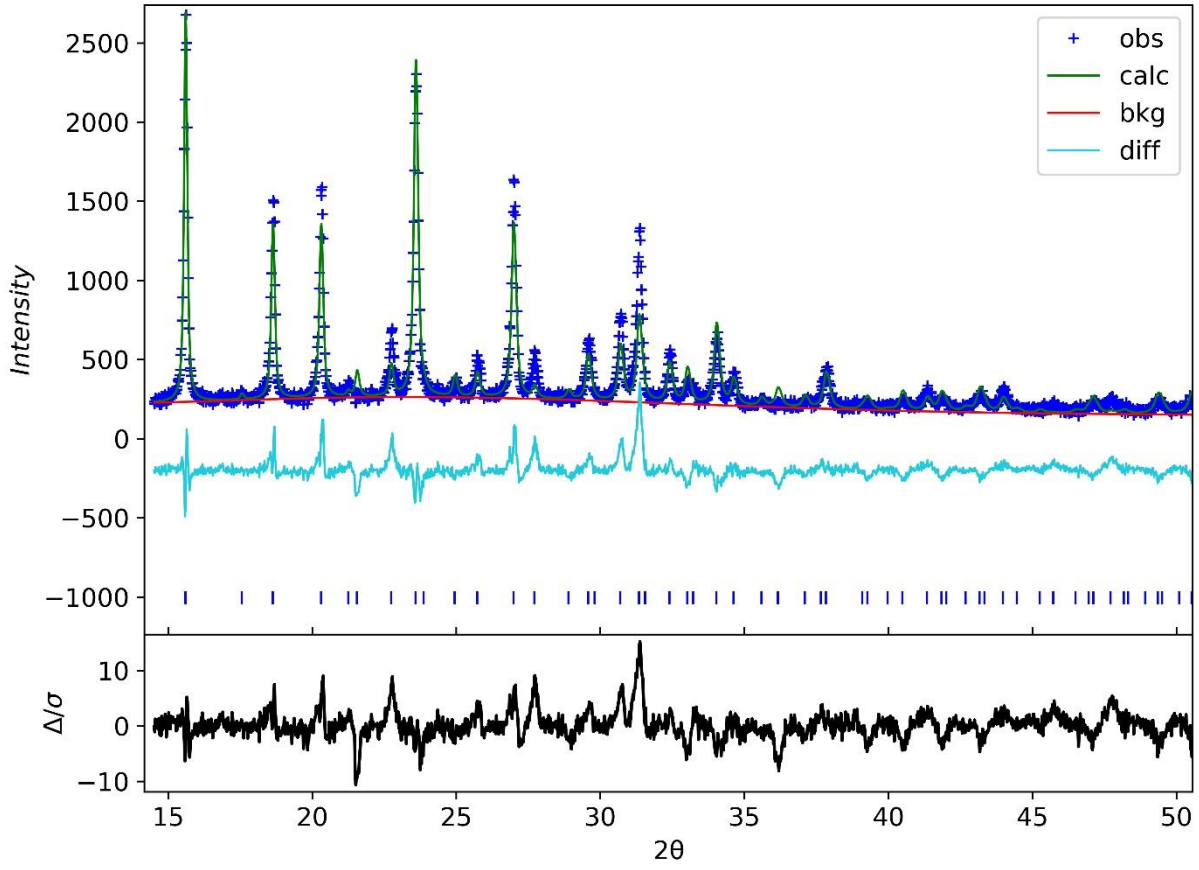

Figure 2.6: Comparison of XRD observed pattern of Silicon SRM 640e and calculated pattern by Rietveld refinement.

2.3.3 Infrared spectroscopy

IR spectroscopy is a common method to study the vibrational bonds of zeolites during adsorption and catalysis. The full range of IR (10-10000 cm-1) can be divided into three regions, namely near-IR (3000-10000 cm^{-1}), mid-IR (300-3000 cm^{-1}) and far-IR (10-300 cm^{-1}). Only molecules with permanent or induced dipole will be able to interact with IR radiation, resulting in the formation of vibrational bands. From a quantum mechanical point of view, these molecules exhibit discrete levels of vibrational energies to which transitions can occur during the absorption of IR radiation. Subsequently, the energy levels can be described by the Schrödinger equation:

$$\hat{\mathrm{H}}\Phi = E\Phi \qquad \text{Equation 2.12}$$

where $\hat{\mathrm{H}}$ is the Hamiltonian, Φ is the eigenfunction and E is the energy eigenvalue. To solve this equation, an appropriate model such as the anharmonic oscillator that accounts for the potential and kinetic energies of an actual molecule is applied and the corresponding vibrational energy can be described as[86]:

$$E(v) = hv_r\left(v + \frac{1}{2}\right) + hv_r x_a\left(v + \frac{1}{2}\right)^2 + \cdots \qquad \text{Equation 2.13}$$

where h is Planck's constant, v_r is the vibrational frequency, v is the vibrational quantum number and it can have values 0, 1, 2,… and x_a is the anharmonicity constant.

As mentioned above, IR regions can be classified according to the range of wavenumber and thus, the corresponding vibrational energy. In the far-IR region, lattice vibration of framework oxygen and charge-balancing cations in zeolites can be studied. In the mid-IR range, molecular vibrations for surface OH groups, adsorbed probed molecules and framework vibrations can be investigated. Finally, near-IR spectroscopy is common for visualizing overtones and combination modes of hydroxyl sites of a zeolite. While this region is highly useful in the study of zeolites, conventional transmission spectroscopy is likely to fail due to the aggressive radiation scattering

of the zeolitic vibrational bonds, resulting in lower transmitted beam. In the 1980s, Kazansky et al. pioneered the use of diffuse reflectance spectroscopy (DRS) for zeolite characterization, which has shown to be effective in the near-IR region. In this study, the zeolites were characterized using a Nicolet 6700 FTIR equipped with a Praying Mantis diffuse reflectance IR Fourier transform (DRIFT) cell designed by Harrick. Zinc Selenide (ZnSe) was chosen as the material for the cell window because it is water insoluble and chemical resistant. The lower spectral limit, however is around 500 cm^{-1}, which does not permit far-IR spectroscopy of zeolites. To take a DRIFTS spectrum, about 20-30 mg of zeolite powder is placed into the cell and exposed to an IR beam of 32 scans with a resolution of 4 cm^{-1}. The reflected radiation from the sample is then collected by an elliptical mirror and directed to a highly sensitive mercury cadmium telluride (MCT/A) detector. Figure 2.7 shows an IR spectrum of activated fresh Y zeolite at room temperature. The band at 3742 cm^{-1} corresponds to terminal silanol, while the bands at 3635 cm^{-1} and 3545 cm^{-1} are attributed to bridging hydroxyl groups with Brønsted acid character in the supercage and sodalite cages, respectively. Bands that occur below 1400 cm^{-1} are attributed to framework vibrations of zeolites. In cases where adsorbed water is present especially on hydrated Y zeolites, a broad band appears between 3000 – 4000 cm^{-1}, resulting from hydrogen bonding of water with the hydroxyl groups. A band at 1640 cm^{-1} is also attributed to hydroxide radical stretching of water.

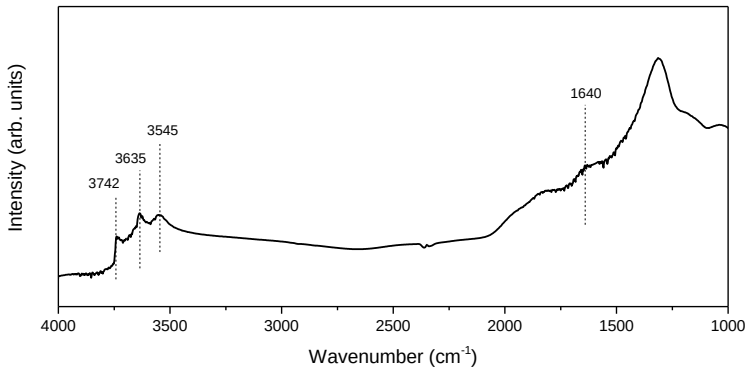

Figure 2.7: IR spectrum of fresh Y zeolite taken at 25 °C after thermal activation.

The quantification of acid sites is of great importance in acid-base interaction in zeolites. An acid site can either be Brønsted or Lewis acidity depending on the type of the corresponding aluminum in the zeolite. Brønsted acid sites are proton donors consists of structural OH groups formed between Si and Al atoms in the zeolite framework. Thus, the number of these sites is equivalent to the number of tetrahedral aluminum species, resulting in a net charge of -1. As discussed in Section 2.2.2, the negative charge is balanced by a proton or monovalent alkali cations. Lewis acid sites are essentially electron acceptors that arise from aluminum-containing extra-framework species. They are usually formed via hydrothermal steaming or dealumination of zeolites, during which the bonds of the Si-O-Al framework bonds are broken and subsequently deposited onto the internal and external surfaces of the zeolite as extra-framework species. Figure 2.8 compares the molecular structure of Brønsted and Lewis acid sites. In fact, Brønsted acid sites can be converted to Lewis acid site via either dihydroxylation or dealumination, resulting in three-coordinated framework Al and extra-framework alumina, respectively. A third way to introduce Lewis acidity is the introduction of metal cations. These acid sites may be detected by IR spectroscopy by adsorbing them with a probe molecule. The molecule should have a basic characteristic and able to differentiate the two acid site. One such molecule is pyridine. Pyridine was used in this study because it interacts different with the acid sites. On Brønsted acid site, pyridine forms pyridinum ion, PyH^+ which is represented by the IR band at 1540 cm^{-1}. The adsorption on Lewis acid site occurs molecular which gives rise to a band at 1450 cm^{-1}.

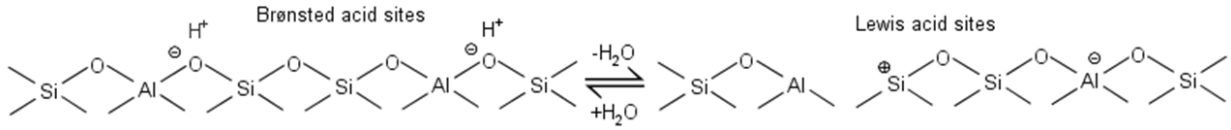

Figure 2.8: Conversion from Brønsted (proton donor) to Lewis (electron acceptor) acid sites via dehydroxylation.

Aside from pyridine, carbon monoxide (CO) is another probe molecule that is very useful for investigating oxidation and coordination states of metal cations. CO has a small kinetic diameter and molecular size, which can reach most of the active sites in the zeolite. When adsorbed on a metal, different CO ligands can form depending on the type of zeolite, CO pressure and adsorption temperature.[87] This interaction between CO and cations gives rise to strong carbonyl vibrational bonds in the region between 2300 – 1800 cm^{-1} that can be observed by IR spectroscopy. It should be mentioned here that upon adsorption of pyridine or CO, the DRIFTS cell was subjected to a vacuum pressure in the order of 10^{-5} Torr so that only chemisorbed bands were being investigated.

2.3.3 Microscopy

Imaging techniques are important characterization tools to relate a zeolite's physical structure to its adsorption or catalytic performance. Since the introduction of electron microscopy in the early 1930s, useful structural information such as surface topology, particle size, pore morphology and metal dispersion could be obtained.[88] For the characterization of zeolite particles in the bulk phase, a FEI manufactured Quanta 250 Scanning Electron Microscope (SEM) coupled with Energy Dispersive X-ray Analysis (EDAX) accessory was used. The zeolites were coated with a gold layer prior to SEM imaging to enhance the electron conductivity. Further analysis of the unit cell of zeolite (~1-2 nm) would require a more powerful instrument with higher magnification. Fortunately, the high voltage transmission electron microscope (TEM) has a much higher resolution (~0.1 nm), which enables imaging of microstructure and lattice fringes of zeolites. The TEM instrument used for this study was a FEI Talos F200X microscope equipped with an X-FEG field emission source and a super X-EDS system. Since zeolites are thick materials, extensive preparation steps are required before the characterization. Zeolite powders are first

lightly crushed in a pestle and suspended in ethanol to create a dilute suspension. A small amount of sample (~0.01 g) is carefully transferred to a carbon-film copper grid, allowing small zeolite crystallites to adhere via electrostatic interaction. Once the ethanol is evaporated and a thin crystallite layer is obtained, the grid is then ready for transfer into the TEM.

2.4 Fixed-Bed Adsorption Experiment

The adsorptive desulfurization performance of fresh Y zeolite and modified Y zeolites were examined using a fixed-bed adsorption experiment in a custom-made quartz column. Figure 2.9 shows a schematic of the experimental setup. The adsorption column has an outside diameter of ¼" and a length of 26 cm. About 0.2-0.3 g of zeolite powders were packed into the column until a standard height is reached. Prior to the adsorption experiment, the zeolites were first activated or reduced with N_2 or H_2, respectively at 400 °C for several hours. Then, a model fuel containing various sulfur compounds dissolved in *n*-octane was fed into the column using a high-performance liquid chromatography (HPLC) pump at flow rate of 0.05 mL/min or a liquid hourly space velocity (LHSV) of approximately 0.002 h^{-1}. 0.5 mL was collected at a consistent interval and quantified for sulfur content using a gas chromatography system equipped with a sulfur chemiluminescence detector (GC-SCD). The GC model is 7890A manufactured by Agilent Technologies. The SCD is a 355 Agilent model that is comprised of a dual plasma burner and a detector. Upon combustion, sulfur monoxide (SO) reacts with ozone to form SO_2, O_2 and chemiluminescent light (< 300-400 nm). The light is optically filtered and detected with a photomultiplier tube. The corresponding signal is then amplified on the display. Table 2.1 provides the GC-SCD method parameters for the sulfur analysis.

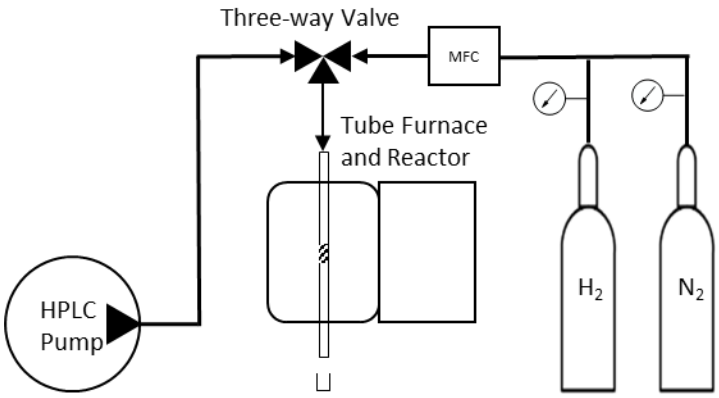

Figure 2.9: A schematic of the fixed-bed adsorption column.

Table 2.1: Method parameters for GC and SCD conditions.

GC conditions		**SCD conditions**	
Inlet:	50:1 split ratio	Base:	300 °C
	300 °C	Furnace:	800 °C and 350-400 torr
Column:	Agilent HP-5 30 m × 320 μm × 0.25 μm	Air:	50 mL/min
	He at 9.1 psi as carrier gas	H_2:	40 mL/min
Oven:	40 °C for 1 min	Ozone:	3-6 psig
	12 °C for 150 °C	Cell:	4-8 torr

Chapter 3

THEORETICAL METHODS

3.1 Introduction

There has been immense amount of interest in computational science due to the advancement of computing power over the past few decades. Nowadays, supercomputers are becoming more reliable in predicting future results based on well-understood scientific notions and principles. In theoretical studies of catalysts and adsorbents, quantum mechanics calculations can be used to predict molecular and surface properties that are difficult to obtain experimentally. Nevertheless, theory and experiment go hand in hand. A set of results from experiments may not be entirely understood without theory and conversely, a theory cannot be formulated in the absence experimental data. Using contributions from theory, correlations can be made between adsorption capacity and adsorbate binding energy. An extensive explanation of quantum mechanics calculation is outside the scope of this dissertation, but can be found elsewhere.[89–91] Thus, the objective of this chapter is to give a brief overview of quantum mechanics or more specifically, theoretical methods to fundamentally understand the bonding between sorbent and sorbate.

Quantum mechanics was developed in the early 1920s by a group of renowned scientists based on revolutionary principles of quantum theory. In 1900, German physicist Max Planck discovered that colors were quantized even though it was believed that light behaved as a wave. He later hypothesized that the energy of electromagnetic waves can take on discrete values. In 1905, Albert Einstein envisioned the photoelectric effect as light traveling in the form of packets or energy quanta, instead of waves. In 1913, Niels Bohr applied Planck's hypothesis of quantization to Ernest Rutherford's experiments that indicated electrons orbited the nucleus. Bohr postulated that the electron's angular momentum was quantized by Planck's constant and was

allowed to jump between quantized "orbits". The ideas that quantities are quantized and that light behaves as particles led to the discovery of photons by Arthur Compton in 1923, who showed that particles of light or photons have momentum. By now, it was well-accepted that light could behave both as a wave and a particle, hence the term, wave-particle duality of light. The demonstration of light's wave-particle duality motivated French physicist Louis de Broglie to show that like light, electrons also display features of waves and particles. However, a German physicist named Werner Heisenberg proposed that since matter acts as waves, it is impossible to measure its energy and position accurately, even in theory. Taking de Broglie's hypothesis and Heisenberg's uncertainty principle into consideration, Austrian physicist Erwin Schrödinger theorized that the behavior of electrons could be treated as matter waves. Equation 2.12 represents the Schrödinger equation.

3.2 Density functional theory

In the field of catalysis or adsorption, it is important to determine the energy of a system for the prediction of reaction and adsorption mechanisms. This can be done by approximating the location of the electrons and minimizing the energy over all possible wavefunctions of the Schrödinger equation or eigenfunctions of Equation 2.12, but it is practically impossible to explicitly solve most systems due to the high number of electrons. Therefore, various mathematical approximations have been applied to solve the Schrödinger equation resulting in various quantum mechanical methods, such as, ab-initio methods, semi-empirical methods and density functional theory (DFT). *Ab initio* methods relies on theory from first principles.[92] They are typically adequate for relatively small systems. For example, the Hartree-Fock (HF) approach attempts to solve the Schrödinger equation by assuming that each electron exists in a uniform field of the nuclei, surrounded by all other electrons.[93,94] This treatment is only an approximation which

excludes the effect of electronic configurations. Semi-empirical methods use parameters derived from experimental data. The advantage using these methods is that they are low-cost and faster than *ab initio* calculations. However, bond energies tend to be overestimated, thus less reliable. The third method is DFT, which started in the 1960s. Pierre Hohenberg and Walter Kohn postulated that the total energy of a system is a unique functional of the total electronic charge density.[95] Later, Kohn and Lu Jeu Sham found that electron density could be correlated to an external potential, which can be mapped to fictitious system of non-interacting electrons with the same electron density. Fortunately, the latter system is solvable using the Kohn-Sham equations below:

$$\left[-\frac{\hbar^2}{2m}\nabla^2 + v_{eff}(r)\right]\psi_i(r) = \varepsilon_i\psi_i(r) \qquad \text{Equation 3.14}$$

$$v_{eff}(r) = v(r) + e^2\int\frac{n(r')}{|r-r'|}d^3r' + \frac{\partial E_{xc}[n(r)]}{\partial n(r)} \qquad \text{Equation 3.15}$$

where $\hbar$ is the Planck's constant, m is the electron mass, $v_{eff}(r)$ is the effective external potential, ε_i is the orbital energy and ψ_i is the one electron Kohn-Sham orbital. The effective external potential can be expanded into three terms shown in Equation 3.15. The first term is attributed to nuclear potential and electromagnetic potential, which could be approximated using pseudopotentials. Pseudopotentials are used to trick the valence electrons into thinking that they are the only electrons in the system, thus less electrons to deal with. The second term, also labeled as $v_H(r)$, is the classical electron-electron interaction. The third term is the exchange correlation potential or $v_{xc}(r)$, which is most problematic since DFT does not provide the actual functional form. Therefore, functionals are developed to approximate the exchange correlation potential. Once an appropriate functional is selected, the resulting orbital energies and orbitals may be used to compute the total energy using the following equation:

$$E = \sum_i \varepsilon_i - \frac{1}{2}e^2 \int\int \frac{n(r)n(r')}{|r-r'|} d^3r d^3r' - \int v_{xc}[n(r)]dr + E_{xc}[n(r)] \qquad \text{Equation 3.16}$$

where the last term represents the exchange correlation functional energy. In this study, the B3LYP hybrid functional was used to represent the exchange correlation. It is a linear combination of HF and DFT electron correlation, providing reliable energetics for metal-ligand interactions.[96] One disadvantage, however, is that it lacks dispersion treatment.

DFT methods use mathematical functions known as basis set to build the quantum mechanical wavefunction for a molecular system. The larger the basis set, the smaller the constraints imposed on the electrons, which allows for more accurate prediction of the exact molecular wavefunctions, but they are also more computationally-expensive. A basis set assigns an atom a group of basis functions, each of which is composed of a linear combination of several Gaussian functions, known as primitives. The 6-31G(*d*,*p*) split-valence basis set used in this PhD study utilizes three primitives comprising each core orbital basis function, as well as two basis functions per valence orbital, consisting of three and one primitive(s), respectively. The *d* term adds a polarization function on heavy atoms, while *p* represents polarization of a *p* orbital on hydrogen atoms. Among the available software packages for DFT calculations, Gaussian 16 has been applied successfully to study the complex structure of zoelites.[97]

3.3 ONIOM calculation

In general, theoretical studies of zeolites can be challenging due to the large unit cell size and complex structure. For instance, the Y zeolite supercell contains 576 framework atoms that are systematically arranged to form repeating units known as building blocks. While the accurate representation of the Y zeolite can be achieved by applying periodic-boundary conditions (PBC), the process can be computationally costly. Meanwhile, the ONIOM (our own *n*-layered integrated

molecular orbital and molecular mechanics) model was found to be very efficient in studying adsorption and reaction mechanisms in zeolites.[98–100] ONIOM calculation allows for the reduction of costs by layering the system into separate regions with different degrees of accuracy.[101,102] The reactive region is treated quantum mechanically (QM) and the extended framework region is treated with a molecular mechanics (MM) force field. The total ONIOM enthalpy (or total energy) of the system is given by:

$$H_{ONIOM} = H_{MM}^{all} + H_{QM}^{active} - H_{MM}^{active} \qquad \text{Equation 3.1}$$

where H_{MM}^{all} is the enthalpy of the entire system, and H_{QM}^{active} and H_{MM}^{active} are the enthalpies of the active site, performed by QM and MM calculations, respectively. The accuracy of ONIOM method depends significantly on the size of the cluster, the accuracy of the theory and the interaction between the layers. In this study, high-level theory layer (reactive region) is treated by the hybrid B3LYP function, while the low-level theory later (extended zeolite region) is treated by molecular mechanics force fields. Figure 3.1 shows an ONIOM representation of HY zeolite that has been cut from the International Zeolite Association (IZA) database.[82]

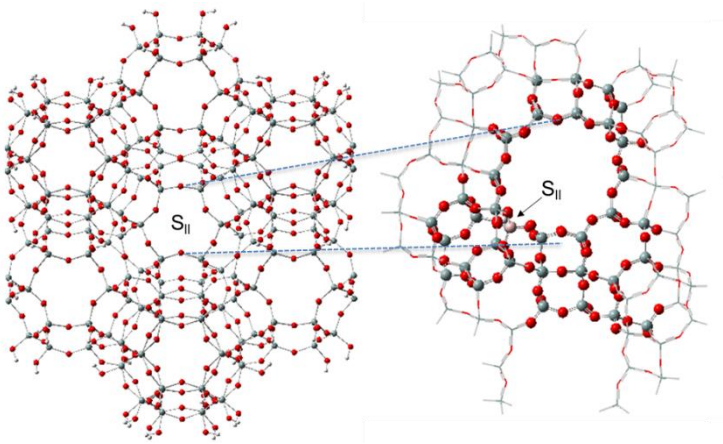

Figure 3.2: Optimized 172T ONIOM cluster model of HY cut from a 240T FAU crystal structure obtained from IZA.[82]

Chapter 4

INVESTIGATION OF METAL-EXCHANGED MESOPOROUS Y ZEOLITES FOR THE ADSORPTIVE DESULFURIZATION OF LIQUID FUELS

4.1 Introduction

Sulfur compounds in transportation fuels, such as diesel and gasoline, are becoming an important global concern, as they pose serious threats to the environment and air quality.[16,103] The Environmental Protection Agency (EPA) regulations regarding air quality policy in the United States, required that the sulfur content in federal gasoline cannot exceed 10 ppmw by January 1st, 2017, while ultra-low sulfur diesel (ULSD) must contain less than 15 ppmw of sulfur.[10,104] Another importance of deep desulfurization is motivated by the extensive use of liquid hydrocarbon fuels for fuel cell applications. Gasoline and diesel are readily available, easily storable and contain high amount of energy density, making them favorable sources of hydrogen gas for fuel cell systems.[17,67,105] However, the operation of fuel cells is restricted even by present strict sulfur regulations. In fact, fuels used in Solid Oxide Fuel Cell (SOFC) and Proton Exchange Membrane Fuel Cell (PEMFC) should be kept below 5 ppmw and 0.1 ppmw of sulfur, respectively.[13,45,67,106]

Thus, there is a great scientific interest to develop effective deep desulfurization methods to remove sulfur compounds from fuels.[18,22,107,108] Concurrently, the recent recession in oil price has driven commercial vehicle sales upwards, which increases the demand for transportation fuels.[109–111] While considerable amount of research has been invested into renewable energy, the energy sector has also focused toward producing more clean fuels derived from oil to meet the rising demand. Conventional hydrodesulfurization (HDS) is currently the most common desulfurization method used in oil refineries. However, to meet the stringent regulations of close

to zero sulfur level, very high operating pressure, temperatures and significant hydrogen consumption must be utilized; these severe conditions are accompanied by high cost and the loss of fuel quality.[18,112,113] Furthermore, conventional HDS of diesel fuels is particularly challenging due to difficulty in removing refractory sulfur compounds, such as dibenzothiophene (DBT) and other substituted DBTs. These conditions altogether make the HDS very expensive and impractical in industrial settings.

To meet the demanding specifications, many desulfurization technologies have been explored either to completely substitute or to compliment the current HDS technology. Some alternative techniques include oxidative desulfurization[114–116], alkylation[117,118], extraction[119,120], biodesulfurization[121,122] and adsorptive desulfurization.[123–126] Among these, sulfur removal via adsorption (adsorptive desulfurization) has been the most promising technique due to the ability to process sulfur-free liquid fuels at ambient conditions. Despite being cost-effective and environment-friendly, the desulfurization performance highly depends on the type of adsorbent. A wide variety of materials have been studied as sorbent materials for sulfur, such as carbon [127,128], oxides[106,129–131], mesoporous materials[132–136], and zeolites.[23,55,64,137–140] The Y zeolite, in particular, has been widely investigated due to the unique faujasite (FAU) pore structure, large surface area, and available surface acidity. The three-dimensional channels, cages and pore diameter of 7.4 Å give the Y zeolite molecular-sieve and shape selective properties, allowing only certain guest species to enter.[141] These properties of Y zeolite make this material one of the most effective zeolites in adsorptive desulfurization. However, the unique microporous nature of the Y zeolites imposes diffusion limitations to refractory sulfur molecules. Additionally the low Si/Al ratio of 2.43 of the Y zeolite results in high Brønsted acid sites (BAS), which play a significant role in sulfur adsorption.[61,142–145]

To overcome the aforementioned limitations, various functionalities, such as mesoporosity and metals, need to be introduced to the zeolite Y. The introduction of mesoporosity allows for more bulkier sulfur compounds, such as dibenzothiophene (DBT) and 4,6-dimethyldibenzothiophene (4,6-DMDBT), to enter the zeolite cages, thus improving accessibility to the active sites. Fu et al. investigated the removal of 4,6-DMDBT through HDS on mesoporous zeolite Y as a support and found that the mesoporosity is favorable for mass transfer and access of aforementioned bulky molecules, consequently increasing the adsorption capacity by 38% compared to the corresponding parent HY zeolite.[146] The introduction of metal cations can contribute to high selectivity and/or capacity for sulfur. Yang et al. performed pioneering studies on the role of ion-exchanged Y zeolites with transition metals on the desulfurization of fuels.[23,147,148] The group demonstrated that Ag-, Cu-, and Ni-exchanged Y zeolites exhibit high capacities for thiophenic molecule adsorption, among which CuY performs the best by producing 15 mL of thiophene-free model fuel per gram of sorbent. They suggested that the adsorption mechanism proceeds via π-complexation and they found that competitive adsorption becomes a major limitation when other aromatics and foreign species are present in the liquid mixture. Song. et al. determined that CeY has the highest selectivity for removing sulfur from jet fuels due to the strong direct sulfur-metal (S-M) interaction, rather than via π-complexation.[46,70] This has been confirmed by Wang et al. when they demonstrated that CeY is selective to thiophenes compared to olefins in the same hydrocarbon feed.[137] Mesoporous materials with metals have been investigated recently for sulfur adsorption. Yang et al. investigated metal halides supported on mesoporous MCM-41 and SBA-51 for the desulfurization of light jet fuel in a fixed-bed adsorption setup.[133] Oliver et. al studied the adsorptive desulfurization of jet fuel using Ag impregnated MCM-41 and mesoporous silica nanoparticles (MSN), which exhibit adsorption capacities of 32.6

mg S/g and 25.4 mg S/g, respectively.[149] In a more recent study, the group synthesized mesoporous S-impregnated zirconia-silica framework and studied its ability to remove BT, DBT, 4-6-DMDBT and naphthalene in a batch process. The combination of Ag and mesoporous silica substantially increased the adsorption capacity to 39.4 mg S/g.[136] However, all the aforementioned studies have been performed using zeolites with relatively high Si/Al ratio. Limited studies have been reported so far in investigating the use of mesoporous Y zeolite.[150] Since it has been already demonstrated in the literature that the Y zeolite is one of the best sorbents for the sulfur removal due to their unique acid sites and ion exchange capability, it would be very interesting to investigate the role of mesoporosity in this type of zeolite.

Thus, the objective of this work is to prepare, characterize and test the role of mesoporous, ion-exchanged Y zeolites on the adsorptive removal of sulfur compounds from liquid fuels. Mesoporosity has been created by using two top-down methods. Ce and Cu were ion exchanged in both the parent and the mesoporous Y. The desulfurization tests have been performed in a fixed bed column, using model fuels spiked with thiophene, benzothiophene and dibenzothiophene. Our results demonstrate that there are diffusion limitations for the refractory sulfur compounds, which can be successfully overcome using mesoporous Y zeolites. Furthermore, metal-exchanged mesoporous Y zeolites are very promising in selectively removing the sulfur compounds.

4.2 Materials and Methods

4.2.1 Preparation of metal-exchanged mesoporous Y zeolites

Fresh NH_4Y zeolite with Si/Al = 2.43 was purchased from Zeolyst International. Mesoporous Y has been prepared using two top-down methods: a) desilication (DS) and b) surfactant-assisted (SA) method. Details on the preparation methods can be found in the

literature.[68,75,151] Briefly, desilication has been performed in a 0.05 M NaOH solution, followed by ion-exchange using 0.1 M NH_4NO_3 and calcination at 550 °C for 5.5 hours.[151] Surfactant-assisted method has been conducted with acid washing of NH_4Y using 0.58 M of citric acid, base treatment using 0.16 M hexadecyltrimethylammonium bromide (CTAB) and 4.4 M ammonium hydroxide (NH_4OH), followed by calcination at 550 °C for 5.5 hrs.[75] Ion-exchanged zeolites were prepared using an ion-exchange method with 5 wt% of the desired metal element. Metal precursors $Ce(NO_3)_3 \cdot 6H_2O$ and $Cu(NO_3)_2 \cdot 2.5H_2O$ with at least 99.99% trace metal were purchased from Sigma-Aldrich. To ensure a complete exchange, zeolites and metal precursors were allowed to stir at room temperature for two full days, followed by subsequent washing and drying. The dried materials were then calcined at the same conditions described previously. The final step involved the reduction of metal ions using pure hydrogen gas at 350 °C for 3 hours. To prepare metal-exchanged mesoporous zeolites, mesoporous DS and SA Y zeolites were ion-exchanged with the desired metal precursor using the same ion-exchange procedure as the parent Y, followed by calcination and reduction.

4.2.2 Reagents

To create a controllable environment and for more credible comparison with the literature, reagent grade n-octane purchased from Sigma Aldrich was used as a model fuel (solvent). The octane was spiked with pure thiophene (TP), benzothiophene (BT) and dibenzothiophene (DBT), all of which were purchased from Sigma Aldrich. For individual testing, 50 ppmw, 100 ppmw and 150 ppmw of TP, BT and DBT, respectively, were prepared. A model fuel containing all three sulfur compounds was also prepared and tested to represent conventional commercial fuels more closely.

4.2.3 Material characterization

Crystallinity and microporosity of the materials have been characterized using X-ray diffraction, obtained using a Bruker D8 advanced x-ray diffractometer. Pore structure and surface area were determined using a Micromeritics ASAP 2020 analyzer and the data were analyzed based on the Brunaeur, Emmert and Teller (BET) method. Brønsted acid sites (BAS) and Lewis acid sites (LAS) in the zeolite as well as metals were qualitatively and quantitatively characterized by pyridine and CO adsorptions, respectively, using a Nicolet 6700 Fourier transform infrared spectrometer (FTIR) equipped with a diffuse reflectance (DRIFT) cell by Harrick. The total amount of metals in the zeolites was determined using an inductively coupled plasma coupled with a mass spectrometer (ICP-MS) following a microwave digestion method.[152] The presence of metal ions and metal oxides on *ex-situ* calcined and reduced zeolites were also characterized using a Shimadzu UV-26000 UV-Vis spectrophotometer.

4.2.4 Fixed-bed adsorption experiment

To test the desulfurization performance of each adsorbent, a fixed-bed adsorption column was custom made. A 30 cm quartz column with a 3/8" outside diameter (OD) and a built-in frit was used to support the adsorbent. The column was packed with zeolite powders until a bed height of 2.5 cm has been reached, fixing the residence time at approximately 0.1 hrs. The zeolite weight varied between 0.3-0.5 g depending on the zeolite content (e.g. presence of metals and/or mesoporosity). The metal-modified samples were reduced under H_2 flow at 350 °C for 1 hour. Metal-free zeolites such as the Parent Y, surfactant-assisted Y and desilicated Y were activated under N_2 flow at 350 °C for 1 hour. The change in color to white after the reduction step confirms that the metal-incorporated zeolites have been activated. Temperature-programmed reduction (TPR) results show distinct Cu(I)Y peaks at 250 °C and 350 °C in the supercage and sodalite cage,

respectively. A model fuel was fed into the column at a flow rate of 0.05 mL/min and the effluent was collected every 0.5 mL until a saturation point was reached. The sulfur content of the effluents was quantified by a chromatography system equipped with a sulfur chemiluminescence detector (GC-SCD).

4.2.5 Heat of adsorption by adsorption isotherm

Adsorption isotherms were collected by a batch method. Solutions containing BT or DBT dissolved in octane with concentrations ranging from 100 ppmw to 600 ppmw were prepared. 5mL of sulfur solution and 50 mg of sorbent were placed inside a flask and allowed to stir for 5 hours. The two adsorption temperatures were 20 °C and 50 °C. After adsorption, the solution was washed and the supernatant liquid was collected and analyzed for sulfur content using the GC-SCD.

4.3 Results

4.3.1 Characterization results

The retention of the original faujasite crystal structure is important for creating sulfur removal and ion-exchange sites. Figure 4.1 shows the XRD results for the parent Y, the mesoporous Y prepared by SA and DS methods, and the Ce and Cu-exchanged Y. Comparing to that of the Y zeolite, the peak intensities for 5% CeY and 5% CuY were reduced due to the presence of foreign entities. Additionally, no peaks of oxides were identified. The mesoporous Y showed a decrease in XRD patterns, where DSY showed lower peak intensity compared to SAY. These reductions in peak intensities were expected, and they suggest that the modifications on the parent material do in fact reduce the crystallinity of the parent Y.[153] Nonetheless, most of the characteristic trends were preserved as shown by the diffraction patterns.

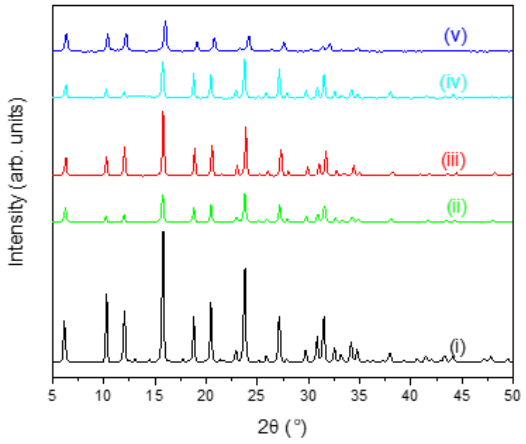

Figure 4.1: XRD patterns of parent and modified Y zeolites: (i) Parent Y, (ii) DSY, (iii) SAY, (iv) CuY, (v) CeY.

Figure 4.2(a) shows the N_2 adsorption/desorption isotherms of all the materials. As expected, the parent Y is very microporous as shown by the high nitrogen uptake at low relative pressure. When mesoporosity is introduced, a reduction in microporosity was observed for both the SAY and DSY. The difference between two types of mesoporous materials (SA and DS) becomes clearer on the pore size distribution graph created by the Density Functional Theory (DFT) method, which is presented in Figure 4.2(b). The SAY shows a uniform distribution of pores ranging between 20-50 Å, whereas the DSY displays a broad range of pores up to about 100 Å. These results are consistent with the literature.[68] Table 4.1 confirms that the mesopore area and pore volume are increased significantly for the mesoporous materials. The N_2 isotherms for 5% CeY and 5% CuY show a slight decrease in the isotherm plateau due to the presence of foreign entities, which is consistent with the reduction of peaks intensity reported by XRD.[154,155] The metal-exchanged mesoporous zeolites depict a combination of trends, wherein the mesopore area and volume were greatly enhanced and the isotherms were slightly decreased due to the presence

of metal ions. Figure 4.2 and Table 4.1 are convincing characteristic results that suggest retention of crystal structure of the modified Y zeolites.

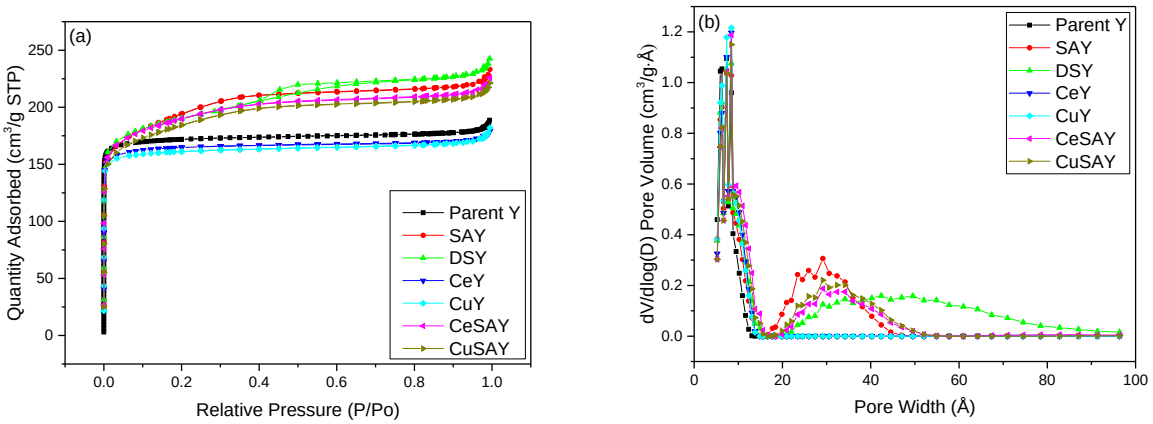

Figure 4.2: (a) Nitrogen adsorption-desorption isotherms and (b) DFT pore size distribution of the parent and modified Y zeolites.

Table 4.1: Surface areas and pore volumes of parent and modified Y zeolites.

Material	S_{tot} (m^2/g)	S_{micro} (m^2/g)	S_{meso} (m^2/g)	V_{tot} (cm^3/g)	V_{micro} (cm^3/g)	V_{meso} (cm^3/g)
Parent Y	574	530	43.9	0.282	0.246	0.036
SAY	693	373	319	0.373	0.172	0.201
DSY	646	446	201	0.368	0.206	0.162
CeY	550	500	50.1	0.273	0.232	0.041
CuY	628	394	57.2	0.281	0.229	0.052
CeSAY	648	413	235	0.342	0.190	0.152
CuSAY	637	411	226	0.336	0.190	0.146

To quantify the acid sites on the sorbent materials, pyridine adsorption experiments were carried out. Pyridine is commonly used as probe molecule for surface acidity detection as the molecule can form pyridium ions with BAS and can bond molecularly to LAS via electron transfer, both of which can be detected using FTIR. Figure 4.3 shows the FTIR results obtained from the pyridine adsorption experiment, where the BAS gives vibration peaks at 1543 cm^{-1} and LAS at

1453 cm^{-1}. As expected, the parent Y contains a high amount of BAS due to the high number of framework alumina. The SAY zeolite shows a reduction in BAS/LAS ratio, suggesting a shift from framework to extra-framework alumina due to the introduction of mesoporosity, as presented in Table 4.2. A more significant shift was reported for the DSY zeolite due to the severe desilication procedure used to introduce mesoporosity. An interesting phenomena was observed for the metal-exchanged Y materials. The introduction of Cu to the parent Y increases the LAS, which is accompanied by a decrease in BAS. On the contrary, pyridine adsorption on CeY revealed higher number of BAS compared to LAS. Similar pyridine adsorption results on CeY and CuY have been reported in previous studies.[156–158] The reason for contrasting BAS/LAS ratios between the two metals could be related to the way the metals are distributed, which will be discussed based on the CO adsorption results in the next section. The determination of total amount of metals was carried out using an ICP-MS. The amount of Cu and Ce metals in each Y-type adsorbent is reported in Table 4.2. The ICP results show that the metal content in each metal-modified material is close to 5 wt%, which validates the ion-exchange procedure and agrees with the theoretical values.

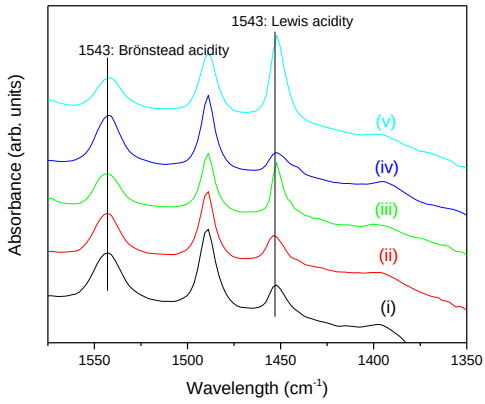

Figure 4.3: FTIR spectra of pyridine adsorption on parent and modified Y: (i) Parent Y, (ii) DSY, (iii) SAY, (iv) CuY, (v) CeY.

Table 4.2: Brønsted and Lewis acid sites, and metal content in each adsorbent.

Material	Brøsted Acidity* (μmol / g cat)	Lewis Acidity* (μmol / g cat)	Ratio	Ce** (wt%)	Cu** (wt%)
Parent Y	113.9	30.2	3.77	-	-
SAY	98.2	35.0	2.81	-	-
DSY	56.6	43.9	1.29		
CeY	82.1	20.5	4.00	5.5	-
CuY	43.7	69.3	0.63	-	4.9
CeSAY	-	-	-	5.6	-
CuSAY	-	-	-	-	4.6

* Brønsted and Lewis acid sites were calculated using pyridine adsorption
** Ce and Cu metal content were determined using ICP-MS

CO is one of the most-used probe molecules for investigating oxidation and coordination states of ions. The kinetic diameter of a CO molecule is 0.376 nm which enables it to easily access the interconnecting channels and pores of the Y zeolite.[159,160] Figure 4.4 shows the FTIR spectra of CO adsorption on parent Y and ion-exchanged Y zeolites. The various vibrational peaks correspond to CO interactions with different active sites within the zeolite. Figure 4.4(a) illustrates the FTIR spectra of CO adsorbing onto CeY. At low partial pressure of CO, the IR spectrum is relatively flat. As the partial pressure of CO increased, three vibrational peaks at 2170, 2119, and 1636 cm^{-1} emerged, which could be easily desorbed upon evacuation. This finding suggests the absence of CO-to-metal interaction. To confirm this, a spectrum of CO adsorption on parent Y was included in Figure 4.4(a) and it was observed to be very similar to that of physisorbed CO on CeY. The broad band on the far right at 1636 cm^{-1} represents the interaction of CO with the aluminosilicate framework.[161] At 80 °C, almost all the physisorbed CO has been desorbed from CeY. Figure 4.4(b) shows the FTIR spectra of CO adsorption on CuY zeolite. The main difference with CuY is seen at low partial pressure of CO. Two very stable characteristic peaks at 2144 cm^{-1} and 2158 cm^{-1} correspond to Cu on active sites II and II', respectively, both of which are located

on the hexagonal planes of the sodalite cages.[159,162,163] These stable peaks confirmed that CO was chemisorbed on CuY, as opposed to being physisorbed on parent Y and CeY, as shown previously. At elevated CO concentration, new vibrational bands are formed as a result of the decomposition of the initial monocarbonyl species to Cu(I)-$(CO)_2$ dicarbonyl species. The bands at 2158 and 2179 cm^{-1} correspond to asymmetrical and symmetrical stretches of dicarbonyl CO on Cu(I) at site II.[159,162] The peak at 2137 cm^{-1} suggests that some monocarbonyl Cu(I)-CO are still present at high CO partial pressure. A higher temperature (ca. 180 °C) was required to remove the strongly bound CO from CuY.

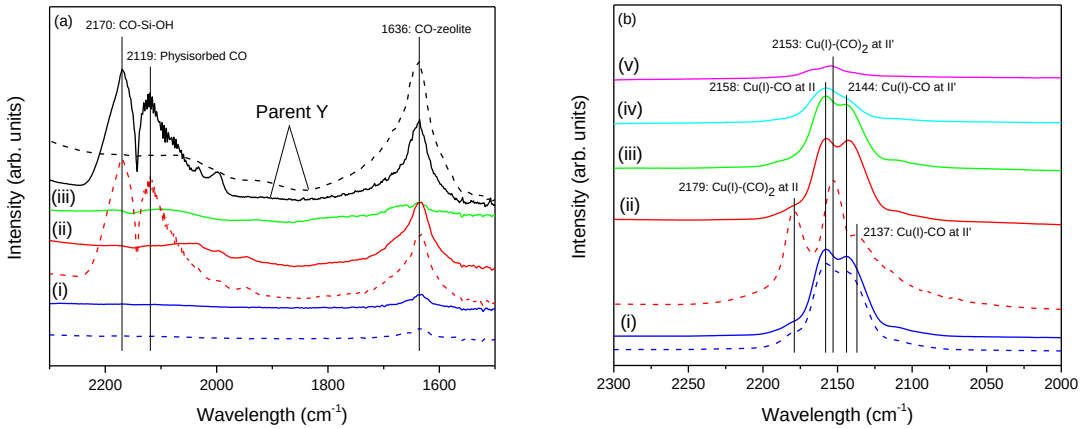

Figure 4.4: FTIR spectra of CO adsorption on (a) CeY and (b) CuY at the following conditions: (i) 0.25% CO, (ii) 5% CO, (iii) outgassed at 80 °C, (iv) outgassed at 150 °C, and (v) outgassed at 180 °C. The dotted lines (- - -) represent the spectra after outgassing

The difference in strength of chemisorbed CO on Ce or Cu can be explained by understanding the faujasite structure and its active sites. Metal cations can occupy three main sites in the zeolite framework. Site I and I' are located at the center of the hexagonal prism and inside the sodalite cage, respectively. Site II and II' are located at the faces of the 6 membered ring. A schematic showing the available actives sites is included in Figure 4.5. The Y zeolites exhibit sites

I, I', II, and II'. Upon ion-exchange, the metal cations occupy only site II. During calcination, the cations migrate toward the hidden sites (eg. sites II', I' and I). Cu cations have shown to favor any coordination sites, while higher charged cations, such as Ce, exhibit greater affinity for type I and I' sites.[164–166] The pores leading to these sites, however, are relatively small and would not permit the access of CO molecules, and hence the absence of chemisorbed-CO vibrational peaks on CeY samples.

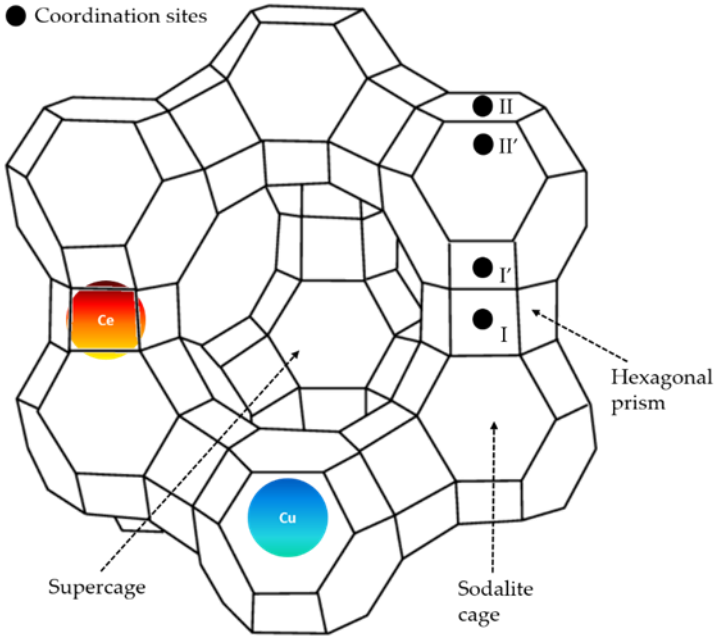

Figure 4.5: Schematic of Y zeolite unit cell and corresponding active sites.

The oxidation state at which the metal-modified materials are used during characterization and testing is important for consistency and precision. This is because uncontrolled layers of oxide forming on the metal ions can prevent or weaken the adsorption of thiophenic molecules.[55,106] As previously demonstrated, small amounts of oxides or metal cations favoring the internal sites cannot be detected by XRD or FTIR. One way to confirm the oxidation state of ion-exchanged zeolites is via UV-Vis spectroscopy. Figure 3.6(a) shows the UV-Vis spectroscopy results of

Parent Y and CeY. The broad band at 250 nm typically refers to metal oxides, which are exhibited by oxidized CeY (CeY ox). The reduced form of CeY shows four characteristic peaks at 222 nm, 237 nm, 254 nm, and 281 nm. According to the literature, the bands at 222 nm and 281 nm are attributed to the transfer of bond charge from O → Ce^{4+}, while the bands at 237 nm and 254 nm are assigned to O → Ce^{3+} bond charge transfer.[167,168] This confirms that the reduced CeY used in adsorption tests was activated. Figure 4.6(b) displays the UV-Vis spectrum of Parent Y and CuY. The peak at 212 nm confirms the presence of Cu^{+} metal ions. Unfortunately, due to the rapid oxidation of CuY, the broad band from 600 nm to 1200 nm prevents the characterization of Cu^{2+} on activated CuY and oxidized CuY (CuY ox).[169] The emergence of oxidation peaks could be eliminated if the activation of zeolites was performed in-situ, but the absence of temperature programmed accessory of UV-Vis prevented the study. Nonetheless, both physical appearance and TPR results confirmed that the zeolites used for the fixed-bed experiments were indeed activated.

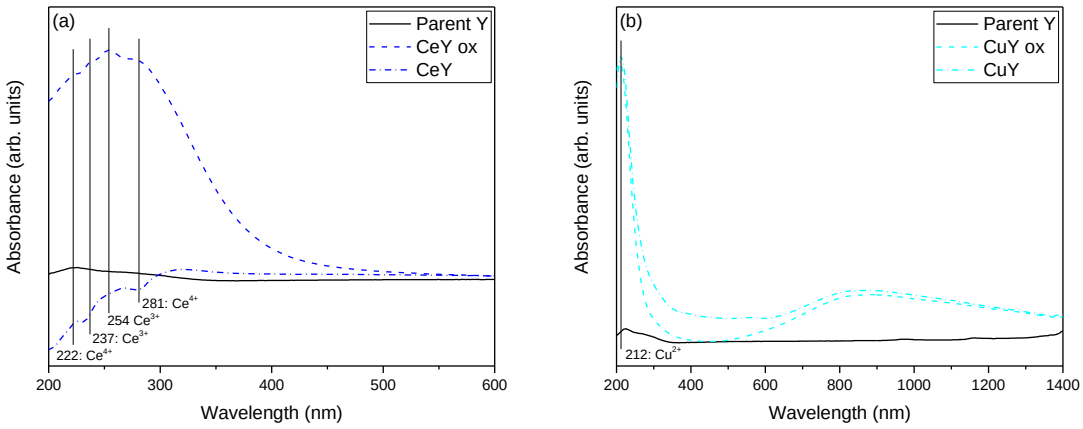

Figure 4.6: UV-Vis spectra of Parent Y, (a) CeY, and (b) CuY zeolites.

4.3.2 Fixed-bed adsorption results

Figure 4.7 shows the breakthrough curves of each of the three different thiophenic compounds on a selection of zeolite materials. Figure 4.7(a) shows the adsorption behavior of 50 ppmw of TP on parent Y and CeY. 5 mL/g of sulfur-free model fuel were produced. This finding demonstrates that the incorporation of metals does enhance desulfurization performance. Figure 4.7(b) shows the breakthrough curve of 100 ppmw BT in octane. Mesoporous SAY zeolite has also been tested to understand if there are any diffusion limitations during adsorption. However, the breakthrough curve of SAY is very similar to that of the parent, which suggests that diffusion limitations of BT to the active sites of the parent Y zeolite do not exist. An increase in adsorption capacity of about 5 mL/g is observed when CeY or CuY were used as the adsorbent, suggesting that metal incorporation improves the TP and BT uptakes. The same sorbent was used for the desulfurization of DBT, but the breakthrough curve of metal-modified Y zeolites no longer improved the sulfur uptake capacity, as seen in Figure 4.7(c). One possible reason is that the sulfur compounds with higher kinetic diameter cannot enter the micropores, thus preventing interactions with the active sites in the sodalite cages. Mesoporous DS and SAY zeolites have been tested and a significant improvement in adsorption capacity was observed as an additional 50 mL/g of sulfur-free was produced. This enhancement suggests that diffusion limitations play a significant role on the adsorption of DBT. The addition of metals to the mesoporous SAY (ie. CeSAY and CuSAY) further increases DBT uptake by about 10 fold, resulting in the production of 125 mL/g of sulfur-free fuel. These results suggest that metal-exchanged mesoporous zeolites enhance both diffusion and selectivity for larger thiophenic compounds.

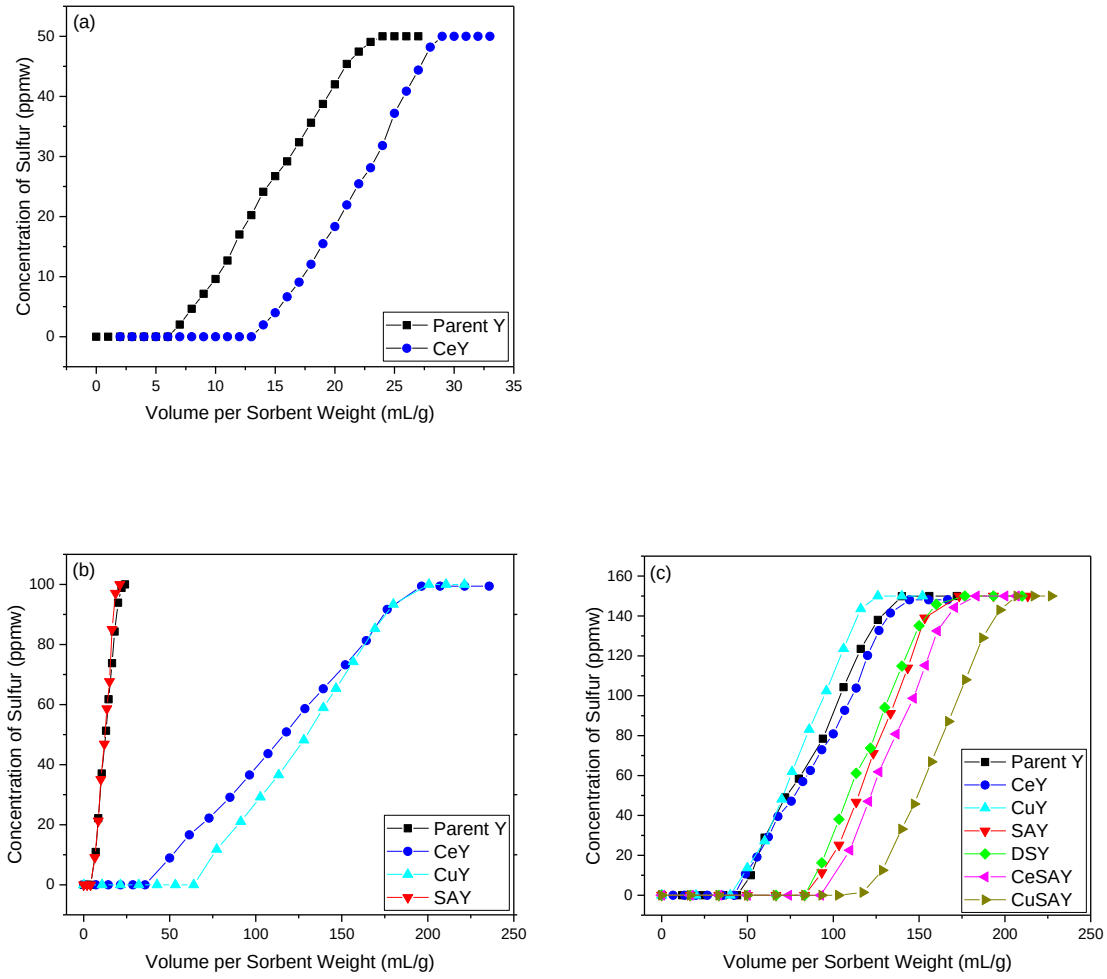

Figure 4.7: Breakthrough curves of (a) TP, (b) BT, and (c) DBT on different adsorbents.

To evaluate the interaction between the sulfur compounds, 100 ppmw of each sulfur compound was mixed in octane and used as feed. Parent Y, CeSAY and CuSAY were used as adsorbents. Figure 4.8(a) shows the breakthrough curve of the simulated liquid fuel on parent Y. The parent Y zeolite produced approximately 15 mL/g of fuel, which could be due to the strong acidity of the material. The adsorption kinetics of each sulfur compound, however, is quite similar, suggesting the absence of selective adsorption. Figure 4.8(b) displays the adsorption of sulfur compounds on CeSAY. A significant increase in sulfur capacity was observed, where high BT and

DBT capacities of 75 mL/g and 100 mL/g were obtained, respectively. The selectivity of each sulfur compound on CeSAY increases in the order of TP < BT < DBT. The different elution times depend on the interaction of each sulfur compound with Ce metal ions. Among them, DBT exhibits the highest electron density, which contributes to the strongest linkage with Ce.[170,171] The strength in electron density decreases with BT followed by TP, which is consistent with the corresponding breakthrough times. Figure 4.8(c) represents the adsorption behavior of model fuel on CuSAY. Similar to CeSAY, the metal-exchanged mesoporous zeolite showed an increase in sulfur capacity compared to the parent Y. The elution times for the different sulfur compounds followed the same order as that of CeSAY. However, earlier elution times were observed with CuSAY, in particular for BT and DBT as shown in Figure 4.8(c). As discussed earlier, the interactions in which Cu and Ce metals engage with sulfur molecules are different. Transition d-block metals, such as Ni and Cu tend to form π-complexations with neighboring aromatic molecules via back-donation of electron density to the π orbitals.[64] The f-block elements, such as Ce, on the other hand, prefer to selectively form direct σ bonds to nearby molecule.[70] Because DBT possesses the highest electron density among the existing sulfur molecules, the Ce ions will most likely bind stronger to DBT than to BT or TP. This explains the higher elution time of BT and DBT on CeSAY compared to CuSAY, which would otherwise be bound via a relatively weaker π-bond interaction. The breakthrough curve of total sulfur is presented in Figure 4.8(d). In conjunction with the individual testing of each compound, metal-exchanged mesoporous zeolites have shown, again, to be the most effective and selective adsorbent for desulfurizing transportation fuels.

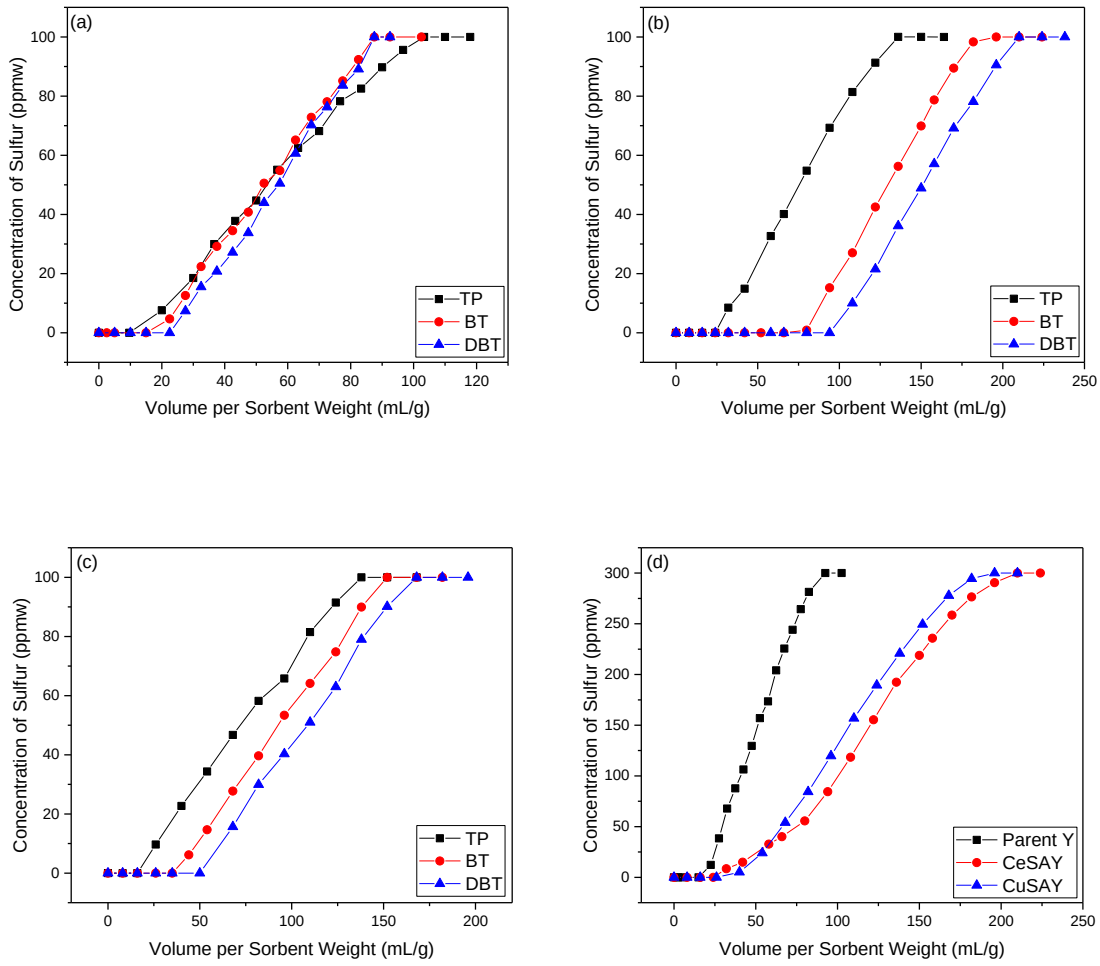

Figure 4.8: Breakthrough curves of model fuel on (a) NH4Y, (b) CeSAY, (c) CuSAY and (d) all sorbents.

4.3.3 Determination of isosteric heat of adsorption

Isosteric heats of adsorption were calculated to determine the strength of each sorbent when interacting with sulfur molecules. The objective is to correlate the heat of adsorption (ΔH_{ads}) values of each material to the corresponding breakthrough performance. The isosteric heats of adsorption differ from calorimetric experiments, such that the values are derived from the analysis of adsorption isotherms at two varying temperatures.[172] Analogous to vapor-solid adsorption, the

enthalpy of adsorption based on the Clausius-Clapeyron equation for liquid-phase adsorption can be written as:

$$\Delta H = -RT^2 \left(\frac{\partial \ln C}{\partial T}\right)_q \qquad \text{Equation 4.1}$$

where C is the equilibrium sulfur concentration (ppmw), T is the adsorption temperature (K), q is the amount of adsorbed sulfur (mmol/g), and R is the universal gas constant. Assuming that the adsorption behavior of sulfur follows the Langmuir isotherm[173], the equilibrium data can be fitted to the following equation:

$$q = \frac{K_L Q_m C}{1 + K_L C} \qquad \text{Equation 4.2}$$

where K_L is the Langmuir constant and Q_m is the maximum amount of adsorbed sulfur. Table 4.3 shows the adsorption parameters and the corresponding heats of adsorptions. TP is not included in this study because bulky sulfur compounds were the main focus. Moreover, TP has been widely studied in the literature.[173,174] CuY exhibits the highest ΔH_{ads} values as strong adsorption exists between the Cu metal and the sulfur molecule. The calculated ΔH_{ads} values of BT and DBT are also close to those calculated by other groups.[159,174] As expected, the adsorption of BT and DBT on the parent Y zeolite is not as strong as on CuY, as also suggested by the breakthrough curves. The similar ΔH_{ads} values of BT and DBT on parent Y shows that the sorbent is not selective and can adsorb equal amount of sulfur compounds, as shown by the breakthrough curve in Figure 4.8(a). ΔH_{ads} values of CuSAY and Ultrastable Y were also determined to investigate the influence of pores on sulfur adsorption. The reported ΔH_{ads} values are relatively low, which suggest that the introduction of mesoporosity or the loss of framework alumina could reduce the adsorption strength between the sulfur and the sorbent.

Table 4.3: Langmuir isotherm parameters and isosteric heats of adsorption for BT and DBT adsorbed on different adsorbents.

Material	Sorbate	T (° C)	K_L (g/mmol)	Q_m (mmol/g)	$-\Delta H_{ads}$ (kJ/mol)
Parent Y	BT	20	0.03980	6.740	21.32
		50	0.01380	5.440	
	DBT	20	0.04234	4.524	22.74
		50	0.01812	3.212	
CuY	BT	20	0.01302	0.758	41.94
		50	0.00611	0.375	
	DBT	20	0.03677	2.909	30.46
		50	0.00742	1.911	
CuSAY	DBT	20	0.02994	3.613	15.56
		50	0.01190	3.632	
USY	DBT	20	0.00411	2.469	15.30
		50	0.00248	2.395	

4.4 Discussion

The goal of the study was to investigate the role of metal-exchanged mesoporous Y zeolites for the adsorptive desulfurization of fuels. Y zeolites are excellent candidates for sulfur adsorption because of their unique pore structure and high density of BAS. Our hypothesis was that the introduction of mesoporosity would allow larger molecules such as DBT to access the internal active sites of the micropores via σ-bonding or π-complexation. Such modification, however, is inevitably accompanied by the loss of some acid sites. Consequently, the change in active site density will impact the surface chemistry and thermodynamic equilibrium. Meanwhile, metal cations can be introduced into the structure via the ion-exchange method to enhance the selectivity of sulfur compounds. Ion exchange capacity of zeolites is determined by the number of Brønsted acid sites. Reducing the acid sites would result in less ion-exchanged metals in the zeolite, making the zeolite less selective.

Up until now, encouraging results have been reported in literature using mesoporous zeolites[175], or siliceous mesoporous MCM-41 or SBA-15. Metals have also been loaded in MCM-41 and SBA-15 materials.[176] However, to the best of our knowledge, studies on metal-exchanged mesoporous Y zeolites for adsorptive desulfurization are scarce or otherwise limited to batch processes only.[123,128,177] Thus, the novelty of this study comes from the intuition that the combination of both functions of metal-exchanged mesoporous Y zeolites can significantly improve the adsorptive desulfurization in a fixed-bed application. Hence, CeSAY and CuSAY zeolites were prepared to test this hypothesis. Figure 4.7(c) confirms the remarkable results from desulfurizing model fuels with CeSAY and CuSAY. Capacity for DBT was significantly increased especially with CuSAY, which reported a 75 mL increase in sulfur-free fuel. To examine the viability of our method, past studies have been compared. Shah et. al investigated the adsorptive performance of Cu-containing SBA-16 which exhibited a capacity up to 40 mL/g for DBT dissolved in *n*-octane.[178] Li et. al performed desulfurization experiments on oxygenated-based activated carbons which effectively removed 60 mL/g of DBT from *n*-octane.[179] Among these materials, metal-exchanged mesoporous Y zeolites have demonstrated predominant desulfurization performance with a high DBT capacity of 125 mL/g. This shows that the proposed metal-exchanged mesoporous zeolites can perform just as effective as other well-distinguished sorbents for desulfurization, if not better.

The strong adsorption capabilities of metal-exchanged mesoporous Y zeolites are also demonstrated in Figure 4.8. DBT exhibits relatively higher electron density than other sulfur molecules, which makes it highly favorable for adsorption on the active sites. The presence of DBT causes steric hindrance due to its high kinetic diameter of ~9 Å[71], and inability for other molecules to access the active sites, suggesting that diffusion can be a limiting factor. The mass

transfer limitations can be overcome by making the parent Y mesoporous. As pore access becomes possible, the thermodynamic equilibrium constant increases, which results in higher sulfur uptake. For smaller sulfur compounds such as TP and BT, the relatively smaller kinetic diameters allow them to access the supercage freely and subsequently the active sites without any diffusion limitations. The comparable breakthrough slopes of TP, BT and DBT suggest that the role of kinetic rate on sulfur adsorption is inconclusive. Thus, we suggest that the adsorptive desulfurization by metal-exchanged mesoporous Y zeolites is mainly driven by thermodynamics. By eliminating diffusion and selectivity limitations, metal-exchanged mesoporous zeolites show high tendency in adsorbing higher amounts of sulfur, especially the refractory sulfur compounds such as DBT.

Our results indicate that Cu has a higher capacity than that of Ce in the adsorption of single sulfur compound. Analysis of our FTIR results clarifies and distinguishes the difference on the location of Ce and Cu metals. In Figure 4.4, chemisorbed CO is absent from the CeY spectrum, whereas strongly-adsorbed CO was observed in the CuY spectrum. CeY occupies very obscure locations such as Site I and I' which are too confined for CO to enter.[165,180] Ce cations favor the migration into the hidden sites, because they can form higher coordination bonds with 6 oxygen ligands.[165] The pores leading to these sites, however, are relatively small and would not permit the access of CO molecules. Hence, the absence of chemisorbed-CO vibrational peaks on CeY samples. Sites II and II' occupied by Cu, on the other hand, are very approachable by CO, as well as for the adsorption of thiophene and other relevant compounds. However, in the mixture of multiple sulfur compounds, Ce cations have shown to be more selective for DBT removal due to strong direct S-M bonds. This could be due to the migration of Ce cations in hidden sites toward the supercage as a result of the tendency to form high energy complexes with thiophenes via the

strong σ bond interaction.[166] These results suggest that the affinity of thiophenic molecules to adsorb on the active sites would depend on the type of metal and its location.

It is also interesting that the affinity of each ion-exchanged material to adsorb each sulfur compound follows the same trend. The elution time is held longest for DBT adsorption, followed by BT and TP subsequently, as shown in Figure 4.7. To confirm this adsorption trend, a mixture of model fuel containing all three sulfur compounds simultaneously were tested on metal-exchanged mesoporous zeolites. Figure 4.8 shows that that DBT is most strongly adsorbed compared to BT and T, confirming the aforementioned trend. This leads us to conclude that DBT exhibits the highest electron density among the competing molecules and thus, would form the highest energy bond with the active site. The validation of this conclusion using computational studies will be the objective of our upcoming work.

Heats of adsorption were also measured to determine the nature and bond strength exhibited between thiophenes and zeolites using the isosteric method.[173] In fact, this particular study was directed mainly toward investigating the effects of metals such as Cu on the heat of adsorption. Results showed that ΔH_{ads} is the highest for CuY for both BT and DBT compounds, which is up to twice as much compared to the parent Y. The increase in ΔH_{ads} shows that Cu metals are responsible for stronger sulfur adsorption, which increases the bond strength between the sorbent and the sorbate. This also indicates that the higher adsorption energy is thermodynamically favored, thus increasing the sorbate uptake at equilibrium on CuY. Notice however, a decrease in ΔH_{ads} for DBT adsorbed on the same sorbent, which is consistent with the unchanged breakthrough curves as a result of diffusion limitation. To confirm the hypothesis, the ΔH_{ads} of DBT on CuSAY was measured and the results showed a decrease in energy value. As explained previously, the introduction of mesoporosity may grant access to diffusion into the internal sites, but the trade-off

is a reduction of adsorption sites. Nonetheless, the heat of adsorption calculation is a useful tool for comparing binding energies of different aromatics.

The design of metal-exchanged mesoporous Y zeolites explores the balance between the embodiment of active metals and mesopores for adsorptive desulfurization of liquid fuels. For instance, overloading of metals can cause formation of oxides that may block zeolite active sites. Also, mesoporosity should be introduced carefully to avoid uncontrolled desilication of material. Our results have shown that most of the crystal structure and microporosity of modified materials were retained. However, if the materials were recycled and regenerated for further adsorption studies, we would expect some physical change over time depending on the method of regeneration.[23,148] The impact of regeneration on the lifetime of sorbent is an important subject from economic and environmental standpoints, thus will be addressed in our next studies. Overall, good correlation has been demonstrated between theoretical insight and experimental results as shown by the good agreement between breakthrough performance and the predicted ΔH_{ads} of each material.

Finally, it should be pointed out that in this study a linear hydrocarbon – octane - has been used as a model fuel. However, fuels like gasoline or diesel contain a vast number of other chemical components, which might have an inhibiting effect on the adsorption of sulfur compounds. For example, aromatic molecules may compete with the sulfur compounds for the same adsorption sites in zeolites, thus inhibiting the adsorption of the latter. The viability and practicality of metal-exchanged mesoporous zeolites in the presence of other aromatic hydrocarbons, such as benzene, toluene and naphthalene should be explored in future studies.[23,156]

4.5 Conclusions

Breakthrough measurements of adsorptive desulfurization have been investigated on parent Y, mesoporous Y, metal-exchanged Y and metal-exchanged mesoporous Y zeolites. metal-exchanged mesoporous zeolites, prepared by ion-exchanging mesoporous SAY zeolites with Ce or Cu, exhibit high sulfur adsorptive properties. The experimental results showed that CuSAY zeolite produced 125 mL/g of DBT-free liquid fuel, followed by 100 mL/g by CeSaY. metal-exchanged mesoporous zeolites enhance both accessibility to the active sites and selectivity for thiophenic compounds with high kinetic diameter. This enhancement is driven by the presence of metals which create more active sites to bind with the sulfur either via π-complexation or the direct S-M σ bond. The incorporation of mesoporosity can provide access of bulky sulfur compounds to the active sites. For each material tested, the preference for adsorbing sulfur compounds from octane followed the order of TP < BT < DBT. This trend agreed with the ΔH_{ads} values of each sorbent-sorbate interaction. In a model fuel containing a mixture of all sulfur compounds, CeSAY exhibited the highest sulfur capacity due to strong selective adsorption. This study shows that metal-exchanged mesoporous Y zeolite is a promising candidate for industrial deep desulfurization of transportation fuels. Finding the optimum balance between the pore structure and metals in a metal-exchanged mesoporous zeolite is essential for maximizing capacity and selectivity for sulfur compounds.

Chapter 5

REMOVAL OF BENZOTHIOPHENE AND DIBENZOTHIOPHENE FROM HYDROCARBON FUELS USING CUCE MESOPOROUS Y ZEOLITES IN THE PRESENCE OF AROMATICS

5.1 Introduction

Recent decline in crude oil price has reinforced the utilization of processed fuels in various sectors such as industrial, infrastructure, commercial and transportation.[18] The 55% drop in oil price since 2013 sees a consequential decrease in the price of processed fuels, such as commercial gasoline, diesel fuel and jet fuel as seen in Figure 5.1.[181] Furthermore, the discovery of new oil reserves promotes interest in the utilization of fossil-based fuels, especially in the transportation sector.[182] Hence, while renewable energy (e.g. based on biomass resources[183,184]) is still receiving considerable attention, adequate supply and reasonable cost of fossil-based fuels inevitably promote the production of gasoline and diesel. The increasing demand in fossil-based fuels, however, quickly become a global concern when lethal emissions into the atmosphere are taken into account. According to the Environmental Protection Agency (EPA), transportation fuels contribute about 50% of nitrogen oxide (NO_x) and 5% of sulfur oxide (SO_x) emitted annually.[185,186] The SO_x emission may seem insignificant, but it has been proven that only a small amount of sulfur contamination, could lead to catalytic converter failures or even fuel cell electrode poisoning.[4,67] If sulfur levels are not properly monitored, traces of sulfur oxides can impede the activity of automotive catalysts and electrocatalysts by altering the surface properties and consequently, influencing the efficiency and activity of the catalysts.[187] Without proper implementation of sulfur

removal mechanism, the emitted SO_2 can react with water vapor in the atmosphere to form sulfuric acid, which is one of the precursors of acid rain.[16,17]

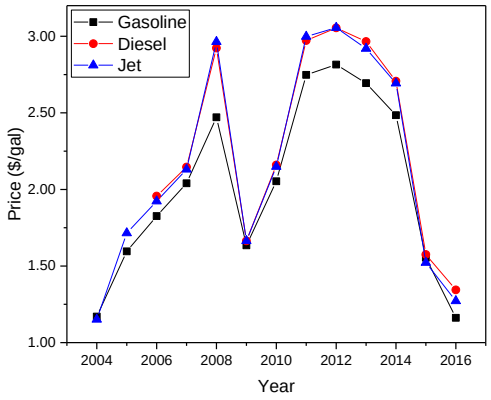

Figure 5.1: Prices of Petroleum Products since 2004.[181]

To prevent this growing problem, the EPA has introduced mandatory transportation fuel regulations, which limit the sulfur concentrations in gasoline and diesel fuel to 10 and 15 ppmw, respectively.[10] While the aforementioned sulfur standards may be attainable by conventional desulfurization methods, fuel cell membranes require their electrolytes to contain less than 1 ppmw of sulfur.[16,17] Furthermore, refractory sulfur compounds in diesel fuel such as thiophene-derived compounds are very stable, rendering the cleavage of C-S bond impossible without involving excessive energy. Due to their refractive and abundant nature, considerable amount of sulfur compounds can still be found in fuels after the fluid catalytic cracking (FCC) process.[3,188,189] Conventional hydrodesulfurization (HDS) is widely used in the refinery to remove sulfides, mercaptans and thiophenes. HDS, however, lacks the capability to produce zero-level sulfur fuels without the use of energy-intensive conditions, such as high pressure and hydrogen consumption.[18] At these severe conditions excessive hydrogenation of aromatics in fuels negatively affects other properties of fuel, such as Research Octane Number (RON) etc.

Adsorptive desulfurization can be a promising alternative or complementary technology to HDS, because it has the potential to be regenerative, cost-effective, environment-friendly, while operating at ambient conditions. The streamlined design and synthesis of such adsorbents can render sulfur removal rational towards intensified on–purpose technologies. The utilization of zeolites as liquid-phase sulfur adsorbents is receiving significant attention lately, as they have shown to be very effective in gas-phase sulfur removal in the 1990s.[190–192] As a result, the synthesis and modification of novel adsorbents have received tremendous attention in adsorptive desulfurization. Among the widely discovered sulfur-selective adsorbents[128,131,133,136,139,140], faujasite (FAU) Y zeolite has shown to be a promising sorbent material due to the unique 3-dimensional (3D) pore structure and available active (acid) sites. The average-sized micropores of 7.4 Å and inter-connecting sodalite cages allow only certain molecules to access the internal active sites located in their supercage.[68] The highly dense Brønsted acid sites (BAS) act as an adsorption platform by donating proton to nearby adsorbate molecules. While this is highly advantageous in the removal of small molecules in various adsorption applications[47,193–197], the microposority of Y zeolites may restrict the transport of refractory sulfur compounds with large kinetic diameter, such as dibenzothiophene (DBT) and other alkyl-branched dibenzothiophenes. Moreover, competitive adsorption imposed by the presence of aromatics, such as benzenes and naphthalenes in gasoline and diesel fuel, respectively, can also impede the selectivity of sulfur compounds. Thus, the overall desulfurization performance could be significantly compromised. These challenges can altogether cause a major drawback in the effort to meet federal sulfur standards assigned by the EPA.[10]

It is clear that the aforementioned challenges must first be apprehended before adsorptive desulfurization can become an industrially viable technology. The physical and chemical properties of Y zeolite can be easily altered by tuning the Si/Al ratio either via desilication or

dealumination techniques.[68] Furthermore, the relatively high amount of protons in acidic Y zeolites make them ideal materials for ion-exchanging metal cations. Many research groups have taken various steps to modify the Y zeolite using different state-of-art techniques, such that the mass-transfer resistance and selectivity limitations of the parent material can be overcome. One approach to minimize diffusion limitations is by introducing mesopores via a bottom-up synthesis or a top-down modification.[68] Mesoporous materials with pores ranging from 2 – 50 nm have been extensively studied and utilized for various applications, especially in catalysis.[198–201] More recently, mesoporous zeolites have proven to be promising sorbents in the desulfurization of liquid fuels. Tian et al. investigated the sulfur removal from model fuel containing various thiophenic compounds and found that desilicated H-beta zeolite removes about twice as much total sulfur, compared to the parent beta zeolite.[175] In relation to this, the Wang group suggested that the sulfur capacity of jet fuel increases by three-fold with the large pore SBA-15 compared to the parent zeolite.[202] A similar result was also observed by Yang et al. as mesoporous materials, such as SBA-15 and MCM-41, improved the mass transfer of sulfur compounds to the adsorption sites, when used as supports.[176] While the introduction of larger pores may improve the kinetics of these larger molecules, the role of adsorption equilibrium on the overall desulfurization performance should not be completely ignored. The introduction of mesopores will inevitably cause a partial loss of active sites responsible for adsorbing sulfur. One effective way to introduce mesoporosity without sacrificing too much microporosity, is by using a hydrophobic mesopore-template as demonstrated by Li et al.[203] They synthesized mesoporous aluminosilicate (MAS) using cetyltrimethylammonium bromide (CTAB) as a directing agent and discovered that it exhibits 20% higher sulfur adsorption capacity compared to NaY and MCM-41 for the desulfurization of diesel. Furthermore, as demonstrated by Oliver and co-workers[136], the pore size optimization of silica-

zirconia templated by dodecylamine (DDA) allows for better sorbent regenerability and higher adsorption capacity of 12.4 $mgS.g^{-1}$ compared to its counterpart templated by the longer hexadecylamine (HDA).

As previously discussed, the introduction of mesoporosity may inevitably remove some internal active sites responsible for sulfur adsorption. This loss can be replenished by incorporating active metal cations with high sulfur affinity. The role of metals in the selective adsorption of sulfur has been studied in the past. Yang and colleagues were pioneering founders of the strong π-complexation sorbents.[204] They conducted gas-phase desulfurization experiments and molecular orbital calculations on CuY and AgY in the presence of thiophene and benzene, and showed that the materials exhibited higher adsorption capacity compared to NaY. These promising results allowed the Yang group to extend the excellent performance of π-complexation sorbents, as well as other newly developed sorbents, such as NiY and ZnY, toward liquid-phase desulfurization, with CuY reporting the highest sulfur capacity.[64,139,147,148,205] The π-type interaction displays remarkable capacity of sulfur, however, becomes ineffective if competing additives are present in the fuel.[70] Song et al. realized this potential drawback and proposed σ-forming sorbents that can adsorb thiophenes more selectively via the direct σ-bond.[65,70] They showed that NiY was able to adsorb 1.7 times more sulfur from commercial gasoline compared to CuY, which led them to explore other high positive charge cations including f-block elements, such as Ce that have the tendency to complex with the S atom directly. The selective nature of σ-type sorbents has been confirmed by other groups in different desulfurization studies.[106,138,206] In a similar work, LaHUSY was used to selectively remove BT and DBT in the presence of naphthalene[153], which demonstrates the ability of lanthanides to form two types of bonding with the sulfur compounds. Yang et al. also

investigated the effect of both naphthalene and benzene on the removal of BT using modified activated carbons.[126]

In our previous work[207], we introduced a novel desulfurization sorbent that exhibits high sulfur capacity with low mass transfer resistance. The metal-exchanged mesoporous Y zeolites contained hierarchical pores designed to eliminate diffusion limitations, while keeping an adequate amount of internal active sites for sulfur adsorption. Commercial fuels contain various types of organic compounds, and thus their role in adsorptive desulfurization must not be neglected. In this study, we rationally introduced bimetals into our hierarchical zeolites to further enhance the selective adsorption of sulfur compounds from a model fuel mixture. The utilization of bimetallic systems on adsorption has yet to be fully understood, as only limited studies of metal combinations exchanged in zeolites have been reported. One of the pioneers was Song and co-workers when they found that CuCeY displayed a 3-fold increase in adsorption capacity of model gasoline compared to CuY.[140] They proposed that this improvement was due to the synergistic interaction between Cu and Ce. Wang et al. have demonstrated that the desulfurization performance of NiCeY in removing DBT from a feed of 5% toluene and 95% octane, is higher compared to the performance of NiY and CeY.[123] More recently, a group from Northeast Petroleum University in China presented encouraging results on deep adsorptive desulfurization using bimetal-exchanged Y zeolites.[208,209] They showed that in both batch and fixed-bed adsorption, CuCeY can adsorb more sulfur from a model fuel containing toluene or cyclohexane via the π-complexation and S-M bond interactions compared to the monometallic counterpart. With benzothiophene (BT) being the biggest sulfur compound tested, the breakthrough point was extended by at least 50 mL/g and 30 mL/g on CuCeY compared to CeY and CuY, respectively. To the best of our knowledge, there are no studies on the adsorptive desulfurization performance of bimetal-exchanged mesoporous Y

zeolites in a mixture of aromatics. Hence, the current work highlights the role of metals, bimetals (Cu and Ce) and mesoporosity in Y zeolites on the desulfurization of model fuels, containing benzothiophene and dibenzothiohene, in a fixed-bed adsorber. The influence of benzene and naphthalene as a competing aromatic in the fuel has been tested. Mechanistic studies have also been performed to correlate the mechanism of sulfur adsorption to each metal-exchanged zeolite.

5.2 Materials and Methods

5.2.1 Preparation of bimetal-exchanged mesoporous Y zeolites

CBV300 (NH_4Y) was obtained from Zeolyst International and used as starting material. The preparation of mesoporous Y was conducted using the surfactant-assisted (SA) method developed by Garcia-Martinez et al.[68,75] Metal-exchanged mesoporous Y was prepared by first tailoring the mesoporous Y, followed by ion-exchange using either Ce or Cu nitrate precursors to make CeSAY or CuSAY, respectively. The mesoporous Y zeolite is labeled as "SAY." The procedure and conditions have been described in our previous work.[207] To prepare bimetal-exchanged CuCeY or bimetal-exchanged CuCeSAY, the zeolites were first ion-exchanged with Ce nitrate precursor due to higher ion-exchange selectivity, followed by ion-exchange with Cu nitrate precursor.[210] Ce exhibits higher ion-exchange selectivity to replace protons in the zeolite extra-framework, thus should be introduced first prior to Cu.[162,166] Both SAY and metal-exchanged zeolites were calcined at 525 °C to evaporate undesired organics.

5.2.2 Reagents

Three model fuels were prepared: 1) reagent grade *n*-octane + 20 wt% benzene; 2) reagent grade *n*-octane + 1% naphthalene; 3) reagent grade *n*-octane + 1% methyl-naphthalene, to simulate commercial jet and diesel fuels, respectively.[211,212] The aforementioned model fuels were spiked

with 100 ppmw of benzothiophene (BT) and 100 ppmw of dibenzothiophene (DBT). All the chemicals and reagents were purchased from Sigma Aldrich.

5.2.3 Material characterization

Transmission electron microscopy (TEM) studies were carried out in a FEI Talos F200X microsope operating at 200 kV. The instrument is equipped with a X-FEG field emission source and a super X-EDS system. A small amount of zeolite suspended in ethanol was deposited onto a carbon-film copper grid. Once the ethanol has been evaporated, the copper grid was placed into the TEM to observe the crystallinity and porosity of the zeolites, as well as the presence of metal nanoparticles. Surface area, pore volume and surface structure of the materials, which had been outgassed at 120 °C, were characterized using a Micromeritics ASAP 2020 analyzer and the data were analyzed based on the Brunaeur, Emmert and Teller (BET) method. The bulk content of metals in the zeolites were determined using an inductively coupled plasma with a mass spectrometer (ICP-MS). The reduction conditions of the materials were characterized by temperature-programmed reduction (TPR) in 3% H_2 using a PerkinElmer Pyris 1 thermogravimetric analyzer (TGA). Each material was subjected to a temperature ramp from 50 °C to 1000 °C at a rate of 5 °C/min, and the temperature at which the weight loss occurs was recorded, while the amount of H_2 consumed was used to estimate the metal content.

5.2.4 Fixed-bed adsorption experiment

All adsorption-breakthrough experiments were conducted in a custom-made quartz column with an outside diameter of ¼” and a height of 26 cm. The column was packed with 0.2-0.3 g of zeolite powders until a consistent height of 3 cm has been reached. Prior to each adsorption experiment, the column containing the packed-bed of metal-free zeolites was activated at 450 °C for 2 hours under constant N_2 gas flow. Metal-containing zeolites were activated in H_2 gas at the

same conditions as above. After activation, the column was allowed to cool under flowing N_2 or H_2 to prevent contact with air. Next, the model fuel was allowed to flow through the packed bed at 0.05 mL/min flow rate. A gas-chromatograph (GC) vial was placed right below the column exit to collect 0.5 mL of effluent droplets at consistent time intervals. The collected effluents were transferred to a GC system equipped with a sulfur chemiluminescence detector (GC-SCD) for analysis of sulfur content, and the collected data was used to construct a breakthrough curve.

5.2.5 Adsorptive mechanistic studies by infrared spectroscopy

Diffuse Reflectance Infrared Fourier Transform Spectra (DRIFTS) were collected using a Nicolet 6700 Fourier transform infrared (FTIR) spectrometer equipped with a DRIFT cell made by Harrick Scientific and ZnSe window dome. Each spectrum was recorded using 32 scans with a resolution of 4 cm^{-1} at increments of 50 °C from 100 °C to 500 °C for BT and from 200 °C to 500 °C for DBT. The FTIR spectrometer was connected to a stainless steel line, mass flow controllers and a Edwards T-Station 75 turbomolecular vacuum pump to allow *in-situ* study of sulfur adsorption and desorption. About 20-30 mg of zeolite powder was loaded into the DRIFT cell and degassed at 450 °C under N_2 or H_2 flow for 2 hours. After being cooled down to 100 °C, BT vapor was introduced from a reservoir onto the zeolite and allowed to adsorb for about 10 minutes until saturation was achieved. After adsorption, the sample was purged, evacuated and then subjected to temperature-programmed desorption (TPD) until the regeneration of the original sample was observed. As for DBT, the sulfur solids were added directly to the sample after cooling and allowed to adsorb at 200 °C, followed by the same desorption steps described above. The analysis of all spectra was done using OMNIC 9.4 software.

5.2.6 Diffusion measurements by infrared spectroscopy

DRIFTS spectra of each sample were collected at a desorption temperature of 473 K under a vacuum pressure of 10^{-5} mbar. Relevant spectral envelope of DBT spectrum (ca. 1500 cm^{-1} to 1350 cm^{-1}) was integrated over the Y zeolite overtone bands (ca. 2100 cm^{-1} - 1750 cm^{-1}) were monitored by taking a series of scans. The spectra were collected using the same method described in Section 4.2.5. To determine the diffusion coefficient, the slope of the desorption curve within the first minute was measured and substituted into the following equation[200]:

$$D_{ns} = \frac{\pi}{4} r^2 (slope)^2 \qquad \text{Equation 5.1}$$

Where D_{ns} is the nonsteady state diffusion coefficient and r is the particle radius. The initial slope represents the linear relationship between the rate of desorption and the square root of time, enabling the comparison of diffusion length and mass transfer between samples.[200,213] While D_{ns} may yield a qualitative perspective of the diffusivity of DBT, the values are likely to be perturbed by the presence of physisorbed molecules in the nearby vicinity. In order to exclusively account for chemisorbed DBT, the values must be corrected by a factor of C_T/C_0:

$$D_{ss} = \frac{C_T}{C_0} D_{ns} \qquad \text{Equation 5.2}$$

Where D_{ss} is the steady state diffusion coefficient, C_T is the concentration of adsorbed DBT in the zeolite, and C_0 is the initial concentration of DBT introduced into the DRIFTS cell. C_T can be obtained from calibration curves measured over each zeolite. The calibration curves were derived from the integration of DBT desorption bands over the same Y zeolite overtone bands.

5.3 Results

5.3.1 Characterization results

TEM images of the parent Y, SAY and CeCuY were taken at low magnification to prevent the destruction of samples by the electron beam. The images were captured at the edges of these zeolites to avoid any amorphous region that may arise from the material modification procedure, as well as to elucidate the quality of crystal structures. Figure 5.2 shows the structural properties of the parent Y at the nanoscale level. Micropores, as small as 1 nm, were observed (Figure 5.2(b)). Figure 5.2(c) highlights the diffraction pattern of the sample, confirming the crystalline nature of the parent Y. TEM images of the modified Y zeolites are shown in Figure 5.3. Figure 5.3(a) shows that the mesoporous Y zeolite contains pores around ~4 nm, which is close to the size of the CTAB micelle.[75] In Figure 5.3(b), Scanning Transmission Electron Microscopy (STEM) equipped with elemental mapping highlights Cu and Ce in the CeCuY zeolite. The size of the unreduced metal nanoparticles is relatively small (~2-3 nm) compared to the size of a zeolite particle (~500 nm) and they are well-dispersed in the zeolite extra-framework. Notice that each metal occupies distinct sites in the zeolite.

The physicochemical properties of the materials characterized by N_2 adsorption/desorption are summarized in Table 5.1. As previously shown, the presence of foreign entities, such as Ce and Cu cations, slightly reduced the surface areas and the microporosity of the parent Y.[207] The introduction of mesopores (eg. SAY, CeSAY, CuSAY, CuCeSAY) reduce the microporosity, while increasing the mesopore suface area and volume of the parent Y. While this is expected, crystallinity of all materials are still comparable as suggested by our previous studies.[207] The SAY zeolites displayed an increase in surface area and pore volume with pores ranging between 20-50 Å. The chemical composition of the metal-exchanged materials determined by ICP-MS are also

summarized in Table 5.1. The ICP results show that the metal content in each metal-modified material is within the theoretical value of 5 wt% of metal loading, validating the ion-exchange procedure.

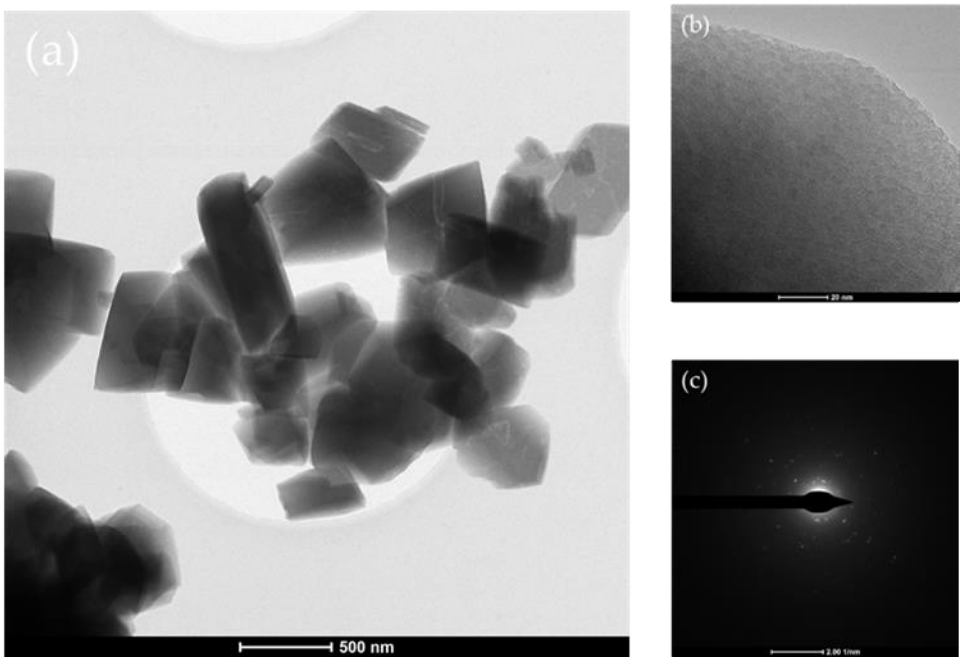

Figure 5.2: Low-magnification TEM images of Y zeolite (a) nanoparticles, (b) micropores and (c) diffraction pattern.

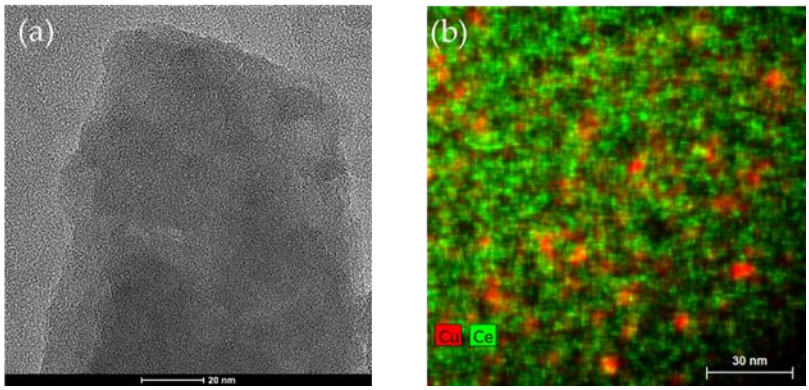

Figure 5.3: (a) Low-magnification TEM image of mesoporous (SAY) zeolite and (b) STEM image of bimetallic (CeCuY) zeolite.

Table 5.1: Physical and chemical properties of parent and modified Y zeolites.

Material	S_{tot} (m^2/g)	S_{micro} (m^2/g)	S_{meso} (m^2/g)	V_{tot} (cm^3/g)	V_{micro} (cm^3/g)	V_{meso} (cm^3/g)	*Ce*** (wt%)	*Cu*** (wt%)
Parent Y	574	530	43.9	0.282	0.246	0.036	-	-
CeY	550	500	50.1	0.273	0.232	0.041	5.5	-
CuY	528	475	52.8	0.281	0.229	0.052	-	4.9
CuCeY	549	492	57.2	0.284	0.221	0.063	2.5	2.7
SAY	692	426	319	0.373	0.192	0.201	-	-
CeSAY	648	413	235	0.342	0.190	0.152	5.6	-
CuSAY	637	411	226	0.336	0.190	0.146	-	4.6
CuCeSAY	646	419	227	0.362	0.198	0.164	3.1	2.7

** Ce and Cu metal content were determined using ICP-MS

The TPR profile of metal-exchanged and mesoporous metal-exchanged Y zeolites has been previously reported.[63] Prior to exposure to H_2, the materials were first calcined *in-situ* under N_2 at 500 °C for 1 hour and allowed to cool to 50 °C. According to the TPR profile of metal-exchanged Y zeolites, the reduction peak that appears just below 200 °C can be attributed to the reduction from Cu^{2+} to Cu^{+}.[214] The TPR profile of CeY exhibits a broad peak at ca. 600 °C, which indicates a reduction from Ce^{4+} to Ce^{3+}, consistent with that reported in the literature.[156,215] While the peaks are not as obvious when plotted on the same scale as CuY, a proper rescale of the peak around 600 °C shows the reduction peak of Ce cations as indicated in the inset. The low intensity of Ce reduction peak could be due to the location of Ce cations on the internal sites of zeolite that require higher H_2 pressure to reduce. Nonetheless, the presence of Ce cations has been verified by ICP following a strong digestion procedure to leach the cations out of the sodalite cages. The incorporation of both metal cations into the Y zeolite results in a reduction peak similar to that of CuY. The TPR profile of CuCeY also shows a slight shift of reduction peak to higher temperature, displaying the influence of Ce on the dispersion and reduction behavior of Cu cations.

5.3.2 Fixed-bed adsorption results

Figure 5.4 shows the breakthrough curves of BT and DBT in a mixture of 80% *n*-octane and 20% benzene on parent and modified Y zeolites. Figure 5.4(a) shows that BT breaks through very early on parent Y and reaches saturation within 5 mL/g of feed. When Ce cations were incorporated in the Y zeolite, the breakthrough point was extended from 0.5 mL/g to 8.5 mL/g indicating an increase in the adsorption of BT. CuY showed an even higher adsorption capacity of about 12 mL/g, before traces of BT compounds were detected. An interesting observation to consider here is the different slope of the breakthrough curves. It seems that the kinetics of BT adsorption on the CeY and CuY are different. This might be attributed to the different configurations of BT adsorption on the two metals. When both Ce and Cu cations were used in the Y zeolite, the ability to adsorb BT increased even more to 15 mL/g of sulfur-free fuel.

The adsorptive desulfurization of DBT in the presence of benzene is presented in Figure 5.4(b). Similar to BT, the adsorption capacity of the parent Y is very poor. Previous studies have shown that the poor performance of Y to remove refractory sulfur compounds, such as DBT and 4,6-DMDBT, can be attributed to diffusion limitations.[150,176,207,216] To overcome the aforementioned challenges, SAY was used as a sorbent. It successfully produced at least twice the amount of DBT-free effluent compared to parent Y. The addition of Ce cations to the mesoporous SAY (CeSAY) did not improve the desulfurization performance, most likely due to the allocation of Ce cations on sites that are inaccessible for DBT to enter. CuSAY, on the other hand, showed remarkable improvement in the adsorption capacity of DBT, as the addition of Cu cations extended the breakthrough point from 10 mL/g to 20 mL/. The promising performance of bimetal Y on BT removal, along with the encouraging results of metal-exchanged mesoporous Y, motivated the use of bimetal-exchanged mesoporous Y (CuCeSAY) for the DBT removal. As observed in Figure

5.4(b), CuCeSAY dramatically increases the adsorption capacity of DBT to more than 30 mL/g of clean fuel.

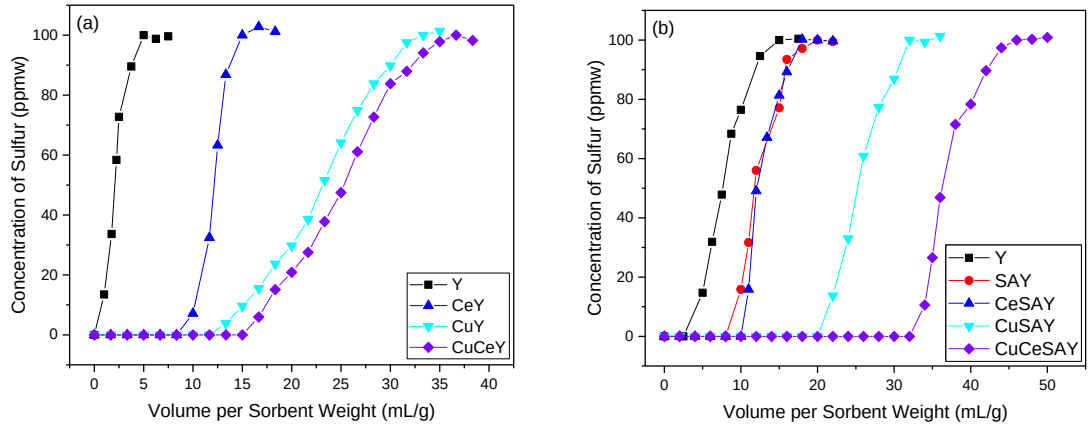

Figure 5.4: Breakthrough curves of (a) BT and (b) DBT in a mixture of 80% n-octane and 20% benzene on various Y zeolite adsorbents.

Although significant amount of BT exists in the gasoline range fuels, some BT and especially all DBT is found in the diesel. Diesel also contains aromatics such as naphthalenes and alkyl-naphthalenes. To understand the effect of the simultaneous presence of heavier aromatics on the adsorption of BT and DBT, we performed adsorption experiments using model fuels containing 1 wt% naphthalene and 1 wt %1-methyl-naphthalene in n-octane.

Figure 5.5 shows the adsorption results of BT and DBT in the model fuel containing 1% naphthalene in *n*-octane. As expected, the parent Y zeolite exhibits the lowest BT and DBT capacities and the presence of naphthalene only exacerbates the relatively poor sulfur uptake. For the desulfurization of BT, both metal-exchanged zeolites show higher adsorption capacity, with CeY removing up to 1.5 mL/g and CuY about 2.5 mL/g on BT, respectively (Fig.5.5(a)). This trend is similar to that observed in the removal of BT in 20% benzene. By combining both Ce and Cu, the breakthrough is extended to 5 mL/g of BT-free fuel, confirming that the synergy between

the two metals leads to stronger adsorption of sulfur. Figure 5.5(b) displays the effect of naphthalene on the desulfurization of DBT. Both SAY and CeSAY displays slightly higher DBT capacity compared to parent Y. The presence of Ce did not improve the desulfurization performance. This phenomenon can be attributed to the limited accessibility of the metal, which has been discussed previously. CuSAY, on the other hand, drives the adsorption capacity to 20 mL/g of clean fuel, which is higher than the capacity observed by CeSAY and SAY. The best sorbent is still, by far, CuCeSAY with a DBT adsorption capacity of about 45 mL/g. This suggest that the synergistic interaction between Ce and Cu metals plays an important role on the adsorption of refractory sulfur compounds, while the mesoporosity yields higher bulk mass transfer to the internal active sites. While naphthalene is predominant in diesel and jet fuels, other aromatic hydrocarbons, such as alkyl-naphthalenes are also present, and can affect the selective adsorption of BT and DBT. Figure 4.6 shows the effect of another aromatic compound (1-methy-lnaphthalene) on BT and DBT removal. Both Figures 5.6(a) and 5.6(b) show that the breakthrough may occur earlier. This result could be due to steric hindrance imposed by the methyl group on naphthalene. Nonetheless, results still indicate that CuCeSAY can still maintain a relatively high sulfur capacity, despite the presence of competing aromatics with similar structure.

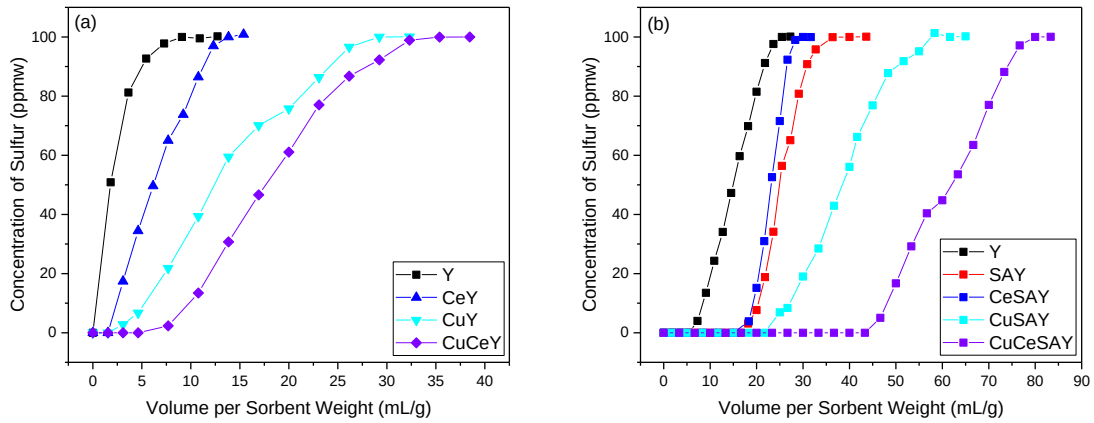

Figure 5.5: Breakthrough curves of (a) BT and (b) DBT in a mixture of 99% n-octane and 1% naphthalene on various Y zeolite adsorbents.

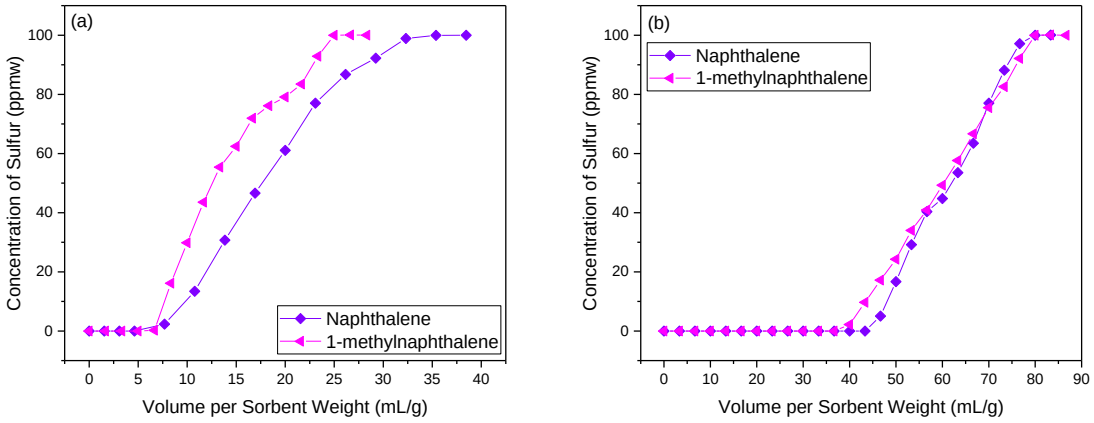

Figure 5.6: Breakthrough curves of (a) BT and (b) DBT adsorbed over CuCeSAY in a mixture of 99% n-octane and 1% naphthalene or 1% 1-methylnaphthalene.

5.3.3 In-situ DRIFTS studies

The adsorption mechanism of sulfur compounds from liquid fuels highly depends on the type of metals in the zeolite and their interaction. To understand the mechanism of BT and DBT adsorption on (bi)metallic zeolites, we performed *in*-situ DRIFTS experiments in a temperature and atmosphere controlled reaction chamber. Figure 4.8 shows the DRIFT spectra of BT on (I) CuY, (II) CeY and (III) CuCeY zeolites recorded from TPD under vacuum in the (a) zeolite region and in the (b) C=C region. Vibrational bands ranging from 3500 cm^{-1} to 3750 cm^{-1} are characteristic of the zeolite hydroxyl region. The peak at 3743 cm^{-1} is attributed to terminal SiOH, while the bands at 3545 cm^{-1} and 3635 cm^{-1} are attributed to hydroxyl groups in the zeolite framework.[75,159] Any peaks observed above 3000 cm^{-1}, are attributed to vibrational stretches of C-H bond of the aromatic rings. Peaks ranging from 1600 cm^{-1} to 1300 cm^{-1} are mostly due to vibrational stretches of C=C bond of the aromatic rings.

Benzothiophene adsorption on CuY

Figure 5.8(a)(I) and (b)(I) show the adsorption of BT on CuY. It appears that the acidic hydroxyl sites (ca. 3545 cm^{-1} and 3636 cm^{-1}) of CuY are occupied rapidly upon exposure to BT vapor. A small change in the intensity of the 3743 cm^{-1} band can be seen, indicating that the external silanol groups are also participating in the BT adsorption. However, sulfur compounds exhibit higher affinity to adsorb onto the Brønsted acid sites compared to the silanol. As BT vapor began to saturate the zeolite adsorption sites, new peaks start to appear. The band located at 3080 cm^{-1} is due to C-H stretching, which confirms the adsorption of BT. By subjecting the sample to TPD, the physisorbed BT vapor is removed from the cell, and the chemisorbed BT can be studied more closely. The adsorption of BT on CuY triggers vibrational stretches and bending of C=C

bonds that consequently show up in regions below 1700 cm^{-1}, as seen in Figure 5.8(b)(I). As CuY undergo thermal desorption, vibrational bands at 1425 cm^{-1}, 1450 cm^{-1}, 1585 cm^{-1} and 1635 cm^{-1} are observed. To understand the significance of these bands, they can be compared to vibrational bands of free BT and of BT-adsorbed on CuO (Figure 4.7(a) and Figure 5.7(b), respectively). In the high wavenumber region, free BT exhibits a peak at 3080 cm^{-1}, which is due to C-H vibration, while the peak at 1460 cm^{-1} corresponds to symmetrical C=C vibrations. Upon adsorption of BT on the zeolite surface, a shift in the frequency of vibration is expected due to the change in electron density.[137,217] Thus, the peak due to free BT may be shifted to higher or lower wavenumbers (blue shift or red shift, respectively). A red shift in wavenumber suggests a decrease in vibration frequency due to a reduction in electron density of the adsorbing species. This occurs when an aromatic ring stacks above an active site via π-complexation, in which the metal cation backdonates electron density to the anti-bonding π-orbital of the sulfur ring.[218] Based on the present BT desorption spectra, it can be suggested that the peak at 1425 cm^{-1} is attributed to the symmetrical C=C stretching vibration of free BT, which has been shifted to a lower wavenumber. The red shift of the C=C stretching peak suggests an elongation/deformation of the ring due to a reduction in electron density, which can occur when BT ring is adsorbed on Cu via π-complexation.

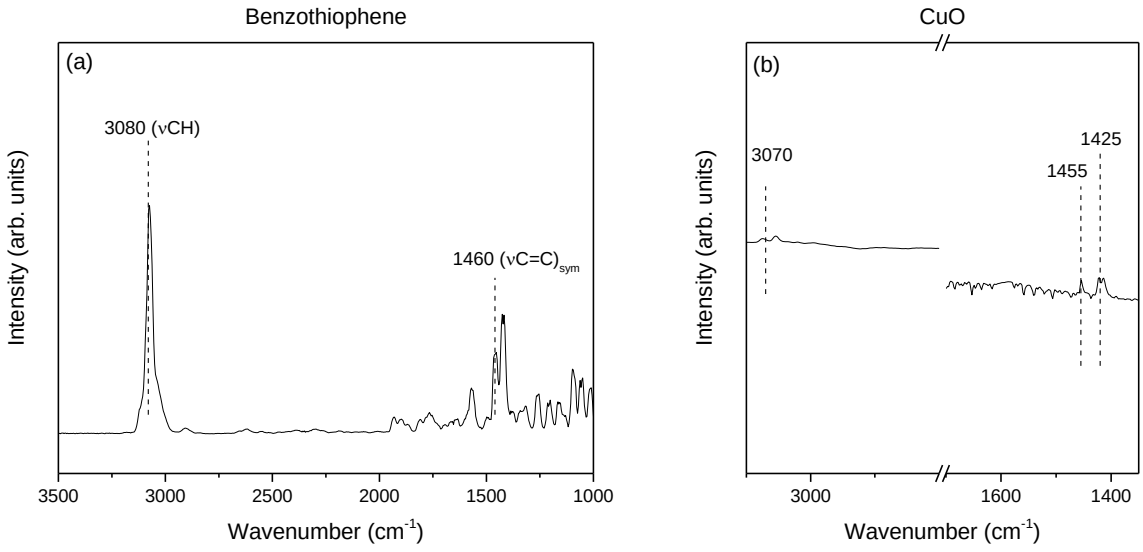

Figure 5.7: IR spectra of (a) free benzothiophene (BT) and (b) BT on CuO at 100 °C.

Benzothiophene adsorption on CeY

Figure 5.8(a)(II) and (b)(II) show the IR spectra of BT adsorption on CeY. It appears that BT adsorption on CeY exhibits the same IR bands generated on CuY, with the addition of an extra peak at 1490 cm^{-1}. This peak is attributed to C=C bonds. The appearance of this peak at higher wavenumber relative to free BT (1460 cm^{-1}) can be ascribed to an increase in electron density of the BT ring, implying that the adsorption of BT on Ce occurs via direct σ-bond interaction, in addition to π-complexation.[171] These results suggest that Ce can adsorb aromatic sulfur compounds via two types of adsorption modes, which makes it highly beneficial in selective adsorption of sulfur in a mixture of aromatics. This phenomenon was also observed by other rare earth metals or lanthanides-exchanged zeolites.[145,218] One interesting observation is the existence of a shoulder peak near the hydroxyl region at 3515 cm^{-1}. This shoulder peak could be attributed to the interaction of Ce cation on the type I' site and the zeolite framework, which could lead to

perturbation in the hydroxyl vibrational frequency.[219] This scenario is absent from the CuY zeolite, since Cu cations are mostly populated in the supercage.

Benzothiophene adsorption on CuCeY

Figure 5.8(a)(III) and (b)(III) show the IR spectra of BT adsorption on CuCeY. The peaks are similar to the ones observed with CuY and CeY. These include vibrational bands at 1425 cm^{-1} and 1490 cm^{-1} which resulted from π-complexation and σ-bond interaction of BT and CeCuY zeolite. Interestingly, in the case of CuCeY, the 3635 cm^{-1} vibrational band is not recovered even at high desorption temperatures (500 °C). This observation suggests that higher temperatures are required to completely desorb BT from the surface, which suggests a stronger interaction between CuCeY and BT compared to the interaction of BT with CuY and CeY. This is also true in the C=C region, where the C=C bond stretching is still apparent even at 500 °C. This result indicates strong interaction between the sorbent and the sorbate. Another interesting observation is the presence of bands below 3000 cm^{-1} on CeY and CuCeY, but not on CuY. These bands are usually characteristic of sp3-hybridized C-H bonds, which could be due to the elongation of BT ring. This type of interaction can only occur when there is a direct σ interaction as displayed by Ce and CuCeY.

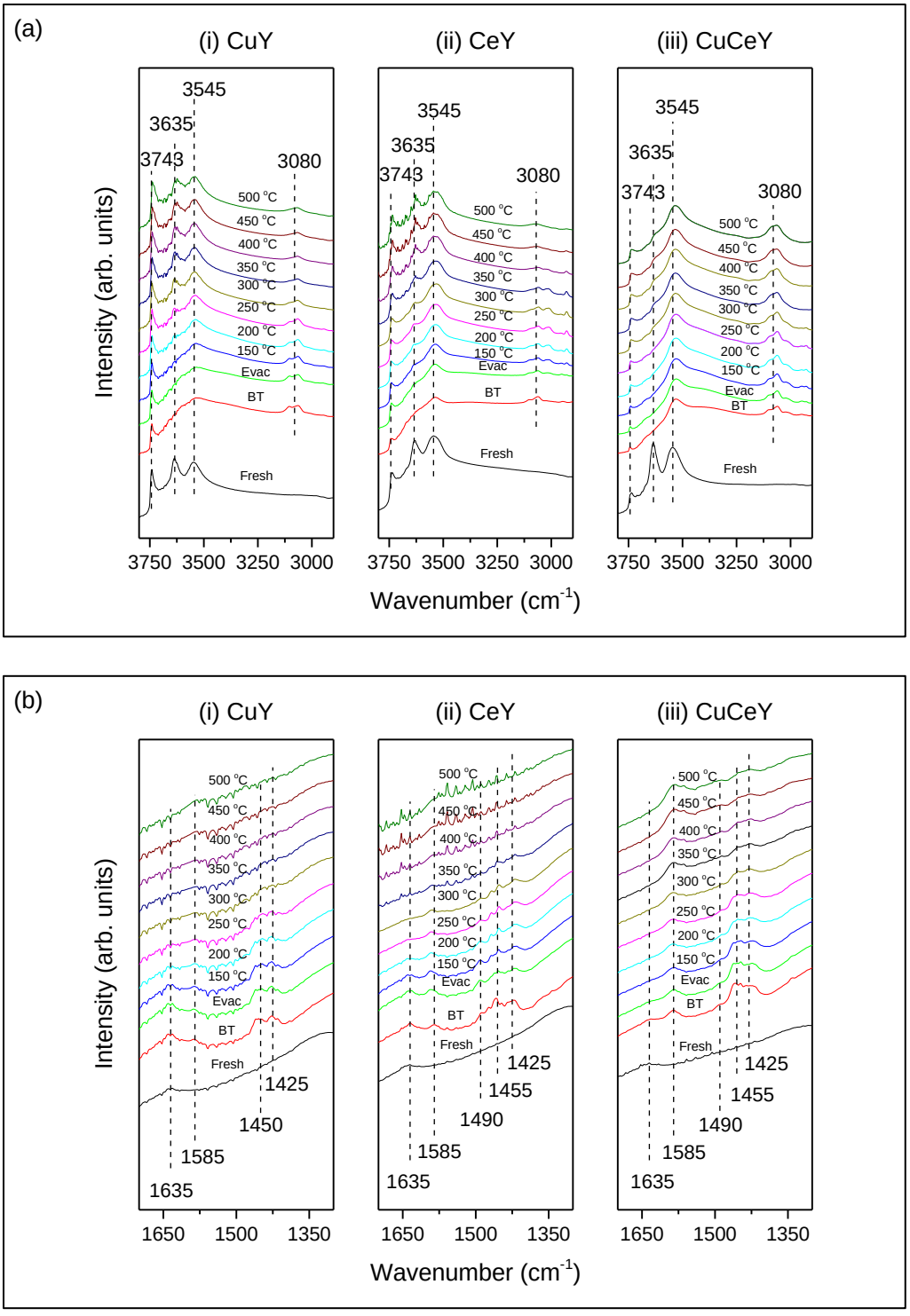

Figure 5.8: FTIR spectra during BT adsorption and temperature-programmed desorption on (i) CuY, (ii) CeY and (iii) CuCeY of the (a) zeolitic region and the (b) C=C region of the sulfur molecule.

5.3.4 Mass transfer studies of mesoporous Y zeolite

To investigate the mass transfer limitations of DBT adsorption in Y zeolite, we conducted desorption experiments via *in situ* DRFITS. The bands due to desorption of DBT (ca. from 1350 cm^{-1} to 1500 cm^{-1}) were integrated over the zeolite overtone band (ca. from 2100 cm^{-1} to 1750 cm^{-1}) in real time and were plotted against the square root of time, as shown in Figure 5.9. DBT desorbs more rapidly on SAY compared to Y, as indicated by the steepness of the desorption curves. This behavior can be attributed to the available mesopores in SAY, which allow DBT, a relatively large sulfur compound, to diffuse more rapidly towards the internal active sites. For qualitative comparison, the slope of each curve was taken to calculate the nonsteady state and ultimately, the steady state diffusion coefficients of DBT on each zeolite, as depicted in Table 5.2. Due to the incorporation of mesopores, SAY exhibits 4.5x the diffusivity compared to the microporous Y. This result confirms that hierarchical pore zeolites can reduce diffusion limitation, and thus effectively increasing the sulfur adsorption capacity, as shown by the breakthrough curves in Figures 5.4, 5.5 and 5.6.

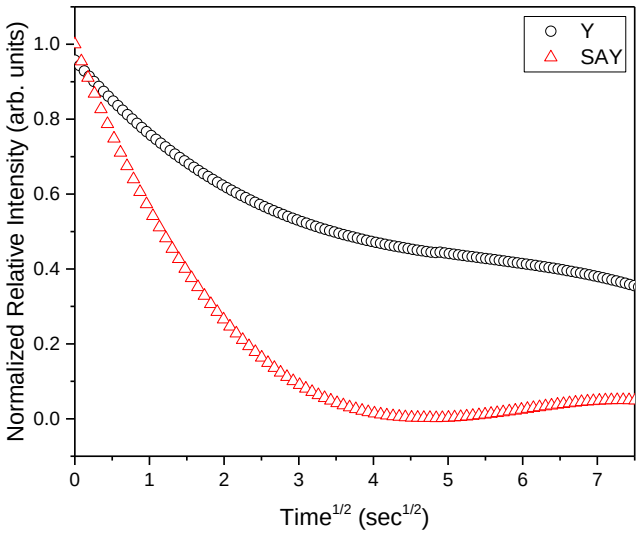

Figure 5.9: Desorption of DBT at 473 K from Y and mesoporous Y (SAY) under 10^{-5} mbar.

5.4 Discussion

In our previous work we studied the adsorptive desulfurization of BT and DBT on Cu, Ce and CuCeY zeolites using n-octane as a model fuel.[207] Motivated by the encouraging results of that work, here, we investigate the adsorptive desulfurization of BT and DBT in the presence of aromatic hydrocarbons. Our previous work showed that metal-exchanged Y zeolite exhibits high sulfur adsorption capacity in *n*-octane. This present study has focused on: a) the effect of aromatics on the adsorptive desulfurization of sulfur compounds from fuels, and b) the mechanism of adsorption of sulfur compounds on Y zeolites. Benzene, naphthalene and methyl-naphthalene were used as the competing aromatic molecules. Benzene is an aromatic molecule found in the gasoline range fuel, but it was used is this study as the primary model molecule, due to the simplicity of its structure. Naphthalene and methyl-naphtalene were also used as model aromatics, because they are abundant in jet and diesel range fuels.

The breakthrough curves in Figure 5.4 reveal that the sulfur compounds show up much earlier when benzene is present in the fuel, compared to the aromatic-free sulfur fuel.[207] The addition of benzene resulted in a decrease in breakthrough volume of about 5 mL/g on the parent Y. According to the literature, Y zeolites can adsorb aromatic compounds via π-complexation and/or direct H-bonding, but these interactions are relative weak and unselective.[220] As a result, the parent Y can adsorb benzene and thus, compromising the selective adsorption of thiophenic compounds. Without benzene in the feed, CeY and CuY both reported very high adsorption capacities for BT, where 35 mL/g and 65 mL/g of clean fuel were produced, respectively.[207] However, in the presence of benzene, the same sorbents were not able to meet the same results; thus, less than 15 mL/g of BT-free fuel was produced. The highest capacity of BT in the presence of benzene, however, was displayed by CuCeY, which resulted to 15 mL/g of BT-free fuel. One

interesting observation about these results is that the breakthrough curves show different adsorption slopes. A steep slope was seen on parent Y and CeY, whereas a gradual increase in sulfur concentration was displayed on CuY and CuCeY. The difference in slope could be attributed to different adsorption kinetics, which are dictated by mass transfer to the active site and/or the type of adsorption configuration.[221–223] Ce cations have been shown to preferentially disperse within the sodalite cage, which is too small for thiophenic compounds to enter. The limited amount of accessible Ce sites cause the sorbent to be saturated more rapidly. Moreover, Ce cations have shown to favor strong σ-bond formation by donating a 4f electron to sulfur, which could also increase the adsorption kinetics.[224] These characteristics of Ce result in fast adsorption rate, leading to a steeper slope compared to Cu.

Similar trends were also observed on the removal of DBT. On parent Y, DBT broke through as early as 3 mL/g of liquid feed, which is about 15 times faster than it was compared to the desulfurization of the same compound without benzene.[207] Note that the elution time of DBT was longer relative to that of BT. In our previous work, we have shown that electron density increases with the size of sulfur compound, which explains the tendency to adsorb of DBT to adsorb more strongly than BT on the parent Y.[207] The same trend is also observed on metal-exchanged and SAY zeolites, confirming the preferential order to adsorb the aforementioned sulfur compounds. SAY showed higher adsorption capacity of DBT, producing 8 mL/g of sulfur free liquid fuel in the precence of benzene. In the presence of naphthalene and 1-methylnaphthalene, CuCeSAY produced up to 45 mL/g and 40 mL/g of DBT-free fuel. As expected, the removal of DBT is mass transfer limited due to the large kinetic diameter, and thus the introduction of mesopores allowed the larger molecule to access the internal active sites of the micropores. The effect of mesoporosity on the adsorption of DBT was also observed in our in situ IR studies.

Results (not shown here) have displayed the lack of vibrational bands on parent Y zeolites, indicating the absence of DBT adsorption. The easier diffusion of DBT in mesoporous Y compared to the corresponding microporous was also confirmed by the diffusion measurements in Section 5.3.4.

Surprisingly, the breakthrough curve of CeSAY was similar to that of SAY, suggesting little or no improvement of sulfur removal. According to the literature, Ce cations develop high preference to coordinate mainly with type I' sites, which are located in the sodalite cages.[165,180] This may be the reason for the low adsorption capacity of CeSAY, since DBT may be too large to access the sodalite cage. Meanwhile, 20 mL/g of DBT-free fuel was produced by CuSAY, which is twice as much compared to metal-free SAY. This improvement is a result of the relatively strong interaction that Cu metals can form with DBT via π-complexation and the more accessible type II and II' sites which Cu occupies.[164,225]

We also performed more modifications to our mesoporous Y material by ion-exchanging mesoporous Y with two metal cations (Ce and Cu) to make CuCeSAY. While limited studies on metal-exchanged mesoporous zeolites for sulfur adsorption have been reported, the role of bimetal mesoporous Y zeolite has yet to be explored.[150,177] Moreover, bimetal-exchanged zeolites have been proven to possess high selectivity and capacity for sulfur compounds.[171,209] The performance of CuCeSAY is demonstrated in Figure 5.4(b), which shows a 3-fold increase in sulfur removal capacity compared to the performance of SAY. To the best of our knowledge, this is yet the highest DBT adsorption capacity observed. Yang and co-workers conducted similar fixed-bed adsorption experiment of DBT in 20% benzene and 80% *n*-octane and showed that CuY had the highest adsorption capacity by producing 20 mL/g of DBT-free fuel, followed by siliceous MCM-41 and activated carbon (AC).[226] This confirms our hypothesis that in addition to the enhancement in mass

transfer, the synergistic effect of Cu and Ce metals increases the selectivity and capacity for DBT in the presence of benzene. It is important to note that Ce alone does not possess high capacity of sulfur as shown in Figures 5.4 and 5.5 for either BT or DBT. Additionally, the coordination of Ce cations in the sodalite cages do not warrant easy access to these sites. Yet, the presence of Ce seemed to play an important role when used as a secondary metal in CuCeSAY as demonstrated from the breakthrough curve. According to Shan et al. the presence of Ce species in the extra-framework speeds up the auto-reduction of Cu^{2+} to Cu^{+} and consequently enhances the density of Cu^{+} cations, which is the optimum oxidation state to adsorb sulfur molecules.[210] The tendency of each metal to occupy different coordination sites in the extra-framework, as suggested by the TEM images in Figure 5.3(b), leads to a higher probability that most of the active sites have been ion-exchanged with either Ce or Cu. The resulting bimetal-exchanged mesoporous Y zeolite has shown to exhibit exceptional desulfurization capabilities.

These results have also been confirmed by our desorption studies using *in-situ* DRIFT. As demonstrated in Figure 5.7, the synergistic effect of Cu and Ce in zeolite Y leads to a relatively high recovery temperature. Similarly, Figure 5.8 shows that it takes a higher temperature to completely desorb DBT from CuCeSAY. It has also been shown that the recovery of the supercage is relatively slower during the desorption of both BT and DBT. This suggests that the interaction between the sulfur compounds and active sites occurs predominantly in the supercage. This also explains the relatively low sulfur capacity of Ce and CeSAY compared to other modified material (Figures 5.4 and 5.5), since Ce is mostly found in the sodalite cages. Although the adsorption of sulfur on Ce is strong and selective, the location and the tendency to form strictly one-to-one σ bond do not contribute to higher sulfur capacity. Meanwhile, CuY and CuSAY have shown higher adsorption capacity because of the possibility of multilayer adsorption via π-stacking.[227]

Nonetheless, the presence of Ce in the inner cages has shown to increase the strength and dispersion of Cu. This is evidenced by both the remarkable breakthrough results shown by the fixed-bed experiment, as well as the extremely strong sorbent-sorbate interaction shown by the DRIFT analysis. The role of Ce on the electronic properties of Cu for sulfur adsorption will be investigated in our future studies. The adsorption studies of both benzene and naphthalene also shed light on the selectivity of bimetallic CuCeY and CuCeSAY zeolites. It was apparent that benzene and naphthalene desorbed at lower temperature compared to BT and DBT, respectively. Subsequently, the adsorption of the aromatics proceeded via π-complexation only, which makes CuCeY and CuCeSAY more selective for sulfur compounds in the presence of competing aromatics.

5.5 Conclusions

In this study we have explored the effect of aromatics, such as benzene, naphthalene and methyl-naphthalene, on the adsorptive desulfurization of BT and DBT from model fuels. Among the tested Y zeolite sorbents, bimetal-exchanged zeolites, prepared by ion-exchanging Y zeolites with Cu and Ce, have shown to exhibit high capacity for BT. Such improvement is a result of the synergistic interaction between the two metal cations that lead to stronger interaction with BT via π-complexation and/or σ-bonding. Consequently, about 15 mL/g and 5 mL/g more BT-free fuel in the presence of benzene and naphthalene, respectively, were produced using CuCeY, compared to parent Y. During the adsorptive desulfurization of DBT, diffusion limitations and the presence of benzene, naphthalene and methyl-naphthalene, severely affected the high capacity of zeolite. We proposed that bimetallic mesoporous zeolite (CuCeSAY) would overcome these challenges. The experimental results indicated that CuCeSAY exhibits relatively high DBT capacity of about 32

mL/g in the presence of benzene, and 45 mL/g in the presence of naphthalene. The significant removal of DBT was also attributed to synergistic effects of: a) the mesopores in Y, which provided access for DBT to the metal cations, and b) of Cu and Ce in CuCeSAY, which resulted in stronger interaction and more adsorption configurations. The tendency to adsorb the tested sulfur compounds follow the order of BT < DBT, suggesting that the influence of electron density on adsorptive desulfurization should not be neglected. From this study, the prepared CuCeSAY has shown to exhibit high potential to become a prominent adsorbent material in commercial and industrial applications. Our future goal is to implement this novel and industrially-viable technology toward real gasoline, jet fuel and diesel.

Chapter 6

ADSORPTIVE DESULFURIZATION OF 4,6-DIMETHYLDIBENZOTHIOPHENE ON BIMETALLIC MESOPOROUS Y ZEOLITES: EFFECTS OF CU AND CE COMPOSITION AND CONFIGURATION

6.1 Introduction

The recurring uncertainty in global oil price in recent years has contributed to several implications in the energy world. The decline in fuel price has especially promoted vehicle sales by about 30% since 2012, following the outburst of oil supply.[228,229] Figure 6.1 shows an inverse correlation between conventional gasoline and diesel fuel prices, and the U.S. vehicle car sales from 2012 to 2016.[181,230] While consumers take advantage of more affordable transportation fuels, air quality and consequently human health are inevitably exposed to toxic pollutants emitted by the rapid growth of automobiles, as shown in Figure 6.1.[231] In view of the new U.S. energy policy, the production of clean fossil-derived fuel will continue to remain the country's main source of energy.[232,233] Afterall, 80% of the world energy consumption still relies on fossil fuels as an energy source.[2] As a result of discovery of new oil wells and development of advanced drilling technologies, fossil-based fuels will continue to dominate the energy sector in the foreseeing future. This is a great concern, because extensive consumption of fossil fuels inversely leads to greater carbon and other toxic emissions.[234]

Among these emissions, sulfur remains one of the most harmful post-combustion substances. The combination of its abundance in nature[15] and continuous stringent regulations imposed by the U.S. Environmental Protection Agency (EPA) to limit sulfur concentrations in federal gasoline and diesel fuels, demands the development of effective and versatile deep

desulfurization technologies.[10] The current, state-of-the-art hydrodesulfurization (HDS) process fails to remove refractory sulfur compounds, such as dibenzothiophenes and alkylated-dibenzothiophenes, unless severe conditions are applied.[18]

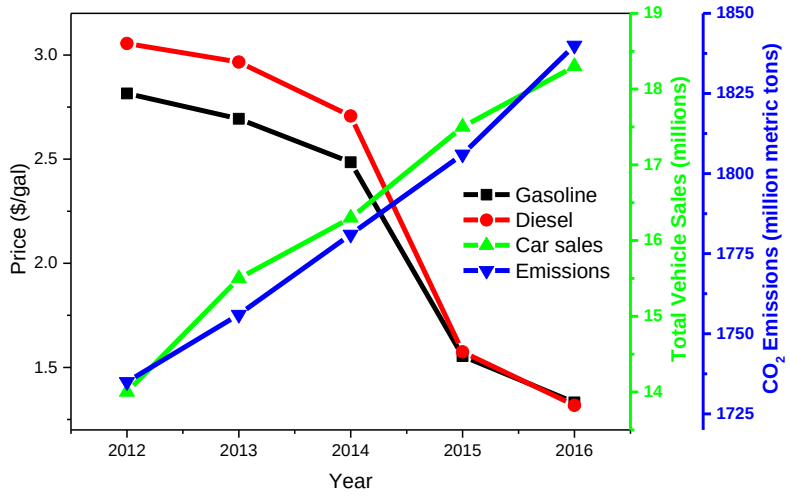

Figure 6.1: The effect of oil prices on total vehicle sales and carbon dioxide emission.[228,229]

Among these emissions, sulfur remains one of the most harmful post-combustion substances. The combination of its abundance in nature[15] and continuous stringent regulations imposed by the U.S. Environmental Protection Agency (EPA) to limit sulfur concentrations in federal gasoline and diesel fuels, demands the development of effective and versatile deep desulfurization technologies.[10] The current, state-of-the-art hydrodesulfurization (HDS) process fails to remove refractory sulfur compounds, such as dibenzothiophenes and alkylated-dibenzothiophenes, unless severe conditions are applied.[18]

Faujasite (FAU)-derived Y zeolites are great sorbent candidates for sulfur adsorption, due to their high surface area, uniform microporosities and most importantly, available acidic (Brønsted) active sites. While the aforementioned properties play effective roles in removing smaller sulfur compounds, such as thiophenes (TP) and benzothiophenes (BT),[207] the

microporosity of the Y zeolite and the presence of structurally and chemically similar cyclic hydrocarbons may restrict the desulfurization performance of refractory sulfur compounds with large kinetic diameter, such as 4,6-dimethyldibenzothiophene (4,6-DMDBT).[64,68] Consequently, for enhanced desulfurization performance, the adsorption of 4,6-DMDBT must proceed without diffusion limitations and selectivity challenges.

It is critical to synthesize adsorbent materials that can overcome the aforementioned challenges to be commercially viable. Among the alternative desulfurization processes, adsorptive desulfurization using zeolites is a very promising technology, which has shown tremendous growth in adsorption capabilities ever since the pioneering work of Yang et al. and Song et al. [16,64,205,235,236] In fact, such efforts by pioneering groups have been recognized since decades ago. Yang and co-workers investigated the adsorptive desulfurization of transportation fuels, such as gasoline, diesel and jet fuels using Cu(I)-, Ni(II)-, and Zn(II)-Y zeolites as sorbents, out of which Cu(I)-Y outperforms the rest.[139] The high adsorption capacity of Cu(I)-Y has been attributed to the strong π-complexation interaction, as predicted by molecular orbital calculations. Song et al. screened and evaluated various types of metal-exchanged zeolites (e.g. Cu, Ni, Zn, Pd, and Ce) for their adsorptive capabilities of model jet fuel and commercial jet fuel.[140] Among the tested metal-exchanged zeolites, Ce-exchanged Y reported the highest adsorption capacity of sulfur compounds within the vicinity of other aromatics, due to direct sulfur-metal (σ-bond) interaction. For example, Ce^{4+}, an f-block element, exhibits higher tendency to interact directly with the sulfur atom in the ring via a σ-bond, rather than form π-complexes.[237] More recently, bimetallic systems have been widely studied to understand the synergistic effects of metal combinations.[238] Song et al. investigated the combination of transition metals and lanthanides in Y zeolites for the adsorptive desulfurization of model fuels.[209,239] Both CuCeY and AgCeY exhibited high adsorption affinity

for thiophene or benzothiophene in the presence of toluene or cyclohexane, due to strong synergistic interaction between the two metals. Wang and co-workers performed adsorptive desulfurization experiments of dibenzothiophene in *n*-octane and toluene, and showed that NiCeY exhibited much higher adsorption capacity compared to NiY and CeY.[123] It is, therefore, evident that the bimetal-exchanged zeolites are crucial for selective adsorption of sulfur, most likely because the thiophene rings can interact with the metals via two types of adsorption modes (i.e. π-complexation and σ-bond).

Besides selectivity, the adsorbent may also experience diffusion limitations when refractory sulfur compounds are present. Specifically, the removal of 4,6-DMDBT and other alkyl-derived dibenzothiophenes is restricted by large kinetic diameters and steric hindrance. This limitation can be ultimately controlled by inducing mesoporosity to the adsorbent material. Hierarchical pore zeolites have been widely explored in several desulfurization processes, such as oxidative desulfurization [240,241] and HDS.[242,243] In 2009, Yang et al. realized that metal-exchanged Y zeolite, such as CuY that exhibits excellent desulfurization performance may fail to remove large sulfur compounds due to pore diffusion limitations.[176] They demonstrated that $AgNO_3$-supported mesoporous sorbents produced significantly better desulfurization performance on high-sulfur jet fuels. Another research group synthesized hierarchical beta zeolites via alkaline treatment, which exhibit 35% higher benzothiophene and dibenzothiophene capacity compared to that of the parent zeolite.[175] In our previous work, both ion-exchanged metals and mesoporous zeolites have proven to play significant and distinct roles in effective, as well as, selective desulfurization performance.[207] Recently, we have investigated the mechanism of adsorptive desulfurization over bimetal-exchanged mesoporous zeolites via molecular level experiments.

Results suggested that the coexistence of Cu and Ce is highly important in the selective adsorption of sulfur even in the presence of competing aromatics, such as benzene or naphthalene.[63]

This work exploits the adsorption selectivity and capacity of the previously studied CuCeSAY for the removal of 4,6-DMDBT with and without the presence of aromatic compounds. Additionally, the ratio and configuration of Cu/Ce are varied, and their resulting impact on the selective adsorption of 4,6-DMDBT is evaluated. To the best of our knowledge, studies on adsorptive desulfurization of 4,6-DMDBT are very limited, owing to the difficulty in removing the aforementioned bulky and unreactive sulfur compound from diesel. In this study, we report the results of dynamic adsorption tests of 4,6-DMDBT on mesoporous Y ion exchanged with Ce and Cu. The adsorption tests were performed in the presence of naphthalene, and the regeneration and lifetime of the adsorbents were investigated. The effect of metal composition and configuration is also studied. To understand the impact of the different metals on the 4,6-DMDBT adsorption, we performed fundamental studies using Fourier transform infrared spectroscopy (FTIR) under *in-situ* conditions.

6.2 Experimental Section

6.2.1 Materials

Y zeolite (Si/Al = 2.43) in NH_4 form was purchased from Zeolyst International. Mesoporous Y zeolites were prepared using the surfactant-assisted method developed by Garcia-Martinez et al.,[68,75,76] which are labeled as "SAY." Then, metal-exchanged mesoporous Y zeolites were prepared using an ion-exchanged method described in our previous work.[207] CuSAY containing 5 wt% Cu and CeSAY containing 5 wt% Ce were produced. Bimetallic mesoporous Y zeolites were synthesized by first ion-exchanging SAY with 2 wt% Ce at room temperature,

followed by 2 wt% Cu to obtain CuCeSAY as the final product. The reason the metals were introduced in this order has been explained previously.[63] The modified zeolites were then washed and dried at 80 °C overnight. All prepared zeolites were finally calcined at 535 °C for 6 hours. The regeneration of the spent sorbent was accomplished by heating the zeolite in air at 500 °C for 5 hours, followed by reduction in H_2 at 400 °C for 5 hours. The composition and configuration of metals were also varied by changing the amount of metal exchanged and the order of exchange, respectively. The resulting bimetal-exchanged mesoporous zeolite is labeled as "(a%)Cu(b%)CeSAY," where (a%) is the wt% of Cu and (b%) is the wt% of Ce. In a reverse order, (b%)Ce(a%)CuSAY was also prepared. The metal loadings ranged from 2 wt%, 5 wt%, and 10 wt%. The regeneration conditions were realized from running a temperature gravimetric analysis (TGA) on the saturated zeolite.

6.2.2 Reagents

The model fuel was prepared by dissolving 100 ppmw of 4,6-DMDBT in reagent grade *n*-octane. A simulated diesel feed was also prepared by mixing 100 ppmw of 4,6-DMDBT and 1% naphthalene into *n*-octane, as it is the solvent of choice for most adsorption studies. All chemicals were purchased from Sigma Aldrich.

6.2.3 Characterization

The diffraction pattern and crystalline structure of each material were identified using a Bruker D8 advanced X-ray diffractometer (XRD). Surface topographical analysis and surface elemental mapping were performed on the materials using a FEI manufactured Quanta 250 Scanning Electron Microscope (SEM) coupled with Energy Dispersive X-ray Analysis (EDAX) accessory. All samples were coated with gold prior to SEM characterization for better electron conductivity. High-resolution transmission electron microscopy (TEM) images were also collected

with a FEI Talos F200X microscope operated at 200 kV, for which the preparation procedures have been reported previously.[63] All samples were supported on a carbon-film copper grid. The intrinsic location of metal cations were mapped using the scanning transmission electron microscope-energy dispersive x-ray spectroscopy (STEM-EDS) detector. X-ray photoelectron spectroscopy (XPS) measurements were performed with a Kratos AXIS Ultra DLD XPS system, using monochromatic Al kα x-rays and 40 eV pass energy, for characterization of metal oxidation state and quantification of the sample surface. The bulk metal loading in the zeolite was calculated using an inductively coupled plasma equipped with a mass spectrometer (ICP-MS) after the zeolites were treated with acid (concentrated HNO_3 and HCl) digestion.

6.2.4 Fixed-bed adsorption experiment

A custom-made quartz column with an inside diameter of 3.95 mm and a length of 26 mm was used to simulate a packed bed reactor. The catalyst bed, supported by a circular filter paper, was packed with zeolite powders weighing from 0.2 to 0.3 g, keeping the bed height constant at 3cm. The packed catalyst bed was then subjected to thermal reduction under H_2 flow 500 °C for 2 hours. Upon cooling to ambient temperature, liquid fuel was allowed to flow through the column using a high-performance liquid chromatography (HPLC) pump at a rate of 0.05 mL/min. 0.5 mL of fuel effluent was collected at consistent intervals and analyzed for its sulfur concentration using a gas-chromatograph-sulfur chemiluminescence detector (GC-SCD).

6.2.5 Mechanistic studies by infrared spectroscopy

The mechanism of 4,6-DMDBT adsorption on various Y zeolites was studied by Diffuse Reflectance Infrared Fourier Transform Spectroscopy (DRIFTS) using a Nicolet 6700 Fourier transform infrared (FTIR) spectrometer and a DRIFT cell manufactured by Harrick. The cell was equipped with a ZnSe window top dome and connected to a vacuum system of 10^{-5} mbar

maintained by an Edwards T-Station 75 turbomolecular vacuum pump. The DRIFTS spectra were recorded with 32 scans per spectrum at a resolution of 4 cm^{-1}. The spectrum of fresh zeolite was recorded and used as a background for subsequent scans. About 20-30 mg of zeolite was added to the DRIFT cell, in which it was degassed at 475 °C under N_2 or H_2 flow. After 2 hours, the zeolite was cooled to 200 °C, at which about 5 mg of 4,6-DMDBT solids were added to the top of the sample and allowed to melt. A temperature-programmed desorption (TPD) study was then carried out from 200 °C to 500 °C. All IR spectra were analyzed using the OMNIC 9.4 software.

6.3 Results

6.3.1 Characterization results

Physicochemical properties were determined using a Micromeritics ASAP 2020 analyzer and the results are displayed in Figure 6.2 and Table 6.1. All isotherms for the mesoporous Y (SAY) zeolites show Type H4 hysterisis loop and reversible Type IV isotherms, suggesting the presence of mesoporosity. The pore size distribution graph created by the Density Functional Theory (DFT) method is presented in Figure 6.2(b). Table 6.1 shows that the surface area and pore volume are similar across all modified zeolites, suggesting retention of crystal structure of the modified Y zeolites. The mesoporous SAY zeolite shows ordered mesoporosity at approximately 35 Å, while it retains most of the original microporosity. The introduction of metals in the SAY does not affect significantly the surface area and the pore volume of the original sorbent. A detailed description of the pore structure of the SAY zeolites can be found in our previous publication.[207]

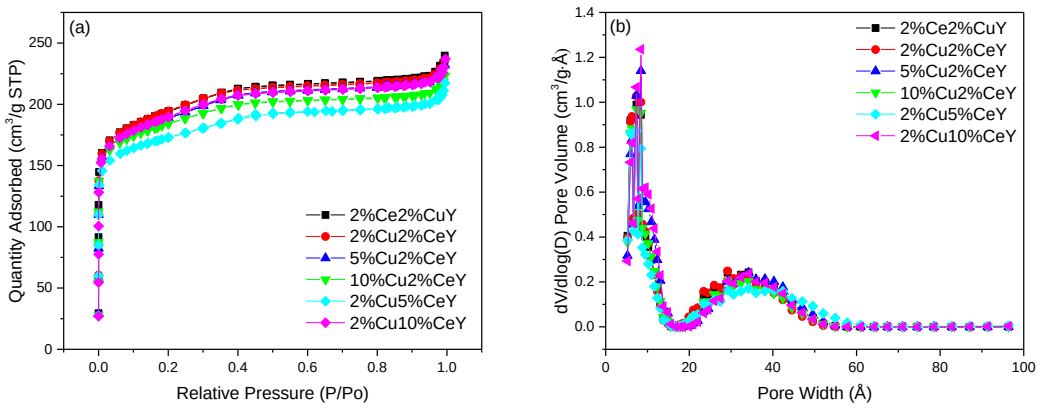

Figure 6.2: (a) Nitrogen adsorption-desorption isotherms and (b) DFT pore size distribution of various ion-exchanged Y zeolites.

Table 6.1: Surface areas and pore volumes of various ion-exchanged Y zeolites.

Material	S_{tot} (m^2/g)	S_{micro} (m^2/g)	S_{meso} (m^2/g)	V_{tot} (cm^3/g)	V_{micro} (cm^3/g)	V_{meso} (cm^3/g)
2%Ce2%CuSAY	663	409	253	0.552	0.19	0.362
2%Cu2%CeSAY	664	406	259	0.543	0.188	0.355
5%Cu2%CeSAY	642	401	242	0.537	0.186	0.351
10%Cu2%CeSAY	627	402	225	0.524	0.186	0.338
2%Cu5%CeSAY	588	395	193	0.51	0.183	0.327
2%Cu10%CeSAY	648	394	254	0.538	0.182	0.356

Figure 6.3 shows the XRD patterns of parent Y and modified Y zeolites before reduction. As expected, the parent Y exhibits high microporosity and crystalline structure, but the peaks corresponding to these characteristics were smaller in the presence of mesoporosity (e.g. SAY). The reduction in characteristic peaks can be attributed to the partial loss of silica and alumina during the introduction of mesopores.[68] The addition of metal cations further decreased the intensity of the peaks, especially the Ce cations due to high ion-exchange selectivity. Nonetheless, the characteristic peaks of parent Y and modified Y zeolites are very comparable to each other, which indicates that the original Y zeolite structure is retained. Additionally, no Cu or Ce

characteristic peaks can be observed, suggesting that little or no metal oxides were formed. The relative crystallinity of the modified Y zeolites (assuming 100% crystallinity of parent Y) was quantified and summarized in Table 6.2.

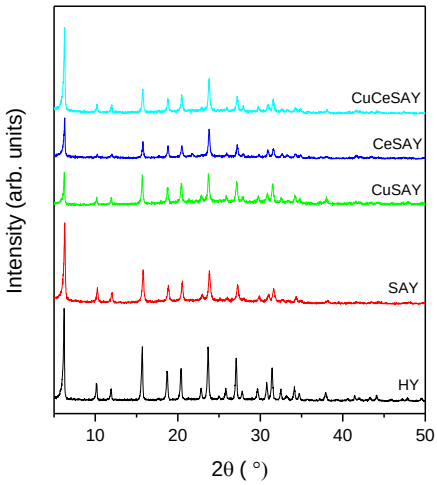

Figure 6.3: XRD patterns of parent Y and modified Y zeolites.

Table 6.2 shows that the concentrations of metal cations measured by ICP, are very close to that of the nominal values. SEM surface morphologies were imaged and are displayed in Figure 6.4. The images were taken at 90000x magnification and the insets display the corresponding surface metal composition obtained via elemental mapping. The size of zeolite particles are similar for all metal-exchanged mesoporous materials, ranging from 400 nm to 800 nm. SEM characterization was performed on unreduced samples to prevent the migration of metal cations into the internal coordination sites, which has been demonstrated previously.[164,244,245] A closer look at the images reveals extremely small particles in the nanoscale range, which could be attributed to well-dispersed metal nanoparticles on the external surface of the zeolites. Elemental mapping was also conducted on each metal- exchanged zeolite to determine the composition of metals on the external surface and the results are located in the inset of SEM images. CuSAY exhibits

approximately 5.5 wt% of Cu (Figure 5.4(a)), which is close to the theoretical and ICP values (Table 6.2). Meanwhile, CeSAY displays a higher weight loading of Ce on the surface (Figure 6.4(b)) than the theoretical calculation, which could be due to higher intrinsic affinity. On CuCeSAY (Figure 6.4(c)), the Cu surface loading was close to the nominal value, while no Ce metal was identified on the surface. We hypothesize that this observation might be due to the fact that Ce has been reported to prefer the internal sites.[157,166,180]

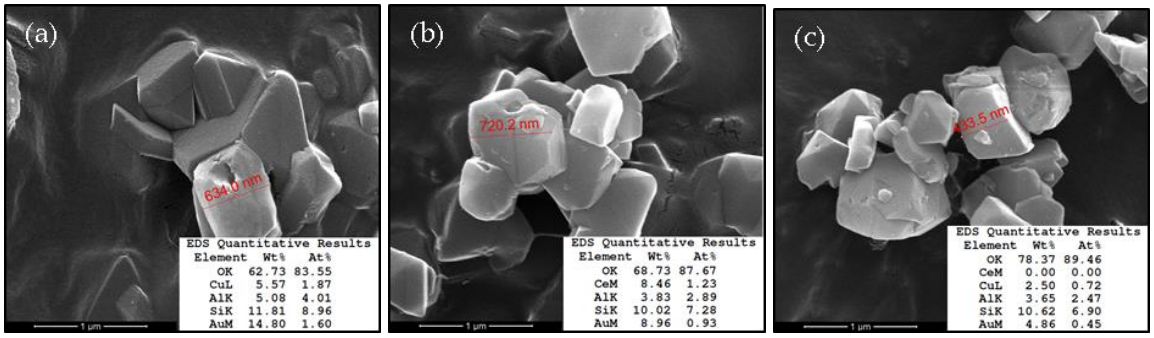

Figure 6.4: SEM images of unreduced (a) CuSAY, (b) CeSAY and (c) CuCeSAY taken at 20 kV and magnification of 11000x.

Table 6.2: XRD relative crystallinity, EDS elemental analysis and ICP metal loading of parent and modified Y zeolites.

	XRD	**ICP**	
Material	% crystallinity	Ce (wt%)	Cu (wt%)
SAY	79	-	-
CuSAY	70	-	4.6
CeSAY	68	5.6	-
CuCeSAY	65	3.1	2.7

Figures 6.5 and 6.6 show the XPS core level spectra of CeSAY, CuSAY and CuCeSAY. The quantitative distribution of oxidation states of Cu and Ce was recorded under *in*-situ reduction conditions as described in the experimental procedure, and they are shown in Table 6.3. Based on

the Ce 3d spectra, the samples containing Ce exhibit a stand-alone Ce^{4+} peak at 916.5 eV and a mixture of Ce^{3+} and Ce^{4+} at the range of 880 – 910 eV. These peaks can be deconvoluted into six peaks characteristic of two oxidation states of Ce (Ce^{3+} and Ce^{4+}) on the surface. While it has been suggested that Ce^{3+} in the outer cage of the Y zeolite can be easily oxidized to Ce^{4+},[246] the X-ray beam from the XPS could also induce reduction of cerium from 4+ to 3+ [247]. The ratio between Ce^{3+} and Ce^{4+} can be calculated using the following equation taken from Yu et. al [248]:

$$Ce^{4+}\% = \frac{u'''}{14} \times 100\% \qquad \text{Equation 5.1}$$

where *u'''* is the percent area of Ce^{4+} peak at 916.5 eV. From this equation, it was determined that approximately 90% of the Ce on CeSAY, and approximately 95% of Ce on CuCeSAY is Ce^{4+}. The Cu 2p spectra of CuSAY and CuCeSAY both indicate that most of Cu on the surface exists as Cu^{+}, to which is assigned the peak at 932 eV.[249]

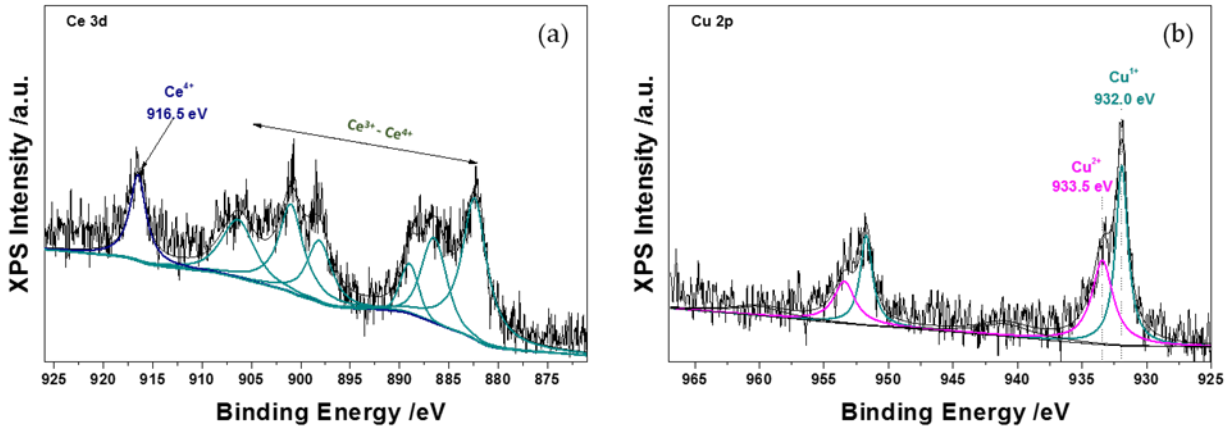

Figure 6.5: XPS spectra of (a) Ce 3d and (b) Cu 2p in CeSAY and CuSAY, respectively.

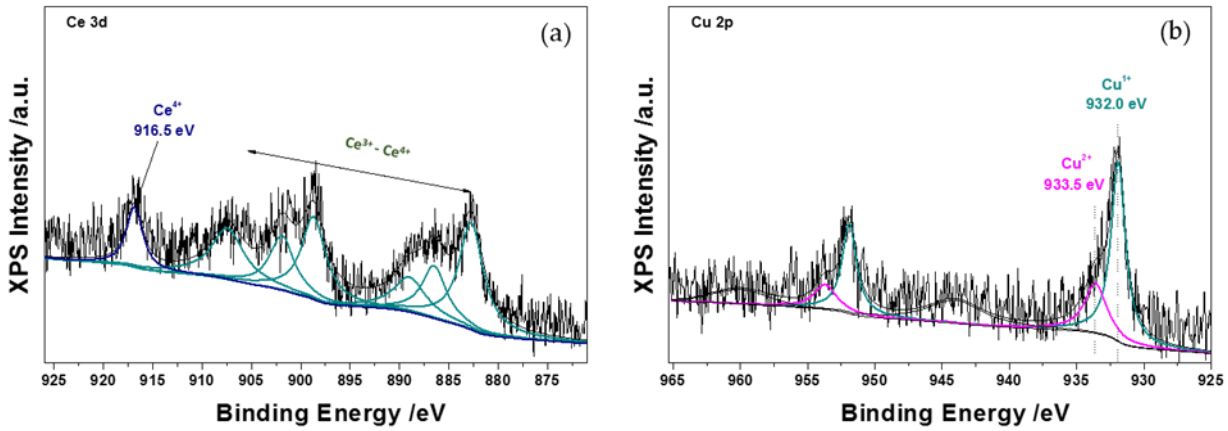

Figure 6.6: XPS spectra of (a) Ce 3d and (b) Cu 2p in CuCeSAY.

Table 6.3: Distribution of oxidation states of modified Y zeolites determined quantitatively by XPS analysis.

	Distribution of Oxidation States			
Zeolite	Ce^{3+}	Ce^{4+}	Cu^{+}	Cu^{2+}
CeSAY	9%	91%	0	0
CuSAY	0	0	55%	45%
CuCeSAY	15%	85%	75%	25%

To obtain high-resolution representation of zeolite crystalline structure and metal speciation, TEM studies were carried out. Figure 6.7 shows the TEM images of reduced CuSAY, CeSAY and CuCeSAY at low magnification to prevent the electron beam from destroying the material. The dark areas are zeolite particles consisting of lattice fringes (lines) and intracrystalline mesoporosity (holes) of about 4 nm. The periodic fringes indicate that the materials have retained most of the zeolite crystalline structure. The uniform distribution of mesopores suggests that the SA method was carried out successfully without compromising the integrity of the zeolite. All zeolite samples show an average particle size of about 500 nm, consistent with SEM micrographs. Dark field STEM was further used to investigate the zeolite mesoporosity as shown in Figure 5.8. The dark areas are zeolites and the lighter dots correspond to ~3-4 nm of mesopores, consistent with the size of the CTAB micelles.[250] The same areas were subjected to STEM analysis with

elemental mapping to further investigate the nature of Cu and Ce metals as shown at the inset of Figure 6.8. The metal nanoparticles are less than 1 nm in size, and occupy specific extra-framework coordination sites, as indicated by the EDS elemental mapping. Our hypothesis is that Cu occupies the external sites of the zeolite (e.g. site II located on the six-membered ring face of the sodalite cage) and Ce, most likely, occupies the internal sites (e.g. site I' located inside the sodalite cage, opposite of site I in the center of the hexagonal prism).

The TEM figures also show a higher dispersion of Ce compared to Cu (after subtracting from Cu grid background), supporting the previous claim that the ion-exchange selectivity of Ce is high. The particle size of Cu may seem larger than that of Ce as it is more easily oxidized.[251,252]

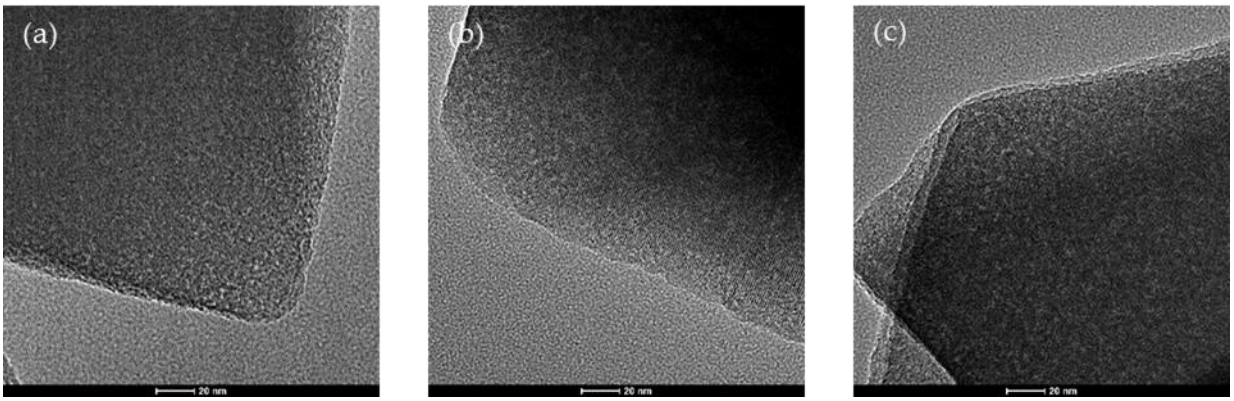

Figure 6.7: Low-magnification TEM micrographs of unreduced (a) CuSAY, (b) CeSAY and (c) CuCeSAY taken at 200 kV and magnification of 130000x.

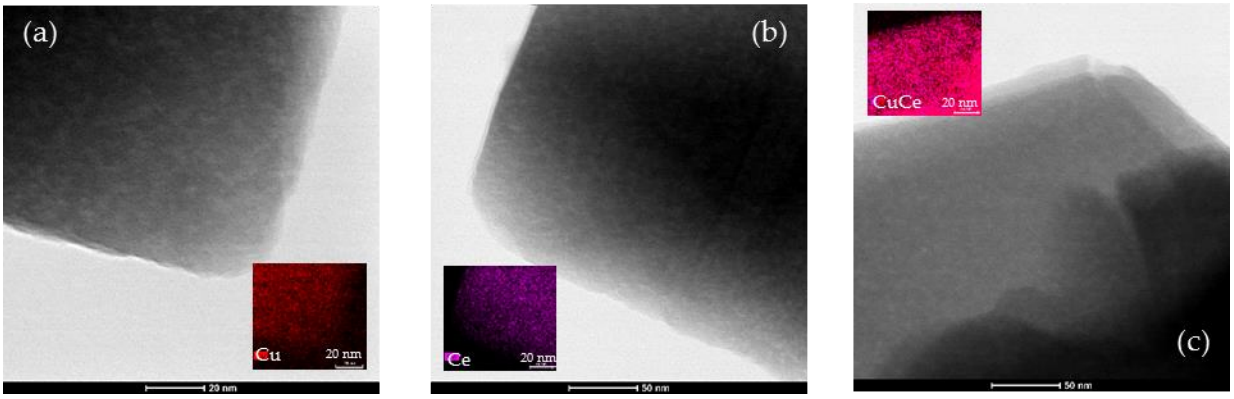

Figure 6.8: STEM-EDS mapping of unreduced (a) CuSAY, (b) CeSAY and (c) CuCeSAY taken at 200 kV and magnification of 450000x.

6.3.2 Mechanistic results

The modified zeolites were subjected to *in-situ* temperature-programmed desorption (TPD) in a DRIFTS reaction chamber to better understand the modes of adsorption, binding configurations and regeneration behavior between the sorbent and the sorbate. The spectra of free 4,6-DMDBT as observed by attenuated total reflection (ATR) and predicted density functional theory (DFT) calculations have been provided elsewhere.[253] A complete vibrational assignment of each theoretical peak has been attempted in an effort to rationalize our spectral interpretation and they are provided in Table 6.4.

Table 6.4: Complete assignment of IR frequencies of 4,6-DMDBT.

Predicted frequency, cm^{-1}	IR exp. frequency, cm^{-1}	Vibrational modes	Vibrating atoms and/or functional groups	Visualization
448.6	464.8	CSC bending CH_3 wagging CCC bending	C_4-S-C_9 Me_20, Me_24 $C_2C_3C_{24}$, $C_{11}C_{10}C_{20}$	
483	501.3	CSC scissoring CH_3 wagging CH in plane bending In-plane ring deformation	C_4-S-C_9 Me_20, Me_24 C_2H_7(C), C_1H_{19}(C), C_6H_8(C), $C_{13}H_{16}$(A), $C_{12}H_{18}$(A), $C_{11}H_{15}$(A) Aro_1, Aro_9	
498.6	513.1	CH_3 twisting CH out of plane bending Ring torsion	Me_20, Me_24 C_2H_7(+), $C_{11}H_{15}$(+), C_1H_{19}(-), C_6H_8(-), $C_{13}H_{16}$(-), $C_{12}H_{18}$(-) Aro_1, Aro_9	
508.4	526.4	CSC rocking* CH_3 wagging Ring twisting mode	C_4-S-C_9 Me_20, Me_24 Aro_1(C), Aro_9(A)	

522.6	539.9	CH_3 twisting Ring torsion Ring torsion*	Me_20, Me_24 Aro_1, Aro_9 Thio_17	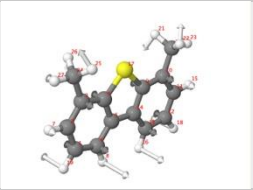
577	577	CH_3 wagging CCC symmetric stretching CCC bending CH in-plane bending	Me_20, Me_24 $C_1C_2C_3$, $C_{10}C_{11}C_{12}$ Aro_1, Aro_9 C_1H_{19}(A), $C_{12}H_{18}$(A)	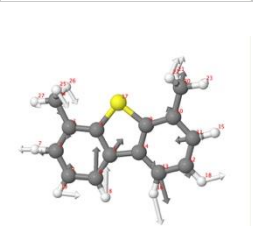
605.6	631.4	Ring breathing C-C stretching In-plane ring deformation Ring beating*	Thio_17 C_3C_{24}, $C_{10}C_{20}$ Aro_1, Aro_9 Thio_17	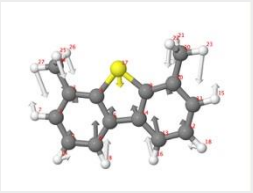
745.4	765.9	Ring torsion CCC out of plane bending CH out of plane bending	Thio_17 $C_2C_1C_6$, $C_{11}C_{12}C_{13}$ C_2H_7(-), C_1H_{19}(-), C_6H_8(-), $C_{13}H_{16}$(+), $C_{12}H_{18}$(+), $C_{11}H_{15}$(+)	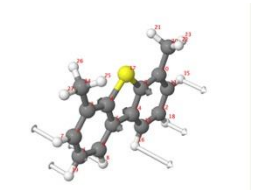
767.1	798.8	CSC symmetric stretching CCC symmetric stretching CH in plane bending	C_4-S-C_9 $C_2C_1C_6$, $C_{11}C_{12}C_{13}$, $C_3C_4C_5^*$, $C_{14}C_9C_{10}^*$ C_2H_7(A), C_6H_8(C), $C_{13}H_{16}$(A), $C_{11}H_{15}$(C)	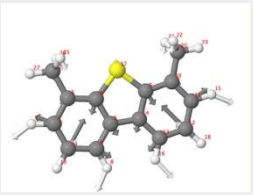
793.3	825.4	CH_3 twisting CH out of plane wagging	Me_20, Me_24 C_2H_7, C_1H_{19}, C_6H_8, $C_{13}H_{16}$, $C_{12}H_{18}$, $C_{11}H_{15}$	
921.7	958.3	CH_3 twisting CH out of plane bending	Me_20 $C_{13}H_{16}$(+), $C_{11}H_{15}$(-)	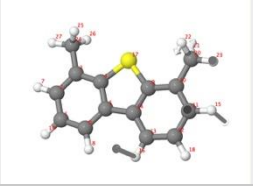

951.7	986.5	Ring breathing CH_3 wagging CH in plane bending In-plane ring deformation	Thio_17 Me_20, Me_24 C_1H_{19}(C), $C_{12}H_{18}$(A) Aro_1, Aro_9	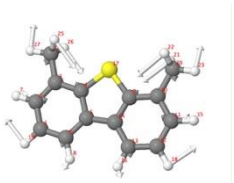
988.7	1014.7	CH_3 twisting CH out of plane bending	Me_20(s), Me_24(w) C_2H_7(-), C_1H_{19}(+), C_6H_8(-), $C_{13}H_{16}$(+), $C_{12}H_{18}$(-), $C_{11}H_{15}$(+)	
1010.7	1049.1	CH_3 wagging Ring twisting	Me_20, Me_24 Aro_1(C), Aro_9(C)	
1060.3	1099.1	CH_3 twisting CC out of plane bending CH out of plane bending	Me_20(w), Me_24(s) C_3C_{24} C_2H_7(-)	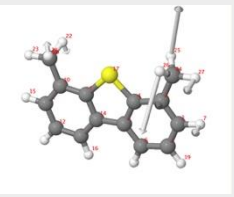
(1062.1)	Coupled with 1099.1	CH_3 twisting CC out of plane bending CH out of plane bending	Me_20(s), Me_24(w) C_3C_{24} C_2H_7(-)	
1071.7	1112.4	CSC asymmetric stretching CH_3 wagging CCC bending CH in-plane bending	C_4-S-C_9 Me_20, Me_24 Aro_1, Aro_9 C_2H_7(C), $C_{11}H_{15}$(C)	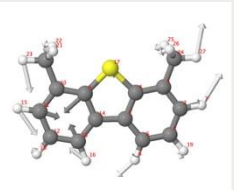
1089.7	1135.9	CSC symmetric stretching CH_3 wagging CCC bending CH in-plane bending	C_4-S-C_9 Me_20, Me_24 Aro_1, Aro_9 C_2H_7(C), $C_{11}H_{15}$(A)	

1125.1	1167.2	CSC asymmetric stretching CH_3 wagging CCC bending CH bending	C_4-S-C_9 Me_20, Me_24 $C_2C_1C_6$, $C_{11}C_{12}C_{13}$ C_2H_7(C), C_6H_8(A), $C_{13}H_{16}$(A), $C_{11}H_{15}$(C)	
1175.1	1222.7	CH bending CH in-plane bending (Kekule)	$C_{24}H_{27}$, $C_{20}H_{23}$ C_1H_{19}(A), C_2H_7(C), $C_{12}H_{18}$(A), $C_{11}H_{15}$(C)	
1205.6	1247	CH bending CH in-plane bending (Kekule)	$C_{24}H_{27}$, $C_{20}H_{23}$ C_2H_7(A), C_1H_{19}(C), C_6H_8(A), $C_{13}H_{16}$(A), $C_{12}H_{18}$(C), $C_{11}H_{15}$(A)	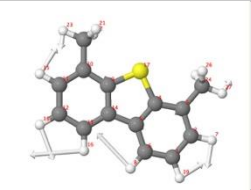
1286.2	1328.3	CH_3 wagging Ring twisting	Me_20, Me_24 Aro_1(A), Aro_9(C)	
1363.5	1413.6	CH_3 wagging CC stretching (Kekule) Ring breathing*	Me_20, Me_24 Aro_1, Aro_9 Thio_17	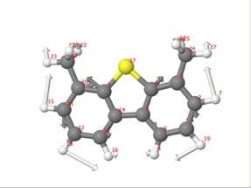
(1366.6)	Coupled with 1413.6	CH_3 wagging CC stretching (Kekule) Ring deformation*	Me_20, Me_24 Aro_1, Aro_9 Thio_17	
1466.8	1525.1	CH_3 scissoring CH in-plane bending Ring in-plane deformation	Me_20, Me_24 C_2H_7(C), C_1H_{19}(A), C_6H_8(A), $C_{13}H_{16}$(A), $C_{12}H_{18}$(A), $C_{11}H_{15}$(C) Aro_1, Aro_9	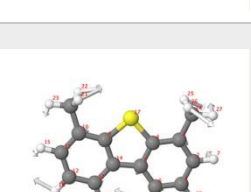
1493.7	1544.4	CH_3 twisting	Me_20(w), Me_24(s)	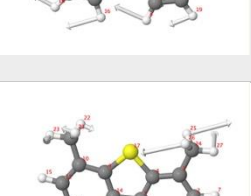

(1494.3)	Coupled with 1544.4	CH_3 twisting	Me_20(s), Me_24(w)	
1507.7	1558.5	CH_3 scissoring CH in-plane bending	Me_20, Me_24 C_2H_7(A), C_1H_{19}(A), C_6H_8(C), $C_{13}H_{16}$(A), $C_{12}H_{18}$(C), $C_{11}H_{15}$(C)	
1512.4	1570.1	CH_3 scissoring CH in-plane bending	Me_20, Me_24 C_2H_7(A), C_1H_{19}(C), C_6H_8(C), $C_{13}H_{16}$(C), $C_{12}H_{18}$(C), $C_{11}H_{15}$(A)	
1679.1	1747.5	CH_3 scissoring CC stretch (Kekule) Ring in-plane deformation*	Me_20, Me_24 Aro_1, Aro_9 Thio_17	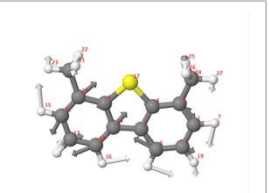
(1690.4)	Coupled with 1747.5	CH_3 scissoring CC stretch (Kekule) Ring in-plane deformation*	Me_20, Me_24 Aro_1, Aro_9 Thio_17	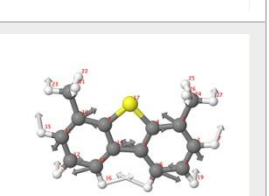
3206.4	3327.8	CH stretching	C_2H_7, C_1H_{19}, C_6H_8, $C_{13}H_{16}$, $C_{12}H_{18}$, $C_{11}H_{15}$	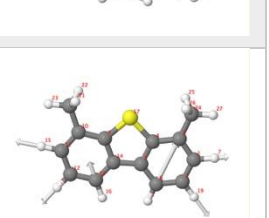

Notations:

1. Me_, Aro_ and Thio_ stands for methyl group, aromatic ring (6-rember) thiophene ring, respectively. Numbers after underline (e.g. Aro_9) indicates the label of carbon (or sulfur) atom contained in this functional group to differentiate among various groups.
2. For in-plane bending, twisting, there are C or A in parentheses indicates ‘clockwise’ (C) or ‘anti-clockwise’ (A) with respect to center of 6-member aromatic rings (imaginary points, not exist in molecule).
3. As for out of plane bending mode, (+) and (-) are added to distinguish between bending ‘towards’ (+) or ‘away from’ (-) the molecular plane. Such vibrational movements in ring torsion mode are not denoted for brevity.
4. (s) and (w) indicates the intensity of methyl groups vibrations, strong or weak, relative to each other.

5. * means that a functional group or chemical bond has equivalent vibration intensity with other groups, however, it is induced by atoms that vibrate in other groups.

Figure 6.9 shows the FTIR spectra collected at increasing temperature upon exposure of each of the modified zeolites to 4,6-DMDBT. The band at 3740 suggests vibrational stretching of the terminal silanol, while bands at 3630 and 3555 cm^{-1} correspond to vibrational stretches of hydroxyl species in the supercage and sodalite cage, respectively.[254,255] Both CeSAY and CuCeSAY display a shoulder band below 3555 cm^{-1}, implying that at least one extra adsorption mode can be attributed to the presence of Ce cations in the sodalite cage.[63,256] This shoulder band is not observed on CuSAY. The bands ranging from 3100 to 2700 cm^{-1} are attributed to C-H stretches of 4,6-DMDBT. It is well known that bands below 3000 cm^{-1} are characteristic of sp3 hybridized hydrocarbons,[257] and in our case can be attributed to the methyl groups of the 4,6-DMDBT. In addition, the emergence of these bands can also be attributed to a possible elongation of the sp2 C-H stretches of the 4,6-DMDBT on the Y zeolites. Dissociation of the 4,6-DMDBT is unlikely, because the color of the zeolites remained unchanged even at temperature as high as 500 °C, suggesting that the sulfur molecule was adsorbed molecularly, rather than being reacted to form coke. A quick glance of the three metal-exchanged zeolites suggests that a very high temperature is required to completely desorb 4,6-DMDBT from these materials, due to the strong interaction between the exchanged metal and the sulfur compounds. As temperature in the cell was increased, the terminal silanols on all three zeolites were regenerated first, followed by the hydroxyl sites. This suggests that the Brønsted acid sites play a more important role in the adsorption capability of the materials as compared to the external silanols. It is also apparent that CuCeSAY is harder to regenerate as compared to CuSAY and CeSAY, as evidenced by the C-H vibrational bands with higher intensity below 3100 cm^{-1} at 400 °C. This suggests that a stronger

bond interaction is formed, which consequently prevents the sulfur compound from being easily desorbed.

The key interaction responsible for the adsorption strength and regeneration property of each zeolite can be better explained by examining the C=C vibrational modes. Figure 6.10 displays the IR spectra of adsorbed 4,6-DMDBT in the C=C vibrational region. The weak band at 1640 cm^{-1} (not labeled) can be assigned to hydroxide radical stretching of H_2O, suggesting that the zeolite is mostly degassed and the cell environment is primarily dry.[258] This is consistent with the absence of strong O-H stretch at the 3000-3400 cm^{-1} region, as shown in Figure 6.9. Subsequent bands at 1570 and 1450 cm^{-1} correspond to symmetric and antisymmetric aromatic C=C stretches of the thiophene ring. Figure 6.10 shows the IR spectra of SAY and metal-modified SAY zeolites upon adsorption of 4,6-DMDBT. With the exception of SAY, the bands at 1570 and 1450 cm^{-1} are still present even at 400 °C, which shows the importance of metals on the selective adsorption of 4,6-DMDBT. The band at 1515 cm^{-1} is indicative of a possible C=C shift of free 4,6-DMDBT from 1570 cm^{-1} due to the loss of electron density. This band can be observed in Figure 6.10(b) and (d) on CuSAY and CuCeSAY, respectively, as 4,6-DMDBT was adsorbed via the π-stacking of the 4,6-DMDBT ring. On the other hand, Figure 6.10(c) and (d) show a blue shift of a C=C vibrational band from 1450 to 1480 cm^{-1} during the adsorption of 4,6-DMDBT on CeSAY and CuCeSAY, respectively. The presence of this band might be the result of an increase in electronic current density of the sulfur-containing conjugated ring and can, therefore, could be attributed to a direct S-M (or σ-bond) interaction between the Ce metal and the sulfur atom.[145] This mechanism has also been studied and observed for smaller thiophenic compounds shown in our previous publication.[207] It has been observed that the band shift at 1480 cm^{-1} may not be as intense as the shift observed

by other smaller thiophenic compounds adsorbed on CeY zeolites, because 4,6-DMDBT was introduced by melting the solid, instead of vaporizing it from a reservoir.

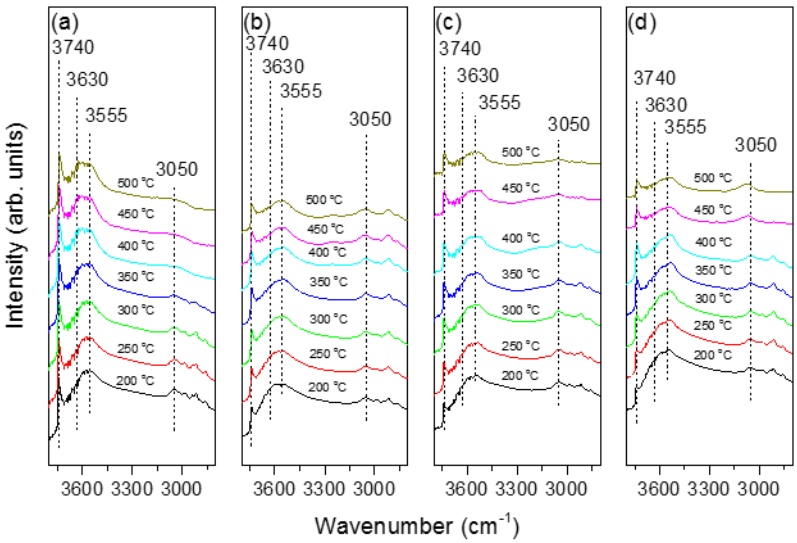

Figure 6.9: IR-TPD spectra of adsorbed 4,6-DMDBT on (a) SAY, (b) CuSAY, (c) CeSAY and (d) CuCeSAY in the zeolitic region.

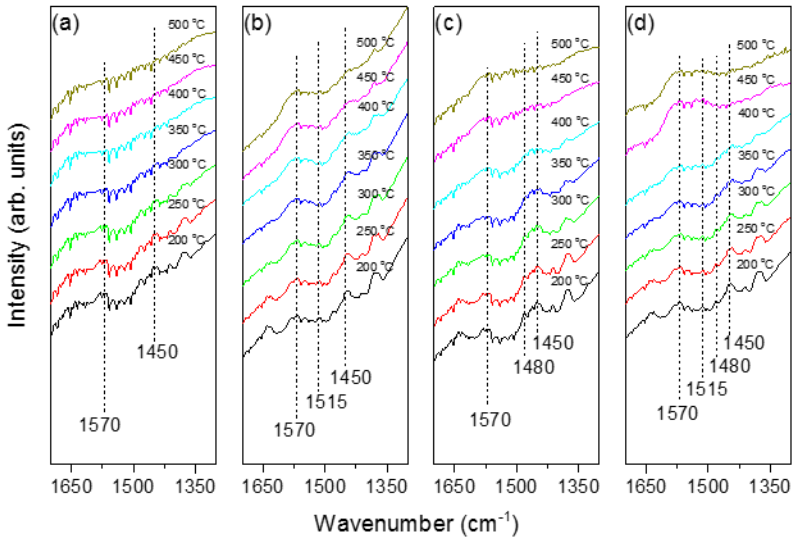

Figure 6.10: IR-TPD spectra of adsorbed 4,6-DMDBT on (a) SAY, (b) CuSAY, (c) CeSAY and (d) CuCeSAY in the C=C region.

6.3.3 Fixed-bed adsorption results

While spectroscopic studies may be a powerful tool to understand the adsorption mechanism of sulfur molecules on zeolites on the molecular level, dynamic adsorption tests are necessary to understand the capacity of sorbents and the kinetics of adsorption. Dynamic fixed-bed experiments can not only quantitatively and qualitatively explain the adsorption of sulfur molecules on the sorbents, but can also serve as pilot technology to mimic industrial operating conditions. Figure 6.11 shows the breakthrough curves of the various Y zeolites on the adsorption of 100 ppmw of 4,6-DMDBT from *n*-octane. It is clear that the unmodified Y zeolite displays very poor desulfurization performance, because the presence of micropores prevents the bulky 4,6-DMDBT from accessing the internal active sites, rendering the sorbent incompetent for refractory sulfur compounds. When mesopores were introduced in the Y zeolite (SAY), the breakthrough curve was extended substantially from 0 to nearly 150 mL/g of 4,6-DMDBT-free fuel. This is a strong indication that the adsorption of 4,6-DMDBT on the parent Y is diffusion limited, and thus, the presence of mesopores shortens the diffusion length by granting the adsorbate unrestricted access to the internal active sites. The incorporation of Ce metals into the mesoporous SAY, however, failed to improve the breakthrough curve of SAY. This might be attributed to the location of Ce cations in the sodalite cages. The preferential coordination of Ce cations on type I' sites makes it challenging for 4,6-DMDBT to directly interact with those sites. This was also observed during the adsorption of dibenzothiophene (DBT) in our previous study.[63] When Cu was added to the mesoporous SAY, the breakthrough curve was extended to nearly 175 mL/g of 4,6-DMDBT-free fuel. Based on our spectroscopic results, CuCeSAY may outperform CuSAY since a higher temperature was required to completely desorb the sulfur and subsequently, regenerate the active sites. This suggests that a very strong interaction exists between CuCeSAY and 4,6-DMDBT. The

breakthrough curve shows that CuCeSAY has a capacity of almost 200 mL/g, which is about 25 mL/g more than CuSAY. This underscores the synergistic effect of Cu and Ce that dramatically increases the capacity and selectivity of 4,6-DMDBT.

To better simulate the diesel fuel, 1% naphthalene was added to the feed mixture of *n*-octane and 4,6-DMDBT. As shown in Figure 5.12, the capacity of CuCeSAY was suppressed by at least 5-fold, due to the presence of aromatics. To increase the adsorption of 4,6-DMDBT, we studied the effect of two zeolite modifications: a) the composition of metals in the zeolite, and b) the order in which the metals were introduced. Table 5.5 summarizes the elemental compositions of each modified zeolite determined by ICP.

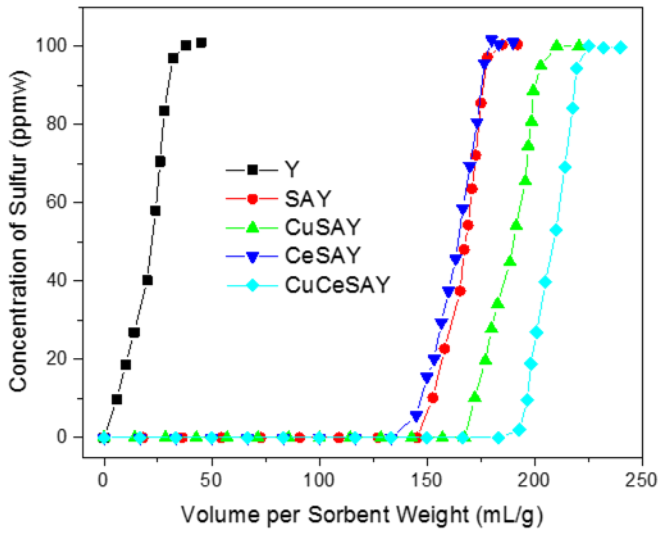

Figure 6.11: Breakthrough curves of 100 ppmw of sulfur in 4,6-DMDBT dissolved in n-octane on various Y zeolite adsorbents.

Table 6.5: Elemental composition of Ce and Cu on various metal-exchanged mesoporous zeolites.

Zeolite	Ce	Cu
2Ce2CuSAY	1.9%	1.9%
2Cu2CeSAY	1.6%	1.7%
5Cu2CeSAY	1.8%	2.8%
10Cu2CeSAY	1.7%	2.7%
2Cu5CeSAY	5.7%	1.4%
2Cu10CeSAY	8.0%	0.9%
5Cu10CeSAY	5.9%	0.9%
10Cu10CeSAY	6.9%	1.4%

Figure 6.12(a) shows the comparison between two metal-exchanged mesoporous Y zeolites with identical metal loading, but different order in which they were introduced (Materials 1 and 2 on Table 6.5). Thus, in CuCeSAY, Ce was introduced first followed by Cu; while in CuCeSAY, Ce was introduced first followed by Cu. The results indicate that 2%Ce2%CuSAY performed very poorly, as the adsorption capacity of 4,6-DMDBT was only 20 mL/g, compared to 35 mL/g by 2%Cu2%CeSAY. This confirms the validity of our ion-exchange technique, which dictates that Ce should be exchange first, followed by Cu. This configuration was adopted for subsequent modified mesoporous Y zeolites.

Next, the amount of Cu was varied from 2 wt% to 5 wt% and 10 wt%, while keeping Ce constant at 2 wt% (Materials 2, 3 and 4 in Table 6.5). The ICP results show that the Cu amount did not increase significantly, which suggests that the zeolite has reached the maximum ion-exchange capacity. Figure 6.12(b) shows that both 5%Cu2%CeSAY and 10%Cu2%CeSAY zeolites exhibit lower 4,6-DMDBT capacity compared to 2%Cu2%CeSAY. This is consistent with the ICP results, which showed similar amount of metals in all the adsorbents. Additionally, access of the Ce metals to the internal sites was further restricted.

Figure 6.12(c) shows the effect of Ce as the concentration was varied from 2 wt% to 10 wt%, while keeping the concentration of Cu fixed at 2 wt% (Materials 2, 5 and 6 in Table 6.5). Contrary to Cu, the increase in Ce loading actually contributed to higher sulfur uptake, with 2%Cu10%CeSAY exhibiting the highest 4,6-DMDBT capacity of about 50 mL/g. This is equivalent to a saturation adsorption capacity of 6.8 mg S/g, calculated using the equation reported elsewhere.[139] While there has been limited fixed-bed studies on dynamic adsorption of alkyl-DBT in the presence of aromatics, Duan et al. did show that CeY exhibited a capacity of 3.33 mg S/g using a feed containing 300 ppmw of 4,6-DMDBT in *n*-nonane.[145] To the best of our knowledge the 2%Cu10%CeSAY has shown the highest adsorption capacity so far in literature, for 4,6DMDBT, among any other Y sorbent in the presence of aromatics. However, we should make clear that other sorbents reported in literature (aside Y), such as the UMCM-150, UMCM-150$(N)_1$, UMCM-150$(N)_2$ by Park et al.[259] as well as the Boron Nitride Mesoporous Nanowires by Xiong et al.[260] have exceeded much higher capacities for 4,6-DMDBT. According to the literature, ICP results also confirmed the increase of Ce loading in the zeolite with values close to the theoretical calculations. Finally, we increased the Cu loading on 10%CeSAY zeolite from 2 wt% to 5 wt% and 10wt% (Materials 6, 7 and 8 in Table 5.5). ICP results revealed no increase in the amount of Cu in the zeolites, while Figure 6.12(d) shows no improvement on the adsorption of 4,6-DMDBT.

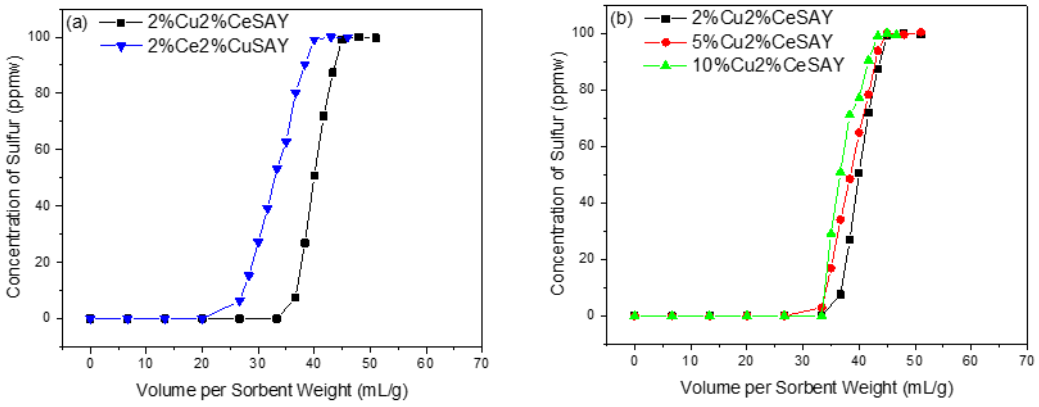

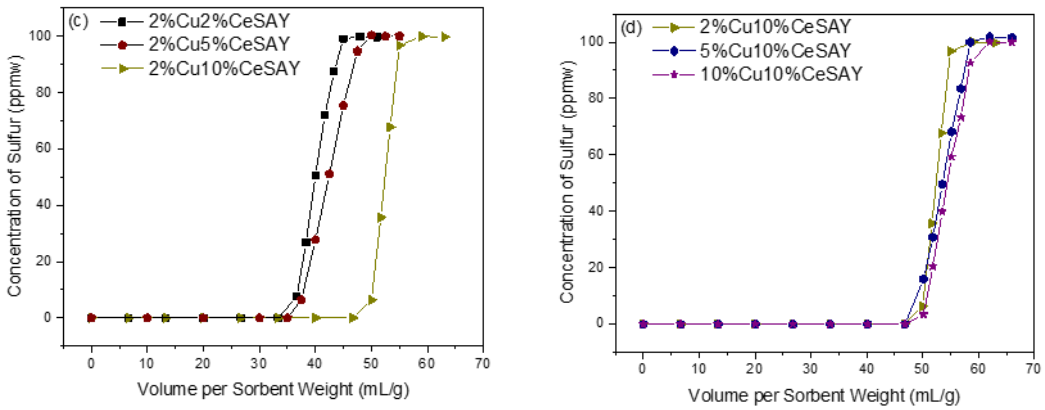

Figure 6.12: Breakthrough curves of 100 ppmw of 4,6-DMDBT and 1 wt% naphthalene in n-octane adsorbed on mesoporous Y zeolites following the effects of: a) metal configuration, b) Cu concentration on 2%CeSAY, c) Ce concentration on 2%CuSAY and d) Cu concentration on 10%CeSAY.

2%Cu10%CeSAY was selected as the optimum material to study the effect of regeneration and lifetime. Figure 6.13 shows the breakthrough curves of regenerated 2%Cu10%CeSAY. Upon thermal treatment in air at 500 °C for 4 hrs and activation under reducing gas at 325 °C for 2.5 hrs, the zeolite still displayed similar desulfurization performance. The first and second regenerated zeolites both produced close to 50 mL/g of 4,6-DMDBT-free fuel, similar to the capacity observed on the corresponding fresh zeolite. Figures 6.14 and 6.15 show that the diffraction pattern and physicochemical properties of the sorbent before and after regeneration were similar, respectively. Figure 6.14 shows the XRD spectra of the fresh and used 2%Cu10%CeSAY after the two thermal cycles. Some reduction in the intensity of the peaks is apparent, which suggests loss in crystallinity. However, most of the characteristic diffraction peaks of the zeolite are still present after two regeneration cycles, suggesting that the crystal structure was mostly retained. Figure 6.15 (a) and (b) compares the N2 adsorption/desorption and the pore size distribution, respectively, of the 2%Cu10%CeSAY as fresh and after the two cycles of thermal regeneration. After the two regeneration cycles, the zeolite has lost some microporosity, while the ordered mesopores have

collapsed to random and more broad range mesopores. This is expected as a result of the thermal treatment. The results are also in agreement with the loss of microporosity observed by XRD. As a result, the adsorbent was still active and preserved high adsorption capacity after two regeneration cycles. Our future studies will involve more experiments on the regenerability and the longevity of the sorbent.

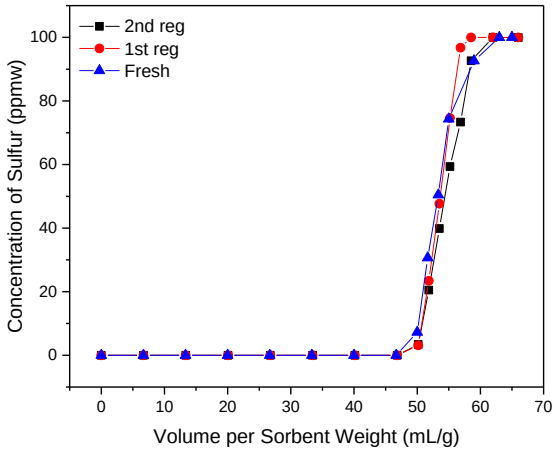

Figure 6.13: Breakthrough curves of 100 ppmw of 4,6-DMDBT and 1 wt% naphthalene in n-octane adsorbed on fresh and regenerated 2%Cu10%CeSAY.

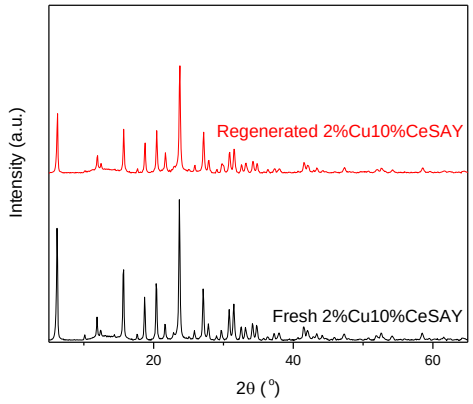

Figure 6.14: XRD spectra of 2%Cu10%CeSAY before and after regeneration.

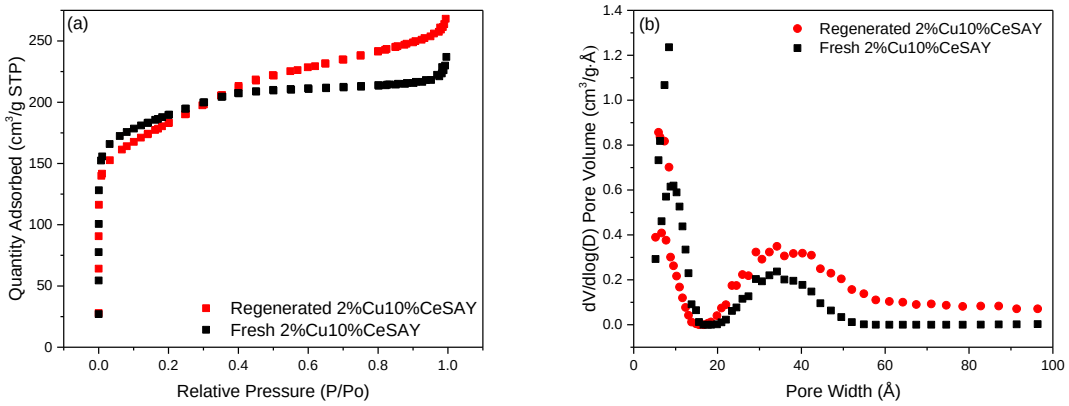

Figure 6.15: N2 adsorption-desorption and (b) DFT pore distribution of 2%Cu10%CeSAY before and after regeneration.

Zhang et al. conducted fixed-bed adsorption experiments with 100 ppmw of 4,6-DMDBT dissolved in *n*-octane without competing aromatics and their Ni-based SBA-15 sorbent produced about 30 mL/g of clean fuel.[155] Bu and co-workers studied the adsorptive desulfurization of 0.27% 4,6-DMDBT and 0.16% naphthalene dissolved in hexadecane on wood-derived activated carbon.[261] The sorbent (S_{BET} = 1100 m^2/g), despite having a very high surface area, exhibited a sulfur capacity of about 20 mL/g. In our studies, it was also observed that the increase in Cu loading in the supercage did not improve the sulfur capacity of the zeolite. According to the ICP results, Cu reached its ion-exchange capacity limit at approximately 2 wt%, in the presence of Ce. Even though Ce prefers to occupy type I' sites in the sodalite cages,[262] increasing the Ce density would lead to higher probability for incoming sulfur compounds to gain access to stronger direct S-M σ-bonding in the internal cages. When combined, the synergistic effect of Cu and Ce increased the uptake of sulfur. From the XPS analysis in Table 6.3, Ce plays an important role as a promoter to increase the density of Cu^+ in the zeolite from 55% to 75%, the oxidation state that has shown to increase the capacity of sulfur.[147,156]

6.4 Discussion

In this study, a refractory sulfur compound, 4,6-DMDBT, was used as a model molecule to investigate the adsorption capability over (bi)metal-exchanged mesoporous zeolites. The tailored CuCeSAY exhibited highly-ordered mesopores and highly-dispersed metal cations. These properties made the zeolite selective and effective for the adsorption of heavy sulfur compounds.[263–265] As shown in the breakthrough curves, CuCeSAY had an outstanding desulfurization capacity of nearly 200 mL/g of 4,6-DMDBT-free fuel. A thorough analysis of Figure 6.11 shows that mesoporosity significantly contributed to this improvement. The parent Y barely removed any 4,6-DMDBT, most likely because the micropores caused poor accessibility of the bulky molecule to the internal active sites of the zeolite. Mesoporous SAY, on the other hand, overcame this limitation and subsequently increased the uptake of 4,6-DMDBT by about 150 mL/g. Further improvement of the breakthrough curve was observed as metals, such as Ce and/or Cu were exchanged to replace the proton. On the new site, the metal cation formed a stronger bond either via π-complexation or direct σ-bond interaction with the adsorbing sulfur compound. The incorporation of metals activated high energy bonds, as shown spectroscopically by our FTIR results.

A summary of breakthrough points of 4,6-DMDBT and smaller thiophenic compounds from our previous studies[207] is shown in Table 6.5. This comparison has not been studied before, and yet it is important to effectively demonstrate the role of pore structure and metals. For a given zeolite, the breakthrough point increases with the size of the thiophenic compound. For example, 153 mL/g of 4,6-DMDBT was the breakthrough point for SAY, but the breakthrough point was 60 mL/g lower for DBT. This is followed by a much lower breakthrough point for BT with only 6.5 mL/g of sulfur-free fuel produced. Other groups have shown that the affinity of each sulfur

compound to be adsorbed is attributed to the electron density on the S atom of the aromatic compound.[140,149] As the kinetic diameter of thiophenic molecule increases, the electron density on the corresponding S atom increases. Table 6.6 shows that the adsorption of bulky sulfur compounds, are diffusion limited, which can be addressed by the mesoporous SAY zeolites. Their kinetic diameters are also displayed in parenthesis. Thus, as shown in Table 6.6, the breakthrough point of DBT was increased from 52 to 93 mL/g and the breakthrough point of 4,6-DMDBT was increased from 10 to 153 mL/g when zeolite Y was replaced by SAY.

By ion-exchanging Ce and then Cu metals into the mesoporous Y zeolite, we discovered that about 50 mL/g of 4,6-DMDBT-free fuel could be produced. The high capacity of the material can be attributed to synergistic effect of Cu and Ce. The synergy between Cu and Ce is apparent in the TPD profile, which was studied by *in-situ* DRIFTS. CuCeSAY zeolite shows characteristic bands of π-complexation and σ-bond interaction, evidenced by shifts to lower and to higher wavenumbers, respectively, as compared to the corresponding IR bands of free 4,6-DMDBT. In fact, the band shifts may not be that obvious as 4,6-DMDBT was introduced by melting over the zeolite sample, making it harder to identify chemisorbed-only peaks. It is evident that the C=C band shift of BT to a higher a wavenumber from 1450 to 1490 cm^{-1} due to σ-bonding is most notable, especially on CeY. As the size of sulfur compounds increases from BT to DBT and finally 4,6-DMDBT, this blue shift becomes less obvious, making it harder to compare the characteristics bands and draw conclusions regarding the adsorption modes and energies.

Table 6.6: Breakthrough points of studied sulfur compounds adsorbed over various Y zeolites.

	Breakthrough points (mL/g)			
Material	TP[a] (5.3 Å)[b]	BT[a] (6 Å)[b]	DBT[a] (9 Å)[b]	4,6-DMDBT (≥ 9 Å)[b]
Parent Y	7.0	7.0	52.0	10.0
CeY	14.0	50.0	49.0	-
CuY	-	77.0	50.0	-
SAY	-	6.5	93.0	153.0
CeSAY	-	-	110.0	145.0
CuSAY	-	-	117.0	172.0
CuCeSAY	-	-	-	193.0

[a] Taken from our previous publications [63,207]
[b] Kinetic diameters in parenthesis

While the adsorptive desulfurization of 4,6-DMDBT in *n*-octane using bimetallic mesoporous Y zeolite has shown promising results, it does not fully capture the commercial potential of this technology. It is imperative to study the effect of aromatics on the selective removal of 4,6-DMDBT. Thus, 1% naphthalene was incorporated into the model fuel mixture and different ion-exchanged mesoporous zeolites with various metal loadings and orders of Ce and Cu were studied. The results in Figure 6.12 showed that 2%Cu10%CeSAY exhibited the highest 4,6-DMDBT capacity among the different zeolites. As explained in the results section, the order at which the metals are incorporated in the zeolites has a significant impact on the adsorption. This suggests that Cu and Ce coordinate very differently in the Y zeolite extra-framework.[266] Although 10%Ce2%CuSAY produced slightly higher sulfur adsorption compared to 2%Cu2%CeSAY, the increase of Ce loading compensated for the unfavorable location of the Ce metal. However, the improvement was small. Having the Ce metal in the sodalite cage, while Cu being on the outer cage in 2%Cu10%CeSAY, produced about two times more clean fuel compared to 2%Cu2%CeSAY. To the best of our knowledge this is the highest 4,6-DMDBT breakthrough point reported by Y sorbent in the presence of aromatics by a dynamic fixed bed experiment.

6.5 Conclusions

Following the encouraging results from the fixed-bed experiment, it was decided that the sustainability of this process should also be investigated by examining the regenerability of the spent sorbent. For this study, the best sorbent, 2%Cu10%CesAY was selected to study the effect of regeneration. After each regeneration cycle, the zeolite was exposed to the same sulfur feed and the breakthrough curve was analyzed. As indicated in Figure 6.13, almost 100% of sulfur capacity could be recovered even after 2 regeneration cycles. Wang et. al studied the feasibility of regenerated Cu(I)Y and found that it exhibited similar desulfurization performance as that of fresh Cu(I)Y after 300 ppmw of DBT adsorption in the presence of 20 wt% benzene.[226] However, the regeneration conditions were much longer than those reported in our study (e.g. 10 hours for heat treatment and 18 hours for reduction). Yang and co-workers, on the other hand, investigated the regenerability of Ce(IV)-Y adsorbents for the adsorptive desulfurization of diesel feed, as well as Cu(I)-Y on γ-Al_2O_3 support for the sulfur removal of jet fuel.[148,267] They only studied two regeneration cycles, in which about 96% and 74% of the adsorption capacities were recovered for Ce(IV)-Y and Cu(I)-Y, respectively. This suggests that 2%Cu10%CesAY has a longer desulfurization lifetime and great potential for the desulfurization of commercial fuels. In our future studies we plan to demonstrate the effect of various rare earths on the adsorptive desulfurization of liquid fuels, as well as their optimum loading on the sorbent. The synergy between Ce and Cu will be further investigated using theoretical and synchrotron studies.

Chapter 7

FUNDAMENTAL UNDERSTANDING OF SULFUR ADSORPTION ON ION-EXCHANGED Y ZEOLITES USING DENSITY FUNCTIONAL THEORY AND NATURAL ORBITAL ANALYSIS

7.1 Introduction

Refractory sulfur compounds such as alkylated-dibenzothiophenes (DBT) are commonly found in heavy oils such as diesel. Upon combustion, these compounds are emitted into the atmosphere as SOx, a precursor of acid rain. Due to their low reactivity and bulky structure, extremely costly and energy-demanding processes are required to meet the stringent sulfur regulations. Currently, hydrodesulfurization (HDS) is the conventional method for converting alkylated-DBT from transportation fuels, either via hydrogenation (HYD) or direct desulfurization (DDS) to hydrogen sulfide (H_2S).[268] Regardless of the reaction pathway, both HYD and DDS reactions require extremely high energy to break the bonds of alkylated-DBT. Moreover, it has been shown that the presence of alkyl groups of DBT results in steric hindrance, causing the inhibition of C-S cleavage in the DDS pathway.[269,270] A comprehensive review on the effect of molecular size and alkyl derivatives on the relative HDS reactivity has been published by Chunshan Song.[18]

Due to cost and reactivity challenges in HDS accompanied by strict sulfur mandates, there is a growing interest in exploring ultra-deep desulfurization alternative technologies to either complement or replace the conventional HDS technology. Some of the main alternative methods have been discussed in detail by Lee et al.[20] Among them, adsorptive desulfurization (ADS) continues to be one of the most studied alternative desulfurization methods owing to their economical and environmental advantages, while simultaneously producing fuels containing little

to no sulfur at ambient conditions.[271–275] More importantly, the effectiveness of ADS relies on the key properties of the utilized sorbent. Among the commonly studied materials, Y zeolites have shown to be ideal sulfur adsorbents because they consists of interconnecting channels, cages and hexagonal prisms, resulting in unique 3-dimentional pore structures, high surface area and available acid sites. However, due to the microporous nature of Y zeolites, further structure modifications are compulsory to make the internal active sites readily available for the adsorption of alkyl-DBTs. In addition, sulfur selectivity is another limiting factor of ADS in the presence of structurally similar aromatic compounds, such as naphthalene. Our previous studies showed that the introduction of well-ordered mesoporosity using the surfactant-assisted method was extremely beneficial in overcoming diffusion limitations involving refractory sulfur compounds.[63,207] We also investigated the synergistic effects of Cu and Ce on the selective removal of 4,6-dimethyldibenzothiophene (4,6-DMDBT) using spectroscopy, which suggested strong binding energy and multiple adsorption configurations between the metals and the sulfur compound.[253]

Two main types of adsorption mechanism have been proposed in the literature. Yang et al. displayed the excellent sulfur capacity of CuY compared with AgY, NiY and ZnY, which they attributed to relatively strong π-complexation bonds.[23,139] The parallel stacking of the sulfur ring above the metal allows for electron transfer from the *p* orbital of the sulfur ring to the empty *s* orbital of the Cu, commonly known as σ-bonding, as well as the simultaneous backdonation of electrons from the filled *d* orbitals of the metal to the antibonding *p** orbital of the sulfur ring. For π-complexation sorbents such as those studied by Yang et al., *d*-π* backdonations play an important role in defining the adsorption strengths of π-complexation. On the other hand, Song and co-workers indicated that f-block elements such as Ce in CeY zeolites have high affinity to bind with sulfur via a direct sulfur-metal (S-M) bond rather than π-complexation.[140] They

explained that this type of interaction is highly advantageous for selective removal of sulfur from commercial fuels containing competing aromatics. Since the publication of these pioneering studies by both groups, there has been substantial effort in the adsorption/separations community to investigate the adsorption capacity of sulfur over different metals or metal combinations such as FeY, LaY, ZnY, CuZnY, ZnNdY, NiNdY, CuCeY, CuLaY, NiCeY and AgCeY.[67,123,138,153,156,171,210,271]

Over the past decades, most studies on sulfur removal from transportation fuels using modified Y zeolites have been conducted in a fixed-bed adsorption unit, in which breakthrough curves are generated to determine the sulfur adsorption capacity.[64,67,140] In terms of overcoming mass transfer limitations, a good agreement has been well documented between well-ordered mesoporosity and enhanced capacity of alkyl-DBTs.[20] However, minimal attempts have been made to fundamentally elucidate the role of metal cations on the selectivity and capacity of different thiophenic compounds. While empirical evidence provides useful insight regarding the role of metals on the adsorption performance, information about electronic properties, binding energies and adsorption configurations have been lacking. Meanwhile, theoretical study using density functional theory (DFT) is an efficient tool to make accurate predictions about the molecular energetics and coordination modes of ligand-metal interactions.[276]

In the past, theoretical methods have been successfully applied to predict molecular energetics and adsorption trends of smaller molecules[277–279] including elemental sulfur compounds such as SO_2, H_2S and CS_2.[280–282] Yang et al. were one of the first groups to study the adsorption behavior of thiophene (on CuCl and AgCl) using molecular orbital calculations, which showed a good correlation between calculated binding energies and observed adsorption capacities. By using natural bond orbital (NBO) analysis, they were able to inspect electron distribution more closely,

which led to the fundamental understanding of π-complexation interactions. Nonetheless, the chloride is a much smaller anion compared with the zeolite framework, therefore resulting in very different electron redistribution when coordinated with a metal cation.[283,284] They later demonstrated with CuZ cluster (Z = 2T; T = Al, Si) that the zeolite anion is more electronegative than chloride, thus increasing the electropositivity of Cu^+ to accept more electrons from sulfur.[285] Around the same time, Velu et al. attempted to establish a correlation between observed sulfur selectivity over σ-type adsorbents (e.g. CeY) with electron density on the sulfur atom obtained using molecular orbital calculations.[140] Several years later, Liu et al. used DFT to show the adsorption mechanism of benzothiophene (BT), dibenzothiophene (DBT) and alkyl-DBT on 6T CuY zeolite cluster, which could proceed either via η^2 (π-complexation) or η^1S (direct S-M σ) adsorption modes.[286] To explain the possible adsorption pathways of BT and DBT over CuY, NiY and CeY, Wang et al. carried out DFT calculations using a 12T zeolite cluster.[287] Information about bond lengths, Mayer bond orders and adsorption energies was used to draw conclusions on the most energetically-favored adsorption mechanism and configuration for the respective clusters. A similar 12T cluster consisting of a six-membered ring was used by Gao et al. to theoretically calculate the bond distances, adsorption energies and Mulliken charge population related to the adsorption of TP, BT and DBT on rare-earth exchanged Y zeolites.[224] Their results indicated that the thiophenic compounds adsorb preferably via the lying configuration (π-complexation).

Due to the complex structure of the Y zeolite framework, most theoretical studies were conducted using an extremely small model cluster, consisting of a six-membered ring, the center of which represents the adsorption site. While this has shown to provide some insight regarding sulfur adsorption, the Y zeolite unit cell also contains a supercage, sodalide cages and hexagonal prisms made up of tetrahedral molecules that can interact with sulfur adsorbate via van der Waals

(vdW) interactions and in some cases, long-range electrostatic interactions.[100,288] The vdW interactions especially can strongly affect the binding energies and adsorption modes, thus must not be neglected. Herein, our group has proposed a construction of a bigger cluster to better represent true environment inside the Y zeolite unit cell and to properly account for all types of interactions. A two-layer our-own *n*-layered integrated molecular orbital and molecular mechanics (ONIOM) model was employed, where the small high-level-theory layer consists of the chemically important part (e.g. the adsorption site) of the zeolite and the low-level-theory layer encompasses the rest of the outer framework. This strategy has been used effectively to compute the binding energies of relatively small linear and aromatic molecules adsorbed on Y zeolites[98,289–291], but to the best of knowledge, there are no reports of the ONIOM method used to study the adsorption of thiophenic compounds over ion-exchanged Y zeolites. In this study, we performed the two-layer ONIOM study on the adsorption of TP, BT, DBT and 4,6-DMDBT over HY and CuY. For comparison, the adsorptions of benzene and naphthalene were also explored. Natural bond orbital (NBO) analysis was also carried out to relate electron transfer to the adsorption modes. Information gathered from DFT calculations and NBO analysis were then used to explain and validate the adsorption behavior in experiments from our previous work.

7.2 Computational Methods

7.2.1 Cluster structure model

Faujasite (FAU) crystal structure obtained from the International Zeolite Association (IZA) database was used to build the Y zeolite cluster (Figure 7.1(a)).[82] It is essential that the right cluster size is used for the calculation, which means that key zeolite structural features such as the supercage, sodalite cage, hexagonal prism and extra-framework coordination sites should be

included. To build a reasonably-sized cluster, an active site is first created by replacing a Si atom with an Al atom, resulting in a minus one charge, which can be compensated by a proton to form a Brønsted acid site, or a metal cation, on which adsorption or reactions can potentially occur. Because Y zeolites contain different extra-framework coordination sites (e.g. sites I, I', II, and II'), it is important to select one that is both experimentally- and theoretically-feasible to represent the adsorption site. Based on Rietveld refinement, CO adsorption by FTIR[160,292] and Monte Carlo simulation[224,287], the most appropriate site to study is site II, which is located on the surface of the six-membered hexagonal window, coordinated by three framework oxygen atoms. While studies have shown that other sites may be well-populated with extra-framework cations and more energetically favorable, they are not as accessible compared with site II, especially for refractory sulfur compounds. After all, this location has been shown to be the most active for various catalytic reactions and adsorption processes.[72,266,293] The full zeolite cluster was then completed by adding six consecutive tetrahedral coordination spheres to the Al atom, and dangling Si-O bonds were saturated with H atoms with a fixed S-H bond length of 1.47 Å. Figures 6.1 shows the resulting ONIOM model, represented by a 172T zeolite cluster with clear features of the supercage and sodalite cages. The ball-and-bond atoms represent the high-level-theory layer, consisting of 63 T atoms and a cation, which means all the atoms up to the fourth tetrahedral coordination sphere. The low-level theory layer, also known as the real layer, is displayed with a wireframe, which includes the fifth and sixth tetrahedral coordination spheres. As will be discussed below, even though the two layers were treated with different levels of theory, their significance on binding strengths cannot be overlooked.

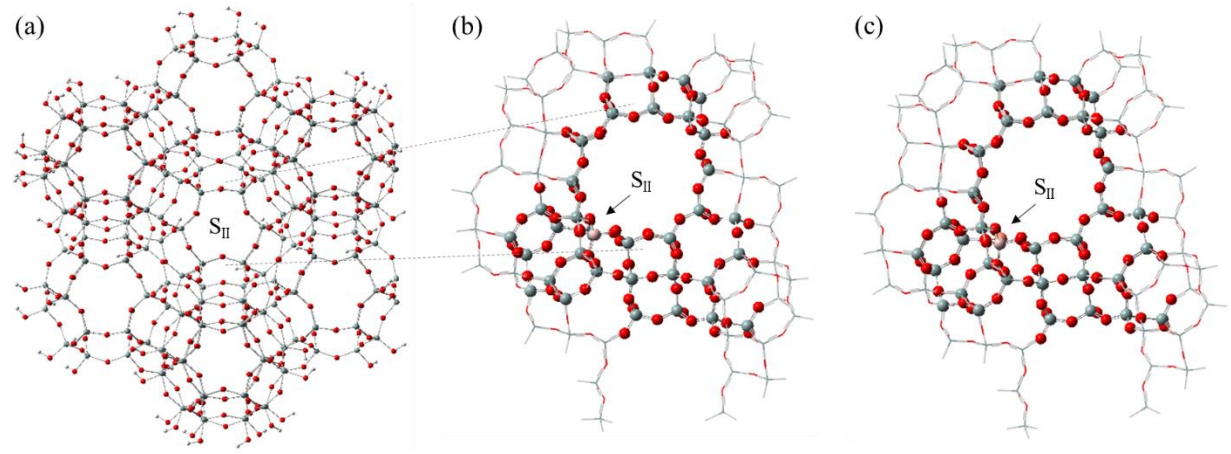

Figure 7.3: (a) A 240T FAU crystal structure obtained from IZA[82]. Optimized 172T ONIOM cluster models of (b) HY and (c) CuY. The high-theory QM layer is portrayed by the ball-and-bond representation. The low-theory MM layer is shown as wireframe. S_{II} represents Site II.

7.2.2 Theory levels

All DFT calculations were performed with the Gaussian 16 software[97], during which the two-layer ONIOM method was applied. The total ONIOM enthalpy (or total energy) of the system is given by:

$$H_{ONIOM} = H_{MM}^{all} + H_{QM}^{active} - H_{MM}^{active} \qquad \text{Equation 7.1}$$

where H_{MM}^{all} is the enthalpy of the entire system, which can be treated with less expensive (MM) molecular mechanics level. $H_{QM}^{active}$is the enthalpy of the active site, for which a high-level quantum mechanics (QM) approach is used. For the high level QM layer, the Becke three-parameter exchange functional[294] and Lee-Yang Parr correlation functional (B3LYP)[96] was used. The low level MM region was treated by molecular mechanics universal force fields (UFF)[295] to capture vdW forces and electrostatic interactions. The 6-31G(*d*,*p*) basis set was used for all atoms including reactants. Prior to structure optimization, the QM layer including the adsorbates was allowed to relax, while the MM layer was frozen to preserve the integrity of the zeolite framework. Vibrational frequencies were calculated and the resulting thermal corrections were applied to

single-point energy calculation to obtain the binding enthalpies, calculated by the following equation:

$$\Delta H_{ads} = H_{complex} - (H_{zeolite} + H_{sulfur}) \quad \text{Equation 7.2}$$

where $H_{complex}$ is the total energy of the sulfur adsorbed on the cluster, $H_{zeolite}$ is the energy of the optimized zeolite cluster and H_{sulfur} is the energy of the free thiophenic molecule.

NBO analysis was performed only on the QM layer using NBO 7.0[296] with the same functional and basis set as the DFT calculations. Second order perturbation theory was used to estimate the energetic significance between donor-acceptor orbitals. Molecular orbitals with the highest stabilization energy, E(2) were analyzed more closely to obtain the total charges (or electron occupancy) on the sulfur adsorbate and zeolite cluster to further explain the adsorption energies and configurations determined by DFT and adsorption capacities observed in experiments..

7.3 Rietveld Refinement

Rietveld refinement was performed on x-ray diffraction (XRD) zeolite pattern using the Generalized Structure Analysis System 2 (GSAS-II) software to determine the location of cations in the zeolite.[84] LeBail fitting was first performed to determine the best possible fir to the data. Then, the starting atomic coordinates, unit cell size and isotropic parameters of CuY were obtained elsewhere.[72,164] The initial fractional occupancy of each element was obtained by chemical analysis. The space group was set to $Fd\bar{3}m$ and restraints were imposed on Si-O and Al-O bond distances, as specified in Section 2.3.2. After parameters such as scale factor, background, unit cell, atomic position, isotropic factor, peak shape and peak width, a Fourier difference map calculation was conducted to determine the missing Cu cations.

7.4 Results

7.4.1 Location of extra-framework Cu cations

Figure 7.2 shows the observed and calculated patterns of CuY, as well their difference. The resulting residuals are as follow: R_{wp} = 13.431% and χ^2= 2.04, confirming the quality of fit. Table 1 shows the final atomic parameters of fully refined CuY. The metal loading of Cu is consistent with that determined by chemical analysis, which is approximately 5 wt%. Three Cu positions were identified: Sites I' (0.05238, 0.05238, 0.05238), II' (0.08910, 0.08910, 0.08910) and II (0.05238, 0.05238, 0.05238), ordered in increasing concentration. It has been shown that Cu cations are driven to site I' by heat treatment, but some remain in sites II and II'.[266,297,298]

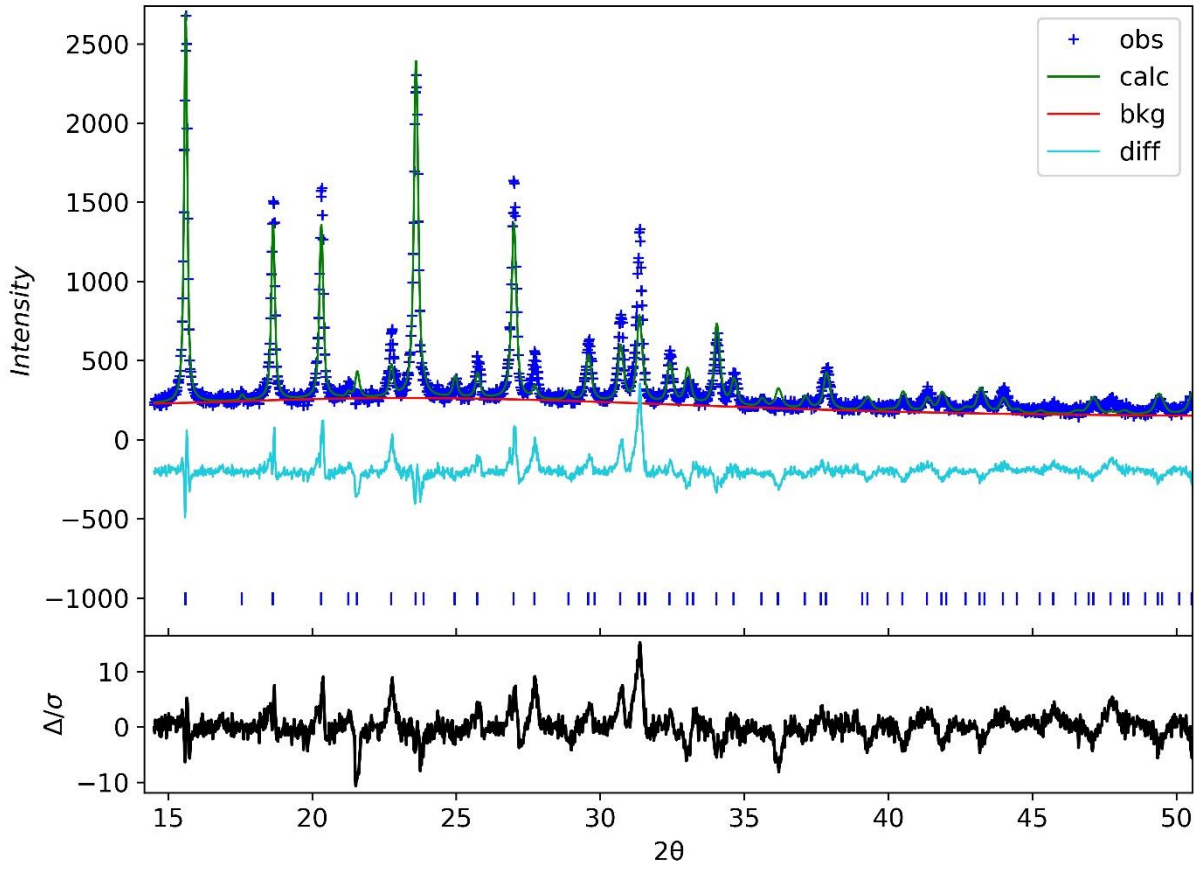

Figure 7.2: Observed, calculated and difference profiles and reflection positions of CuY.

Table 7.1: Atomic parameters from Rietveld refinement of CuY

atom	x	y	z	frac	site	u_{iso}
Si	0.04129	-0.0026	0.06714	0.6667	192i	0.00000
Al	0.04129	0.30320	0.12579	0.3333	192i	0.00000
O1	0.00000	0.90055	0.09945	1.0000	96h	0.00000
O2	0.00528	0.86540	0.00528	1.0000	96g	0.00000
O3	0.06714	-0.02612	0.06714	1.0000	96g	0.00000
O4	0.07824	0.31242	0.07824	1.0000	96g	0.00000
Cu(II)	0.26295	0.26295	0.26295	0.1500	32e	0.00000
Cu(II')	0.08910	0.08910	0.08910	0.2380	32e	0.00000
Cu(I')	0.05238	0.05238	0.05238	0.3050	32e	0.00000

7.4.2 Adsorption energies and configurations of thiophenic compounds on zeolite clusters

Several starting configurations were applied to the thiophenic compounds and the most energetically-stable optimized adsorption configuration over HY and CuY zeolite clusters are reported in Tables 7.2 and 7.3, respectively, along with their corresponding adsorption enthalpies. It is evident from Table 7.2 that the optimized thiophenic molecules have energetically converged to a position far away from the Brønsted acid site of HY cluster. Regardless of the different starting configurations, all sulfur compounds could be seen drifting away from the active area towards the wall of the supercage, eventually conforming to a random orientation. This phenomena suggest that the interaction between sulfur and the surrounding zeolite framework is more energetically-favored via vdW interactions compared with hydrogen bonding with the proton. Table 7.2 also shows that the adsorption enthalpies of the sulfur compounds on HY increase in the order of T > BT > DBT > 4,6-DMDBT, which suggests a correlation between the adsorption capability and the number of benzene rings.

A different adsorption configuration was observed when H was replaced by Cu, as seen in Table 7.3. For adsorption systems involving the CuY cluster, the optimized geometry shows that all sulfur compounds exhibit lying configurations on top of the Cu cation. This suggests that the

adsorption of sulfur on the active site is more energetically-preferred than it is on the surrounding zeolite well, as seen for HY. As a result, a significant increase in binding strength was observed for all sulfur compounds. The lying configuration suggests that sulfur adsorbs on Cu via π-complexation, as suggested by experiments.[207] The π-complexation bond has been shown to be significantly stronger than vdW forces, thus enhancing the adsorption capacity of sulfur on CuY.[299] However, the adsorption enthalpies of sulfur on CuY exhibit different trends compared with those of HY. The adsorption enthalpy increases from TP to BT, but decreases from -151.9 to -142.9 kJ/mol for DBT. The adsorption of 4,6-DMDBT yields a similar ΔH_{ads} as DBT. This slight decrease in adsorption enthalpy for refractory sulfur compounds could be due to steric hindrance, whereby imposing orientational restraints that prevent the most favorable adsorption configuration on Cu. Another reason for this ambiguity is that there could other interactions between Cu and thiophenic molecules that were not fully captured by our two-layer ONIOM cluster. Nevertheless, the role of π-complexation on increased adsorption energy is the main takeaway, and therefore was further studied using NBO analysis.

Table 7.2: Adsorption configurations and enthalpies of sulfur compounds on HY cluster.

Cluster	Sulfur	Side View	Top View	ΔH_{ads} (kJ/mol)
HY	TP	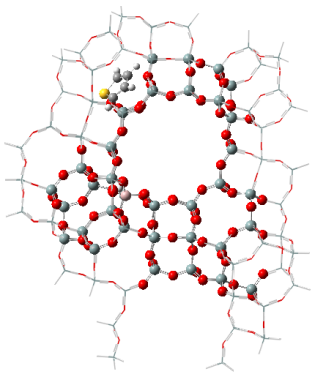	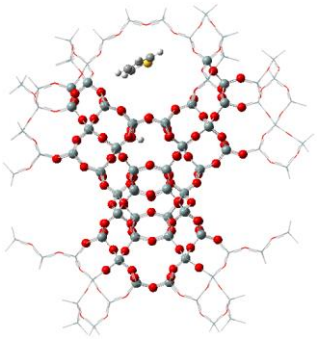	-50.8
	BT	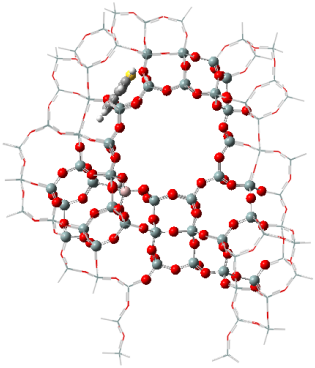	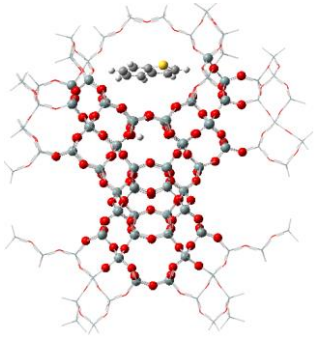	-64.1
	DBT	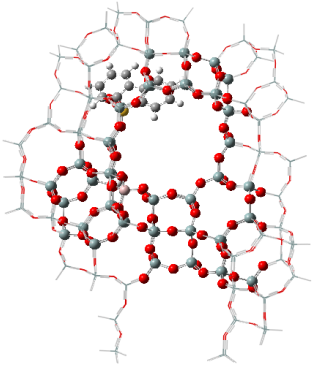	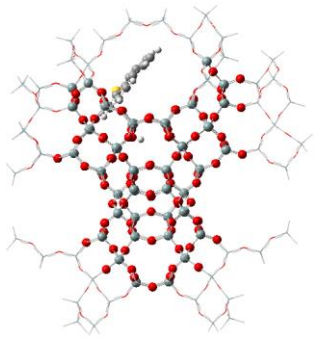	-79.3
	4,6-DMDBT	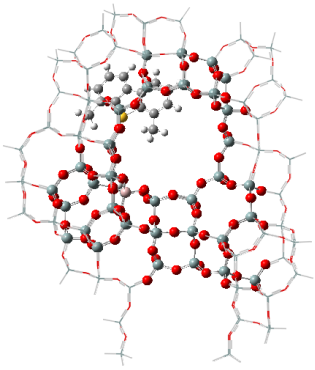	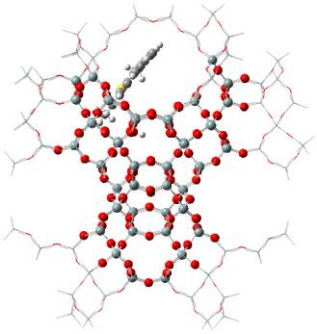	-91.1

Table 7.3: Adsorption configurations and enthalpies of sulfur compounds on CuY cluster.

Cluster	Sulfur	Side View	Top View	ΔH_{ads} (kJ/mol)
CuY	TP	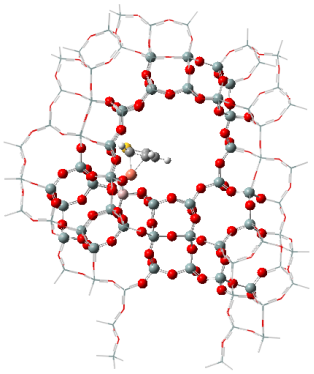	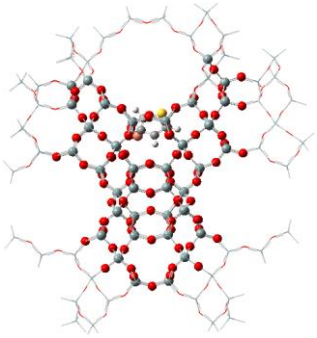	-139.9
	BT	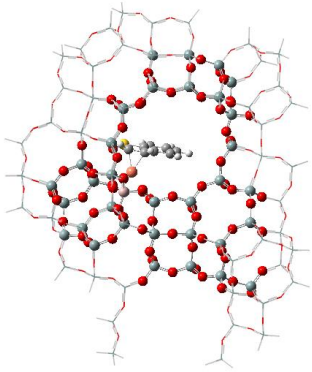	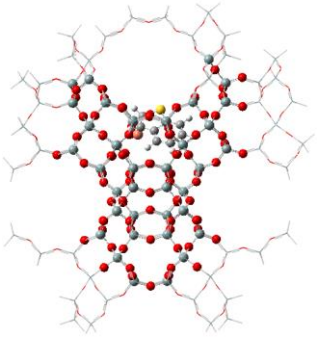	-151.9
	DBT	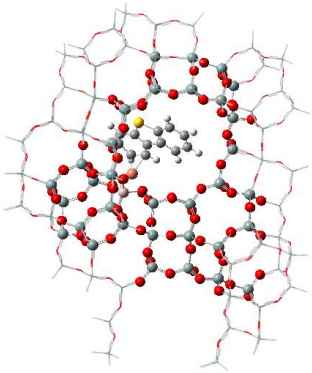	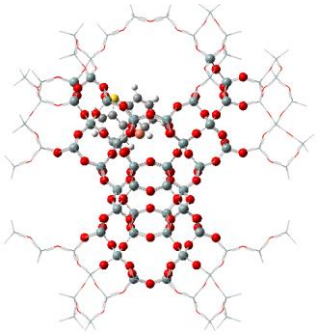	-142.9
	4,6-DMDBT	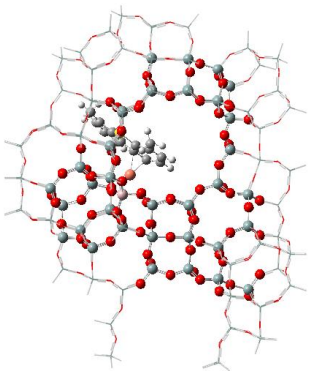	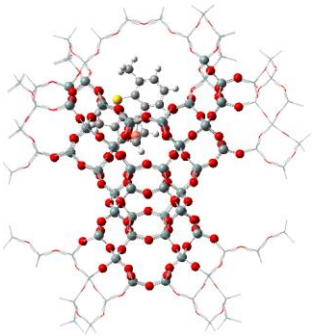	-142.7

Table 7.4: Adsorption configurations and enthalpies of aromatics on CuY and HY clusters.

Cluster	Sulfur	Side View	Top View	ΔH_{ads} (kJ/mol)
HY	Benzene	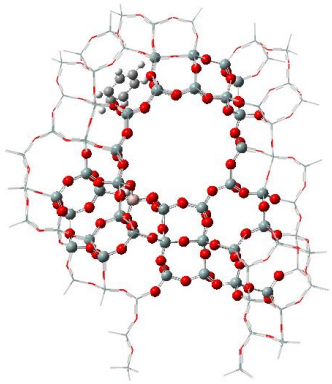	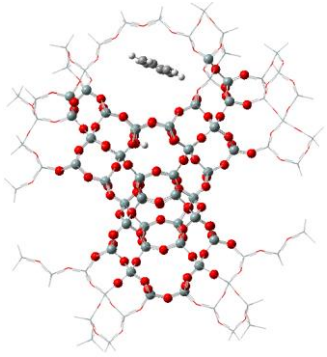	-55.7
	Naphthalene	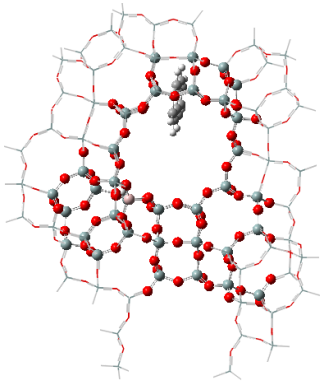	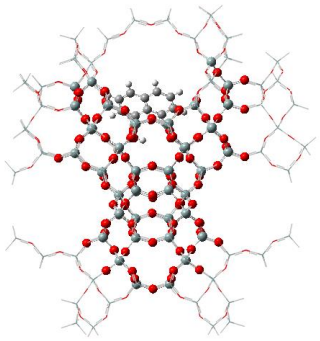	-65.2
CuY	Benzene	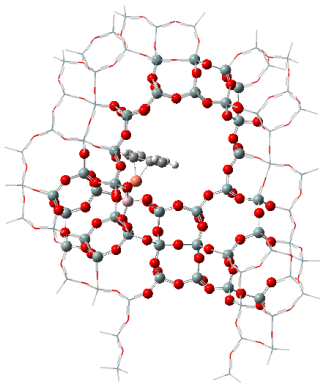	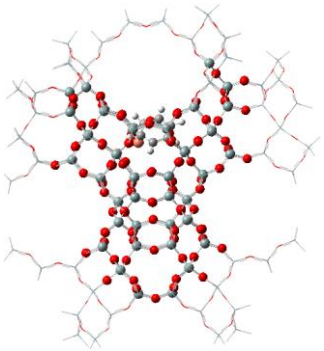	-124.7
	Naphthalene	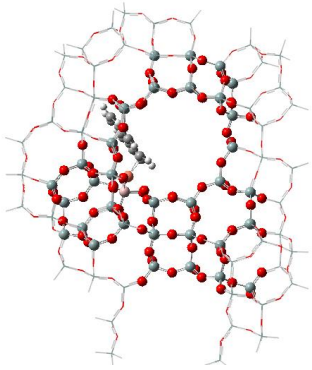	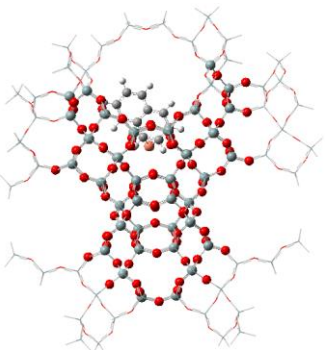	-142.6

To compare the selectivity of sulfur with aromatics commonly found in transportation fuels, enthalpy calculations were also performed on the adsorptions of benzene and naphthalene on HY and CuY. Table 7.4 shows that benzene and naphthalene adsorb on HY via similar configurations as those by the sulfur compounds, during which the aromatic compounds prefer to interact directly with the wall of the zeolite supercage rather than the Brønsted acid site. The corresponding adsorption enthalpies are -55.7 kJ/mol and -65.2 kJ/mol, respectively, which are similar, if not slightly higher than those of TP and BT. This suggests that the HY is not very selective for sulfur compounds in the presence of aromatics, which explains the loss in adsorption capacity on HY in our experimental work.[63] Table 7.4 also shows the optimized structure of aromatic-CuY complexes and the corresponding adsorption enthalpies. On CuY, the adsorption enthalpies suggest strong binding of aromatics on CuY than on HY. This observation is similar to the adsorption of sulfur compounds as the coordination with the Cu cation is more energetically-favored compared with the proton or the zeolite framework in HY. Moreover, the enthalpies of the corresponding aromatics are less than that of sulfur compounds, suggesting that Cu plays a better role in selective adsorption of sulfur in transportation fuels compared with HY.

7.4.3 NBO analysis

NBO analysis was carried out on the high-theory QM layer after optimization and frequency calculations by DFT. Table 7.5 shows only molecular orbitals of the TP-CuY, BT-CuY, DBT-CuY and 4,6-DMDBT-CuY complexes with relatively high E(2) values, and the corresponding donor NBOs and accepter NBOs using the localized Lewis structure representation (e.g. one-center nonbonding electron pairs and two-center bonding electron pairs). For clarity, only the sulfur adsorbate and Cu are shown to prevent convolution of atoms. In the TP-CuY system, interactions involving C251 and C252 atoms are most significant, especially for LP(Cu250) →

π*(C251-C252) with an E(2) value of 53.86 kcal/mol. This suggests that a substantial amount of electron is transferred from the valence *d* orbitals of Cu^+ ($1s^2 2s^2 2p^6 3s^2 3p^6 3d^{10}$) to the antibonding *p** orbitals of TP. Reversely, a significant amount of electron transfer with an E(2) of 48.86 kcal/mol is detected for π(C251-C252) → LP*(Cu250), which suggests a σ-donation of electrons from the *p* orbitals of TP to the empty 4*s* orbital of Cu^+. Other interactions with relatively intense energy are also displayed, including various C=C interactions, which are attributed to the delocalization of the conjugated ring of TP. The BT-CuY complex shows a similar trend to that of TP-CuY in terms of energetic importance. The highest E(2) value was displayed by LP(Cu250) → π*(C257-C258), suggesting a backdonation of electrons from the *d* orbitals of Cu^+ to the *p** orbitals of TP, in particular the C257-C258 double bonds. This makes sense as the cartoon in Table 6.4 shows that Cu250 interacts strongly with C257-C258. For the complexes of DBT-CuY and 4,6-DMDBT-CuY, the optimized configuration shows that the adsorption occurs via the benzene ring, rather than the thiophenic ring. Nevertheless, the interaction between Cu and the closest C=C bonds exhibit the highest E(2). For the sake of brevity, only interactions higher than 5 kcal/mol are reported for these large molecules.

Energetic contributions between the molecular orbitals of aromatics and CuY were also examined and results are shown in Table 7.6. The highest E(2) value is approximately 25 kcal/mol, which is lower than those of sulfur-metal complexes. Similar to the previous study with sulfur compounds, the highest E(2) values are observed on Cu and the closest C=C bonds, confirming a strong interaction between the two groups via π-complexation. Additionally, interactions of C=C bonds within the benzene rings also yielded relatively high E(2) values, suggesting delocalization of electron density within the π orbitals of the aromatic ring.

Table 7.5: Second-order perturbation theory analysis of various sulfur-metal complexes.

Complex	Donor NBO	Acceptor NBO	E(2) (kcal/mol)
TP-CuY 	LP(Cu250)	π*(C251-C252)	53.86
	π(C251-C252)	LP*(Cu250)	48.86
	LP(S255)	LP*(Cu250)	10.68
	π(C251-C252)	π*(C253-C254)	9.18
	π(C253-C254)	π*(C251-C252)	15.25
	LP(S255)	π*(C251-C252)	19.38
	LP(S255)	π*(C253-C254)	21.25
	π*(C251-C252)	π*(C253-C254)	31.84
BT-CuY 	LP(Cu250)	π*(C257-C258)	54.71
	π(C257-C258)	LP*(Cu250)	50.96
	π(C257-S265)	LP*(Cu250)	5.78
	LP(S265)	LP*(Cu250)	10.51
	π(C251-S265)	LP(C252)	8.97
	π(C251-S265)	LP(C256)	7.94
	π(C251-S265)	π*(C257-C258)	12.50
	π(C257-S268)	LP(C252)	14.66
	π*(C251-C265)	π*(C257-C258)	11.35
DBT-CuY 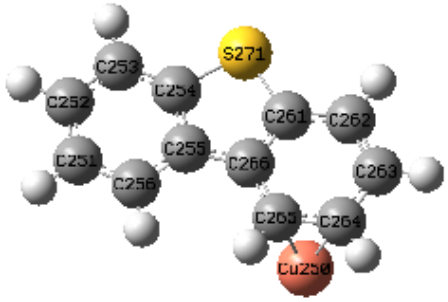	σ(Cu250-C264)	LP*(Cu250)	11.35
	π(C261-S271)	LP(C254)	25.39
	π(C261-S271)	LP*(C262)	8.37
	π(C261-S271)	LP(C266)	9.41
	π(C264-C265)	LP*(Cu250)	7.46
	LP(C254)	π*(C261-S271)	30.3
	LP(C265)	LP*(Cu250)	28.42
	LP(266)	LP*(C256)	12.80
	σ*(Cu250-C264)	LP*(Cu250)	30.14
4,6-DMDBT-CuY 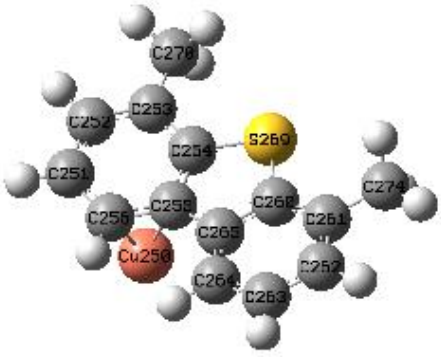	LP(Cu250)	LP(C255)	36.58
	LP(Cu250)	LP(C256)	38.72
	π(C254-C255)	LP*(Cu250)	5.01
	π(C255-C256)	LP*(Cu250)	6.68
	π(C255-C256)	LP*(Cu250)	6.16
	LP(C255)	LP*(Cu250)	11.59
	LP(C256)	LP*(Cu250)	20.99
	π(C252-C253)	π*(C254-S269)	5.00
	π(C254-C255)	π*(C253-C254)	5.00
	π(C260-S269)	LP(C254)	28.92
	π(C260-S269)	LP*(C261)	7.41
	π(C260-S269)	LP(C265)	8.29
	LP(C254)	π*(C260-S269)	16.70
	LP(C264)	π*(C260-S269)	5.77

Table 7.6: Second-order perturbation theory analysis of various aromatics-metal complexes.

Complex	Donor NBO	Acceptor NBO	E(2) (kcal/mol)
Benzene-CuY 	π(Cu250-C252) π(C252-C253) π(C251-C252) LP(C253) π*(Cu250-C252)	LP*(C251) LP*(Cu250) π*(Cu250-C252) LP*(Cu250) LP*(Cu250)	10.67 6.77 7.50 25.73 27.05
Naphthalene-CuY 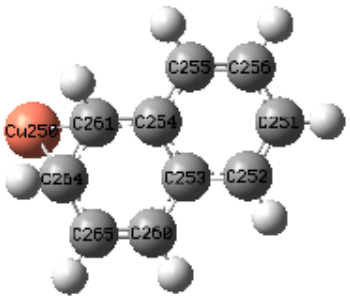	π(C250-C264) π(C254-C261) π(C261-C264) π(C261-C264) π(Cu250-C264)	LP(Cu265) LP*(Cu250) LP*(Cu250) π*(Cu250-C264) LP*(Cu250)	10.09 7.16 8.48 6.89 25.93

The most important donor-acceptor interactions with relatively high E(2) values were further investigated for electron occupancies and charge transfer from population analysis of natural atomic orbital (NAO). Table 7.7 shows the electron occupancy of the Cu cation and the C=C bonds of various sulfur compounds with which it is interacting. In this study, we report only electron occupancies of the Cu outer-shell orbitals to represent the electron transfer to and from the bound C=C bonds. Table 7.7 shows that the change in occupancy (ΔOc) of the 4*s* orbital of Cu increases upon adsorption, while a loss of electron occupancy was observed in the 3*d* orbitals. It should be noted that the 3*d* orbitals consists of $3d_{xy}$, $3d_{xz}$, $3d_{yz}$, $3d_{xy}$, $3d_{x2y2}$, and $3d_{z2}$ atomic orbitals, and the total electron occupancy, $\sum 3d$ is reported in Table 7.7. As suggested by the second-order perturbation theory, a strong overlap between the valence orbitals or Cu and C=C bond of TP allows for σ-donation from the π-bonds to the empty 4s orbital of Cu^+, and a simultaneous backdonation of electrons from the 4*d* orbitals of Cu^+ to the antibonding π^*-bonds of the sulfur

adsorbate. The sum of occupancies in both orbitals is negative, which indicates a higher contribution by the electron backdonation from Cu^+ to the sulfur ring. The two-way electron transfer between Cu and TP confirms that the sulfur compound adsorbs on the adsorption site via π-complexation. For BT-CuY complex, the change in occupancy in both 4*s* and 3*d* orbitals of Cu increases, which is consistent with the increase in the energetic significance in Table 7.5 and the adsorption energies in Table 7.3. This has also been shown experimentally, where larger sulfur compounds bind more strongly on π-adsorbents.[300] Contrary to BT-CuY, the adsorption of DBT on CuY showed that the change in occupancy in the 4*s* orbital is no longer positive, indicating a loss of electron density. The cartoon on the left in Table 7.7 also shows that the C=C bond of the benzene ring is bound to Cu, instead of one of the two C=C bonds attached to the S atom. One possible explanation to this unexpected trend is that the π-bonds of the benzene ring may be causing a redistribution of electrons on the outer-shell orbitals of Cu.[162,286] This may also explain the slight decrease in adsorption enthalpy of DBT on CuY. Nonetheless, the negative net change in electron occupancy suggests that the backdonation of electrons from Cu to the antibonding π* orbitals of DBT contributes significantly to the adsorption strength of the complex. The 4,6-DMDBT-CuY also shows a negative change in electron occupancy in the 4*s* orbital of Cu. The sulfur compound is seen to adsorb on Cu via one of its benzene rings, similar to the adsorption of DBT. However, the increasing change in occupancy of the 3*d* orbitals suggests that once again, the benzene rings have an effect on the electron transfer between Cu and 4,6-DMDBT. Moreover, the effect of methyl groups on the adsorption interaction must be considered and will be discussed in the following section.

Table 7.7: Valence electron density occupancies of Cu and C=C bonds of sulfur compounds.

Complex	Valence NAO occupancy		
	Atom	Orbital	ΔOc
TP-CuY 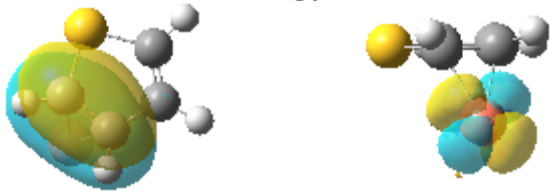	Cu250	4s Σ3d	0.0039 -0.1715
BT-CuY 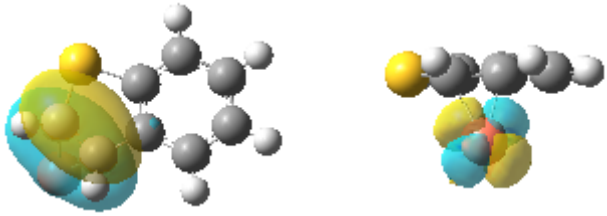	Cu250	4s Σ3d	0.0060 -0.1820
DBT-CuY 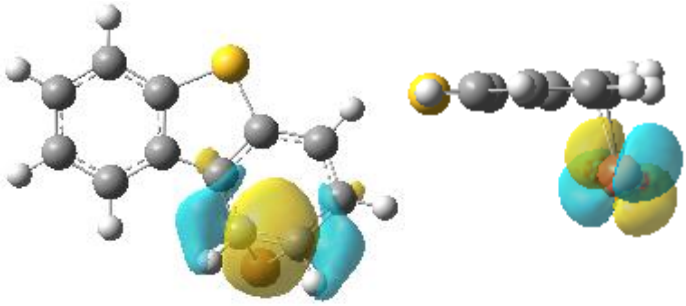	Cu250	4s Σ3d	-0.0087 -0.1398
4,6-DMDBT-CuY 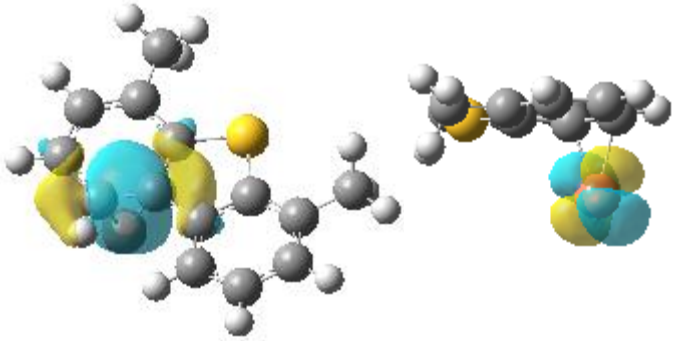	Cu250	4s Σ3d	-0.0374 -0.0929

7.5 Discussion

Because of the advancement in quantum mechanical methodologies and supercomputers, theoretical researchers have the capability and resources to run DFT calculations on bigger and more sophisticated systems such as the zeolite. In this study, a two-layer ONIOM cluster was built to simulate the adsorption site of an ion-exchanged Y zeolite, located at site II. Although sites I' and II' have shown to occupy more cations, they are inaccessible for sulfur compounds. The resulting model is a 172T zeolite cluster divided into two layers with different theoretical treatment, also known as the QM/MM method. The well-known B3LYP functional was used to represent the effects of exchange and correlation as it is computationally less expensive to run and is reliable for most interactions involving covalent bonds.[285] The 6-31G(*d,p*) basis set was used to describe the sulfur and zeolite atoms. The DFT results show that sulfur adsorbs differently on HY and CuY as indicated in Table 7.2 and 7.3. Contrary to the general consensus that Brønsted acid sites contribute to the adsorption of thiophenic molecules[142,154,301], the sulfur compounds are most stable when interacting with the zeolite framework of the supercage via vdW interactions. An increasing trend in adsorption energy is realized in the order of TP < BT < DBT < 4,6-DMDBT on HY. As the sulfur compounds get larger, a bigger surface of atoms is interacting with the zeolite framework, leading to more vdW forces and stronger binding. Meanwhile, the same adsorption mode was observed for all sulfur compounds adsorbed on CuY, which is via the π-stacking of the molecule. Table 7.3 shows that the sulfur compounds adsorbed in a lying configuration, slightly tilted above the Cu cation. This is consistent with the results obtained by others.[285,287] This is also similar to the adsorption mode of aromatics on CuY as shown in Table 7.4. However, TP or BT with similar ring size as benzene and naphthalene, respectively, exhibited slightly higher binding energies than the aromatics, suggesting that sulfur compounds are adsorbed more selectively on

Cu. It is also apparent that the adsorption enthalpies do not correlate with the size of sulfur compounds adsorbed on CuY. Even though the adsorption of BT showed a higher adsorption energy than that of TP, the values decreased for DBT and 4,6-DMDBT. This is not surprising as Yang et al. have reported that the adsorption energy stopped following the increasing trend at DBT.[285] They attributed this steric hindrance of benzene rings and methyl groups on refractory sulfur compounds such as DBT and 4,6-DMDBT, which consequently decreases the adsorption enthalpy. Our group has shown experimentally that steric effects could be overcome by introducing mesoporosity, which not only grants large sulfur compounds exclusive access to the internal active sites, but also the freedom to find the most favorable adsorption configuration. The idea of incorporating pore effects in DFT calculations is an interesting topic and will be one of the objectives of our future work.

NBO analysis is a powerful tool to scientifically explain the adsorption mechanism of sorbent-sorbate systems by analyzing localized electronic contributions (instead of the delocalized molecular orbital analysis) of natural bond orbital. The energetic importance is determined by the second order perturbation theory, which examines all possible interactions between Lewis-type (filled) NBOs and non-Lewis (unfilled) NBOs. Only systems involving CuY were investigated with NBO to fundamentally understand the nature of π-type adsorption. Afterall, the optimized adsorption configuration on HY was very random and is very sensitive to a number of parameters such as initial states of sulfur compound, theory level, basis set and type of metal cation. Table 7.7 gives a summary of the NBO analysis including the most active overlapping orbitals depicted in the cartoons and the corresponding electron occupancy in the valence orbitals of Cu. These information should help us map the electron transfer between the participating orbitals and consequently draw conclusions about the type of interactions involved. For example, the overall

change in occupancy in 4*s* and 3*d* orbitals of Cu upon TP or BT adsorption shows a back-and-forth interaction, as a result of the forward σ-donation from the π-bond of the sulfur compound to the empty 4*s* orbital of Cu, and the simultaneous backdonation of electron density from the filled 3*d* orbitals of Cu to the antibonding π* orbitals of the adsorbate. Only the valence orbitals of Cu are shown as there are too many donor-acceptor NBO interactions within the conjugated C=C π-bonds as suggested in Table 7.5. Besides, electron redistribution and delocalization in the thiophenic and/or benzene rings have shown to influence the electron occupancies in valence orbitals, thus deeming the analysis of electron transfer challenging.[302,303] A correlation can be drawn between the increasing change in electron occupancy and the increasing E(2) values of LP → π* interactions from the second order perturbation analysis for TP and BT. However, the trend stops with DBT and 4,6-DMDBT, additional benzene rings and methyl groups of which play an important role on the electron delocalization between the adsorbates and Cu. Other groups have reported that while larger sulfur compounds are theoretically expected to bind more strongly due to stronger vdW forces and larger electron density on the S atom as seen for HY systems, a common trade-off is steric hindrance.[286,300,304] Therefore, we propose two possible solutions for future work: 1) the introduction of mesoporosity in the ONIOM model to better represent mesoporous Y zeolites used in experiments; and 2) the use of more powerful theory, including effective core potential for Cu and larger basis set to fully capture vdW interactions. The inhibiting effect of other heterocyclic compounds such as nitrogen-containing compounds should also be investigated using our ONIOM model as both experiments and DFT have shown that nitrogen is more strongly adsorbed than sulfur on π-type such as CuY.[18,305,306] Recently, we built ONIOM clusters of CeY and CuCeY, which have shown to adsorb sulfur more selectively especially in the presence of aromatics.[63,253] The results of these calculations will be discussed in the future.

7.6 Conclusions

A two-layer ONIOM cluster was used to study the adsorption mechanisms and energies of TP, BT, DBT and 4,6-DMDBT from transportation fuels on HY and CuY. The adsorption of sulfur on HY takes place far away from the adsorption site, close to the skeletal structure of the zeolite supercage mainly via vdW interactions. When compared with aromatics, sulfur compounds were adsorbed less strongly on HY, indicating that HY is a poor sorbent for desulfurization. A substantial increase in binding energy was observed for all sulfur compounds adsorbed on CuY. Moreover, the adsorption strength was stronger than those of aromatics, suggesting better selectivity of sulfur. Second order perturbation theory and NBO analysis indicate a significant amount of electron transfer between the outer-shell orbitals of Cu and sulfur, specifically the C=C bond. The semi-tilted lying configuration of sulfur compounds on top of Cu allows the NBO orbitals of two component to overlap, consequently causing the delocalization and sharing of electrons between the two moieties. These key features confirm that the interaction between Cu and sulfur is via π-complexation, agreeing with the relatively high adsorption enthalpies and remarkable adsorption capacity of CuY. Steric hindrance due to benzene rings and alkyl groups have shown to slightly suppress the adsorption strength of DBT and 4,6-DMDBT on CuY. Nonetheless, the adsorption energies agree well with the stabilization energies and change in occupancy, which confirms that NBO is very useful for fundamental studies of adsorption and catalysis. Our future objective is to use these advanced theoretical tools to screen other types of transition metals and lanthanides for the development of highly selective sulfur adsorbents.

Chapter 8

CONCLUSIONS

The ultimate goal of this thesis was to develop an environmental-friendly and cost-effective deep desulfurization alternative for sulfur removal from transportation fuels, to meet stringent sulfur standards regulated by the EPA. From this PhD work, adsorptive desulfurization (ADS) using metal-exchanged mesoporous Y zeolites has shown promise as a potential standalone or complementary deep desulfurization technology to conventional HDS. Chapter 4 focused on the use of novel and systematic techniques to introduce well-ordered mesoporosity and active metals to enhance the sulfur capacity and selectivity. The desulfurization performance of thiophene (TP) and benzothiophene (BT) was improved by the addition of Cu and Ce due strong interactions of π-complexation and direct S-M σ-bonding, respectively. For refractory sulfur compounds such as dibenzothiophere (DBT), access to the internal active site is limited by the relatively large kinetic diameter. Diffusion limitation of DBT was overcome by the introduction of mesoporosity, which shortens the diffusion length to the active sites, and consequently increasing the sulfur capacity. Adsorption strength was investigated using isosteric heat of adsorption calculations, which showed a correlation with the breakthrough curves determined from the adsorption experiment.

Commercial fuels such as gasoline and diesel contain a considerable amount of aromatic hydrocarbons, which were not considered in the previously. Chapter 5 investigated the effect of aromatics on the selectivity of previously studied sulfur compounds. Benzene, commonly found in gasoline, or naphthalene, in diesel, was added to the model fuel containing BT or DBT, respectively. Adsorption experiments were carried out to determine the ability of each zeolite to desulfurize the aforementioned sulfur compounds in the presence of aromatics. It was shown that bimetallic (CuCe) Y zeolites were very effective due to the synergistic effects of Cu and Ce. The

adsorption mechanisms of sulfur on these metals were further studied, at the molecular level, using DRIFTS-FTIR under vacuum conditions. From the shifts in IR bands upon adsorption, it was observed that sulfur adsorbs on Cu and Ce via π-complexation. The blue shifts in CeY and CuCeY indicated that sulfur also adsorbs on Ce through the direct S-M σ-bond, consistent with the results from Chapter 4. Finally, TPR-IR results showed that very high temperature was required to desorb sulfur from CuCeY and to regenerate the zeolite, suggesting the synergistic advantage of bimetals on selective sulfur adsorption.

Despite the promising breakthrough of ADS technology, numerous efforts have still been made to further advance conventional HDS. To date, HDS is adequate for removing various types and sizes of sulfur compounds in commercial fuels, except alkyl-DBTs. The presence of alkyl groups causes steric hindrance, consequently leading to low HYD and DDS activities. Chapter 6 aimed to further advance bimetallic mesoporous Y zeolites for the adsorptive removal of 4,6-DMDBT in the presence of naphthalene. This study revealed that metal composition and configuration can be controlled to obtain the most optimum sorbent for sulfur removal. As a result, 2%Cu10%CeSAY displayed the highest 4,6-DMDBT capacity with promising regeneration capabilities. This proved that the synergy between two different metals plays an important on the increase of sulfur selectivity and capacity of a sorbent, and therefore should be investigated at the theoretical level.

Finally, Chapter 7 explored the use of high-level computing and theory from first principles to fundamentally explain the adsorption mechanism and binding energy of sulfur on modified zeolites. Using the cationic position determined by Rietveld refinement, a two-layer ONIOM model was used to represent the complex structure of a Y zeolite, wherein the active adsorption site was treated with expensive high-level theory, while the surrounding skeletal framework was

modeled by a low-level semi-empirical method. The resulting cluster was subjected to a QM/MM DFT calculation, from which optimized adsorption configurations and binding enthalpies were obtained. Next, NBO analysis was used to demonstrate electron transfer between the most energetically-significant natural bond orbitals of the sorbent-sorbate complex. It was found that the electron occupancy or charge transfer is highly correlated to the binding energy, which is also an accurate descriptor of the sulfur adsorption capacity from fixed-bed adsorption experiments. This suggests that DFT is a very effective computational tool to screen for other active metals with high sulfur capacity and selectivity, and shed light on the corresponding adsorptive pathway.

While ADS using modified zeolites has shown to be extremely effective in providing the world with clean energy, there is still additional work that must be done before it can be considered commercially-viable. As discussed in this thesis, commercial fuels also contain aromatics and more importantly, nitrogen- and oxygen- containing compounds that are strong inhibitors of ADS. Selective removal of refractory sulfur compound is still the biggest challenge in ultra-deep desulfurization of transportation fuels, even in HDS. Therefore, it is up to future researchers and scientists to develop new sorbents that not only removes sulfur selectively, but also maintains the quality of the fuel. The combination of experimental data and computational calculations is essential to bridge the gap between fundamental studies and real-world applications. On a last note, fossil fuels will continue to dominate the energy world, especially in the transportation sector, increasing the demand for clean energy. This demand may not be met by a single desulfurization process, but a combination of two or more may just be the solution of the future. Future work should include studies of other metal combinations and technologies, while simultaneously addressing the diffusion, capacity and techno-economical aspects of the sorbent.

APPENDIX I: PUBLICATIONS AND PRESENTATIONS

Publications

- Lee, K. X., Wang, H., Karakalos, S., Tsilomelekis, G. & Valla, J. A. Adsorptive Desulfurization of 4,6-Dimethyldibenzothiophene on Bimetallic Mesoporous Y Zeolites: Effects of Cu and Ce Composition and Configuration. *Ind. Eng. Chem. Res.* **58**, 18301–18312 (2019).

- Lee, K. X. & Valla, J. A. Adsorptive desulfurization of liquid hydrocarbons using zeolite-based sorbents: a comprehensive review. *React. Chem. Eng.* **4**, 1357–1386 (2019).

- Lee, K. X., Tsilomelekis, G. & Valla, J. A. Removal of benzothiophene and dibenzothiophene from hydrocarbon fuels using CuCe mesoporous Y zeolites in the presence of aromatics. *Appl. Catal. B Environ.* **234**, 130–142 (2018).

- Lee, K. X. & Valla, J. A. Investigation of bifunctional zeolites for the adsorptive desulfurization of fuels. *Appl. Catal. B Environ.* **201**, 359–369 (2017).

- Mahoney, E. G., Sheng, W., Cheng, M., Lee, K. X., Yan, Y. & Chen, J. G. Analyzing the electrooxidation of ethylene glycol and glucose over platinum-modified gold electrocatalysts in alkaline electrolyte using in-situ infrared spectroscopy. *J. Power Sources* **305**, 89–96 (2016).

- Kelly, T. G., Lee, K. X. & Chen, J. G. Pt-modified molybdenum carbide for the hydrogen evolution reaction: From model surfaces to powder electrocatalysts. *J. Power Sources* **271**, 76–81 (2014).

Conference Oral Presentations

- Crowl, T. B., Lee, K. L. & Valla, J. A. Investigation of rare earth exchanged on zeolite y for adsorptive desulfurization of model fuels in the presence of aromatics. *AIChE Fall Annual Meeting,* Orlando, FL (2019).

- Lee, K. L., Tsilomelekis, G. & Valla, J. A. Investigating the effect of Cu and Ce loading in mesoporous Y zeolite for the adsorptive desulfurization of 4,6-dimethyldibenzothiophene. *AIChE Fall Annual Meeting,* Pittsburgh, PA (2018).

- Lee, K. L., Tsilomelekis, G. & Valla, J. A. Adsorptive desulfurization of 4,6-dimethyldibenzothiophene on bimetallic mesoporous Y zeolites: effect of Cu and Ce composition and configuration. *NECS Spring Annual Meeting,* Worcester, MA (2018).

- Lee, K. L., Tsilomelekis, G. & Valla, J. A. Experimental studies of 4,6-dimethyldibenzothiophene adsorption on metal-exchanged mesoporous Y zeolites. *AIChE Fall Annual Meeting,* Minneapolis, MN (2017).

- Lee, K. L. & Valla, J. A. Selective removal of refractory sulfur compounds from hydrocarbon fuels using bimetallic mesoporous Y zeolites. *NEERF Fall Annual Meeting,* Worcester, MA (2017).

- Lee, K. L. & Valla, J. A. Diffusion and adsorptive desulfurization studies on bifunctional zeolites. *AIChE Fall Annual Meeting,* San Francisco, CA (2016).

- Lee, K. L. & Valla, J. A. Bifunctional zeolites for the adsorptive desulfurization of model fuels. *ACS Fall Annual Meeting,* Philadelphia, PA (2016).

- Lee, K. L. & Valla, J. A. Adsorption application for desulfurization of transportation fuels using bifunctional zeolites. *NECS Spring Annual Meeting,* Providence, RI (2016).

- Lee, K. L. & Valla, J. A. Investigation of bifunctional zeolites for the adsorptive desulfurization of fuels. *AIChE Fall Annual Meeting,* Salt Lake City, UT (2015).

Conference Poster Presentations

- Lee, K. L., Sokol, H. J., Caratzoulas, S., Tsilomelekis, G. & Valla, J. A. Investigation sulfur adsorption capability of ion-exchange y zeolites using density functional theory and IR spectroscopy. *AIChE Fall Annual Meeting,* Orlando, FL (2019).

- Lee, K. L., Tsilomelekis, G. & Valla, J. A. Selective removal of refractory sulfur compounds from hydrocarbon fuels using bimetallic mesoporous y zeolites. *Cabot Student Materials Research Forum,* Boston, MA (2018).

- Lee, K. L., Tsilomelekis, G. & Valla, J. A. Selective removal of refractory sulfur compounds from hydrocarbon fuels using bimetallic mesoporous y zeolites. *NAM Meeting,* Denver, CO (2017).

- Lee, K. L., Tsilomelekis, G. & Valla, J. A. Selective removal of refractory sulfur compounds from hydrocarbon fuels using bimetallic mesoporous y zeolites. *NECS Spring Annual Meeting,* Storrs, CT (2017).

- Lee, K. L., Tsilomelekis, G. & Valla, J. A. Selective removal of refractory sulfur compounds using metal-exchanged mesoporous y zeolites. *Annual UCONN SoE Poster Competition,* Storrs, CT (2017).

- Lee, K. L., Martino, C. & Valla, J. A Evaluation of hierarchical pore structure zeolites for adsorptive desulfurization of model fuels. *ACS Fall Annual Meeting,* Boston, MA (2015).

APPENDIX II: COPYRIGHT

Reprint permission for Figures 1.1-1.5

Author reusing their own work published by the Royal Society of Chemistry

You do not need to request permission to reuse your own figures, diagrams, etc, that were originally published in a Royal Society of Chemistry publication. However, permission should be requested for use of the whole article or chapter except if reusing it in a thesis. If you are including an article or book chapter published by us in your thesis please ensure that your co-authors are aware of this.

Reuse of material that was published originally by the Royal Society of Chemistry must be accompanied by the appropriate acknowledgement of the publication. The form of the acknowledgement is dependent on the journal in which it was published originally, as detailed in 'Acknowledgements'.

Reprint permission for Figures 4.1-4.8 and Tables 4.1-4.3

Reprint permission for Figures 5.1-5.9 and Table 5.1

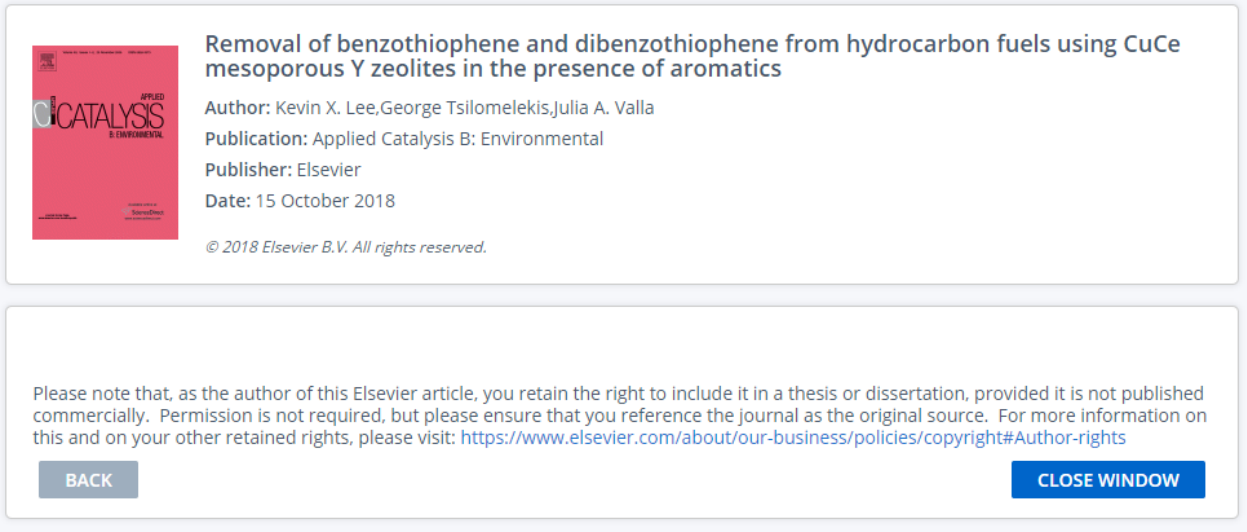

Removal of benzothiophene and dibenzothiophene from hydrocarbon fuels using CuCe mesoporous Y zeolites in the presence of aromatics

Author: Kevin X. Lee,George Tsilomelekis,Julia A. Valla

Publication: Applied Catalysis B: Environmental

Publisher: Elsevier

Date: 15 October 2018

Please note that, as the author of this Elsevier article, you retain the right to include it in a thesis or dissertation, provided it is not published commercially. Permission is not required, but please ensure that you reference the journal as the original source. For more information on this and on your other retained rights, please visit: https://www.elsevier.com/about/our-business/policies/copyright#Author-rights

BACK CLOSE WINDOW

Reprint permissions for Figures 6.1-6.15 and Tables 6.1-6.6

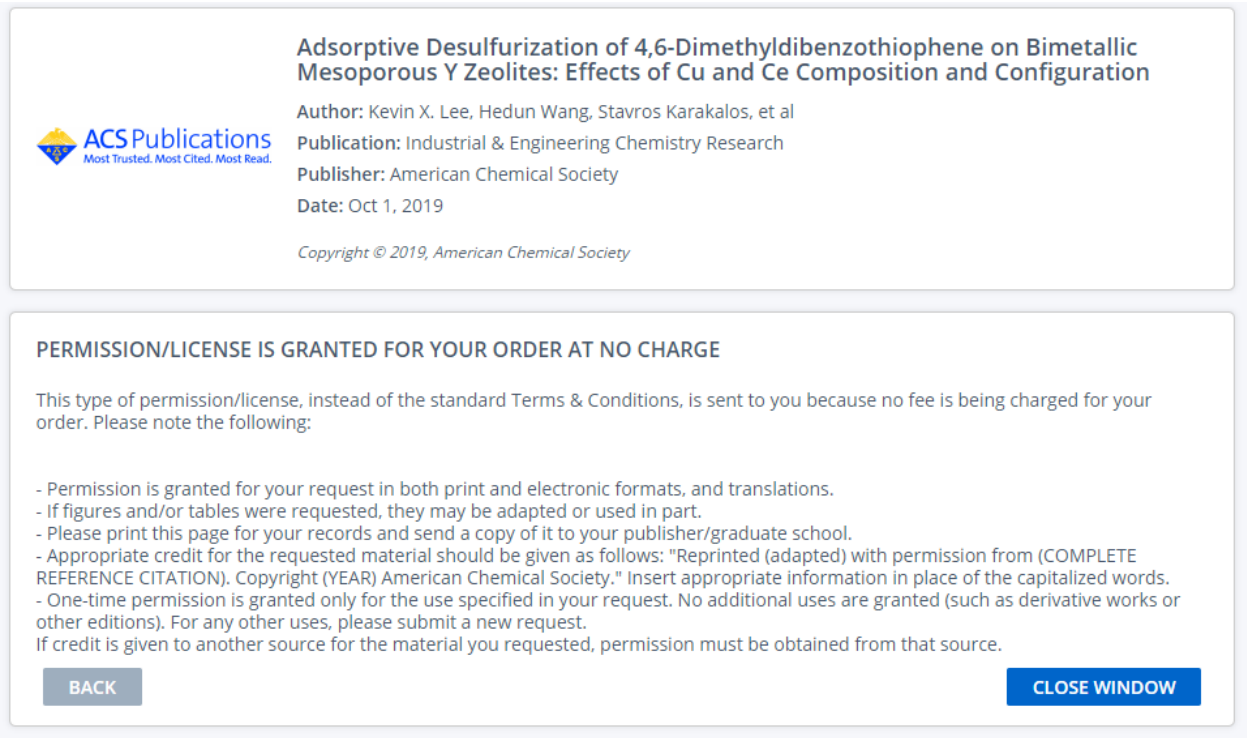

Adsorptive Desulfurization of 4,6-Dimethyldibenzothiophene on Bimetallic Mesoporous Y Zeolites: Effects of Cu and Ce Composition and Configuration

Author: Kevin X. Lee, Hedun Wang, Stavros Karakalos, et al

Publication: Industrial & Engineering Chemistry Research

Publisher: American Chemical Society

Date: Oct 1, 2019

PERMISSION/LICENSE IS GRANTED FOR YOUR ORDER AT NO CHARGE

This type of permission/license, instead of the standard Terms & Conditions, is sent to you because no fee is being charged for your order. Please note the following:

- Permission is granted for your request in both print and electronic formats, and translations.
- If figures and/or tables were requested, they may be adapted or used in part.
- Please print this page for your records and send a copy of it to your publisher/graduate school.
- Appropriate credit for the requested material should be given as follows: "Reprinted (adapted) with permission from (COMPLETE REFERENCE CITATION). Copyright (YEAR) American Chemical Society." Insert appropriate information in place of the capitalized words.
- One-time permission is granted only for the use specified in your request. No additional uses are granted (such as derivative works or other editions). For any other uses, please submit a new request.

If credit is given to another source for the material you requested, permission must be obtained from that source.

BACK CLOSE WINDOW

ADDENDUM

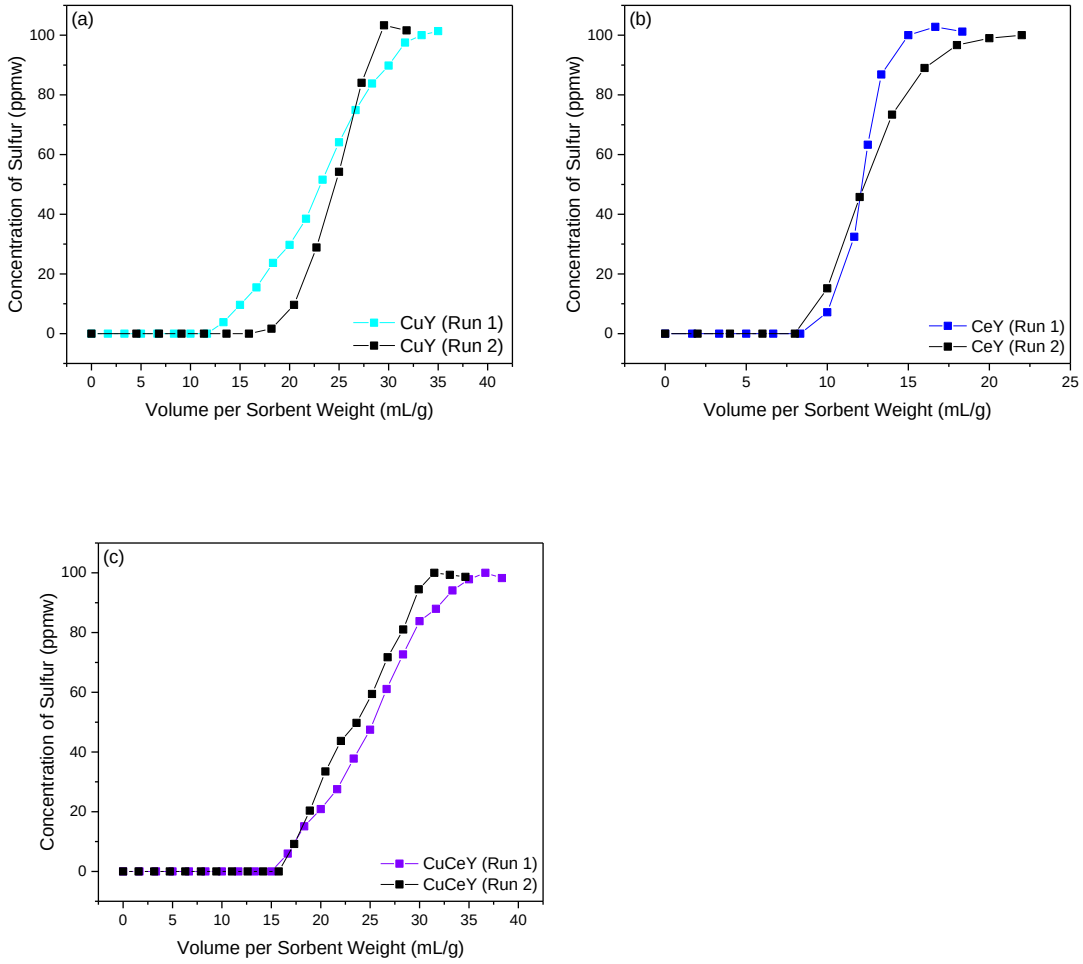

Breakthrough curves of benzothiophene in a mixture of 80% n-octane and 20% benzene over (a) CuY, (b) CeY and (c) CuCeY.

The figures above show the reproducibility of the breakthrough curves, each ran by two separate individuals. The colored data points (Run 1) represent breakthrough curves ran by me, while the black data points (Run 2) correspond to experiments performed by my labmate, Tyler Crowl. It should be noted that each experiment may take up to two full days, depending on the capacity of the sorbent, making it challenging to run multiple experiments for reproducibility purposes. Nonetheless, the figures above show similar results between two separate experiments. Because the experiments were ran on two separate occasions with different volumetric intervals and sorbent weight, the normalized volume of effluent is different for the two runs. In the future, same data points on the x-axis should be utilized to enable the calculation of standard deviation.

REFERENCES

1. U.S. Energy Information Administration. *September 2019 Monthly Energy Review*. *U.S. Energy Information Administration* vol. 24 (2019).
2. Mohr, S. H., Wang, J., Ellem, G., Ward, J. & Giurco, D. Projection of world fossil fuels by country. *Fuel* **141**, 120–135 (2015).
3. Valla, J. A., Lappas, A. A. & Vasalos, I. A. Catalytic cracking of thiophene and benzothiophene: Mechanism and kinetics. *Appl. Catal. A Gen.* **297**, 90–101 (2006).
4. Valla, J. A., Lappas, A. A., Vasalos, I. A., Kuehler, C. W. & Gudde, N. J. Feed and process effects on the in situ reduction of sulfur in FCC gasoline. *Appl. Catal. A Gen.* **276**, 75–87 (2004).
5. Brunet, S., Mey, D., Pérot, G., Bouchy, C. & Diehl, F. On the hydrodesulfurization of FCC gasoline: A review. *Appl. Catal. A Gen.* **278**, 143–172 (2005).
6. Bremmer, G. M., van Haandel, L., Hensen, E. J. M., Frenken, J. W. M. & Kooyman, P. J. The effect of oxidation and resulfidation on (Ni/Co)MoS2 hydrodesulfurisation catalysts. *Appl. Catal. B Environ.* **243**, 145–150 (2019).
7. Ermakova, A., Mashkina, A. V. & Sakhaltueva, L. G. Kinetic study of catalytic hydrogenation of thiophene on a palladium sulfide catalyst. *Kinet. Catal.* **43**, 528–535 (2002).
8. Gates, B. C. & Topsøe, H. Reactivities in deep catalytic hydrodesulfurization: Challenges, opportunities, and the importance of 4-methyldibenzothiophene and 4,6-dimethyldibenzothiophene. *Polyhedron* **16**, 3213–3217 (1997).
9. Ho, T. C. A theory of ultradeep hydrodesulfurization of diesel in stacked-bed reactors. *AIChE J.* **64**, 595–605 (2018).
10. U.S. Environmental Protection Agency. EPA sets Tier 3 motor vehicle emissions and fuel standards. https://www.epa.gov/regulations-emissions-vehicles-and-engines/final-rule-control-air-pollution-motor-vehicles-tier-3 (2014).
11. The International Council On Clean Transportation. An Introduction To Petroleum Refining and the Production of Ultra Low Sulfur Gasoline. *Energy Econ. Appl. Optim.* 1–38 (2011).
12. Armaroli, N. & Balzani, V. The hydrogen issue. *ChemSusChem* **4**, 21–36 (2011).
13. Duarte, F. A., Mello, P. de A., Bizzi, C. A., Nunes, M. A. G., Moreira, E. M., Alencar, M. S., Motta, H. N., Dressler, V. L. & Flores, É. M. M. Sulfur removal from hydrotreated petroleum fractions using ultrasound-assisted oxidative desulfurization process. *Fuel* **90**, 2158–2164 (2011).
14. Alptekin, G., DeVoss, S., Dubovik, M., Monroe, J., Amalfitano, R. & Israelson, G. Regenerable sorbent for natural gas desulfurization. *J. Mater. Eng. Perform.* **15**, 433–438 (2006).
15. Blumberg, K. O., Walsh, M. P. & Pera, C. Low-Sulfur Gasoline & Diesel: The Key to Lower Vehicle Emissions. http://www.theicct.org/sites/default/files/publications/Low-Sulfur_ICCT_2003.pdf (2003).
16. Song, C. & Ma, X. New design approaches to ultra-clean diesel fuels by deep desulfurization and deep dearomatization. *Appl. Catal. B Environ.* **41**, 207–238 (2003).
17. Kim, J. H., Ma, X., Zhou, A. & Song, C. Ultra-deep desulfurization and denitrogenation of diesel fuel by selective adsorption over three different adsorbents: A study on adsorptive selectivity and mechanism. *Catal. Today* **111**, 74–83 (2006).
18. Song, C. An overview of new approaches to deep desulfurization for ultra-clean gasoline,

diesel fuel and jet fuel. *Catal. Today* **86**, 211–263 (2003).
19. Sikarwar, P., Gosu, V. & Subbaramaiah, V. An overview of conventional and alternative technologies for the production of ultra-low-sulfur fuels. *Rev. Chem. Eng.* **0**, (2018).
20. Lee, K. X. & Valla, J. A. Adsorptive desulfurization of liquid hydrocarbons using zeolite-based sorbents: a comprehensive review. *React. Chem. Eng.* **4**, 1357–1386 (2019).
21. Ahmad, W. *Sulfur in Petroleum*. *IGI Global* (2016).
22. Babich, I. V. & Moulijn, J. a. Science and technology of novel processes for deep desulfurization of oil refinery streams: A review. *Fuel* **82**, 607–631 (2003).
23. Hernández-Maldonado, A. J. & Yang, R. T. Desulfurization of Liquid Fuels by Adsorption via π Complexation with Cu(I)−Y and Ag−Y Zeolites. *Ind. Eng. Chem. Res.* **42**, 3103–3110 (2003).
24. Khan, N. A., Kim, C. M. & Jhung, S. H. Adsorptive desulfurization using Cu–Ce/metal–organic framework: Improved performance based on synergy between Cu and Ce. *Chem. Eng. J.* **311**, 20–27 (2017).
25. Ahmed, I. & Jhung, S. H. Adsorptive desulfurization and denitrogenation using metal-organic frameworks. *J. Hazard. Mater.* **301**, 259–276 (2016).
26. Cychosz, K. A., Wong-Foy, A. G. & Matzger, A. J. Liquid phase adsorption by microporous coordination polymers: Removal of organosulfur compounds. *J. Am. Chem. Soc.* **130**, 6938–6939 (2008).
27. Schnobrich, J. K., Lebel, O., Cychosz, K. A., Dailly, A., Wong-Foy, A. G. & Matzger, A. J. Linker-directed vertex desymmetrization for the production of coordination polymers with high porosity. *J. Am. Chem. Soc.* **132**, 13941–13948 (2010).
28. He, W.-W., Yang, G.-S., Tang, Y.-J., Li, S.-L., Zhang, S.-R., Su, Z.-M. & Lan, Y.-Q. Phenyl Groups Result in the Highest Benzene Storage and Most Efficient Desulfurization in a Series of Isostructural Metal-Organic Frameworks. *Chem. - A Eur. J.* **21**, 9784–9789 (2015).
29. Shah, M. S., Tsapatsis, M. & Siepmann, J. I. Hydrogen Sulfide Capture: From Absorption in Polar Liquids to Oxide, Zeolite, and Metal-Organic Framework Adsorbents and Membranes. *Chem. Rev.* **117**, 9755–9803 (2017).
30. McNamara, N. D., Neumann, G. T., Masko, E. T., Urban, J. A. & Hicks, J. C. Catalytic performance and stability of (V) MIL-47 and (Ti) MIL-125 in the oxidative desulfurization of heterocyclic aromatic sulfur compounds. *J. Catal.* **305**, 217–226 (2013).
31. Yang, Y., Chiang, K. & Burke, N. Porous carbon-supported catalysts for energy and environmental applications: A short review. *Catal. Today* **178**, 197–205 (2011).
32. Silas, K., Ghani, W. A. W. A. K., Choong, T. S. Y. & Rashid, U. Carbonaceous materials modified catalysts for simultaneous SO2/NOx removal from flue gas: A review. *Catal. Rev. - Sci. Eng.* **00**, 1–28 (2018).
33. Yu, C., Qiu, J. S., Sun, Y. F., Li, X. H., Chen, G. & Zhao, Z. Bin. Adsorption removal of thiophene and dibenzothiophene from oils with activated carbon as adsorbent: Effect of surface chemistry. *J. Porous Mater.* **15**, 151–157 (2008).
34. Moreira, A. M., Brandão, H. L., Hackbarth, F. V., Maass, D., Ulson de Souza, A. A. & Guelli, S. M. A. Adsorptive desulfurization of heavy naphthenic oil: Equilibrium and kinetic studies. *Chem. Eng. Sci.* **172**, 23–31 (2017).
35. Saleh, T. A. Simultaneous adsorptive desulfurization of diesel fuel over bimetallic nanoparticles loaded on activated carbon. *J. Clean. Prod.* **172**, 2123–2132 (2018).
36. Liu, X., Liu, L., Osaka, Y., Huang, H., He, Z., Bai, Y., Li, S., Li, J. & Huhetaoli. Study on desulfurization performance of MnO2-based activated carbon from waste coconut shell for

diesel emissions control. *J. Mater. Cycles Waste Manag.* **20**, 1499–1506 (2018).
37. Prajapati, Y. N. & Verma, N. Adsorptive desulfurization of diesel oil using nickel nanoparticle-doped activated carbon beads with/without carbon nanofibers: Effects of adsorbate size and adsorbent texture. *Fuel* **189**, 186–194 (2017).
38. Seredych, M., Wu, C. T., Brender, P., Ania, C. O., Vix-Guterl, C. & Bandosz, T. J. Role of phosphorus in carbon matrix in desulfurization of diesel fuel using adsorption process. *Fuel* **92**, 318–326 (2012).
39. Fuertes, A. B., Marbán, G. & Nevskaia, D. M. Adsorption of volatile organic compounds by means of activated carbon fibre-based monoliths. *Carbon N. Y.* **41**, 87–96 (2003).
40. Kharisov, B. I., González, M. O., Quezada, T. S., de la Fuente, I. G. & Longoria, F. Materials and nanomaterials for the removal of heavy oil components. *J. Pet. Sci. Eng.* **156**, 971–982 (2017).
41. Tran, D. T., Palomino, J. M. & Oliver, S. R. J. Desulfurization of JP-8 jet fuel: Challenges and adsorptive materials. *RSC Adv.* **8**, 7301–7314 (2018).
42. Menzel, R., Iruretagoyena, D., Wang, Y., Bawaked, S. M., Mokhtar, M., Al-Thabaiti, S. A., Basahel, S. N. & Shaffer, M. S. P. Graphene oxide/mixed metal oxide hybrid materials for enhanced adsorption desulfurization of liquid hydrocarbon fuels. *Fuel* **181**, 531–536 (2016).
43. Shakirullah, M., Ahmad, I., Ishaq, M. & Ahmad, W. Study on the role of metal oxides in desulphurization of some petroleum fractions. *J. Chinese Chem. Soc.* **56**, 107–114 (2009).
44. Garces, H. F., Galindo, H. M., Garces, L. J., Hunt, J., Morey, A. & Suib, S. L. Low temperature H2S dry-desulfurization with zinc oxide. *Microporous Mesoporous Mater.* **127**, 190–197 (2010).
45. Zhang, J. C., Song, L. F., Hu, J. Y., Ong, S. L., Ng, W. J., Lee, L. Y., Wang, Y. H., Zhao, J. G. & Ma, R. Y. Investigation on gasoline deep desulfurization for fuel cell applications. *Energy Convers. Manag.* **46**, 1–9 (2005).
46. Velu, S., Ma, X. & Song, C. Zeolite-based adsorbents for desulfurization of jet fuel by selective adsorption. *ACS Div. Fuel Chem. Prepr.* **47**, 447–448 (2002).
47. Roostaei, N. & Tezel, F. H. Removal of phenol from aqueous solutions by adsorption. *J. Environ. Manage.* **70**, 157–164 (2004).
48. Hussain, M., Abbas, N., Fino, D. & Russo, N. Novel mesoporous silica supported ZnO adsorbents for the desulphurization of biogas at low temperatures. *Chem. Eng. J.* **188**, 222–232 (2012).
49. Beck, J. S. *et al.* A New Family of Mesoporous Molecular Sieves Prepared with Liquid Crystal Templates. *J. Am. Chem. Soc.* **114**, 10834–10843 (1992).
50. Tang, Q., Hu, S., Chen, Y., Guo, Z., Hu, Y., Chen, Y. & Yang, Y. Highly dispersed manganese oxide catalysts grafted on SBA-15: Synthesis, characterization and catalytic application in trans-stilbene epoxidation. *Microporous Mesoporous Mater.* **132**, 501–509 (2010).
51. Zhang, F. M., Liu, B. S., Zhang, Y., Guo, Y. H., Wan, Z. Y. & Subhan, F. Highly stable and regenerable Mn-based/SBA-15 sorbents for desulfurization of hot coal gas. *J. Hazard. Mater.* **233**–**234**, 219–227 (2012).
52. Song, L., Bu, T., Zhu, L., Zhou, Y., Xiang, Y. & Xia, D. Synthesis of organically-inorganically functionalized MCM-41 for adsorptive desulfurization of C4 hydrocarbons. *J. Phys. Chem. C* **118**, 9468–9476 (2014).
53. Ren, X., Miao, G., Xiao, Z., Ye, F., Li, Z., Wang, H. & Xiao, J. Catalytic adsorptive desulfurization of model diesel fuel using TiO2/SBA-15 under mild conditions. *Fuel* **174**,

118–125 (2016).
54. Yang, R. T. *Adsorbents: Fundamentals and Applications*. *A John Wiley & Sons, Inc.* (2003).
55. Velu, S., Song, C., Engelhard, M. H. & Chin, Y. H. Adsorptive removal of organic sulfur compounds from jet fuel over K-exchanged NiY zeolites prepared by impregnation and ion exchange. *Ind. Eng. Chem. Res.* **44**, 5740–5749 (2005).
56. Ozekmekci, M., Salkic, G. & Fellah, M. F. Use of zeolites for the removal of H2S: A mini-review. *Fuel Process. Technol.* **139**, 49–60 (2015).
57. Burakov, A. E., Galunin, E. V., Burakova, I. V., Kucherova, A. E., Agarwal, S., Tkachev, A. G. & Gupta, V. K. Adsorption of heavy metals on conventional and nanostructured materials for wastewater treatment purposes: A review. *Ecotoxicol. Environ. Saf.* **148**, 702–712 (2018).
58. Zanin, E. *et al.* Adsorption of heavy metals from wastewater graphic industry using clinoptilolite zeolite as adsorbent. *Process Saf. Environ. Prot.* **105**, 194–200 (2017).
59. Přech, J. Catalytic performance of advanced titanosilicate selective oxidation catalysts – a review. *Catal. Rev. - Sci. Eng.* **60**, 71–131 (2018).
60. Liang, J., Liang, Z., Zou, R. & Zhao, Y. Heterogeneous Catalysis in Zeolites, Mesoporous Silica, and Metal–Organic Frameworks. *Adv. Mater.* **29**, 1–21 (2017).
61. Nair, S., Shahadat Hussain, a. H. M. & Tatarchuk, B. J. The role of surface acidity in adsorption of aromatic sulfur heterocycles from fuels. *Fuel* **105**, 695–704 (2013).
62. Lee, K. X. & Valla, J. A. Investigation of bifunctional zeolites for the adsorptive desulfurization of fuels. *Sep. Div. 2015 - Core Program. Area 2015 AIChE Annu. Meet.* **2**, 1041–1043 (2015).
63. Lee, K. X., Tsilomelekis, G. & Valla, J. A. Removal of benzothiophene and dibenzothiophene from hydrocarbon fuels using CuCe mesoporous Y zeolites in the presence of aromatics. *Appl. Catal. B Environ.* **234**, 130–142 (2018).
64. Yang, R. T., Hernández-Maldonado, A. J. & Yang, F. H. Desulfurization of transportation fuels with zeolites under ambient conditions. *Science* **301**, 79–81 (2003).
65. Kim, J. H., Ma, X., Zhou, A. & Song, C. Ultra-deep desulfurization and denitrogenation of diesel fuel by selective adsorption over three different adsorbents: A study on adsorptive selectivity and mechanism. *Catal. Today* **111**, 74–83 (2006).
66. US EPA National Center for Environmental Assessment, Research Triangle Park Nc, I. O. & Long, T. Integrated Science Assessment (ISA) for Sulfur Oxides – Health Criteria (External Review Draft). (2016).
67. Bhandari, V. M., Ko, C. H., Park, J. G., Han, S. S., Cho, S. H. & Kim, J. N. Desulfurization of diesel using ion-exchanged zeolites. *Chem. Eng. Sci.* **61**, 2599–2608 (2006).
68. Li, K., Valla, J. & Garcia-Martinez, J. Realizing the commercial potential of hierarchical zeolites: New opportunities in catalytic cracking. *ChemCatChem* **6**, 46–66 (2014).
69. Hernández-Maldonado, A. J. & Yang, R. T. New Sorbents for Desulfurization of Diesel Fuels via π-Complexation. *AIChE J.* **50**, 791–801 (2004).
70. Ma, X., Velu, S., Kim, J. H. & Song, C. Deep desulfurization of gasoline by selective adsorption over solid adsorbents and impact of analytical methods on ppm-level sulfur quantification for fuel cell applications. *Appl. Catal. B Environ.* **56**, 137–147 (2005).
71. Van de Voorde, B., Hezinová, M., Lannoeye, J., Vandekerkhove, A., Marszalek, B., Gil, B., Beurroies, I., Nachtigall, P. & De Vos, D. Adsorptive desulfurization with CPO-27/MOF-74: an experimental and computational investigation. *Phys. Chem. Chem. Phys.* 10759–10766 (2015) doi:10.1039/c5cp01063b.

72. Weitkamp, J. & Puppe, L. *Catalysis and Zeolites*. (Springer Berlin Heidelberg, 1999). doi:10.1007/978-3-662-03764-5.
73. Christensen, C. H., Schmidt, I. & Christensen, C. H. Improved performance of mesoporous zeolite single crystals in catalytic cracking and isomerization of n-hexadecane. *Catal. Commun.* **5**, 543–546 (2004).
74. Tao, Y., Kanoh, H., Abrams, L. & Kaneko, K. Mesopore-modified zeolites: Preparation, characterization, and applications. *Chem. Rev.* **106**, 896–910 (2006).
75. García-Martínez, J., Johnson, M., Valla, J., Li, K. & Ying, J. Y. Mesostructured zeolite Y—high hydrothermal stability and superior FCC catalytic performance. *Catal. Sci. Technol.* **2**, 987 (2012).
76. Garcia-Martinez, J., Johnson, M. M. & Valla, J. A. United States Patent 8,486,369. (2013).
77. Loewenstein, W. The distribution of aluminum in the tetrahedra of silicates and aluminates. *Am. Mineral.* **39**, 92–96 (1954).
78. Breck, D. W. *Zeolite Molecular Sieves: Structure, Chemistry and Use*. (Wiley, 1974).
79. Ward, J. W. *Molecular Sieve Catalysts, in Applied Industrial Catalysis*. vol. 3 (Academic Press, 1984).
80. Turnes Palomino, G., Bordiga, S., Zecchina, A., Marra, G. L. & Lamberti, C. XRD, XAS, and IR characterization of copper-exchanged Y zeolite. *J. Phys. Chem. B* **104**, 8641–8651 (2000).
81. Brunauer, S., Emmett, P. H. & Teller, E. Adsorption of Gases in Multimolecular Layers. *J. Am. Chem. Soc.* **60**, 309–319 (1938).
82. Baerlocher, C. & McCusker, L. Database of Zeolite Structures. *International Zeolite Association* http://www.iza-structure.org/databases/ (2016).
83. Rietveld, H. M. Line profiles of neutron powder-diffraction peaks for structure refinement. *Acta Crystallogr.* **22**, 151–152 (1967).
84. Larson, A. C. & Dreele, R. B. Von. General Structure Analysis System (GSAS). *Los Alamos Natl. Lab. Rep.* LAUR 86-748 (2000).
85. Toby, B. H. EXPGUI, a graphical user interface for GSAS. *J. Appl. Crystallogr.* **34**, 210–213 (2001).
86. Ferraro, J. R., Nakamoto, K. & Brown, C. W. *Introductory Raman Spectroscopy*. *Introductory Raman Spectroscopy: Second Edition* (Elsevier, 2003). doi:10.1016/B978-0-12-254105-6.X5000-8.
87. Spoto, G., Bordiga, S., Scarano, D. & Zecchina, A. Well defined CuI(NO), CuI(NO)2 and CuII(NO)X (X = O- and/or NO2-) complexes in CuI-ZSMS prepared by interaction of H-ZSM5 with gaseous CuCl. *Catal. Letters* **13**, 39–44 (1992).
88. Edington, J. W. *Practical electron microscopy in materials science*. (Van Nostrand Reinhold Co., 1976).
89. Parr, R. G. & Weitao, Y. *Density-Functional Theory of Atoms and Molecules*. (Oxford University press, 1989). doi:10.1038/154101a0.
90. Kohc, W. & Holthausen, M. C. *A Chemist's Guide to Density Functional Theory*. (Wiley-VCH, 2001). doi:10.1021/ja004799q.
91. Hammer, B. & Nørskov, J. K. Theoretical surface science and catalysis—calculations and concepts. *Adv. Catal.* **45**, 71–129 (2000).
92. Foresman, J. B. & Frisch, A. *Exploring Chemistry With Electronic Structure Methods.pdf*. *Exploring Chemistry with Electronic Structure Methods* (Gaussian, Inc., 2013). doi:10.1002/adma.200400767.

93. Fock, V. ‘Selfconsistent field’ with interchange for sodium. *Zeitschrift für Phys.* **62**, 795 (1930).
94. Hartree, D. R. The Wave Mechanics of an Atom with a Non-Coulomb Central Field Part I Theory and Methods. *Math. Proc. Cambridge Philos. Soc.* **24**, 89–110 (1928).
95. Hohenberg, P. & Kohn, W. Inhomogeneous Electron Gas. *Phys. Rev.* **136**, B864–B871 (1964).
96. Lee, C., Yang, W. & Parr, R. G. Development of the Colle-Salvetti correlation-energy formula into a functional of the electron density. *Phys. Rev. B* **37**, 785–789 (1988).
97. Frisch, M. J. *et al.* Gaussian 16, Revision C.01. *Gaussian Inc.* Wallingford CT (2016) doi:10.1159/000348293.
98. Patet, R. E., Caratzoulas, S. & Vlachos, D. G. Adsorption in zeolites using mechanically embedded ONIOM clusters. *Phys. Chem. Chem. Phys.* **18**, 26094–26106 (2016).
99. Liu, B., Zhao, Z., Wang, D., Liu, J., Chen, Y., Li, T., Duan, A. & Jiang, G. A theoretical study on the mechanism for thiophene hydrodesulfurization over zeolite L-supported sulfided CoMo catalysts: Insight into the hydrodesulfurization over zeolite-based catalysts. *Comput. Theor. Chem.* **1052**, 47–57 (2015).
100. Sun, Y., Zheng, D., Pei, S. & Fan, D. New Theoretical Insights into the Contributions of Poly(methylbenzene) and Alkene Cycles to the Methanol to Propene Process in H-FAU Zeolite. *J. Phys. Chem. C* **121**, 16216–16237 (2017).
101. Maseras, F. & Morokuma, K. IMOMM: A new integrated ab initio + molecular mechanics geometry optimization scheme of equilibrium structures and transition states. *J. Comput. Chem.* **16**, 1170–1179 (1995).
102. Dapprich, S., Komáromi, I., Byun, K. S., Morokuma, K. & Frisch, M. J. A new ONIOM implementation in Gaussian98. Part I. The calculation of energies, gradients, vibrational frequencies and electric field derivatives. *J. Mol. Struct. THEOCHEM* **461**–**462**, 1–21 (1999).
103. Stanislaus, A., Marafi, A. & Rana, M. S. Recent advances in the science and technology of ultra low sulfur diesel (ULSD) production. *Catal. Today* **153**, 1–68 (2010).
104. Ma, X., Sakanishi, K. & Mochida, I. Hydrodesulfurization reactivities of various sulfur compounds in diesel fuel. *Ind. Eng. Chem. Res.* **33**, 218–222 (1994).
105. Pieterse, J. a Z., Van Eijk, S., Van Dijk, H. a J. & Van Den Brink, R. W. On the potential of absorption and reactive adsorption for desulfurization of ultra low-sulfur commercial diesel in the liquid phase in the presence of fuel additive and bio-diesel. *Fuel Process. Technol.* **92**, 616–623 (2011).
106. Xue, M., Chitrakar, R., Sakane, K., Hirotsu, T., Ooi, K., Yoshimura, Y., Toba, M. & Feng, Q. Preparation of cerium-loaded Y-zeolites for removal of organic sulfur compounds from hydrodesulfurizated gasoline and diesel oil. *J. Colloid Interface Sci.* **298**, 535–542 (2006).
107. Breysse, M., Djega-Mariadassou, G., Pessayre, S., Geantet, C., Vrinat, M., Pérot, G. & Lemaire, M. Deep desulfurization: Reactions, catalysts and technological challenges. *Catal. Today* **84**, 129–138 (2003).
108. Topsøe, H. Developments in operando studies and in situ characterization of heterogeneous catalysts. *J. Catal.* **216**, 155–164 (2003).
109. Bowler, T. Falling oil prices: Who are the winners and losers? *BBC News* http://www.bbc.com/news/business-29643612 (2015).
110. Krauss, C. Oil Prices: What’s Behind the Drop? Simple Economics. *The New York Times* http://www.nytimes.com/interactive/2016/business/energy-environment/oil-prices.html

(2016).
111. Wang, Q. & Li, R. Impact of cheaper oil on economic system and climate change: A SWOT analysis. *Renew. Sustain. Energy Rev.* **54**, 925–931 (2016).
112. Wang, Y., Latz, J., Dahl, R., Pasel, J. & Peters, R. Liquid phase desulfurization of jet fuel by a combined pervaporation and adsorption process. *Fuel Process. Technol.* **90**, 458–464 (2009).
113. Wang, Y., Geder, J., Schubert, J. M., Dahl, R., Pasel, J. & Peters, R. Optimization of adsorptive desulfurization process of jet fuels for application in fuel cell systems. *Fuel Process. Technol.* **95**, 144–153 (2012).
114. CHICA, A., CORMA, A. & DOMINE, M. Catalytic oxidative desulfurization (ODS) of diesel fuel on a continuous fixed-bed reactor. *J. Catal.* **242**, 299–308 (2006).
115. Timko, M. T., Schmois, E., Patwardhan, P., Kida, Y., Class, C. a, Green, W. H., Nelson, R. K. & Reddy, C. M. Response of Different Types of Sulfur Compounds to Oxidative Desulfurization of Jet Fuel. *Energy & Fuels* **28**, 2977–2983 (2014).
116. Wu, X., Bai, Y., Tian, Y., Meng, X. & Shi, L. Gasoline Desulfurization by Catalytic Alkylation over Methanesulfonic Acid. *Bull. Korean Chem. Soc.* **34**, 3055–3058 (2013).
117. Zheng, X. D., Dong, H. J., Wang, X. & Shi, L. Study on olefin alkylation of thiophenic sulfur in FCC gasoline using La2O3-modified HY zeolite. *Catal. Letters* **127**, 70–74 (2009).
118. Jiang, X., Nie, Y., Li, C. & Wang, Z. Imidazolium-based alkylphosphate ionic liquids - A potential solvent for extractive desulfurization of fuel. *Fuel* **87**, 79–84 (2008).
119. Li, F., Kou, C., Sun, Z., Hao, Y., Liu, R. & Zhao, D. Deep extractive and oxidative desulfurization of dibenzothiophene with C5H9NO·SnCl2 coordinated ionic liquid. *J. Hazard. Mater.* **205**–**206**, 164–70 (2012).
120. Zhang, S., Zhang, Q. & Zhang, Z. C. Extractive Desulfurization and Denitrogenation of Fuels Using Ionic Liquids. *Ind. Eng. Chem. Res.* **43**, 614–622 (2004).
121. Martin, A. B., Alcon, A., Santos, V. E. & Garcia-Ochoa, F. Production of a Rhodococcus erythropolis IGTS8 biocatalyst for DBT biodesulfurization: influence of operational conditions. *Energy and Fuels* **19**, 775–782 (2005).
122. Davoodi-Dehaghani, F., Vosoughi, M. & Ziaee, A. A. Biodesulfurization of dibenzothiophene by a newly isolated Rhodococcus erythropolis strain. *Bioresour. Technol.* **101**, 1102–1105 (2010).
123. Wang, J., Xu, F., Xie, W. J., Mei, Z. J., Zhang, Q. Z., Cai, J. & Cai, W. M. The enhanced adsorption of dibenzothiophene onto cerium/nickel-exchanged zeolite Y. *J. Hazard. Mater.* **163**, 538–543 (2009).
124. Meng, C., Fang, Y., Jin, L. & Hu, H. Deep desulfurization of model gasoline by selective adsorption on Ag+/Al-MSU-S. *Catal. Today* **149**, 138–142 (2010).
125. Samadi-Maybodi, A., Teymouri, M., Vahid, A. & Miranbeigi, A. In situ incorporation of nickel nanoparticles into the mesopores of MCM-41 by manipulation of solvent-solute interaction and its activity toward adsorptive desulfurization of gas oil. *J. Hazard. Mater.* **192**, 1667–1674 (2011).
126. Wang, Y. & Yang, R. T. Desulfurization of liquid fuels by adsorption on carbon-based sorbents and ultrasound-assisted sorbent regeneration. *Langmuir* **23**, 3825–3831 (2007).
127. Timko, M. T., Wang, J. A., Burgess, J., Kracke, P., Gonzalez, L., Jaye, C. & Fischer, D. A. Roles of surface chemistry and structural defects of activated carbons in the oxidative desulfurization of benzothiophenes. *Fuel* **163**, 223–231 (2016).
128. Yang, Y., Lu, H., Ying, P., Jiang, Z. & Li, C. Selective dibenzothiophene adsorption on

modified activated carbons. *Carbon N. Y.* **45**, 3042–3044 (2007).
129. Huang, L., Qin, Z., Wang, G., Du, M., Ge, H., Li, X., Wu, Z. & Wang, J. A detailed study on the negative effect of residual sodium on the performance of Ni/ZnO adsorbent for diesel fuel desulfurization. *Ind. Eng. Chem. Res.* **49**, 4670–4675 (2010).
130. Watanabe, S., Ma, X. & Song, C. Selective sulfur removal from liquid hydrocarbons over regenerable CeO2-TiO2 adsorbents for fuel cell applications. *ACS Div. Fuel Chem. Prepr.* **49**, 511–513 (2004).
131. Xue, M., Chitrakar, R., Sakane, K., Hirotsu, T., Ooi, K., Yoshimura, Y., Feng, Q. & Sumida, N. Selective adsorption of thiophene and 1-benzothiophene on metal-ion-exchanged zeolites in organic medium. *J. Colloid Interface Sci.* **285**, 487–492 (2005).
132. Li, W., Tang, H., Zhang, T., Li, Q., Xing, J. & Liu, H. Ultra-deep desulfurization adsorbents for hydrotreated diesel with magnetic mesoporous aluminosilicates. *AIChE J.* **56**, NA-NA (2009).
133. Wang, Y., Yang, R. T. & Heinzel, J. M. Desulfurization of jet fuel by π-complexation adsorption with metal halides supported on MCM-41 and SBA-15 mesoporous materials. *Chem. Eng. Sci.* **63**, 356–365 (2008).
134. Liu, B. S., Xu, D. F., Chu, J. X., Liu, W. & Au, C. T. Deep desulfurization by the adsorption process of fluidized catalytic cracking (FCC) diesel over mesoporous Al-MCM-41 materials. *Energy and Fuels* **21**, 250–255 (2007).
135. McKinley, S. G. & Angelici, R. J. Deep desulfurization by selective adsorption of dibenzothiophenes on Ag+/SBA-15 and Ag+/SiO2. *Chem. Commun. (Camb).* 2620–2621 (2003) doi:10.1039/b309249f.
136. Palomino, J. M., Tran, D. T., Kareh, A. R., Miller, C. A., Gardner, J. M. V, Dong, H. & Oliver, S. R. J. Zirconia-silica based mesoporous desulfurization adsorbents. *J. Power Sources* **278**, 141–148 (2015).
137. Wang, H., Song, L., Jiang, H., Xu, J., Jin, L., Zhang, X. & Sun, Z. Effects of olefin on adsorptive desulfurization of gasoline over Ce(IV)Y zeolites. *Fuel Process. Technol.* **90**, 835–838 (2009).
138. Tian, F., Wu, W., Jiang, Z., Liang, C., Yang, Y., Ying, P., Sun, X., Cai, T. & Li, C. The study of thiophene adsorption onto La(III)-exchanged zeolite NaY by FT-IR spectroscopy. *J. Colloid Interface Sci.* **301**, 395–401 (2006).
139. Hernández-Maldonado, A. J., Yang, F. H., Qi, G. & Yang, R. T. Desulfurization of transportation fuels by π-complexation sorbents: Cu(I)-, Ni(II)-, and Zn(II)-zeolites. *Appl. Catal. B Environ.* **56**, 111–126 (2005).
140. Velu, S., Ma, X. & Song, C. Selective Adsorption for Removing Sulfur from Jet Fuel over Zeolite-Based Adsorbents. *Ind. Eng. Chem. Res.* **42**, 5293–5304 (2003).
141. Serrano, D. P., Aguado, J., Morales, G., Rodríguez, J. M., Peral, A., Thommes, M., Epping, J. P. & Chmelka, B. F. Molecular and meso- and macroscopic properties of hierarchical nanocrystalline ZSM-5 zeolite prepared by seed silanization. *Chem. Mater.* **21**, 641–654 (2009).
142. Liao, J., Bao, W., Chen, Y., Zhang, Y. & Chang, L. The Adsorptive Removal of Thiophene from Benzene over ZSM-5 Zeolite. *Energy Sources, Part A Recover. Util. Environ. Eff.* **34**, 618–625 (2012).
143. Nair, S. & Tatarchuk, B. J. Characteristics of sulfur removal by silver-titania adsorbents at ambient conditions. *Adsorption* **17**, 663–673 (2011).
144. Khalafalla, S. E. & Haas, L. A. Active sites for catalytic reduction of SO2 with CO on

alumina. *J. Catal.* **24**, 115–120 (1972).
145. Duan, L., Gao, X., Meng, X., Zhang, H., Wang, Q., Qin, Y., Zhang, X. & Song, L. Adsorption, Co-adsorption, and reactions of sulfur compounds, aromatics, olefins over Ce-exchanged y zeolite. *J. Phys. Chem. C* **116**, 25748–25756 (2012).
146. Fu, W., Zhang, L., Tang, T., Ke, Q., Wang, S., Hu, J., Fang, G., Li, J. & Xiao, F. Extraordinarily High Activity in the Hydrodesulfurization of 4,6-Dimethyldibenzothiophene over Pd Supported on Mesoporous Zeolite Y. *J. Am. Chem. Soc.* **133**, 15346–15349 (2011).
147. Hernández-Maldonado, A. J. & Yang, R. T. Desulfurization of Diesel Fuels by Adsorption via π-Complexation with Vapor-Phase Exchanged Cu(I)−Y Zeolites. *J. Am. Chem. Soc.* **126**, 992–993 (2004).
148. Hernández-Maldonado, A. J. & Yang, R. T. Desulfurization of diesel fuels via π-Complexation with Nickel(II)-exchanged X- and Y-Zeolites. *Ind. Eng. Chem. Res.* **43**, 1081–1089 (2004).
149. Palomino, J. M., Tran, D. T., Hauser, J. L., Dong, H. & Oliver, S. R. J. Mesoporous silica nanoparticles for high capacity adsorptive desulfurization. *J. Mater. Chem. A* **2**, 14890–14895 (2014).
150. Tian, F., Shen, Q., Fu, Z., Wu, Y. & Jia, C. Enhanced adsorption desulfurization performance over hierarchically structured zeolite Y. *Fuel Process. Technol.* **128**, 176–182 (2014).
151. Verboekend, D. & Pérez-Ramírez, J. Design of hierarchical zeolite catalysts by desilication. *Catal. Sci. Technol.* **1**, 879 (2011).
152. Subhan, F., Liu, B. S., Zhang, Y. & Li, X. G. High desulfurization characteristic of lanthanum loaded mesoporous MCM-41 sorbents for diesel fuel. *Fuel Process. Technol.* **97**, 71–78 (2012).
153. Nuntang, S., Prasassarakich, P. & Ngamcharussrivichai, C. Comparative study on adsorptive removal of thiophenic sulfurs over Y and USY zeolites. *Ind. Eng. Chem. Res.* **47**, 7405–7413 (2008).
154. Shi, Y., Zhang, W., Zhang, H., Tian, F., Jia, C. & Chen, Y. Effect of cyclohexene on thiophene adsorption over NaY and LaNaY zeolites. *Fuel Process. Technol.* **110**, 24–32 (2013).
155. Zhang, J., Qiu, G., Fan, L., Meng, X., Cai, Q. & Wang, Y. Enhanced sulfur capacity of durable and regenerable mesoporous sorbents for the deep desulfurization of diesel. *Fuel* **153**, 578–584 (2015).
156. Song, H., Song, H., Wan, X., Dai, M., Zhang, J. & Li, F. Deep desulfurization of model gasoline by selective adsorption over Cu-Ce bimetal ion-exchanged y zeolite. *Fuel Process. Technol.* **116**, 52–62 (2013).
157. Li, J. *et al.* Tuning of acidity in CeY catalytic cracking catalysts by controlling the migration of Ce in the ion exchange step through valence changes. *J. Catal.* **329**, 441–448 (2015).
158. Shi, Y., Yang, X., Tian, F., Jia, C. & Chen, Y. Effects of toluene on thiophene adsorption over NaY and Ce(IV)Y zeolites. *J. Nat. Gas Chem.* **21**, 421–425 (2012).
159. Jiang, M. & Ng, F. T. T. Adsorption of benzothiophene on Y zeolites investigated by infrared spectroscopy and flow calorimetry. *Catal. Today* **116**, 530–536 (2006).
160. Cairon, O. & Loustaunau, a. Adsorption of CO on NaY faujasite: A revisited FT-IR study. *J. Phys. Chem. C* **112**, 18493–18501 (2008).
161. Rakić, V., Dondur, V. & Hercigonja, R. FTIR study of carbon monoxide adsorption on ion-

exchanged X, Y and mordenite type zeolites. *J. Serbian Chem. Soc.* **68**, 409–416 (2003).
162. Borovkov, V. Y., Jiang, M. & Fu, Y. Investigation of Copper Carbonyl Species Formed upon CO Adsorption on Copper-Exchanged Zeolites by Diffuse Reflectance FTIR. *J. Phys. Chem. B* **103**, 5010–5019 (1999).
163. Rakić, V. M., Hercigonja, R. V. & Dondur, V. T. CO interaction with zeolites studied by TPD and FTIR: transition-metal ion-exchanged FAU-type zeolites. *Microporous Mesoporous Mater.* **27**, 27–39 (1999).
164. Turnes Palomino, G., Bordiga, S., Zecchina, a., Marra, G. L. & Lamberti, C. XRD, XAS, and IR characterization of copper-exchanged Y zeolite. *J. Phys. Chem. B* **104**, 8641–8651 (2000).
165. Egerton, T. A. & Stone, F. S. Adsorption of carbon monoxide by zeolite Y exchanged with different cations. *J. Chem. Soc. Faraday Trans. 1 Phys. Chem. Condens. Phases* **69**, 22 (1973).
166. Tempère, J. F., Bozon-Verduraz, F. & Delafosse, D. A kinetic study of the oxidation of cerium ions in an X zeolite. *Mater. Res. Bull.* **12**, 871–879 (1977).
167. Bensalem, A., Muller, J. C. & Bozon-Verduraz, F. Faraday communications. From bulk CeO 2 to supported cerium–oxygen clusters: a diffuse reflectance approach. *J. Chem. Soc., Faraday Trans.* **88**, 153–154 (1992).
168. Timofeeva, M. N., Jhung, S. H., Hwang, Y. K., Kim, D. K., Panchenko, V. N., Mel'gunov, M. S., Chesalov, Y. a & Chang, J.-S. Ce-silica mesoporous SBA-15-type materials for oxidative catalysis: Synthesis, characterization, and catalytic application. *Appl. Catal. A-General* **317**, 1–10 (2007).
169. Texter, J., Strome, D. H., Herman, R. G. & Klier, K. Chemical and spectroscopic properties of copper containing zeolites. *J. Phys. Chem.* **81**, 333–338 (1977).
170. Xia, Y., Li, Y., Gu, Y., Jin, T., Yang, Q., Hu, J., Liu, H. & Wang, H. Adsorption desulfurization by hierarchical porous organic polymer of poly-methylbenzene with metal impregnation. *Fuel* **170**, 100–106 (2016).
171. Song, H., Cui, X., Song, H., Gao, H. & Li, F. Characteristic and Adsorption Desulfurization Performance of Ag–Ce Bimetal Ion-Exchanged Y Zeolite. *Ind. Eng. Chem. Res.* **53**, 14552–14557 (2014).
172. Builes, S., Sandler, S. I. & Xiong, R. Isosteric heats of gas and liquid adsorption. *Langmuir* **29**, 10416–22 (2013).
173. Ma, L. & Yang, R. T. Selective Adsorption of Sulfur Compounds: Isotherms, Heats, and Relationship between Adsorption from Vapor and Liquid Solution. *Ind. Eng. Chem. Res.* **46**, 2760–2768 (2007).
174. Liping, M. & Yang, R. T. Heats of adsorption from liquid solutions and from pure vapor phase: Adsorption of thiophenic compounds on NaY and 13X zeolites. *Ind. Eng. Chem. Res.* **46**, 4874–4882 (2007).
175. Tian, F., Yang, X., Shi, Y., Jia, C. & Chen, Y. Adsorptive desulfurization over hierarchical beta zeolite by alkaline treatment. *J. Nat. Gas Chem.* **21**, 647–652 (2012).
176. Chen, H., Wang, Y., Yang, F. H. & Yang, R. T. Desulfurization of high-sulfur jet fuel by mesoporous π-complexation adsorbents. *Chem. Eng. Sci.* **64**, 5240–5246 (2009).
177. Jiang, J. & Ng, F. T. T. Production of low sulfur diesel fuel via adsorption: An equilibrium and kinetic study on the adsorption of dibenzothiophene onto NaY zeolite. *Adsorption* **16**, 549–558 (2010).
178. Shah, A. T., Li, B. & Abdalla, Z. E. A. Direct synthesis of Cu-SBA-16 by internal pH-

modification method and its performance for adsorption of dibenzothiophene. *Microporous Mesoporous Mater.* **130**, 248–254 (2010).
179. Zhang, W., Liu, H., Xia, Q. & Li, Z. Enhancement of dibenzothiophene adsorption on activated carbons by surface modification using low temperature oxygen plasma. *Chem. Eng. J.* **209**, 597–600 (2012).
180. Djemel, S., Guilleux, M.-F., Jeanjean, J., Tempere, J. F. & Delafosse, D. Effect of Ce3+ ions exchanged in NiX zeolites on the location and reducibility of Ni2+ ions and on the stabilization of a highly dispersed metallic nickel. *J. Chem. Soc. Faraday Trans. 1 Phys. Chem. Condens. Phases* **78**, 835 (1982).
181. U.S. Energy Information Administration. *Spot Prices for Crude Oil and Petroleum Products*. http://www.eia.gov/dnav/pet/pet_pri_spt_s1_d.htm (2016).
182. Rakita, B., Madic, V. & Markovic, D. Competitive strategies of late followers in auto industry: Case study Hyundai-Kia. *Industrija* **45**, 121–146 (2017).
183. Gamliel, D. P., Cho, H. J., Fan, W. & Valla, J. A. On the effectiveness of tailored mesoporous MFI zeolites for biomass catalytic fast pyrolysis. *Appl. Catal. A Gen.* **522**, 109–119 (2016).
184. Gamliel, D. P., Wilcox, L. & Valla, J. A. The Effects of Catalyst Properties on the Conversion of Biomass via Catalytic Fast Hydropyrolysis. (2016) doi:10.1021/acs.energyfuels.6b02781.
185. U.S. Environmental Protection Agency. *Integrated Science Assessment for Oxides of Nitrogen – Health Criteria*. https://www.epa.gov/isa/integrated-science-assessment-isa-nitrogen-dioxide-health-criteria (2016).
186. U.S. Environmental Protection Agency. *Integrated Science Assessment for Sulfur Oxides - Health Criteria*. https://www.epa.gov/isa/integrated-science-assessment-isa-sulfur-dioxide-health-criteria (2009).
187. Sharma, H. N., Sharma, V., Mhadeshwar, A. B. & Ramprasad, R. Why Pt survives but Pd suffers from SOx poisoning? *J. Phys. Chem. Lett.* **6**, 1140–1148 (2015).
188. Valla, J. A., Mouriki, E., Lappas, A. A. & Vasalos, I. A. The effect of heavy aromatic sulfur compounds on sulfur in cracked naphtha. *Catal. Today* **127**, 92–98 (2007).
189. Lappas, A. A., Valla, J. A., Vasalos, I. A., Kuehler, C., Francis, J., O'Connor, P. & Gudde, N. J. The effect of catalyst properties on the in situ reduction of sulfur in FCC gasoline. *Appl. Catal. A Gen.* **262**, 31–41 (2004).
190. Atimtay, A. T., Gasper-Galvin, L. D. & Poston, J. A. Novel supported sorbent for hot gas desulfurization. *Environ. Sci. Technol.* **27**, 1295–1303 (1993).
191. Bakr, A. & Salem, S. H. Naphtha Desulfurization by Adsorption. *Ind. Eng. Chem. Res* **33**, 336–340 (1994).
192. Kikkinides, E. S., Sikavitsas, V. I. & Yang, R. T. Natural-Gas Desulfurization by Adsorption -- Feasibility and Multiplicity of Cyclic Steady-States. *Ind. Eng. Chem. Res.* **34**, 255–262 (1995).
193. Rabo, J. a, Angell, P. H., Kasai, P. H. & Schomaker, V. tudies of cations in zeolites: adsorption of carbon monoxide; formation of Ni ions and Na3+4 centres. **41**, 328–349 (1966).
194. Denayer, J. F., Souverijns, W., Jacobs, P. A., Martens, J. A. & Baron, G. V. High-Temperature Low-Pressure Adsorption of Branched C 5 −C 8 Alkanes on Zeolite Beta, ZSM-5, ZSM-22, Zeolite Y, and Mordenite. *J. Phys. Chem. B* **102**, 4588–4597 (1998).
195. Langmi, H. W. *et al.* Hydrogen adsorption in zeolites A, X, Y and RHO. *J. Alloys Compd.*

356–**357**, 710–715 (2003).
196. Harlick, P. J. E. & Tezel, F. H. An experimental adsorbent screening study for CO2 removal from N2. *Microporous Mesoporous Mater.* **76**, 71–79 (2004).
197. Yusof, A. M. & Malek, N. A. N. N. Removal of Cr(VI) and As(V) from aqueous solutions by HDTMA-modified zeolite Y. *J. Hazard. Mater.* **162**, 1019–1024 (2009).
198. Holm, M. S., Taarning, E., Egeblad, K. & Christensen, C. H. Catalysis with hierarchical zeolites. *Catal. Today* **168**, 3–16 (2011).
199. Lutz, W. Zeolite Y: Synthesis, Modification, and Properties—A Case Revisited. *Adv. Mater. Sci. Eng.* **2014**, (2014).
200. Meunier, F. C., Verboekend, D., Gilson, J. P., Groen, J. C. & Pérez-Ramírez, J. Influence of crystal size and probe molecule on diffusion in hierarchical ZSM-5 zeolites prepared by desilication. *Microporous Mesoporous Mater.* **148**, 115–121 (2012).
201. Moliner, M. Direct Synthesis of Functional Zeolitic Materials. *ISRN Mater. Sci.* **2012**, 1–24 (2012).
202. Meng, X., Qiu, G., Wang, G., Cai, Q. & Wang, Y. Durable and regenerable mesoporous adsorbent for deep desulfurization of model jet fuel. *Fuel Process. Technol.* **111**, 78–85 (2013).
203. Li, W., Liu, Q., Xing, J., Gao, H., Xiong, X., Li, Y., Li, X. & Liu, H. High-efficiency desulfurization by adsorption with mesoporous aluminosilicates. *AIChE J.* **53**, 3263–3268 (2007).
204. Takahashi, A., Yang, F. H. & Yang, R. T. New Sorbents for Desulfurization by π-Complexation: Thiophene/Benzene Adsorption. *Ind. Eng. Chem. Res.* **41**, 2487–2496 (2002).
205. Hernández-Maldonado, A. J. & Yang, R. T. Desulfurization of commercial liquid fuels by selective adsorption via π-complexation with Cu(I)-Y zeolite. *Ind. Eng. Chem. Res.* **42**, 3103–3110 (2003).
206. Lin, L., Zhang, Y., Zhang, H. & Lu, F. Adsorption and solvent desorption behavior of ion-exchanged modified Y zeolites for sulfur removal and for fuel cell applications. *J. Colloid Interface Sci.* **360**, 753–759 (2011).
207. Lee, K. X. & Valla, J. A. Investigation of bifunctional zeolites for the adsorptive desulfurization of fuels. *Appl. Catal. B Environ.* **201**, 359–369 (2017).
208. Song, H., Chang, Y., Wan, X., Dai, M., Song, H. & Jin, Z. Equilibrium, Kinetic, and Thermodynamic Studies on Adsorptive Desulfurization onto Cu I Ce IV Y Zeolite. *Ind. Eng. Chem. Res.* **53**, 5701–5708 (2014).
209. Song, H., Chang, Y. & Song, H. Deep adsorptive desulfurization over Cu, Ce bimetal ion-exchanged Y-typed molecule sieve. *Adsorption* **22**, 139–150 (2016).
210. Shan, J. H., Liu, X. Q., Sun, L. B. & Cui, R. Cu-Ce bimetal ion-exchanged Y zeolites for selective adsorption of thiophenic sulfur. *Energy and Fuels* **22**, 3955–3959 (2008).
211. Sources, M. & Rule, F. Environmental Protection Agency Control of Hazardous Air Pollutants From Mobile Sources; Final Rule. *Fed. Regist.* **72**, (2007).
212. Marr, L. C., Kirchstetter, T. W., Harley, R. A., Miguel, A. H., Hering, S. V. & Hammond, S. K. Characterization of Polycyclic Aromatic Hydrocarbons in Motor Vehicle Fuels and Exhaust Emissions. *Environ. Sci. Technol.* **33**, 3091–3099 (1999).
213. Meunier, F. C., Domokos, L., Seshan, K. & Lercher, J. A. In situ IR study of the nature and mobility of sorbed species on H-FER during but-1-ene isomerization. *J. Catal.* **211**, 366–378 (2002).

214. Meng, T., Ren, N. & Ma, Z. Silicalite-1@Cu-ZSM-5 core-shell catalyst for N2O decomposition. *J. Mol. Catal. A Chem.* **404**–**405**, 233–239 (2015).
215. Bi, Y. S., Dang, G. Y., Zhao, X. H., Meng, X. F., Lu, H. J. & Jin, J. T. Preparation, characterization and catalytic properties of Pd-Fe-zeolite and Pd-Ce-zeolite composite catalysts. *J. Hazard. Mater.* **229**–**230**, 245–250 (2012).
216. Li, Y., Yang, F. H., Qi, G. & Yang, R. T. Effects of oxygenates and moisture on adsorptive desulfurization of liquid fuels with Cu(I)Y zeolite. *Catal. Today* **116**, 512–518 (2006).
217. Foo, G. S., Rogers, A. K., Yung, M. M. & Sievers, C. Steric Effect and Evolution of Surface Species in the Hydrodeoxygenation of Bio-Oil Model Compounds over Pt/HBEA. *ACS Catal.* **6**, 1292–1307 (2016).
218. Zu, Y., Qin, Y., Gao, X., Liu, H., Zhang, X., Zhang, J. & Song, L. Insight into the correlation between the adsorption-transformation behaviors of methylthiophenes and the active sites of zeolites Y. *Appl. Catal. B Environ.* **203**, 96–107 (2017).
219. Thomas, B. & Sugunan, S. Effect of rare earth metal ions on the structural and textural properties of NaFAU-Y zeolite and vapour phase alkylation of benzene with 1-octene. *Indian J. Chem. Technol.* **12**, 676–688 (2005).
220. Gutiérrez-Alejandre, A., Larrubia, M. A., Ramirez, J. & Busca, G. FT-IR evidence of the interaction of benzothiophene with the hydroxyl groups of H-MFI and H-MOR zeolites. *Vib. Spectrosc.* **41**, 42–47 (2006).
221. Vilarrasa-García, E., Azevedo, D. C. S., Braos-García, P., Infantes-Molina, A., Cavalcante, C. L., Jiménez-Jiménez, J., Jiménez-Lopez, A. & Rodríguez-Castellón, E. Synthesis and Characterization of Metal-Supported Mesoporous Silicas Applied to the Adsorption of Benzothiophene. *Adsorpt. Sci. Technol.* **29**, 691–704 (2012).
222. Yang, Y., Burke, N., Zhang, J., Huang, S., Lim, S. & Zhu, Y. Influence of charge compensating cations on propane adsorption in X zeolites: experimental measurement and mathematical modeling. *RSC Adv.* **4**, 7279 (2014).
223. Yelebe, Z. R., Yelebe, B. Z. & Samuel, R. J. CONTAMINANTS FROM INDUSTRIAL WASTEWATER. **5**, (2013).
224. Gao, X., Geng, W., Zhang, H., Zhao, X. & Yao, X. Thiophenic compounds adsorption on Na(I)Y and rare earth exchanged y zeolites: A density functional theory study. *J. Mol. Model.* **19**, 4789–4795 (2013).
225. Turnes Palomino, G., Bordiga, S., Lamberti, C., Zecchina, a. & Otero Areán, C. Vibrational and optical spectroscopic studies on copper-exchanged ferrierite. 199–206 (2002) doi:10.1016/S0167-2991(02)80029-5.
226. Wang, L., Sun, B., Yang, F. H. & Yang, R. T. Effects of aromatics on desulfurization of liquid fuel by π-complexation and carbon adsorbents. *Chem. Eng. Sci.* **73**, 208–217 (2012).
227. Fujiki, J. & Furuya, E. Density functional theory study of adsorption of benzothiophene and naphthalene on silica gel. *Fuel* **164**, 180–185 (2016).
228. Al-sasi, B. O., Taylan, O. & Demirbas, A. The impact of oil price volatility on economic growth. *Energy Sources, Part B Econ. Planning, Policy* **00**, 1–6 (2017).
229. Khan, M. I., Yasmeen, T., Shakoor, A., Khan, N. B. & Muhammad, R. 2014 oil plunge: Causes and impacts on renewable energy. *Renew. Sustain. Energy Rev.* **68**, 609–622 (2017).
230. Autodata Corporation. *United States Total Vehicle Sales*. http://www.tradingeconomics.com/united-states/total-vehicle-sales (2017).
231. U.S. Energy Information Administration. *April 2017 Monthly Energy Review*. https://www.eia.gov/totalenergy/data/monthly/pdf/mer.pdf (2017).

232. National Public Radio. *'America First' Energy Plan Challenges Free Market Realities*. http://www.npr.org/2017/02/07/513905161/trumps-energy-shift-could-bring-higher-gas-prices-analysts-say (2017).
233. Sanderson, B. M. & Knutti, R. Delays in US mitigation could rule out Paris targets. *Nat. Clim. Chang.* **7**, 92–94 (2016).
234. Zweifel, P., Praktiknjo, A. & Erdmann, G. Markets for Liquid Fuels. in *Energy Economics: Theory and Applications* 159–196 (Springer Berlin Heidelberg, 2017). doi:10.1007/978-3-662-53022-1_8.
235. Yang, R. T., Takahashi, A. & Yang, F. H. New Sorbents for Desulfurization of Liquid Fuels by π-Complexation. *Ind. Eng. Chem. Res.* **40**, 6236–6239 (2001).
236. Ma, X., Sun, L. & Song, C. A new approach to deep desulfurization of gasoline, diesel fuel and jet fuel by selective adsorption for ultra-clean fuels and for fuel cell applications. *Catal. Today* **77**, 107–116 (2002).
237. Cotton, F. A., Wilkinson, G., Murillo, C. a. & Bochmann, M. Advanced Inorganic Chemistry. in *John Wiley and Sons, Inc, New York* 1108–1129 (1999).
238. Samokhvalov, A. & Tatarchuk, B. J. Review of Experimental Characterization of Active Sites and Determination of Molecular Mechanisms of Adsorption, Desorption and Regeneration of the Deep and Ultradeep Desulfurization Sorbents for Liquid Fuels. *Catal. Rev.* **52**, 381–410 (2010).
239. Song, H., Gao, H., Song, H., Yang, G. & Li, X. Effects of Si/Al Ratio on Adsorptive Removal of Thiophene and Benzothiophene over Ion-Exchanged AgCeY Zeolites. *Ind. Eng. Chem. Res.* **55**, 3813–3822 (2016).
240. Serrano, D. P., Sanz, R., Pizarro, P., Moreno, I. & Medina, S. Hierarchical TS-1 zeolite as an efficient catalyst for oxidative desulphurization of hydrocarbon fractions. *Appl. Catal. B Environ.* **146**, 35–42 (2014).
241. Leng, K., Sun, Y., Zhang, X., Yu, M. & Xu, W. Ti-modified hierarchical mordenite as highly active catalyst for oxidative desulfurization of dibenzothiophene. *Fuel* **174**, 9–16 (2016).
242. Tang, T., Yin, C., Wang, L., Ji, Y. & Xiao, F. S. Good sulfur tolerance of a mesoporous Beta zeolite-supported palladium catalyst in the deep hydrogenation of aromatics. *J. Catal.* **257**, 125–133 (2008).
243. Huo, Q., Dou, T., Zhao, Z. & Pan, H. Synthesis and application of a novel mesoporous zeolite L in the catalyst for the HDS of FCC gasoline. *Appl. Catal. A Gen.* **381**, 101–108 (2010).
244. Lee, E. F. T. & Rees, L. V. C. Calcination of cerium(III) exchanged Y zeolite. *Zeolites* **7**, 446–450 (1987).
245. Nery, J. G., Mascarenhas, Y. P., Bonagamba, T. J., Mello, N. C. & Souza-Aguiar, E. F. Location of cerium and lanthanum cations in CeNaY and LaNaY after calcination. *Zeolites* **18**, 44–49 (1997).
246. QIU, L. *et al.* Investigation on the cation location, structure and performances of rare earth-exchanged Y zeolite. *J. Rare Earths* **35**, 658–666 (2017).
247. Paparazzo, E., Ingo, G. M. & Zacchetti, N. X-ray induced reduction effects at CeO_2 surfaces: An x-ray photoelectron spectroscopy study. *J. Vac. Sci. Technol. A Vacuum, Surfaces, Film.* **9**, 1416–1420 (1991).
248. Yu, X. & Li, G. XPS study of cerium conversion coating on the anodized 2024 aluminum alloy. *J. Alloys Compd.* **364**, 193–198 (2004).

249. Choung, J. W. & Nam, I. S. Characteristics of copper ion exchanged mordenite catalyst deactivated by HCl for the reduction of NOxwith NH3. *Appl. Catal. B Environ.* **64**, 42–50 (2006).
250. Salem, a. B. S. H. & Hamid, H. S. Removal of sulfur compounds from naphtha solutions using solid adsorbents. *Chem. Eng. Technol.* **20**, 342–347 (1997).
251. Hernández-Maldonado, A. J. & Yang, R. T. Desulfurization of Transportation Fuels by Adsorption. *Catal. Rev.* **46**, 111–150 (2004).
252. Liu, B., Zhu, Y., Liu, S. & Mao, J. Adsorption Equilibrium of Thiophenic Sulfur Compounds on the Cu- BTC Metal − Organic Framework. 1–5 (2012).
253. Lee, K. X., Wang, H., Karakalos, S., Tsilomelekis, G. & Valla, J. A. Adsorptive Desulfurization of 4,6-Dimethyldibenzothiophene on Bimetallic Mesoporous Y Zeolites: Effects of Cu and Ce Composition and Configuration. *Ind. Eng. Chem. Res.* **58**, 18301–18312 (2019).
254. Janin, A., Maache, M., Lavalley, J. C., Joly, J. F., Raatz, F. & Szydlowski, N. FT i.r. study of the silanol groups in dealuminated HY zeolites: Nature of the extraframework debris. *Zeolites* **11**, 391–396 (1991).
255. Gounder, R., Jones, A. J., Carr, R. T. & Iglesia, E. Solvation and acid strength effects on catalysis by faujasite zeolites. *J. Catal.* **286**, 214–223 (2012).
256. Moreira, C. R., Pereira, M. M., Alcobé, X., Homs, N., Llorca, J., Fierro, J. L. G. & Ramírez de la Piscina, P. Nature and location of cerium in Ce-loaded Y zeolites as revealed by HRTEM and spectroscopic techniques. *Microporous Mesoporous Mater.* **100**, 276–286 (2007).
257. Klots, T. D. & Collier, W. B. Heteroatom derivatives of indene. Part 2. Vibrational spectra of benzothiophene and benzothiazole. *Spectrochim. Acta Part A Mol. Biomol. Spectrosc.* **51**, 1273–1290 (1995).
258. Scherzer, J. Infrared spectra of ultrastable zeolites derived from type Y zeolites*1. *J. Catal.* **28**, 101–115 (1973).
259. Park, T. H., Cychosz, K. A., Wong-Foy, A. G., Dailly, A. & Matzger, A. J. Gas and liquid phase adsorption in isostructural Cu 3[biaryltricarboxylate]2 microporous coordination polymers. *Chem. Commun.* **47**, 1452–1454 (2011).
260. Xiong, J., Yang, L., Chao, Y., Pang, J., Zhang, M., Zhu, W. & Li, H. Boron Nitride Mesoporous Nanowires with Doped Oxygen Atoms for the Remarkable Adsorption Desulfurization Performance from Fuels. *ACS Sustain. Chem. Eng.* **4**, 4457–4464 (2016).
261. Bu, J., Loh, G., Gwie, C. G., Dewiyanti, S., Tasrif, M. & Borgna, A. Desulfurization of diesel fuels by selective adsorption on activated carbons: Competitive adsorption of polycyclic aromatic sulfur heterocycles and polycyclic aromatic hydrocarbons. *Chem. Eng. J.* **166**, 207–217 (2011).
262. Takahashi, A., Yang, R. T., Munson, C. L. & Chinn, D. Cu(I)-Y-zeolite as a superior adsorbent for diene/olefin separation. *Langmuir* **17**, 8405–8413 (2001).
263. Crespo, D., Qi, G., Wang, Y., Yang, F. H. & Yang, R. T. Superior sorbent for natural gas desulfurization. *Ind. Eng. Chem. Res.* **47**, 1238–1244 (2008).
264. Araújo, R. S., Azevedo, D. C. S., Rodríguez-Castellón, E., Jiménez-López, A. & Cavalcante, C. L. Al and Ti-containing mesoporous molecular sieves: Synthesis, characterization and redox activity in the anthracene oxidation. *J. Mol. Catal. A Chem.* **281**, 154–163 (2008).
265. Ratnasamy, P. & Srinivas, D. Selective oxidations over zeolite- and mesoporous silica-

based catalysts: Selected examples. *Catal. Today* **141**, 3–11 (2009).
266. Frising, T. & Leflaive, P. Extraframework cation distributions in X and Y faujasite zeolites: A review. *Microporous Mesoporous Mater.* **114**, 27–63 (2008).
267. Hernandez-Maldonado, A. J., Yang, R. T. & Cannella, W. Desulfurization of Commercial Jet Fuels by Adsorption via π-Complexation with Vapor Phase Ion Exchanged Cu(I)−Y Zeolites. *Ind. Eng. Chem. Res.* **43**, 6142–6149 (2004).
268. Whitehurst, D. D., Isoda, T. & Mochida, I. *Present State of the Art and Future Challenges in the Hydrodesulfurization of Polyaromatic Sulfur Compounds*. *Advances in Catalysis* vol. 42 (Elsevier Masson SAS, 1998).
269. Macaud, M., Milenkovic, A., Schulz, E., Lemaire, M. & Vrinat, M. Hydrodesulfurization of alkyldibenzothiophenes: Evidence of highly unreactive aromatic sulfur compounds. *J. Catal.* **193**, 255–263 (2000).
270. Ted Oyama, S., Zhao, H., Freund, H. J., Asakura, K., Włodarczyk, R. & Sierka, M. Unprecedented selectivity to the direct desulfurization (DDS) pathway in a highly active FeNi bimetallic phosphide catalyst. *J. Catal.* **285**, 1–5 (2012).
271. Zhang, Z. Y., Shi, T. B., Jia, C. Z., Ji, W. J., Chen, Y. & He, M. Y. Adsorptive removal of aromatic organosulfur compounds over the modified Na-Y zeolites. *Appl. Catal. B Environ.* **82**, 1–10 (2008).
272. Sentorun-Shalaby, C., Saha, S. K., Ma, X. & Song, C. Mesoporous-molecular-sieve-supported nickel sorbents for adsorptive desulfurization of commercial ultra-low-sulfur diesel fuel. *Appl. Catal. B Environ.* **101**, 718–726 (2011).
273. Khan, N. A., Jun, J. W., Jeong, J. H. & Jhung, S. H. Remarkable adsorptive performance of a metal–organic framework, vanadium-benzenedicarboxylate (MIL-47), for benzothiophene. *Chem. Commun.* **47**, 1306–1308 (2011).
274. Srivastav, A. & Srivastava, V. C. Adsorptive desulfurization by activated alumina. *J. Hazard. Mater.* **170**, 1133–1140 (2009).
275. Zhou, A., Ma, X. & Song, C. Effects of oxidative modification of carbon surface on the adsorption of sulfur compounds in diesel fuel. *Appl. Catal. B Environ.* **87**, 190–199 (2009).
276. Ziegler, T. Approximate Density Functional Theory as a Practical Tool in Molecular Energetics and Dynamics. *Chem. Rev.* **91**, 651–667 (1991).
277. Delabie, A., Pierloot, K., Groothaert, M. H., Weckhuysen, B. M. & Schoonheydt, R. A. Study of the coordination of Cu2+ in zeolite Y: Interaction with water and ammonia. *Microporous Mesoporous Mater.* **37**, 209–222 (2000).
278. Uzunova, E. L., Mikosch, H. & Hafner, J. Theoretical study of transition metal cation exchanged zeolites: Interaction with NO. *J. Mol. Struct. THEOCHEM* **912**, 88–94 (2009).
279. Pirngruber, G. D., Raybaud, P., Belmabkhout, Y., Čejka, J. & Zukal, A. The role of the extra-framework cations in the adsorption of CO2 on faujasite y. *Phys. Chem. Chem. Phys.* **12**, 13534–13546 (2010).
280. Sierraalta, A., Bermudez, A. & Rosa-Brussin, M. Density functional study of the interaction of Cu+ ion-exchanged zeolites with H2O and SO2 molecules. *J. Mol. Catal. A Chem.* **228**, 203–210 (2005).
281. Kumar, P., Sung, C. Y., Muraza, O., Cococcioni, M., Al Hashimi, S., McCormick, A. & Tsapatsis, M. H2S adsorption by Ag and Cu ion exchanged faujasites. *Microporous Mesoporous Mater.* **146**, 127–133 (2011).
282. Chen, X., Shen, B. X., Sun, H., Zhan, G. X. & Huo, Z. Z. Adsorption and Its Mechanism of CS2 on Ion-Exchanged Zeolites y. *Ind. Eng. Chem. Res.* **56**, 6499–6507 (2017).

283. Treesukol, P., Srisuk, K., Limtrakul, J. & Truong, T. N. Nature of the metal-support interaction in bifunctional catalytic Pt/H-ZSM-5 zeolite. *J. Phys. Chem. B* **109**, 11940–11945 (2005).
284. Geng, W., Zhang, H., Zhao, X., Zan, W., Gao, X. & Yao, X. Theoretical studies of the nitrogen containing compounds adsorption behavior on Na(I)Y and rare earth exchanged RE(III)Y zeolites. *J. Mol. Model.* **21**, 1–9 (2015).
285. Yang, F. H., Hernandez-Maldonado, A. J. & Yang, R. T. Selective adsorption of organosulfur compounds from transportation fuels by π-complexation. *Sep. Sci. Technol.* **39**, 1717–1732 (2004).
286. Liu, D., Song, L., Gui, J., Liu, S. & Sun, Z. Adsorption structures of heterocyclic sulfur compounds on Cu(I)Y zeolite: a first principle study. in *Studies in Surface Science and Catalysis* vol. 170 1699–1704 (Elsevier B.V., 2007).
287. Wang, L., Sun, Z., Ding, Y., Chen, Y., Li, Q., Xu, M., Li, H. & Song, L. A theoretical study of thiophenic compounds adsorption on cation-exchanged y zeolites. *Appl. Surf. Sci.* **257**, 7539–7544 (2011).
288. Bobuatong, K. & Limtrakul, J. Effects of the zeolite framework on the adsorption of ethylene and benzene on alkali-exchanged zeolites: An ONIOM study. *Appl. Catal. A Gen.* **253**, 49–64 (2003).
289. Kasuriya, S., Namuangruk, S., Treesukol, P., Tirtowidjojo, M. & Limtrakul, J. Adsorption of ethylene, benzene, and ethylbenzene over faujasite zeolites investigated by the ONIOM method. *J. Catal.* **219**, 320–328 (2003).
290. Pantu, P., Boekfa, B. & Limtrakul, J. The adsorption of saturated and unsaturated hydrocarbons on nanostructured zeolites (H-MOR and H-FAU): An ONIOM study. *J. Mol. Catal. A Chem.* **277**, 171–179 (2007).
291. Sun, Y., Mao, X. & Pei, S. A two-layer {ONIOM} study of thiophene cracking catalyzed by proton- and cation-exchanged {FAU} zeolite. *J. Mol. Model.* **22**, 1–16 (2016).
292. Jardillier, N., Villagomez, E. A., Delahay, G., Coq, B. & Berthomieu, D. Probing CuI-exchanged zeolite with CO: DFT modeling and experiment. *J. Phys. Chem. B* **110**, 16413–16421 (2006).
293. Barthomeuf, D. Basic Zeolites: Characterization and Uses in Adsorption and Catalysis. *Catal. Rev.* **38**, 521–612 (1996).
294. Becke, A. D. Density-functional thermochemistry. III. The role of exact exchange. *J. Chem. Phys.* **98**, 5648–5652 (1993).
295. Rappé, A. K., Casewit, C. J., Colwell, K. S., Goddard, W. A. & Skiff, W. M. UFF, a Full Periodic Table Force Field for Molecular Mechanics and Molecular Dynamics Simulations. *J. Am. Chem. Soc.* **114**, 10024–10035 (1992).
296. Weinhold, F. *et al.* Analysis NBO 7.0. (2018).
297. Castagnola, N. B., Kropf, A. J. & Marshall, C. L. Studies of Cu-ZSM-5 by X-ray absorption spectroscopy and its application for the oxidation of benzene to phenol by air. *Appl. Catal. A Gen.* **290**, 110–122 (2005).
298. Fowkes, A. J., Ibberson, R. M. & Rosseinsky, M. J. Structural characterization of the redox behavior in copper-exchanged sodium zeolite Y by high-resolution powder neutron diffraction. *Chem. Mater.* **14**, 590–602 (2002).
299. Haji, S. & Erkey, C. Removal of Dibenzothiophene from Model Diesel by Adsorption on Carbon Aerogels for Fuel Cell Applications. *Ind. Eng. Chem. Res.* **42**, 6933–6937 (2003).
300. Wang, Y., Yang, F. H., Yang, R. T., Heinzel, J. M. & Nickens, A. D. Desulfurization of

High-Sulfur Jet Fuel by π-Complexation with Copper and Palladium Halide Sorbents. *Ind. Eng. Chem. Res.* **45**, 7649–7655 (2006).
301. Dehghan, R. & Anbia, M. Zeolites for adsorptive desulfurization from fuels: A review. *Fuel Process. Technol.* **167**, 99–116 (2017).
302. Lü, R., Lin, J. & Qu, Z. Theoretical study on interactions between ionic liquids and organosulfur compounds. *Comput. Theor. Chem.* **1002**, 49–58 (2012).
303. Joshi, Y. V., Ghosh, P., Venkataraman, P. S., Delgass, W. N. & Thomson, K. T. Electronic descriptors for the adsorption energies of sulfur-containing molecules on co/mos2, using dft calculations. *J. Phys. Chem. C* **113**, 9698–9709 (2009).
304. Ferreira, L. S. & Trierweiler, J. O. Modeling and simulation of the polymeric nanocapsule formation process. *IFAC Proc. Vol.* **7**, 405–410 (2009).
305. Liu, D., Gui, J. & Sun, Z. Adsorption structures of heterocyclic nitrogen compounds over Cu(I)Y zeolite: A first principle study on mechanism of the denitrogenation and the effect of nitrogen compounds on adsorptive desulfurization. *J. Mol. Catal. A Chem.* **291**, 17–21 (2008).
306. Wu, J., Yan, H., Chen, H., Zhong, A. & Cao, W. Insight into the nature of the interactions of pyridine , funan and thiophene with LiNH 2. *Comput. Theor. Chem.* **1000**, 52–59 (2012).